Dissertation by:
André Hollstein

Vector Radiative Transfer and its Application to the Remote Sensing of Aerosols and Hydrosols

Vector Radiative Transfer and its Application to the Remote Sensing of Aerosols and Hydrosols

André Hollstein

January 16, 2013

Institute for Space Sciences

Dissertation

Submitted to the Department of Earth Sciences of the
Freie Universität Berlin

1. Gutachter: Prof. Dr. Jürgen Fischer
2. Gutachter: Prof. Dr. Ralf Bennartz
Tag der Dissputation: 19. Dezember 2012

Contents

CHAPTER 1

MOTIVATION AND INTRODUCTION

Remote sensing has opened a new chapter for global Earth observations. It is the tool that transforms Earth observation images into quantitative data products. It transforms qualitative statements like "*There is a cloud.*" into quantitative ones: "*There is a cloud, with a cloud top pressure of* $200 \pm 50hPa$ *and liquid water content of* $0.3 \pm 0.1g/m^3$". Remote sensing data products are used in an enormously rich field of applications and research, for instance human health, meteorology, climate, geodesy, biology, or oceanography. Figure 1.1.1 shows an illustrative example. Data from the SEVIRI instrument on board the geostationary satellite MSG is used to produce a pseudo true color image of Earth. The data was used to derive a quantitative cloud top pressure product, which for example can be used in climate studies or for weather prediction.

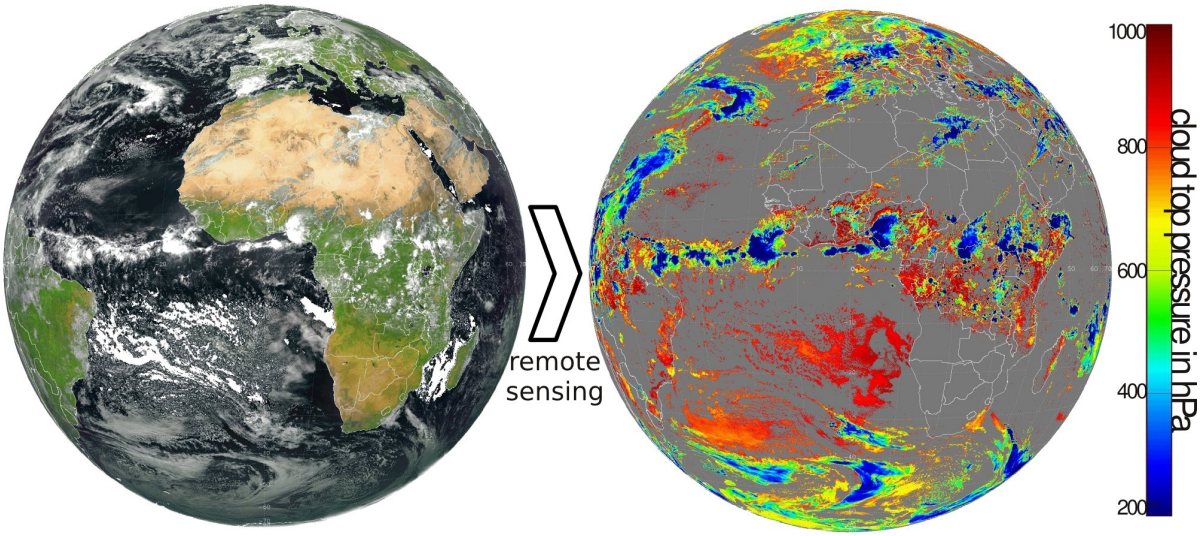

Figure 1.1.1: Image from the 5th of May 2012 from the SEVIRI instrument on board the MSG satellite. A remote sensing algorithm was used to produce a map of a cloud top pressure product using SEVIRI data. Level 1B data from EUMETSAT was used, both images were produced at the Institute for Space Sciences.

This dissertation contains several contributions to the wide research field of remote sensing and radiative transport. In this field of research, several prerequisites are required for a successful retrieval of data products. One of them are accurate measurements of the radiometric properties of the measured light and for some applications this includes polarimetric measurements. Executing such measurements is part of the field of **polarimetry** and Chapter 2 covers techniques that can be used to design optimal polarimeters using polarizing filters and waveplates. Also discussed is a robust technique for the characterization of the optical properties of waveplates.

One of the main tools of remote sensing are accurate **vector radiative transfer** simulations. Chapter 3 deals with the implementation of a vector radiative transfer model for the coupled atmosphere ocean system. The radiative transfer model is based on the MOMO model,

which has a long tradition of successful applications at the Institute for Space Sciences at *Freie Universität Berlin*. In the second section of the chapter, a new but simple approach for the validation of radiative transfer models is proposed.

Three **applications** of the developed model in the field of remote sensing of aerosols and hydrosols are discussed in Chapter 4. The simulated spectral channels range from $400nm$ to $1000nm$ as shown in Figure 1.1.2. The gray areas show the spectral width of the simulated MERIS and OLCI channels. Their measurements are used in a wide range of remote sensing applications for the ocean, land surface, and atmosphere.

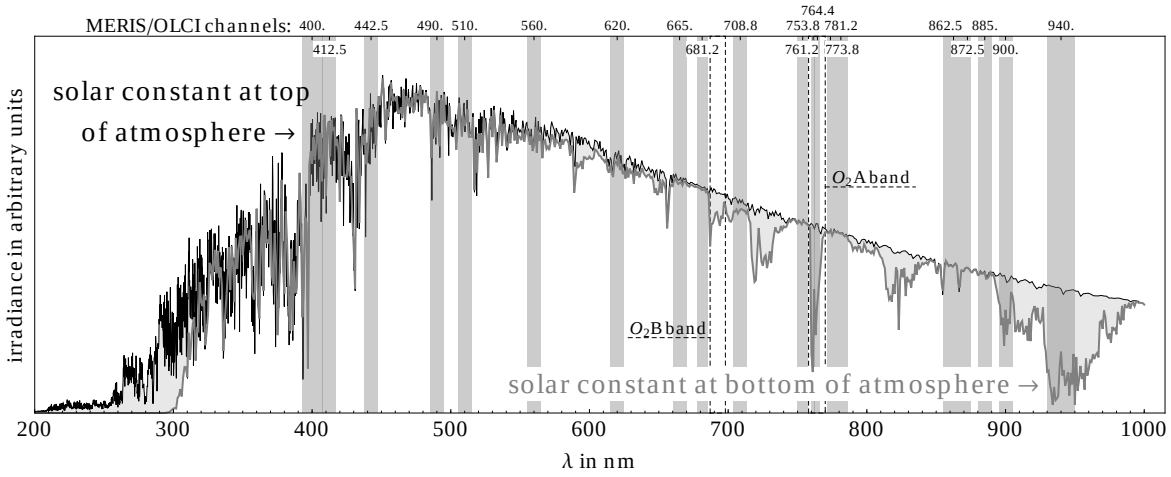

Figure 1.1.2: Direct solar spectrum[1] as it could be measured at the top (black line) and at the bottom (gray line) of the atmosphere if only absorption from atmospheric constituents is considered. The gray boxes show the width and position of measurement channels of the MERIS and OLCI instruments. The dashed lines show the position of the oxygen A and B bands, which are also visible at the bottom of atmosphere spectrum.

Section 4.2 discusses the effects of sea water salinity and temperature on water-leaving radiance and top-of-atmosphere radiance. These effects are widely neglected in current implementations of ocean color remote sensing algorithms. Discussed in Section 4.3 are possibilities for the remote sensing of the aerosol vertical distribution using hyper spectral radiance measurements in oxygen absorption bands. The spectral position of the facilitated oxygen A and B band is also shown in Figure 1.1.2. Simulations for the oxygen A band were performed and applied to set up a simple retrieval scheme for measurements made by the TANSO-FTS instrument on board the GOSAT satellite, which is described in Section 4.4.

The three examples combine theoretical techniques with their application to measured data sets and, next to their content itself, provide a good overview about the applicability of radiative transfer simulations in the research field of Earth observation.

[1] Data was provided by Rasmus Lindstrot and is based on absorption calculations using the HITRAN database.

About This Book

This book is based on research that was conducted for various projects. Most of the results were published by or submitted to peer reviewed journals. Some of the unpublished material was presented at international conferences. The majority of sections is written in the style of a research paper, which means that textbook knowledge is mostly omitted and only referenced. A reader without some background in radiometry, polarimetry, radiative transfer, or inverse modeling might need to consult some of the cited material. Each chapter begins with a short introduction of the general ideas behind the field of research, and references to its basic principles.

Chapter 2 is based on work the for AMSSP project [1] which was funded by DFG. The presented work was published in peer reviewed journals and is reproduced here as Section 2.2 and Section 2.3:

> *André Hollstein, Thomas Ruhtz, Jürgen Fischer, and René Preusker. Optimization of system parameters for a complete multispectral polarimeter.* Applied Optics*, 48:4767–4773, 2009*,

---

> *André Hollstein and Thomas Ruhtz. Method for retrieving the polarization properties of a waveplate assembled in a multispectral, complete polarimeter.* Opt. Lett.*, 34(17):2599–2601, Sep 2009.*

The foundation for both research results was laid in my diploma thesis [4]. After submitting my thesis, I continued to work in this field, extended the original results and, together with my co-authors, published the two papers. The result covered in the first paper is described much more rigorously, a analytic solution for special cases was added, and the propagation of error was included. The results were presented with a poster at the *2009 WE-Heraeus-Seminar on satellite remote sensing of aerosols: techniques, limitations, and validation* and was awarded with the poster prize of its session. The results presented in the second paper are also discussed more rigorously and additional measurements were analyzed.

The advancement of the MOMO radiative transfer model, which is described in Chapter 3, was supported by the WATERRADIANCE project of ESA. Main results of the model development and validation were published in a peer reviewed journal and are reproduced here as Section 3.2 and Section 3.3:

> *André Hollstein and Jürgen Fischer. Radiative Transfer Solutions for Coupled Atmosphere Ocean Systems Using the Matrix Operator Technique.* Journal of Quantitative Spectroscopy and Radiative Transfer*, 113(7):536 – 548, 2012*,

---

> *André Hollstein. Verification of radiative transfer results by inserting them into the RTE: A demonstration for rayleigh scattering.* Journal of Quantitative Spectroscopy and Radiative Transfer*, 113(15):1970 – 1973, 2012.*

The application of the MOMO model to the remote sensing of aerosols and hydrosols as described in Chapter 4 were supported by the WATERRADIANCE and the FLUSS project of ESA. The results for the effects of ocean salinity and temperature were supported by the WATERRADIANCE project. The results, which are covered in Section 4.2, were submitted to a peer reviewed journal and were also presented at the IRS conference 2012:

> *André Hollstein and Jürgen Fischer. Effects of salinity, temperature, and polarzation on top of atmosphere and water leaving radiances for case one waters.* Applied Optics*, 10 2012. doc. ID 169561, accepted 10/17/2012*,
>
> ---
>
> *André Hollstein and Jürgen Fischer. Salinity, temperature and polarization effects for simulated radiances in a case one waters atmosphere ocean system. IRS2012-9, 8 2012.*

The results concerning the remote sensing of aerosol vertical distribution were supported by the FLUSS project, were presented at various internal meetings, and were used for internal reports. Main results were presented at the IRS 2012 conference and a four-page paper was submitted to the peer-reviewed conference proceedings:

> *André Hollstein and Jürgen Fischer. Possibilities for remote sensing of aerosol vertical structure using the O_2A band: A sensitivity study concerning polarization, spectral resolution, instrument level, and various scenes over land. IRS2012-65, 8 2012*,
>
> ---
>
> *André Hollstein and Florian Filipitsch. Possibilities for the retrieval of aerosol vertical profiles from space using hyper spectral radiance measurements in oxygen absorption bands. submitted to the Proceedings of IRS2012, 8 2012.*

The proceedings paper covers only the main results of the conducted research. A much more detailed discussion is given in Section 4.3.

The presented publications were only slightly edited and reformatted for this book. Text and figures were only modified to improve readability and to correct typing errors. The 1st person plural voice (for example, “we show that”) is used in some of the published papers and thus sections of this book. This is inconsistent to some extend, but was kept since the papers were originally published in that way.

CHAPTER 2

POLARIMETRY

Contents

Polarimetry is the science of *metering* the polarization of electro magnetic radiation. Polarization describes the temporal correlation of the electro magnetic field, which forms the radiance field. The radiance field of Earth's atmosphere is perceived by us as daylight and its spectrum[1] as color. Under the physical conditions of Earth's atmosphere, the radiance L is simply proportional to the square of the electric field $\vec{E}$, normalized to the opening angle of the sensor, and $\vec{E}$ is a solution of Maxwell's equation applied to the solar system. Radiance sensors do not measure the current state of the electric field, but rather integrate the radiance over a period of time, and therefore average out the temporal variation of the electric field,[2] The inherent vector nature of the eclectic field is lost by the averaging of a radiance measurement. The real electric field can be constructed as a superposition of plane waves, and the projection of a single wave onto a coordinate system defined by a sensor is shown in Figure 2.1.1.

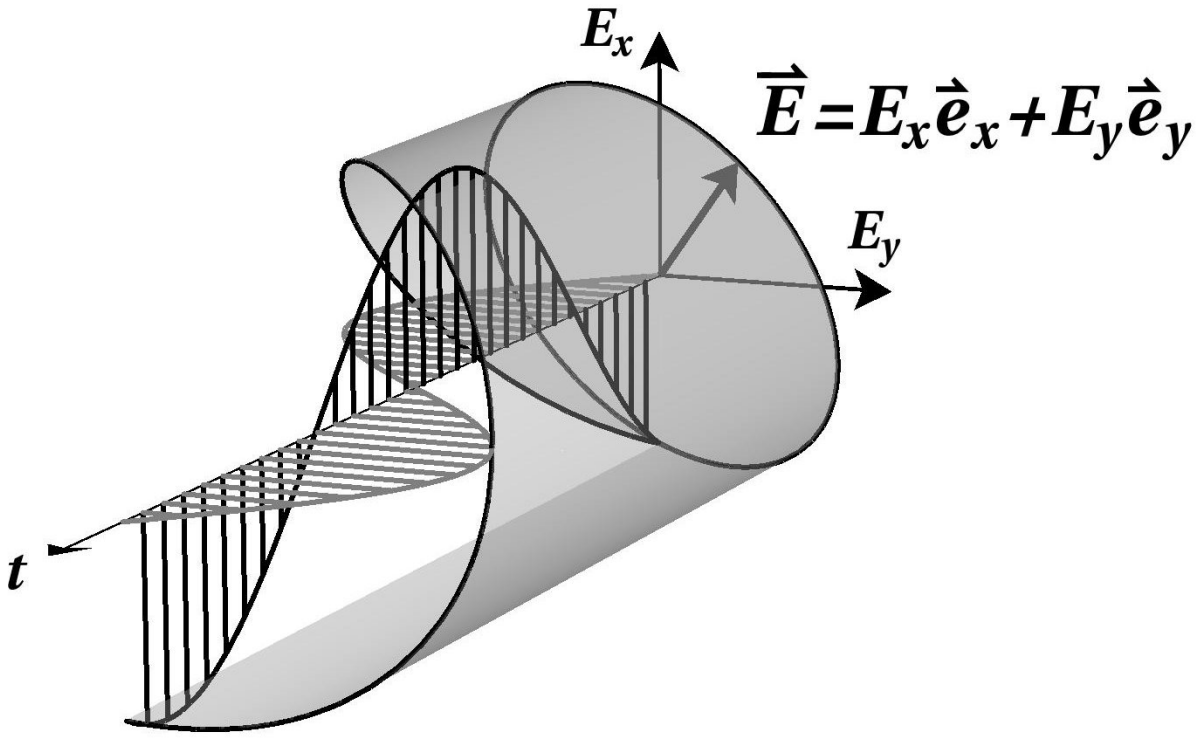

Figure 2.1.1: The electric field $\vec{E}$ and the temporal variation of its components projected to the axes $\vec{e}_x$ and $\vec{e}_y$. The sum of both components is shown as black line and, in the shown case, the electric field vector rotates around the axis of time. Not shown is the $\vec{e}_z$ axis, which is assumed to be perpendicular to the plane spanned by $\vec{e}_x$ and $\vec{e}_y$ and parallel to the viewing direction of the sensor defining this coordinate system.

Shown is the variation of the electric field in time and in the direction of the radiance sensor. The field can be separated into its components projected onto the axes of a coordinate system defined by the viewing geometry of a sensor. In the figure, the $\vec{e}_z$ axis not shown, but it is assumed that it is aligned parallel to the viewing direction of the sensor and perpendicular to the $x-y$ plane. Without loss of generality, let the electric field[3] in this plane be:

[1] Which is true only for the part which the human eye is sensitive to. [2] Much more detailed information can be found in almost any textbook on electrodynamics. A comprehensive and rigorous description is given also in references [11, 12]. A plane electric wave with a wavelength of $400nm$ oscillates in a vacuum roughly $7.5 * 10^{14}$ times in one second, which is a lot. [3] A more rigorous treatment can be found in reference [13] and references therein.

$$\vec{E} := \begin{pmatrix} e^{i(\varphi_x+\omega t)}\mathrm{E}_x \\ e^{i(\varphi_y+\omega t)}\mathrm{E}_y \end{pmatrix} \Rightarrow C_{ij} = \langle E_i E_j^* \rangle, (i,j = x,y), \tag{2.1.1}$$

where $E_{x,y}$ are the field amplitudes, $\varphi_{x,y}$ the field phases, and ω the angular frequency. The $\langle . \rangle$ indicates the averaging of the sensor over time (integration time) and space (opening angle). Using this notation, the coherence matrix C of the field can be calculated and expanded in a basis that spans the space of Hermitian, complex, and 2×2 matrices. The definition of a basis is arbitrary, but a commonly used example in the field of physics are the Pauli matrices $\vec{\sigma}$:

$$\vec{\sigma} = (\sigma_1, \ldots, \sigma_4) = \frac{1}{\sqrt{2}} \left(\begin{pmatrix} 1 & 0 \\ 0 & 1 \end{pmatrix}, \begin{pmatrix} 0 & 1 \\ 1 & 0 \end{pmatrix}, \begin{pmatrix} 0 & -i \\ i & 0 \end{pmatrix}, \begin{pmatrix} 1 & 0 \\ 0 & -1 \end{pmatrix} \right). \tag{2.1.2}$$

The coherence matrix can be written as symbolic scalar product $C = \sum_i \sigma_i s_i =: \vec{S}\vec{\sigma}$ and the expansion coefficients s_i as a symbolic vector $\vec{S}$:

$$\vec{S} := (s_0, s_1, s_2, s_3)^T, \tag{2.1.3}$$

which is the Stokes vector. Its components describe the temporal correlation of the electric field with respect to the chosen basis $\vec{\sigma}$. The task of polarimetry is then to measure the Stokes vector components. A widely used definition of $\vec{\sigma}$ leads to the Stokes vector in (I, Q, U, V) notation, where I is the radiance, Q and U are the linear polarized radiance components, and V is the circular polarized radiance component. This definition shows that polarization is an inherent property of the radiance field, but the values describing it depend on the chosen basis $\vec{\sigma}$, which must be known to compare independent measurements. This arbitrary choice can be a source of error and confusion, but can be used to simplify the math for a particular instrument.

In general, we human beings do not perceive polarization as we see light and color. To study polarization and its properties, we rely on polarimeter instruments, which among other tools, can be built using polarization filters and waveplates. However, the polarization properties of radiation are used in many applications, for instance to enhance contrast for photographs or in special glasses made for hiking, driving, or sailing. In contrast to humans, many animals can perceive polarization [14]. A striking example is the mantis shrimp, which is shown in Figure 2.1.3. It not only has the ability to deal super fast underwater blows, which can even cause cavitation [15], but their eyes operate as a multi-spectral polarimeter [16]. Figure 2.1.2 shows its eye, which has eight different types of photo receptors and in addition receptors that are sensitive to linear and even to circular polarization. This indicates that this creature has a very different understanding of light and color than we humans do.

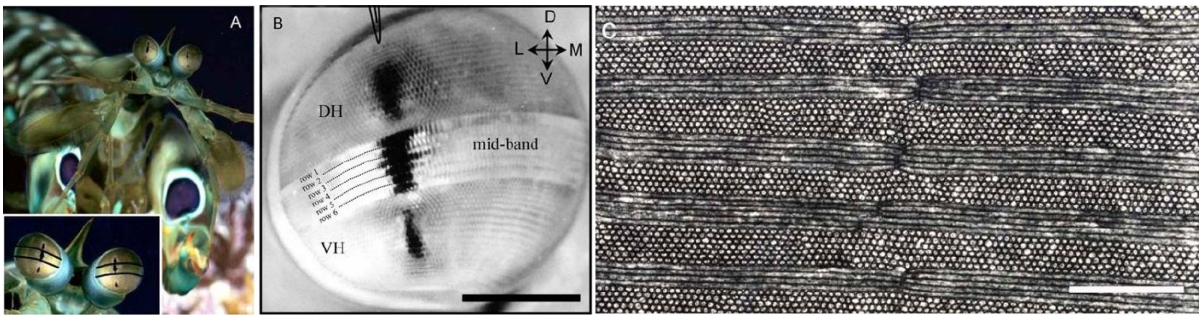

Figure 2.1.2: Images of the mantis shrimp eye [16]. Different rows of the eye (see pannel B and C) contain different photosensitive cells, which are in addition sensitive to polarization.

Figure 2.1.3: Image of the mantis shrimp [17]. They are about 7*cm* in size and can be found from New Caledonia up to the West Indian Ocean.

While the mantis shrimp uses its polarization vision for underwater navigation, environment identification, and communication, we humans can use it, for example, for the remote sensing of clouds and aerosols [18, 19, 20] using ground-, air-, or space-borne polarimeters. Section 2.2 describes a strategy to design optimal multi-spectral polarimeters. This section was published in the peer-reviewed journal *Applied Optics* as:

> *André Hollstein, Thomas Ruhtz, Jürgen Fischer, and René Preusker. Optimization of system parameters for a complete multispectral polarimeter.* Applied Optics*, 48:4767–4773, 2009.*

The design of the described class of polarimeters consists of linear polarization filters, as well as of waveplates. These optical elements have the ability to transform linear polarization states into circular ones and vice versa. Section 2.3 describes a method to robustly characterize these optical elements. Is was published in the peer-reviewed journal *Optical Letters* as:

> *André Hollstein and Thomas Ruhtz. Method for retrieving the polarization properties of a waveplate assembled in a multispectral, complete polarimeter.* Opt. Lett.*, 34(17):2599–2601, Sep 2009.*

2.2 Optimization of System Parameters for a Complete Multispectral Polarimeter

2.2.1 Abstract

A general class of complete multispectral polarimeters is optimized with respect to signal to noise ratio, stability against alignment errors and the minimization of errors regarding a given set of polarization states. The class of polarimeters that are dealt with consists of at least four polarization optics, each with a multispectral detector. A polarization optic is made of an azimuthal oriented waveplate and polarizing filter. A general but not unique analytic solution that minimizes signal to noise ratio is introduced for a polarimeter that incorporates four simultaneous measurements with four independent optics. The optics consist of four sufficient waveplates, where at least one is a quarter waveplate. The solution is stable with respect to the retardance of the quarter waveplate; therefore it can be applied to real world cases where the retardance deviates from $\lambda/4$. The solution is a set of seven rotational parameters that depends on the given retardances of the waveplates. It can be applied to a broad range of real world cases.

Consecutively, a numerical method for the optimization of arbitrary polarimeters of the discussed type is presented and applied to two cases. First, the class of polarimeters that was analytically dealt with is further optimized with respect to stability and error performance with respect to linear polarized states. The second case was a multispectral case for a polarimeter that consists of four optics with real achromatic waveplates. This case was used as the theoretical background for the development of the airborne, complete and multispectral polarimeter AMSSP, which is an instrument for the German research aircraft HALO.

2.2.2 Introduction

The self correlation of a beam of electromagnetic radiation can be represented in form of its real Stokes vector $\vec{S} := \{s_i\}$ and a four dimensional Hermitian $\mathbb{C}^{2\times2} := \{c_{ij}\}$ coherence matrix S. The definition of the polarization parameters s_i and c_{ij} depends on the chosen coordinate systems and may differ from author to author [13]. In most definitions, the first component of the four vector $\vec{S}$ and the *trace* of C are described by the intensity I of the beam. Non-depolarizing optical elements such as polarization filters or waveplates can be described by their $\mathbb{C}^{2\times2}$ Jones matrix [21]. The incident light S is transformed to S' by transmission through the element. The Jones matrix J describing the element transforms the coherence matrices S of the incident lights as follows [22]:

$$S' = JSJ^{\dagger}. \tag{2.2.1}$$

The real vectors of $\vec{S}$ can be represented in three dimensions by capitalizing on the Poincaré sphere [23]. The components s_1 to s_3 are normalized with respect to s_0. The new dimensionless axes $s_i/s_0,\ i = 1, 2, 3$ are then used as axes of a Cartesian coordinate system. Any Stokes vector with a degree of polarization of one, lies on the surface of a sphere with radius one around the origin. Any optical element described by its Jones or Mueller matrix can be represented by the real four vector, whose scalar product with the Stokes vector of the incident light, yields the intensity of the transmitted beam [24].

2.2.3 Instrument design

Calibrated detectors, such as CCD spectrometers or photo diodes, measure the intensity of an incident beam of light. To measure the complete Stokes vector of the beam, one must therefore use known polarizing elements in front of the detector where the transmitted intensity is affected

by all four polarization parameters. Polarizing filters and waveplates with given retardance δ are available off the shelf and a waveplate followed by a polarizer realizes the proposed property. One possible realization with four entrance optics is shown in Figure 2.2.1.

The Jones matrix of an ideal polarizer can be computed as the rotational transformation $R(\theta)$ of a filter matrix F:

$$\begin{aligned} P(\theta) &:= R(\theta)FR(\theta)^\dagger \rightleftharpoons \\ &= \begin{pmatrix} \cos(\theta) & -\sin(\theta) \\ \sin(\theta) & \cos(\theta) \end{pmatrix} \begin{pmatrix} 1 & 0 \\ 0 & 0 \end{pmatrix} \begin{pmatrix} \cos(\theta) & -\sin(\theta) \\ \sin(\theta) & \cos(\theta) \end{pmatrix}^\dagger = \begin{pmatrix} \cos^2(\theta) & \cos(\theta)\sin(\theta) \\ \cos(\theta)\sin(\theta) & \sin^2(\theta) \end{pmatrix}. \end{aligned} \tag{2.2.2}$$

The Jones matrix of an ideal waveplate can be computed by rotating a matrix that introduces a phase shift between the two components of a Jones vector:

$$W(\theta, \delta) := R(\theta)W(\delta)R(\theta)^\dagger = R(\theta) \begin{pmatrix} 1 & 0 \\ 0 & e^{i\delta} \end{pmatrix} R(\theta)^\dagger. \tag{2.2.3}$$

The instrument design consists of four entrance optics followed by a rotated waveplate, a polarizing filter and a detector. See also references [25, 24]. The optical setup can be described by the optics matrix O, which is the dot product of the single elements:

$$O(\delta, \varphi_p, \varphi_{wp}) := P(\varphi_p)W(\varphi_p + \varphi_{wp}, \delta). \tag{2.2.4}$$

The detector measures the intensity of the beam, which is given by:

$$I = Tr\left(OSO^\dagger\right) =: \vec{O}\vec{S}. \tag{2.2.5}$$

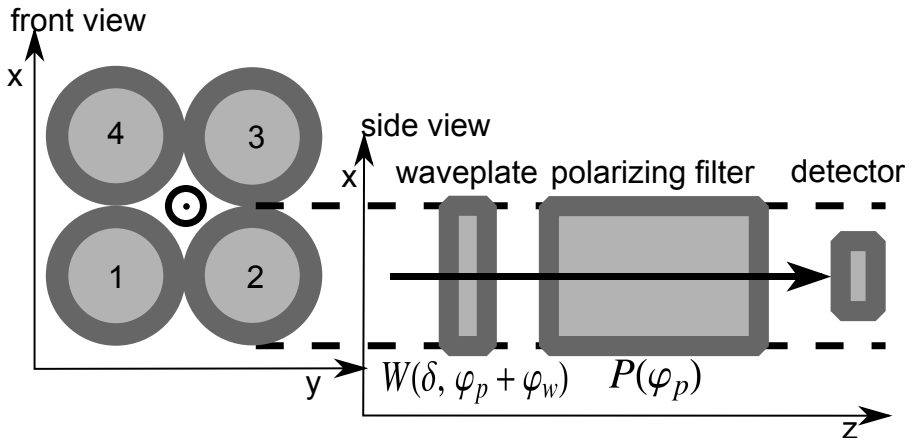

Figure 2.2.1: Sketch of the instrument design with four entrance optics.

The real four vector $\vec{O}$ can be calculated to:

$$\vec{O} = \frac{1}{2} \begin{pmatrix} 1 \\ \sin(2\varphi_p)\cos^2\left(\frac{\delta}{2}\right) + \sin^2\left(\frac{\delta}{2}\right)\sin(2(\varphi_p + 2\varphi_w)) \\ 2\cos(\varphi_w)\sin(\delta)\sin(\varphi_w) \\ \cos(2\varphi_p)\cos^2\left(\frac{\delta}{2}\right) + \cos(2(\varphi_p + 2\varphi_w))\sin^2\left(\frac{\delta}{2}\right) \end{pmatrix}. \tag{2.2.6}$$

This optical setup can be described by three parameters. The angles of the polarizing filter φ_p and waveplate φ_w, and the retardance of the waveplate, which is a given spectral-dependent function. Therefore, a system made of four of those optics can be described by eight free angular parameters and four given retardances for any spectral channel. By setting the angle φ_{p0} of the first polarizer to zero and measuring the other polarizer angles relative to this, one

can reduce the eight free parameters to seven. The retardance and, on a much smaller scale, the angle of the waveplate show a spectral dependency. The spectral dependency of the fast axis for some waveplates angle can be due to circular birefringence of the used quartz crystal.[4] The point on the Poincaré sphere that describes the setup can be calculated by interpreting the vector $\vec{O}$ as Stokes vector. Merging the intensity measurements together in a vector $\vec{I}$ and using the above equation one can define a system matrix A, which is defined as: $A_{i,j} = O(i)_j$. The relation between the measurements $\vec{I}$ and the Stokes vector of the incident light $\vec{S}$ can be written as:

$$\vec{I} = A\vec{S} \quad \Longrightarrow \quad \vec{S} = A^{-1}\vec{I}. \tag{2.2.7}$$

This equation requires that the matrix A is invertible. In addition, Tyo showed in reference [26] that for optimal performance and signal to noise ratio one needs to minimize the condition number of the matrix. The condition number c of a matrix x is defined as:

$$c\,(x) = \|x\|\|x^{-1}\|. \tag{2.2.8}$$

Here we choose the l_2 norm. Other authors have used the l_1 or l_∞ norm, the determinant of the matrix A or reciprocal absolute determinant [24, 25]. It is convenient that for four independent measurements the condition number has an absolute minimum of $3^{1/2}$ [26]. A solution is a set of seven angular parameters that optimizes the system with respect to the given four retardances and a weighting function.

Minimizing the condition number of a system will be one of the main concerns for the next two parts of this paper.

2.2.4 Analytic Solution With Optimal Condition

The demand for angular symmetry in a solution will simplify the issue of minimizing the condition number of the system. Further simplification will be achieved through geometric reasoning. The fully linear polarized states are located around the equator of the Poincaré sphere. By rotating the polarization filter, the accessible states are therefore described by the equator. The states that represents a rotating waveplate in front of a polarizing filter form a curve on the surface of the sphere, which is shown in Figure 2.2.2. The angle of the polarizing filter shifts the whole arch around the equator. The retardance controls the breadth of the arch. The two free angles together with the retardance specify a point on the surface of the sphere. The four considered measurements yield four points which include a tetrahedron. The idea is that minimizing the condition number is related to maximizing the volume of the tetrahedron. It has been shown that maximizing the volume of the tetrahedron is equal to maximizing the determinant of the system matrix A [25]. Once the equator of the Poincaré sphere is defined, the fully circular poles of the sphere are special points. They describe the only axis that leaves the degree of fully linear states invariant under rotations around this axis. The poles can be reached with the setup by using a quarter waveplate at $\pm 45\,^\circ$ relative to its polarization filter. The angle of the polarization filter has no influence for this particular point and will be arbitrarily set to zero. To maximize the volume of tetrahedron, the other three points can be spread out around a constant latitude. The positions of the filters are therefore set to $0\,^\circ$, $60\,^\circ$ and $120\,^\circ$ [27]. The angle and the retardance of the three waveplates are set to be equal for all waveplates to be δ. One optimal setup for $\delta = \lambda/4$ is shown in Figure 2.2.2.

The volume of the enclosed tetrahedron can be calculated by using Equation 2.2.6 to determine the vectors describing the endpoints of the tetrahedron. Let $\vec{V}_c$ describe the circular pole and $\vec{V}_i, i = 1, 2, 3$ the three other setups. Setting the circular pole as the new origin yields the three edges of the tetrahedron: $\vec{v}_i := \vec{V}_c - \vec{V}_i$. The volume V is then proportional to the

[4] From correspondence with the manufacturer

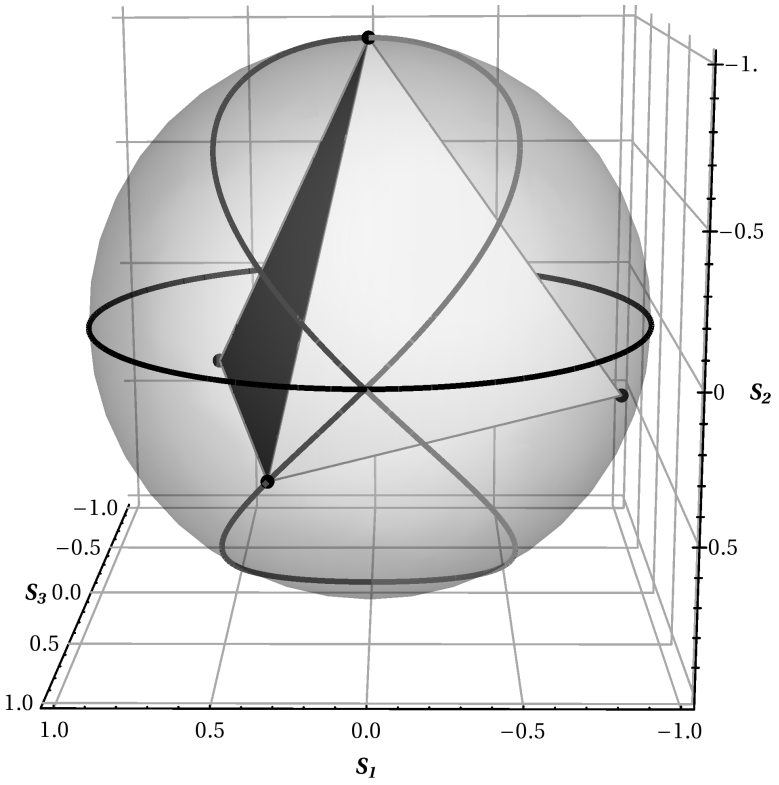

Figure 2.2.2: Four points on the surface of the Poincaré sphere that represent a polarimeter with minimal condition number. The polarimeter consists of four equal quarter waveplates and four polarizing filters.

triple scalar product $\vec{v}_1(\vec{v}_2 \times \vec{v}_3)$. Extreme values of V are calculated by finding the roots of the derivative with respect to φ:

$$0 = \partial_\varphi V \propto \sin(\delta)\cos(2\varphi)\left[\sin(\delta)\sin(2\varphi)+1\right]\left[3\sin(\delta)\sin(2\varphi)-1\right]. \tag{2.2.9}$$

A nontrivial solution can be obtained by setting the third term to zero and finding the root for φ:

$$\varphi = \frac{1}{2}\sin^{-1}\left(\frac{1}{3}\sin(\delta)^{-1}\right). \tag{2.2.10}$$

This first main result is valid if $\sin(\delta)^{-1} \leq \pm 3$. For any given waveplate with retardance $\sin^{-1}(1/3) \leq \delta \leq \pi - \sin^{-1}(1/3)$ the optimal rotation angle can be calculated. We will call those waveplates sufficient. On the Poincaré sphere there is an optimal latitude, which the maximum spaced points have to reach to maximize the volume. This is impossible when the bow is either too small or too wide. For such insufficient retarders the $\mp 45\,^\circ$ solution is optimal in that they reach the highest possible latitude for the given retardance.

The result of four quarter waveplates is shown in Figure 2.2.2. An example with one quarter waveplate and three $\lambda/6$ plates is shown in Figure 2.2.3. The Mollweide projection is used to show the whole surface of the Poincaré sphere. Similar projections will be used later on.

For waveplates with insufficient retardance one uses the $45\,^\circ$ solution and the condition number will rise from 1 for the sufficient case to $\frac{1}{6}\left(5+\sqrt{13}\right) \approx 1.43$ while the retardance approaches 0 or π. In those cases one is using effectively no waveplates and the matrix A simplifies to:

$$A = \begin{pmatrix} \frac{1}{2} & 0 & -\frac{1}{2} & 0 \\ \frac{1}{2} & 0 & 0 & \frac{1}{2} \\ \frac{1}{2} & \frac{\sqrt{3}}{4} & 0 & -\frac{1}{4} \\ \frac{1}{2} & -\frac{\sqrt{3}}{4} & 0 & -\frac{1}{4} \end{pmatrix}. \tag{2.2.11}$$

This option is not optimal in terms of minimized condition number but may by a good choice in terms of cost effectiveness.

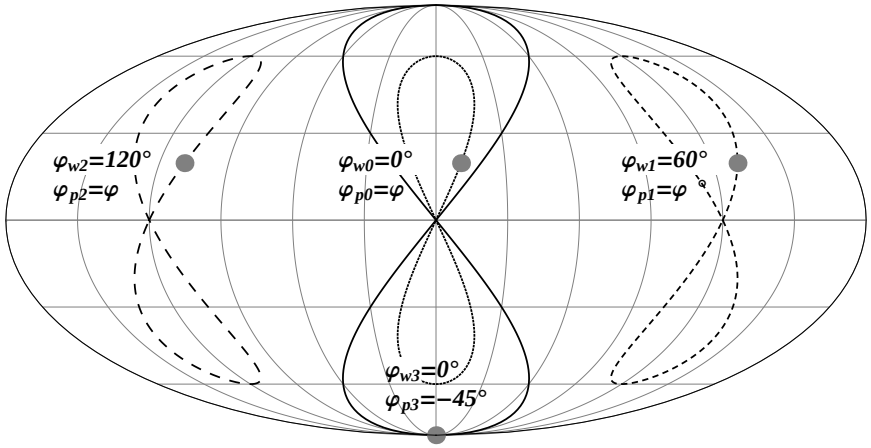

Figure 2.2.3: Optimal solution for a polarimeter with one 1/4 and three 1/6 waveplates; $\delta = \pi/3$, $\varphi = \frac{1}{2}\sin^{-1}\left(\frac{1}{3\sin(\pi/3)}\right)$. The surface of the Poincaré sphere is drawn using the Mollweide projection.

The solution to a more general case can be derived by using the given results from Equation 2.2.10 and 2.2.6. A polarimeter with optimal condition number can be constructed out of one quarter wave plate and three waveplates with sufficiently, but not necessarily, equal retardances. This can be a cost-effective way of constructing a polarimeter for special applications with demands for high precision for non-standard wavelengths. Quarter waveplates can be manufactured for any wavelength from UV-B to the near infrared and are available off the shelf for a range of standard wavelengths such as $780nm$, $808nm$ and $830nm$. Now a solution is presented where just one quarter waveplate and three sufficient ones are needed. The quarter waveplate is used to reach the circular pole, the other ones to reach the known optimal points for quarter waveplates. By using Equation 2.2.10 to calculate the appropriate angle for the waveplate for the given retardance, one has to adjust the spacing of the three polarizing filters to reach optimal condition. This can be done by solving Equation 2.2.6 for the two optics:

$$\vec{O}\left(\theta = 0, \delta = \frac{\pi}{2}, \varphi = \frac{1}{2}\sin^{-1}\left(\frac{1}{3}\right)\right) = \vec{O}\left(\theta', \delta_i, \varphi = \frac{1}{2}\sin^{-1}\left(\frac{1}{3\sin(\delta_i)}\right)\right). \tag{2.2.12}$$

The solution of Equation 2.2.12 for θ' is then an offset $\Delta\theta$ for the particular original values of $\theta_i = 0\,°, 60\,°, 120\,°$. The numerically obtained general result is shown in Figure 2.2.4. This, together with the result from Equation 2.2.10, is a recipe to construct an optimal polarimeter with four sufficient waveplates where at least one is approximately a quarter waveplate.

In the figure the offset for quarter waveplates is zero because they where taken as reference. For a smaller retardance the offset is significantly smaller as for bigger ones, which shows the different behavior of the arch on the surface of the Poincaré sphere as the retardance approaches 0 or π.

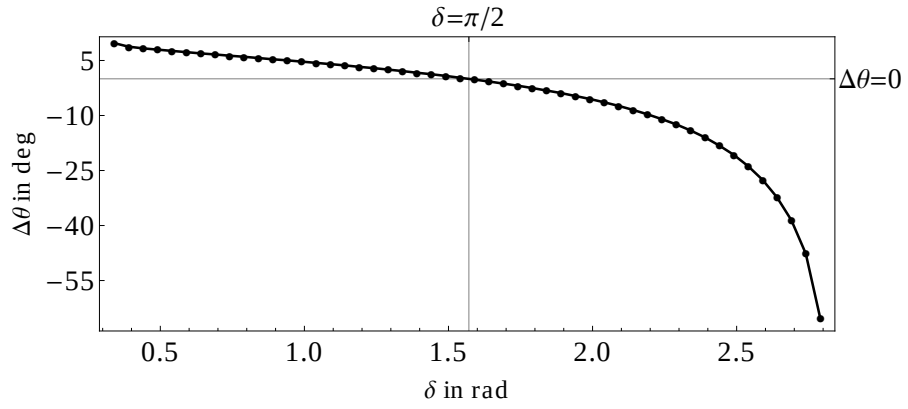

Figure 2.2.4: Offset $\Delta\theta(\delta)$ from the original values $\theta_i = 0\,^\circ, 60\,^\circ, 120\,^\circ$ for arbitrary sufficient waveplates.

2.2.5 Numeric Optimization with Respect to Condition Number and Error Performance

In the previous section, the set of parameters were reduced with symmetry arguments, and optimal solutions for the reduced problem were outlined. Here the full space of the degrees of freedom will be used to obtain optimization with further demands to the solution. Two solutions are given. First, a solution for four quarter waveplates as discussed before. Then the real world case where the retardances of four purchased waveplates are spectral dependent functions, which vary around $\pi/2$. There are seven independent parameters, which lead to a large number of configurations with minimized condition number. In Figure 2.2.5 the two dimensional behavior of the condition number is shown. The marked point represents one optimal choice. The other parameters used for this graph can be found in Table 2.2.1.

0	φ_{p0}	φ_{w0}	φ_{p1}	φ_{w1}	φ_{p2}	φ_{w2}	φ_{p3}	φ_{w3}
$[rad]$	0	1.24	0.03	1.93	1.44	1.29	1.74	1.82
$[deg]$	0	71.02	1.57	110.71	82.35	73.97	99.77	104.48

Table 2.2.1: Numerically obtained values for the polarimeter shown in Figure 2.2.6. All waveplates where chosen to be $\lambda/4$.

From Figure 2.2.5 one can see the complex behavior of the condition number while two parameters are changed. From the various minima, one can choose values for the parameters that lie in a broad area to further stabilize the solution against alignment errors. This leads to the heuristic approach to minimize the condition number and use the additional degrees of freedom to the synchronous optimization of the stability Δ of the condition number in respect to parameter errors. The stability is defined by calculating the scalar product from the uncertainty vector of the parameters and the gradient of the condition number normalized by the number itself. The global minimum of Δ is then one and represents the relative stability of the solution:

$$\Delta = 1 + \frac{\left|\vec{\epsilon}\left(\nabla_{\vec{b}} c(A)\right)^T\right|}{c(\vec{b})}. \tag{2.2.13}$$

For multispectral optimizations the parameters δ_i, φ_{wi} generally depend on wavelengths where φ_{pi} is a constant. For the optimization of the AMSSP [1, 28] instrument a multispectral weighing function f was introduced.

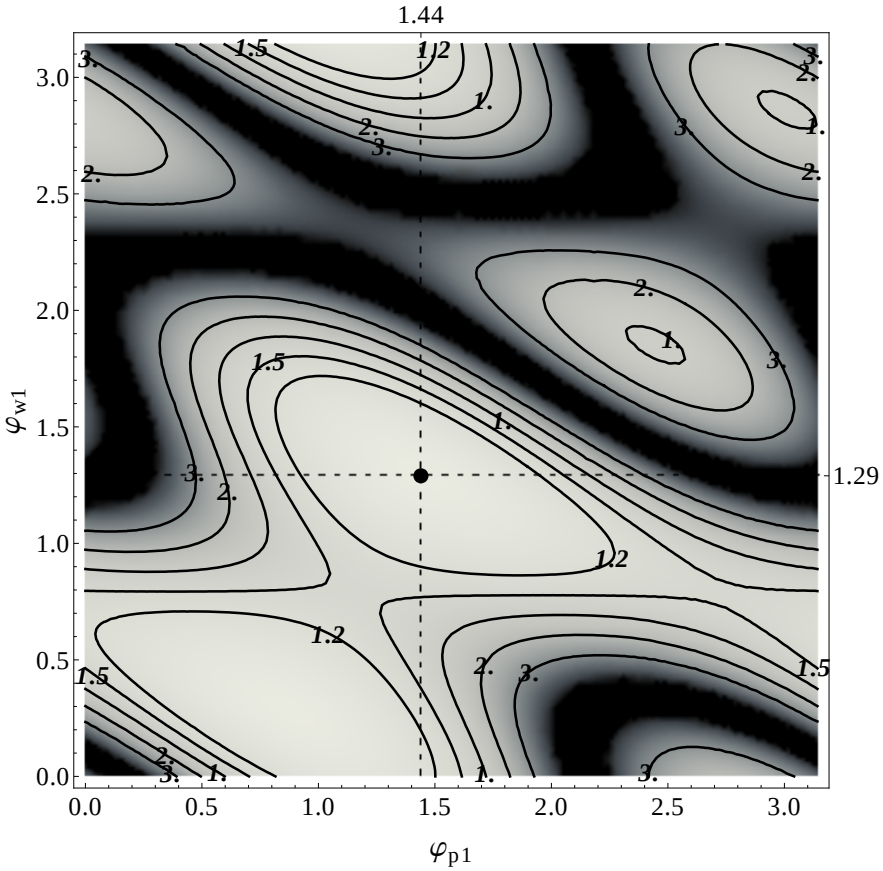

Figure 2.2.5: Behavior of the condition number with respect to the two angular parameters of one optical setup. The marked point represents a solution with minimal condition number for all parameters. Their values can be found in Table 2.2.1.

$$f\left(\vec{\delta}_\lambda, \vec{p}\right) = \frac{1}{\sqrt{2}} \sum_{\lambda_i} \frac{1}{g_{\lambda_i}} \left| \left(\frac{\mathrm{c}(A_\lambda)}{\sqrt{3}}, \Delta(A_\lambda) \right)^T \right|_2 \tag{2.2.14}$$

The function f depends on the spectral dependent retardances, fast axes positions of the waveplates and the fixed values of the polarizing filters. It describes the spectral weighted average with the weights g_{λ_i} over the norm of a vector that contains both optimization parameters. The spectral function of the waveplate fast axes is measured for one arbitrary position and then internally stored as a spectral offset from the mean over the whole function. The varying input parameters for the function are the seven independent parameters. To calculate the value of the function, the spectral dependency of the angle of the fast axis is also taken into account. The resulting parameter for the angle of the fast axis describes then the angular position of the mean over that function. By construction, the function has an absolute minimum at 1.

For the minimization of f the *powel* function of IDL, which proved sufficiently fast and accurate, was used. Depending on the initial values, the algorithm converges towards independent solutions. In the first step, a number of results is calculated with initial values that were taken from a regular grid in the seven dimensional parameter space. Points that lead to initial divergent condition were removed from the grid. This was done by partitioning the full parameter space into four two dimensional parameter values where one point contains the two parameters for one optic. When one is using the same waveplates for all optics any doubling of the subsets will lead to just three effective measurements and a non-invertible system matrix. The reduced grid then contains $N = n(n^2-1)(n^2-2)(n^2-3)$ instead of n^7 points, where n is

the number of grid points in every direction. The results were then used to build a database with optimized setups of condition numbers lower than some chosen cut of value.

By partitioning the grid into subsets and distributing the calculations, the computational effort was parallelized. Now an example for a monospectral optimization for four quarter waveplates is shown. The database contains a number of optimized solutions from which we can choose one that minimizes some additional requirements. We have chosen the error performance with respect to fully linear polarized states. The error estimate for a certain Stokes vector with respect to errors in alignment and retardance uncertainty is given by [26]:

$$\epsilon_S(\vec{S}) = \left\{ A^{-1} \left(\sum_i (\epsilon_{b_i} \partial_{b_i} A) \right) \right\} \vec{S}. \tag{2.2.15}$$

For a minimization function we use the l_2 norm of ϵ_S for a number of equally distributed fully linear polarized states. The average was then calculated and the database was sorted to find the optimal set, which is now also optimized in respect to error performance for the selected sets of Stokes vectors. The result is shown in Figure 2.2.6 and Table 2.2.1. Symmetry was not taken into account for this result.

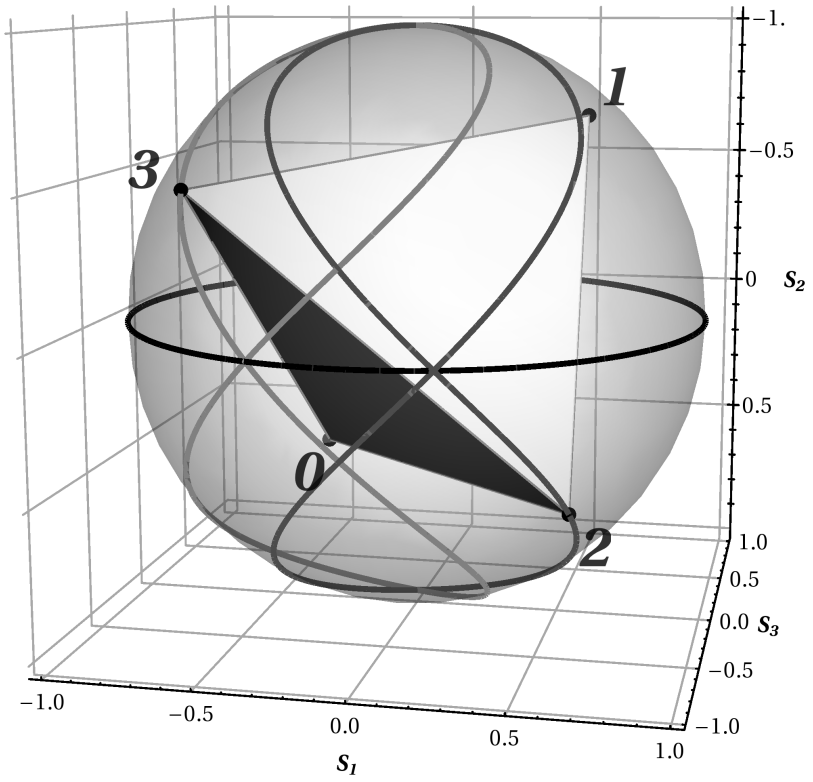

Figure 2.2.6: Numerically obtained result for an optimal polarimeter with additional minimization of measurement errors for fully linear polarized states. The arabic numbers indicate the number of the parameter set from Table 2.2.1.

The obtained result is not unique but minimizes the condition, maximizes the stability of the condition number and minimizes the mean error with respect to linear states. The monospectral setup with four quarter waveplates was chosen to be comparable with the analytic solution from the previous section. The norm of the error vector ϵ_s for both parameter sets for all fully polarized states is shown in Figure 2.2.8.

The algorithm is generally applicable for multispectral systems where the retardance and the waveplate angles are spectral dependent functions. This was used to find optimal parameter values for the multispectral polarimeter AMSSP, which is shown in the next section.

2.2.6 Multispectral Optimization for the Polarimeter AMSSP

The polarimeter AMSSP is a new instrument for the German research aircraft HALO. Its development is funded by the DFG priority program (PP-1294) and under development at the Institute for Space Sciences at the Freie Universtät Berlin. Aim of the polarimeter design was to measure the full Stokes vector in the visible and UV-C band for the remote sensing of aerosol properties. The instrument consists of four optics with achromatic quarter wave plates at 633nm. Multispectral measurements of the retardances are shown in Figure 2.2.7.

Using the outlined procedure, the results in Table 2.2.2 were obtained. In order to save computational time, the spectral resolution for the optimization was reduced to one tenth of the resolution of the used detectors.

The numerically found set of parameters is similar to the analytic solution for four quarter waveplates, where the single parameters are slightly offset to account for the retardance derivations from $\lambda/4$. This highlights the usefulness of the analytic solution applied to a mean value for real spectral-dependent retardances.

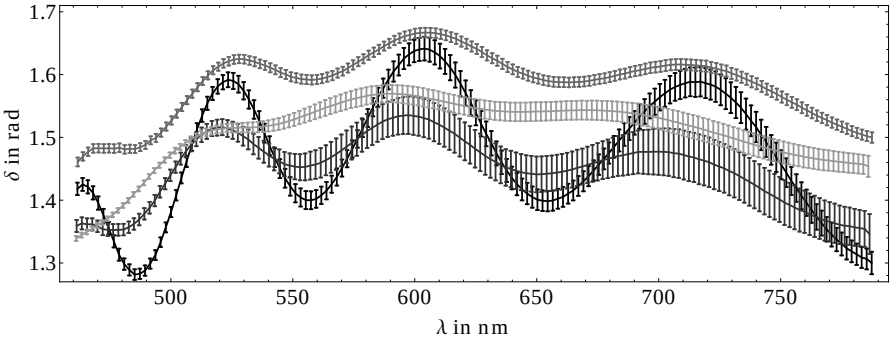

Figure 2.2.7: Multispectral measurement of the spectral retardance of four used achromatic waveplates.

2.2.7 Error Calculation for Polarization Parameters

Calculating the error of the retrieved Stokes vector depends on $4n-1$ parameters, where n is the number of independent measurements taken. The error can be estimated by taking the Taylor expansion of the retrieval to the first order:

$$s_i\left(\vec{x}+\vec{\epsilon}\right) \simeq s_i\left(\vec{x}\right) + \left(\nabla_{\vec{x}} s_i\left(\vec{x}\right)\right)^T \left(\vec{x}+\vec{\epsilon}-\vec{x}\right) = s_i\left(\vec{x}\right) + \left(\nabla_{\vec{x}} s_i\left(\vec{x}\right)\right)^T \vec{\epsilon}. \tag{2.2.16}$$

The error can then be split up into errors with origin from uncertainty about the instrument and errors due to random errors in the detector:

$$\vec{\epsilon}_S = \vec{S}\left(\vec{x}+\vec{\epsilon}\right) - \vec{S}\left(\vec{x}\right) := \underbrace{G_b\vec{\epsilon}_b}_{\text{systematic}} + \underbrace{G_I\vec{\epsilon}_I}_{\text{random}} . \tag{2.2.17}$$

This can be expressed in terms of two error matrices for each error vector:

$$\epsilon \in \mathbb{R}^{7+4+4=15}, G_b \in \mathbb{R}^{4\times 11}, \epsilon_b \in \mathbb{R}^{11}, G_I \in \mathbb{R}^{4x4}, \epsilon_I \in \mathbb{R}^4, \tag{2.2.18}$$

$$[G_b]_{ij} = \partial_{\vec{b}_j} S_i \left(\vec{b}, \vec{I}\right) = \partial_{\vec{b}_j} [A^{-1}\left(\vec{b}\right) \vec{I}]_i, \tag{2.2.19}$$

$$[G_I]_{ij} = \partial_{\vec{I}_j} S_i \left(\vec{b}, \vec{I}\right) = \partial_{\vec{I}_j} [A^{-1}\left(\vec{b}\right) \vec{I}]_i. \tag{2.2.20}$$

This procedure yields the distinct contributions of random and systematic errors to the entire error of the retrieval.

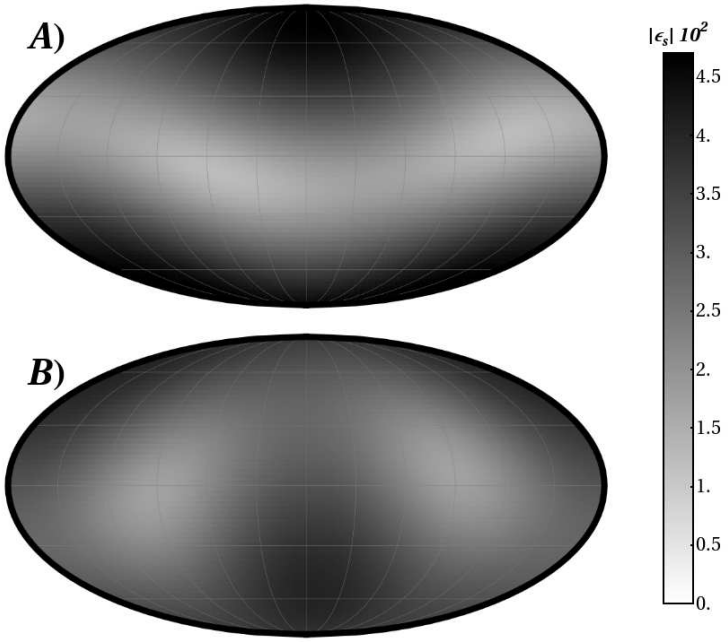

Figure 2.2.8: Norm of the error vector ϵ_s for the numerically obtained result (A) and the analytic solution of Equation 2.2.10 from the former section (B).

	φ_{p0}	φ_{w0}	φ_{p1}	φ_{w1}	φ_{p2}	φ_{w2}	φ_{p3}	φ_{w3}
$[rad]$	0	0.76	1.04	2.96	1.97	3.04	3.12	2.91
$[deg]$	0	43.83	59.83	169.81	113.07	173.94	178.56	166.54

Table 2.2.2: Optimized parameters for the multispectral case.

2.2.8 Conclusion

This research was conducted during the development of an engineering model of the airborne multispectral polarimeter for the AMSSP instrument. There we used the last-mentioned multispectral approach to find a set of optimal values for the polarimeter. The shown analytical solution is a good solution even for multispectral measurements when achromatic waveplates with small spectral dependencies are used. Slightly better values can be obtained by using all degrees of freedom and the additional weighting function. The distinction between the two main error classes shows how much the uncertainty about the optical setup contributes to the total uncertainty of the polarization retrieval.

Acknowledgments

This work was funded by the DFG priority program (PP-1294).

2.3 A Robust Method for Retrieving the Polarization Properties of a Waveplate Assembled in a Multispectral and Complete Polarimeter

2.3.1 Abstract

A robust method for the optical characterization of polarimeter optics for a complete and multispectral polarimeter is presented. The polarimeter optics consist of a waveplate, polarizing filter and a multispectral detector. The method employs a source of unpolarized light and a rotating polarizing filter and retrieves the retardance and the angle of the waveplate. Three independent measurements at distinct angles of the analyzer are used at a time and an arbitrary number of distinct measurement triples can be used to ensure the consistency of the results. The elements of the polarimeter optics must not be moved during the measurement and therefore the method allows to adjust the setup to defined and potentially optimized values for the retrieved properties. This key element of the method was a crucial feature for the design of the multispectral airborne polarimeter AMSSP for the German research aircraft HALO. The application of the method to a single optic of the AMSSP instrument is presented. The variation of the independently retrieved parameters is then used to estimate the maximum uncertainty of the results due to systematic errors.

2.3.2 Introduction and Motivation

A setup made from a waveplate and a polarizing filter can be used as polarimeter optics for complete and multispectral polarimeters [24, 25]. They can be described by the position of the waveplate relative to the polarizing filter, the absolute position of the polarizing filter and the spectral dependent retardance of the waveplate. The positions were used to optimize the polarimeter with respect to signal to noise ratio [24, 25] and error performance [4].

A method of measuring these parameters for a given setup is presented. The method uses a source of unpolarized light and a rotating polarizing filter. The angle of the waveplate will be determined modulo $\pi/2$, which can be dealt with when one is starting with parallel aligned elements.

The method was developed for the airborne polarimeter AMSSP [1, 28], which utilizes no movable parts to increase stability against vibrations and performs simultaneous measurements to avoid errors due to the fast changing of scenes during airborne measurements. Therefore, a characterization method for a fixed setup was needed. The results for a single AMSSP polarimeter optic is presented in the last part of this paper.

2.3.3 Retrieving the Polarization Properties of the Waveplate

The experiment consists of a source of unpolarized light, a rotating polarization filter $P(\theta)$, the polarization optics and a multispectral detector. The Jones matrix of the experiment E is derived from the the product of the Jones matrices of the single components, where P is the Jones matrix for an ideal polarizing filter and W is the Jones matrix for an ideal waveplate with retardance δ rotated by the argument [23]:

$$E := P(\varphi_p)\, W(\delta, \varphi_p + \varphi_w)\, P(\theta)\,. \tag{2.3.1}$$

The arguments $\varphi_p, \varphi_p + \varphi_w$ and θ describe the rotational positions of the elements. The coherence matrix of unpolarized light of unit intensity is given by $1/2\mathbb{I}_2$. The transmitted intensity I' of an incident beam of unpolarized light with intensity I passing through the setup is given by [13]:

$$
\begin{aligned}
I'(\theta) &:= Tr\left(E(\frac{I}{2}\mathbb{I}_2)E^\dagger\right) \\
&= \frac{1}{4}\mathrm{I}\left(\cos\left(2\varphi_\mathrm{w}\right)\cos\left(2\left(\theta-\varphi_p-\varphi_\mathrm{w}\right)\right)-\cos(\delta)\sin\left(2\varphi_\mathrm{w}\right)\sin\left(2\left(\theta-\varphi_p-\varphi_\mathrm{w}\right)\right)+1\right).
\end{aligned}
\tag{2.3.2}
$$

The angle φ_p can be easily determined when the setup is assembled and is therefore considered as known. Three measurement positions θ_i applied to Equation 2.3.2 will be sufficient to eliminate I and to retrieve φ_w and δ. By choosing the θ_i to be the sum of an arbitrary offset Θ and $0, \pi/4$ and $\pi/2$, the system of equations can be simplified and a triple of independent measurements M_i identified by the angle Θ is used to retrieve the parameters:

$$
M_1 := I'(\Theta), \quad M_2 := I'(\Theta+\frac{\pi}{4}), \quad M_3 := I'(\Theta+\frac{\pi}{2}). \tag{2.3.3}
$$

The retrieved parameters must be independent from Θ and therefore variations can be treated as systematic errors. The unknown intensity of the incident beam is given by $I = 2(M_1 + M_3)$ and can be eliminated from the set of equations for the M_i. By using $\vec{m} := (M_1, M_2, M_3)$, the two remaining equations are written as $\vec{m}\vec{a}_i = 0$ and solved for the $\vec{a}_i$:

$$
\vec{a}_1 = (2\alpha+2, 0, 2\alpha-2)^T, \tag{2.3.4}
$$

$$
\vec{a}_2 = (2-2\beta, -4, 2-2\beta)^T. \tag{2.3.5}
$$

The two coefficients α and β are determined as:

$$
\alpha := \cos(\delta)\sin\left(2\left(\theta-\varphi_p-\varphi_w\right)\right)\sin\left(2\varphi_w\right)-\cos\left(2\left(\theta-\varphi_p-\varphi_w\right)\right)\cos\left(2\varphi_w\right), \tag{2.3.6}
$$

$$
\beta := \cos(\delta)\cos\left(2\left(\theta-\varphi_p-\varphi_w\right)\right)\sin\left(2\varphi_w\right)+\sin\left(2\left(\theta-\varphi_p-\varphi_w\right)\right)\cos\left(2\varphi_w\right). \tag{2.3.7}
$$

Solving $\vec{m}\vec{a}_i = 0$ with respect to α and β yields:

$$
\alpha = \frac{\mathrm{M}_3-\mathrm{M}_1}{\mathrm{M}_3+\mathrm{M}_1} =: m_1, \tag{2.3.8}
$$

$$
\beta = \frac{\mathrm{M}_3-\mathrm{M}_2}{\mathrm{M}_3+\mathrm{M}_2} =: m_2. \tag{2.3.9}
$$

Using Equation 2.3.8 and 2.3.9, we obtained the main result of this paper:

$$
\delta = \cos^{-1}\left(\frac{1-m_1^2-m_2^2}{\cos\left(2\varphi_p\right)m_1-\sin\left(2\varphi_p\right)m_2+1}-1\right), \tag{2.3.10}
$$

$$
\varphi_w = \frac{1}{4}\cos^{-1}\left(\frac{\cos(4\varphi_p)\left(m_2^2-m_1^2\right)-2\cos(2\varphi_p)m_1+2\sin(2\varphi_p)m_2+2\sin(4\varphi_p)m_2m_1-1}{\mathrm{m}_1^2+2\mathrm{m}_1\cos(2\varphi_p)+\mathrm{m}_2^2-2\mathrm{m}_2\sin(2\varphi_p)+1}\right). \tag{2.3.11}
$$

With the results from Equations 2.3.10 and 2.3.11, the retardance and the angle of the waveplate can be calculated as a function of the arbitrary offset Θ. Disagreement with respect to Θ can lead to a better insight into possible errors within the experiment. This would not be possible when one is using a fitting algorithm to retrieve the parameters. For quarter waveplates the retardance δ is $\pi/2$ and the second term in Equation 2.3.2 vanishes. For real quarter waveplates this term becomes small with respect to the other ones, which can lead to numeric instability because one is effectively neglecting this term.

2.3.4 Experimental Setup

The results from Equations 2.3.10 and 2.3.11 were used to determine the retardance and the angle of an achromatic quarter waveplate in front of a polarizing filter, which is used as polarimeter optics for the instrument AMSSP. An integrating sphere was used as source for unpolarized light. The polarizing filter was moved using a rotary stage, which is displayed in Figure 2.3.1. One intensity measurement was obtained by averaging over approximately 15 single measurements for any angle θ. The parameters were retrieved as the average over 256 retrievals for independent $\Theta's$ and the parameter error is set to the corresponding standard deviation, which is used as an estimate for the systematic error. The random error of the retrieval alone cannot explain the value of the standard deviation. We believe that this is due to the big opening angle of the standard fiber cupping optic that was used in the experiment. The results of the retrieval are shown in Figure 2.3.2 and Figure 2.3.3.

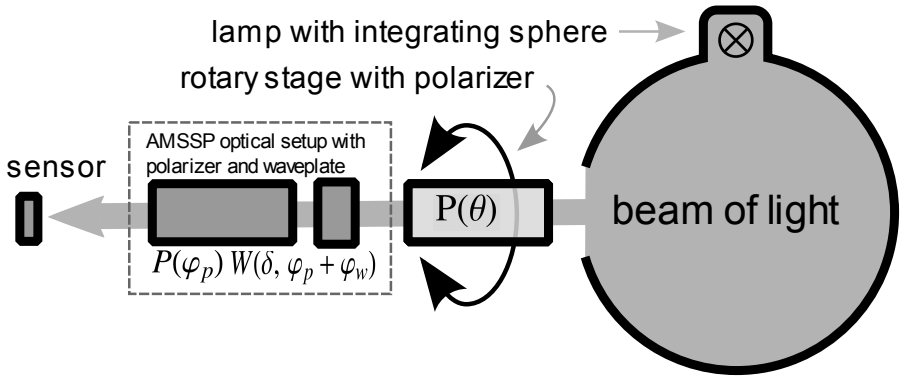

Figure 2.3.1: Optical setup of the experiment.

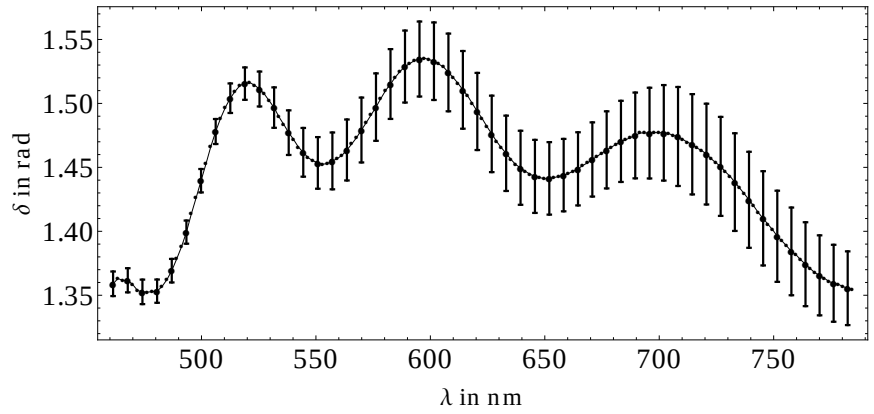

Figure 2.3.2: Retardance for the analyzed achromatic waveplate.

The spectral dependence of the fast axis of the waveplate is due to circular birefringence of the used quartz crystal[5]. The retrieved estimates of the parameters and Equation 2.3.2 were used to calculate model intensities I_M. We compared them with the multispectral measured intensities using the scatter plot technique. The plot shown in Figure 2.3.4 shows good agreement between the calculated model intensities and the measurements, which justifies the preliminary use of the retrieved parameters.

[5] From correspondence with the manufacturer.

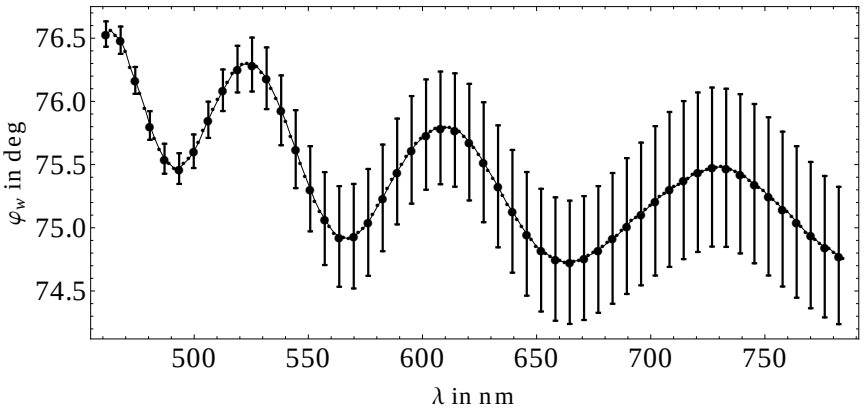

Figure 2.3.3: Result for the fast axis angle of the analyzed waveplate.

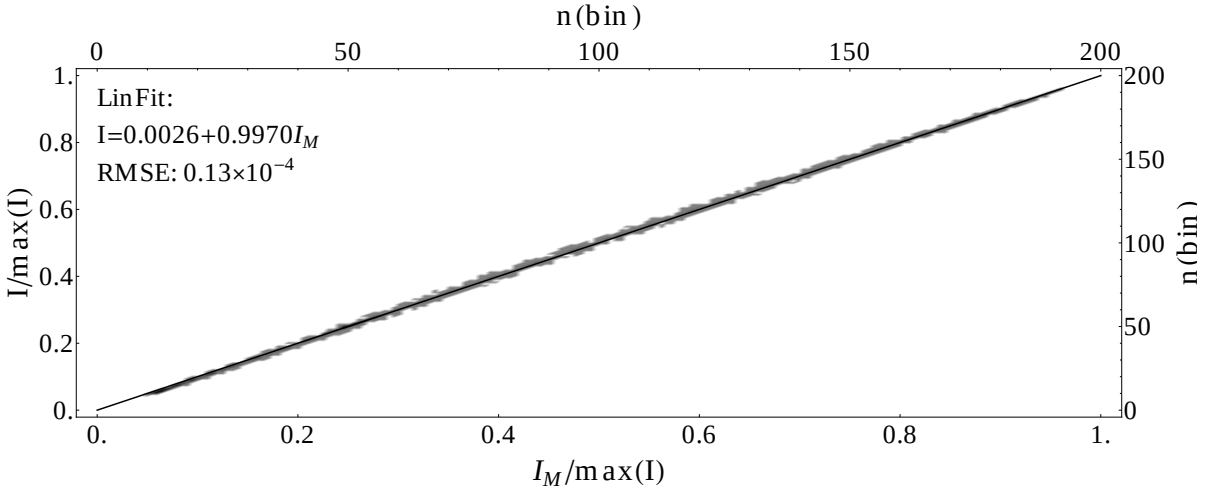

Figure 2.3.4: Scatter plot of the measurements I and model intensities I_M.

2.3.5 Conclusion

A method for retrieving the crucial polarization properties of a waveplate in front of a polarizing filter was presented. The method incorporates multispectral intensity measurements with an integrating sphere and a turning polarization filter in front of the setup. The retardance and the angle of the waveplate are retrieved by using three independent measurements at $\Theta, \pi/4 + \Theta$ and $\pi/2 + \Theta$, where Θ is an arbitrary offset. In the ideal case, for any angle Θ consistent parameters must be retrieved. In the presence of errors, the deviations of the parameters with respect to Θ can lead to insights into error sources of the experiment. The presented experiment shows that the method is applicable.

Acknowledgments

This work was funded by the DFG priority program (PP-1294) and was developed for the AMSSP instrument, which is under development at the Freie Universität Berlin.

CHAPTER 3

VECTOR RADIATIVE TRANSFER

Contents

Radiative transfer simulations are one of the workhorses of remote sensing applications that are based on radiance measurements. The main idea behind such remote sensing schemes is to measure radiance in spectral channels that are sensitive to the parameter one is interested in and then to use radiative transfer simulations to infer the atmospheric state, which explains the measurements and prior knowledge. The resulting state is then called a remote sensing product.

Measurements of diffuse radiance in the visible and shortwave infrared spectral region are mostly determined by scattering and absorption processes, which are shown in Figure 3.1.1. Scattering and absorption is caused by molecules and particulate matter, which are suspended in the atmosphere and ocean. Among them are aerosol particles, water droplets which form clouds, ice crystals, and hydrosols such as chlorophyll and sediment. A general way of simulating measurements of the diffuse radiance is to derive the radiative transfer equation and solve it numerically.

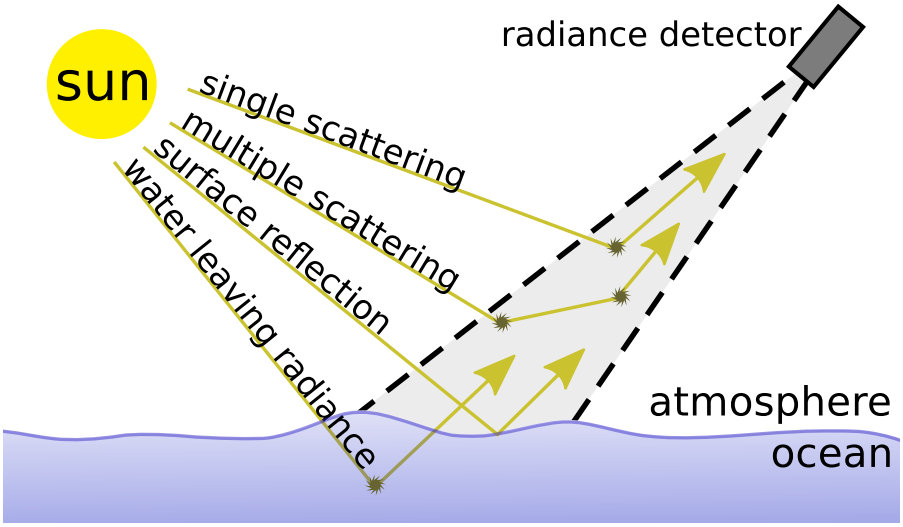

Figure 3.1.1: Shown are major processes that contribute to measurements of diffuse radiance for an atmosphere ocean system. Among them are single and multiple scattering, which are caused by molecules and particulate mater. Also important are reflections from the sea surface and the water leaving radiance. Not shown here are processes due to inelastic scattering in the atmosphere and ocean, and internal radiance sources such as chlorophyll fluorescence.

Several necessary simplifications are the reasoning behind this approach. The first[1] step is to derive the radiative transfer equation from the more fundamental Maxwell equations, since no reasonable way is known to solve them directly for Earth's atmosphere. The result is an integro-differential equation for the radiance field L, which can be measured using a well-collimated detector:

$$\left(\mu\frac{d}{d\tau}-1\right)L(\tau,\mu,\phi)=\underbrace{\omega_0 P e^{-\tau/\mu_s}S_0}_{\substack{\text{single scattering}\\ \text{of solar irradiance}}}+\underbrace{\omega_0\int d\mu' d\phi' P L(\tau,\mu,\phi)}_{\substack{\text{multiple scattering of}\\ \text{diffuse radiance}}}, \tag{3.1.1}$$

where $\vec{x}(\tau)$ is the atmospheric state, τ is the optical thickness, $P(\tau,\vec{x}(\tau))$ is the scattering

[1] The historic development was quite different as one can see when comparing reference [29] with [11]. The presented order is set up in an educational way.

matrix, $\omega_0(\tau, \vec{x}(\tau))$ is the single scattering albedo, S_0 is the solar constant, μ_s is the solar zenith angle, and the angles (μ, ϕ) define the viewing geometry. It is not straightforward to invert this equation for general cases $\vec{x}$ and to express the atmospheric state as simple function F of the radiance measurements $\vec{M} = (L_1, \ldots, L_n)^T$: $\vec{x} = F(\vec{M})$. Hence inverse algorithms[2] are used to construct the *inversion* function F. In many applications, *forward radiative transfer modeling* is used to express the radiance field L_i as function $f(\vec{x})$ of the atmospheric state by solving the radiative transfer equation. Then, the atmospheric state can be derived by minimizing a metric function δ: $\vec{x} = min_{\vec{x}'}\delta(\vec{M}, f(\vec{x}'), \vec{P})$, which depends on the measurements $\vec{M}$, the forward simulations $f(\vec{x})$, and the prior knowledge $\vec{P}$.

Section 3.2 deals with the implementation of a vector forward radiative transfer model for the case of a plane parallel atmosphere ocean system. This section was published in the peer reviewed journal *Journal of Quantitative Spectroscopy and Radiative Transfer* as:

> *André Hollstein and Jürgen Fischer. Radiative Transfer Solutions for Coupled Atmosphere Ocean Systems Using the Matrix Operator Technique.* Journal of Quantitative Spectroscopy and Radiative Transfer*, 113(7):536 – 548, 2012.*

Radiative transfer models use various numeric techniques to solve the radiative transfer equation. They are implemented in various computer languages and can easily contain many thousand lines[3] of code. Errors can be hard to find and model validation is a major step in the development of a radiative transfer model. A standard way of doing that is to compare own simulations with measurements or simulations performed by other models, which is especially interesting if an independent approach was used to solve the radiative transfer equation. Several tables with simulation results have been published in the past,[4] which can be used for simple validation purposes. Problems arise when there is no accepted table available for a feature that the model implements. This is the case even for simple problems, e.g. for the vector radiance field in the coupled atmosphere ocean system or for inelastic scattering in the atmosphere and ocean. For those cases, validation is usually performed by comparing own results with those from other models, which can be a difficult and tedious task. If the differences between two models are larger then the model error,[5] it might be difficult to judge which model result is a better representation of the true value. At the forefront of science, there might not even be another model to compare with. In Section 3.3, a simple but different approach to the validation problem is presented. It was published in the peer-reviewed *Journal of Quantitative Spectroscopy and Radiative Transfer* as:

> *André Hollstein. Verification of radiative transfer results by inserting them into the RTE: A demonstration for rayleigh scattering.* Journal of Quantitative Spectroscopy and Radiative Transfer*, 113(15):1970 – 1973, 2012.*

The presented research is based on the idea that it is difficult to implement a system that finds solutions for the radiative transfer equation,[6] but that it is much easier to implement a system that verifies that a simulation result is in fact the solution of the radiative transfer equation. For the test case of Rayleigh scattering, such a system was implemented in *Mathematica*. The implementation is about 60 lines of code long, which makes it very easy to review the implementation. The proposed setup can be easily extended to an atmosphere ocean case or to inelastic scattering and can be a valuable addition for future validation tasks.

[2] A rigorous introduction can be found in reference [30]. [3] The MOMO model, which is described in Section 3.2, consists of 12214 lines of code. [4] Tables exist for Rayleigh and Mie scattering [31, 32, 33]. Next to other initiatives, tables and inter comparison results are made available by the IPRT group [34]. [5] The model error is often unknown and the presented method can also be used to estimate it. [6] Equation 3.1.1 is one of the simpler forms of the radiative transfer equation. It can become much more complicated if thermal emission or inelastic scattering is to be included.

3.2 Radiative Transfer Solutions for Coupled Atmosphere Ocean Systems Using the Matrix Operator Technique

3.2.1 Abstract

Accurate radiative transfer models are the key tools for the understanding of radiative transfer processes in the atmosphere and ocean, and for the development of remote sensing algorithms. The widely used scalar approximation of radiative transfer can lead to errors in calculated top-of-atmosphere radiances. We show results with errors in the order of $\pm 8\%$ for atmosphere ocean systems with case one waters. Variations in sea water salinity and temperature can lead to variations in the signal of similar magnitude. Therefore, we enhanced our scalar radiative transfer model MOMO, which is in use at the *Freie Universität Berlin*, to treat these effects as accurately as possible. We describe our one-dimensional vector radiative transfer model for an atmosphere ocean system with a rough interface. We describe the matrix operator scheme and the bio-optical model for case one waters. We discuss some effects of neglecting polarization in radiative transfer calculations and effects of salinity changes for top of atmosphere radiances. Results are shown for the channels of the satellite instruments MERIS and OLCI from $412.5nm$ to $900nm$.

3.2.2 Introduction

An accurate and flexible remote sensing scheme has a broad range of possible applications in the field of atmospheric and oceanic research. Virtually all analyses of measurements made by radiance sensors need radiative transfer (RT) calculation results to derive meaningful physical quantities. In this paper, we describe a radiative transfer scheme that is able to calculate the vector radiance field in an atmosphere ocean system (AOS) with a wind blown interface. We assume that the system has no horizontal, but arbitrary vertical structure. Hence, the scheme is a one dimensional vector radiative transfer solver. Similar systems have been described in the past and recent literature, such as the works from Kattawar and Adams [35], Nakajima and Tanaka [36], Takashima [37], Chami [38], Fell and Fischer [39], Chowdhary *et al.* [40], He [41] and Zhai [42] to name a few. The work described in this paper is based on the radiative transfer model MOMO, which is itself based on the work of Fischer and Grassl [43], Fell and Fischer [39] and Bennartz and Fischer [44]. It has a long tradition of successfully developed remote sensing applications, including the sensing of lakes [45], analysis of hyper spectral data to derive surface fluorescence signals [46], the analysis of ocean color data from MERIS measurements [47], and the retrieval of land surface pressure from MERIS data [48]. We decided to upgrade the MOMO FORTRAN code to account for polarization in order to base the development of future remote sensing algorithms on more accurate RT calculations.

Sections 3.2.3 and 3.2.4 introduces the radiative transfer equation and the matrix operator method. Section 3.2.5 and 3.2.6 describes the models for pure ocean water and the bio-optical model for in-water constituents. Section 3.2.7 is devoted to the validation of the code and Section 3.2.13 describes the first applications as mentioned in the abstract.

3.2.3 Radiative Transfer Equation

The differential radiative transfer equation (RTE) given in Equation 3.2.1 states that the change of the diffuse light field $\partial_\tau L(\tau)$ with respect to the optical thickness τ is proportional to both the light field itself, and the diffuse sources $J(\tau)$ at this optical depth:

$$\mu \partial_\tau L(\tau) = -L(\tau) + J(\tau). \tag{3.2.1}$$

The light field is described by a real four-dimensional Stokes vector [49, 13] (and references therein). To find unique solutions, it is necessary to define boundary conditions that define the top and the bottom of the atmosphere. Equation 3.2.2 states that there is no diffuse downward directed radiation at the top of the atmosphere, and Equation 3.2.3 states that the upward directed radiation at the bottom of the AOS is given by the reflection of the downward directed radiation. The surface reflection is modeled using a real 4×4 reflection matrix $R(\mu, \phi, \mu', \phi')$, which depends on the direction of incidence (μ', ϕ') and reflection (μ, ϕ):

$$L(\tau = 0, \mu < 0) = 0, \tag{3.2.2}$$

$$L(\tau = \tau_0, \mu > 0, \phi) = \int_0^1 d\mu' \int d\phi' R(\mu, \phi, \mu', \phi') L(\tau_0, \mu', \phi'). \tag{3.2.3}$$

The complexity of the RTE originates from the coupling of the field by the scattering source term J, which is shown in Equation 3.2.4. It consists of a scattering term for the direct solar radiation and a scattering term for the diffuse field:

$$\begin{aligned}\left(\mu \frac{d}{\mathrm{d}\tau} - 1\right) L(\tau, \mu, \phi) = &\underbrace{\omega_0 P\left(\tau, \mu, \phi, \mu_s, \phi_s\right) e^{-\tau/\mu_s} S_0}_{\text{single scattering term}} \\ &+ \underbrace{\omega_0 \int d\mu' d\phi' P(\tau, \mu, \phi, \mu', \phi') L(\tau, \mu', \phi')}_{\text{diffuse scattering term}},\end{aligned} \tag{3.2.4}$$

where is S_0 the solar constant, the solar position is set to (μ_s, ϕ_s), and ω_0 is the single scattering albedo. We assume that the scattering matrix P only depends on $\phi - \phi'$ and expand L and P in a Fourier series with respect to the expansion coefficient m. The equation then decouples into a series of equations in Fourier space that are now independent of the viewing azimuth angle:

$$\begin{aligned}\left(\mu \frac{d}{\mathrm{d}\tau} - 1\right) L_m(\tau, \mu) = &\ \omega_0 P_m\left(\mu, \mu_s\right) e^{-\tau/\mu_s} \\ &+ \omega_0 \pi \left(1 + \delta_{0m}\right) \int d\mu' P_m(\mu, \mu') L_m(\tau, \mu').\end{aligned} \tag{3.2.5}$$

We discretize Equation 3.2.5 for numerical treatment on a computer system, and split the light field into parts for the upper and lower hemisphere:

$$L_m^+(\tau, \mu) = L_m(\tau, \mu > 0), \tag{3.2.6}$$

$$L_m^-(\tau, \mu) = L_m(\tau, \mu < 0). \tag{3.2.7}$$

Integrations are then replaced by summing over the integrand at Gaussian quadrature points μ_i and multiplying with the Gauss Lobatto weights c_i:

$$\int d\mu \mathrm{f}(\mu) \approx \sum_{i=1}^{k} f\left(\mu_i\right) c_i. \tag{3.2.8}$$

We define matrices that contain the Gaussian points, weights, phase matrix values, and source terms values:

$$c = \mathrm{diag}\,(c_1, \ldots, c_k)\,, \tag{3.2.9}$$
$$M = \mathrm{diag}\,(\mu_1, \ldots, \mu_k)\,, \tag{3.2.10}$$
$$[P_m^{\pm,\pm}]_{i,j} = P_m(\pm\mu_i, \pm\mu'_j); i, j \in 1, \ldots, k, \tag{3.2.11}$$
$$[J_m^{+}]_{i,j} = \omega_0 S_0 [P_m^{++}]_{i,j} e^{\tau/\mu_i}, \tag{3.2.12}$$
$$[J_m^{-}]_{i,j} = \omega_0 S_0 [P_m^{-+}]_{i,j} e^{\tau/\mu_i}, \tag{3.2.13}$$

where δ_{0m} is the Kronecker delta. Defining the matrices $\Gamma_m^{++/--/+-/-+}$ and $\Sigma^{+/-}$ as abbreviations:

$$\Gamma_m^{++} = M^{-1}\left(\mathbf{1} - \omega_0\pi\,(1+\delta_{0m})\,P_m^{++}c\right), \tag{3.2.14}$$
$$\Gamma_m^{+-} = M^{-1}\omega_0\pi\,(1+\delta_{0m})\,P_m^{+-}c, \tag{3.2.15}$$
$$\Gamma_m^{-+} = M^{-1}\omega_0\pi\,(1+\delta_{0m})\,P_m^{-+}c, \tag{3.2.16}$$
$$\Gamma_m^{--} = M^{-1}\left(\mathbf{1} - \omega_0\pi\,(1+\delta_{0m})\,P_m^{--}c\right), \tag{3.2.17}$$
$$\Sigma_m^{\pm} = M^{-1}J_m^{\pm}, \tag{3.2.18}$$

we can insert them into Equation 3.2.5 and write the result as a compact matrix equation:

$$\frac{d}{\mathrm{d}\tau}\begin{pmatrix} L^+ \\ L^- \end{pmatrix} = \begin{pmatrix} -\Gamma_m^{++} & \Gamma_m^{+-} \\ -\Gamma_m^{-+} & \Gamma_m^{-} \end{pmatrix}\begin{pmatrix} L_m^+ \\ L_m^+ \end{pmatrix} + \begin{pmatrix} \Sigma_m^+ \\ -\Sigma_m^- \end{pmatrix}. \tag{3.2.19}$$

3.2.4 Matrix Operator Method

The method is based on the interaction principle which has been described by Twomey *et al.* [50] and later by Grand [51]. It includes any order of scattering and is applicable to systems with any optical thickness.

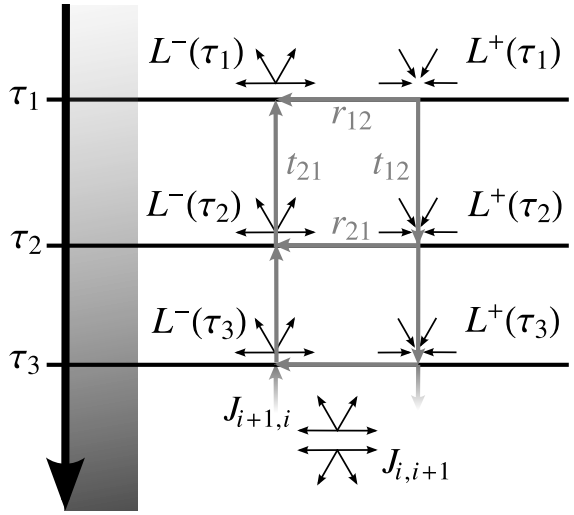

Figure 3.2.1: Interaction Principle.

The interaction principle states that the upward directed light field at a given optical thickness depends linearly on the transmitted light field from a layer at higher optical thickness, and the downward directed intensity at the same level. The interaction coefficients are called reflection r_{ij} and transmission t_{ij} and a schematic is shown in Figure 3.2.1. This holds analogously for the downward directed light field at the lower level:

$$L^+(\tau_2) = t_{21}L^+(\tau_1) + r_{12}L^-(\tau_2) + J_{21}, \tag{3.2.20}$$
$$L^-(\tau_1) = r_{21}L^+(\tau_1) + t_{12}L^-(\tau_2) + J_{12}. \tag{3.2.21}$$

Stating the interaction principle for two consecutive atmospheric layers with three boundaries, one can eliminate the transmission and reflection operators of the intermediate layer. By writing the resulting equations in the same form as the interaction principle, the transmission and reflection operators of the combined layers can be expressed as [50, 52, 53, 35, 39]:

$$\mathbf{t_{31}} = \mathbf{t_{32}}\left(\mathbb{1} - \mathbf{r_{12}r_{32}}\right)^{-1}\mathbf{t_{21}}, \tag{3.2.22}$$
$$\mathbf{t_{13}} = \mathbf{t_{12}}\left(\mathbb{1} - \mathbf{r_{32}r_{12}}\right)^{-1}\mathbf{t_{23}}, \tag{3.2.23}$$
$$\mathbf{r_{31}} = \mathbf{r_{21}} + \mathbf{t_{12}r_{32}}\left(\mathbb{1} - \mathbf{r_{12}r_{32}}\right)^{-1}\mathbf{t_{21}}, \tag{3.2.24}$$
$$\mathbf{r_{13}} = \mathbf{r_{23}} + \mathbf{t_{32}r_{12}}\left(\mathbb{1} - \mathbf{r_{32}r_{12}}\right)^{-1}\mathbf{t_{23}}. \tag{3.2.25}$$

Applying the algorithm for two layers with the same optical properties is known as doubling; applying it to layers with different optical properties as adding.

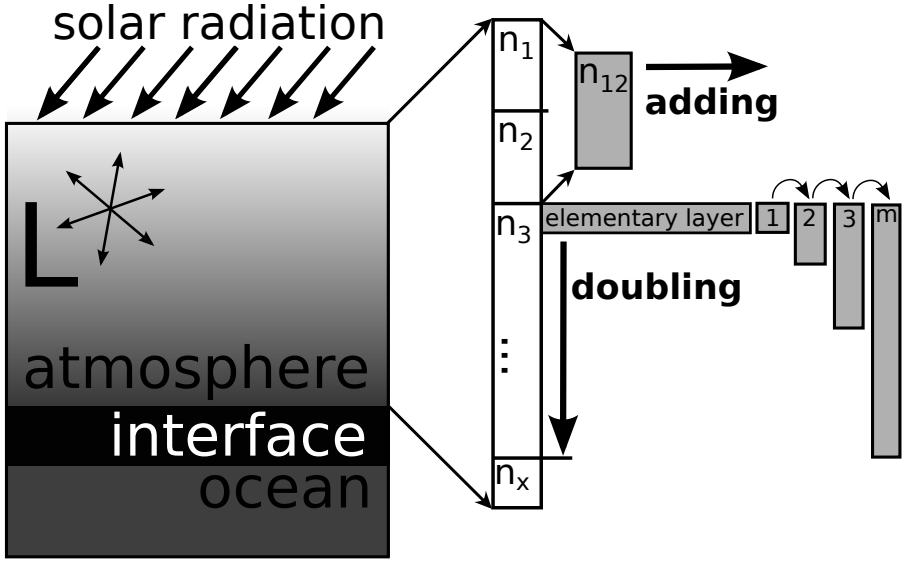

Figure 3.2.2: Doubling and adding scheme.

Figure 3.2.2 shows how this concept is applied to the atmosphere ocean system. The initial optical thickness τ_0 after n doublings grows exponentially like $\tau_n = \tau_o 2^n$ and should be chosen such that final result is independent of τ_o. The layers can be combined using the adding algorithm and the interaction principle can be used to calculate the radiances at inter layer boundaries.

The mathematical foundation of this procedure was published in a series of papers by Grant and Hunt [51, 54] and a result was the differential matrix form of the interaction principle, which has the same form as Equation 3.2.19:

$$\frac{d}{\mathrm{d}\tau}\begin{pmatrix} L^+ \\ L^- \end{pmatrix} = \frac{d}{\mathrm{d}\tau}\begin{pmatrix} t_{01} - \mathbb{1} & r_{10} \\ r_{01} & t_{10} - \mathbb{1} \end{pmatrix}\begin{pmatrix} L^+ \\ L^- \end{pmatrix} + \frac{d}{\mathrm{d}\tau}\begin{pmatrix} J_{01}^+ \\ J_{10}^- \end{pmatrix}. \tag{3.2.26}$$

A comparison of the two equations yields the definition of the elementary transmission and reflection operators:

$$\mathbf{t_{10}} = \mathbb{1} - \mathbf{\Gamma_m^{++}} \mathrm{d}\tau, \tag{3.2.27}$$
$$\mathbf{t_{01}} = \mathbb{1} - \mathbf{\Gamma_m^{-}} \mathrm{d}\tau, \tag{3.2.28}$$
$$\mathbf{r_{01}} = \mathbf{\Gamma_m^{+-}} \mathrm{d}\tau, \tag{3.2.29}$$
$$\mathbf{r_{10}} = \mathbf{\Gamma_m^{-+}} \mathrm{d}\tau. \tag{3.2.30}$$

3.2.5 Sea Water Optical Model

Scattering of radiation by ocean water can be modeled using a Rayleigh-like phase matrix with a depolarization factor of $\delta = 0.039$ [55]. Sources of scattering in the homogeneous water bulk are thermodynamic fluctuations of sea water density and salt ion concentration. A detailed discussion in terms of thermodynamics has been given by Zhang and Hu [56]. As an option for the user we keep the previously used model from Morel [57], which neglects temperature and salinity effects. Morel described a model with exponential spectral dependency with two constants that have been derived from measurements in open oceans:

$$\beta_i^{morel} = 0.00288 \frac{1}{m} * \left(\frac{\lambda}{500nm} \right)^{-4.32}. \tag{3.2.31}$$

The absorption coefficient a_w of pure sea water is taken from the algorithm theoretical basis document (ATBD) of the ESA project WATERRADIANCE [55], which includes data from many sources ([58, 59, 60, 61, 62, 63, 64]). The absorption is modeled as linear expansion with coefficients Ψ_S for salinity, Ψ_T for temperature, and absorption measurements at $T_0 = 20^\circ$ and $S_0 = 0PSU$:

$$a_w(T, S, \lambda) = a_w(T_0, S_0, \lambda) + (T - T_0)\Psi_T(\lambda) + (S - S_0)\Psi_S(\lambda). \tag{3.2.32}$$

The refractive index of air relative to sea water can be calculated using:

$$\begin{aligned} n_{sw}^{air}(T, S, \lambda \in [300nm, 800nm]) = n_0 + \left(n_1 + n_2 T + n_3 T^2\right) S + \\ n_4 T^2 + \frac{n_5 + n_6 S + n_7 T}{\lambda} + \frac{n_8}{\lambda^2} + \frac{n_9}{\lambda^3}, \end{aligned} \tag{3.2.33}$$

with values of the k_i from reference [55]. For longer wavelengths up to $4000nm$, the temperature and salinity dependency at $800nm$ can be used.

The volume scattering coefficient of sea water β_{sw} is the sum of contributions from density fluctuations (β_{df}) and concentration fluctuations (β_{cf}) and has been discussed by Zhang and Hu [56]:

$$\beta_{sw}(\lambda, T, S) = \beta_{df}(\lambda, T, S) + \beta_{cf}(\lambda, T, S). \tag{3.2.34}$$

In Figure 3.2.3 we show relative differences of the model by Morel and that by Zhang and Hu. The variation with salinity and temperature is shown as a set of gray curves and at $400nm$ the relative differences are in the order of 10%.

The variation of the relative refractive index with respect to wavelength, salinity and temperature is shown in Figure 3.2.4. On the scales of temperature and salinity relevant to the Earth's oceans, the changes with salinity are more pronounced than those with temperature.

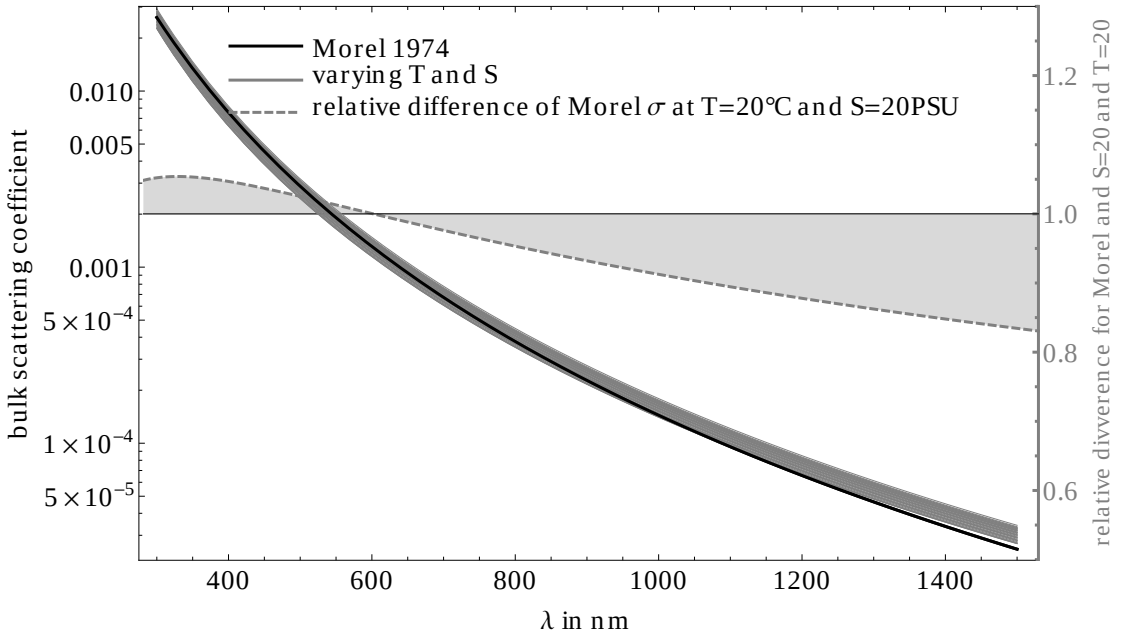

Figure 3.2.3: Volume scattering coefficient with log scale according to the Morel model (in black) and varying with temperature and salinity (in gray). The dashed line represents (right scale) relative differences between the model for a temperature of 20° and salinity of 20PSU.

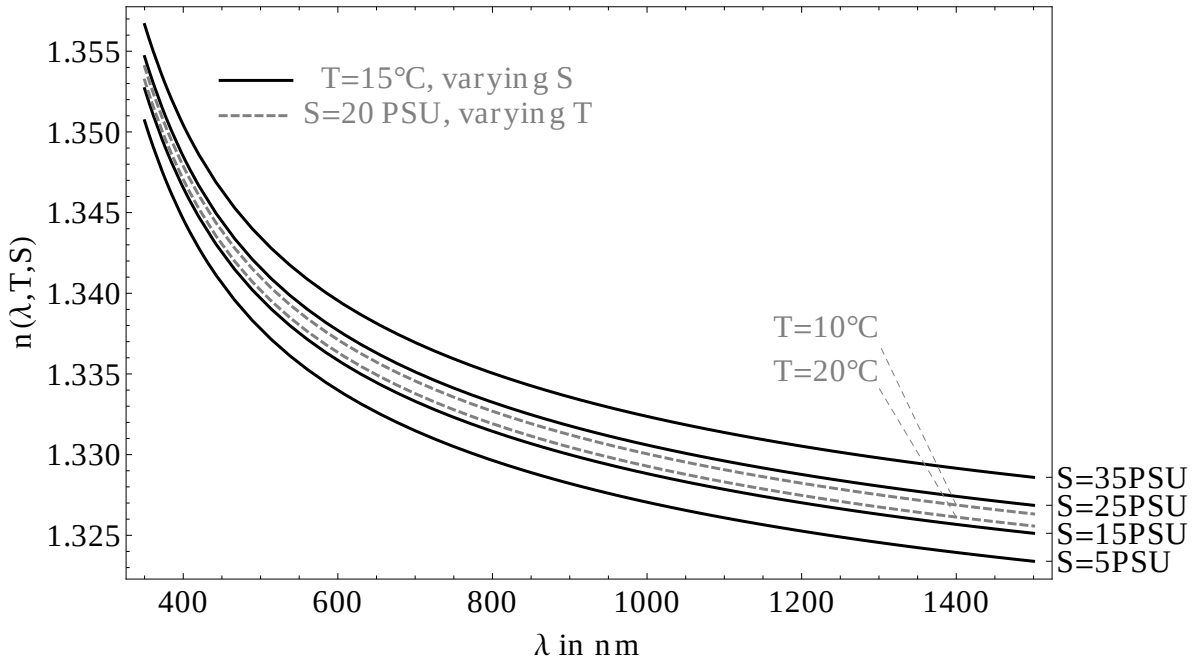

Figure 3.2.4: Relative refractive index with respect to wavelength, salinity and temperature. Variations due to salinity changes at constant temperature are shown with black lines, those with temperature at constant salinity are shown with gray dashed lines.

3.2.6 Bio-Optical Model for Case One Waters

The bio-optical model relates the chlorophyll concentration to its spectrum of inherent optical properties (IOP). The latest measurements of IOPs available to us are from Bricaud *et al.* (from 2010 via personal communication, see also [65]) and include measurements of the single scattering albedo ω_0 and the chlorophyll absorption coefficient a_{chl}; but not the phase matrix.

Information about the shape of chlorophyll phase functions has been given by A. Morel [66], J. Chowdhary [40], M. Chami [38] and others. Spectral constant size distribution parameters and the complex refractive index spectra are input parameters for Mie calculations. We derive the first guess of the imaginary part of the refractive index by using the following equation [65, 67]:

$$n_i(\lambda) = \frac{a_{chl}(\lambda)\lambda}{4\pi}, \tag{3.2.35}$$

where a_{chl} is the chlorophyll absorption coefficient. This simple model assumes that the electric field in a chlorophyll particle is an evanescent wave. To compensate the shortcomings of this simple model, we introduce an offset to the complex refractive index. We use the Levenberg Marquardt method to optimize the size distribution parameters and the offset to find a fit to the measured single scattering albedo spectra. The result is an almost perfect fit to the data, but the phase matrices show unphysical high oscillating phase functions. To overcome this, we add a penalty value to the norm used in the optimization scheme if the backward direction of the resulting phase function is either too small, or shows too strong oscillations. This describes a trade-off between achieving physical phase functions and a better fit of the single scattering albedo spectrum. Figure 3.2.5 shows the resulting single scattering albedo spectra and the measurements for chlorophyll concentrations from $0.1\mu g/l$ to $50\mu g/l$.

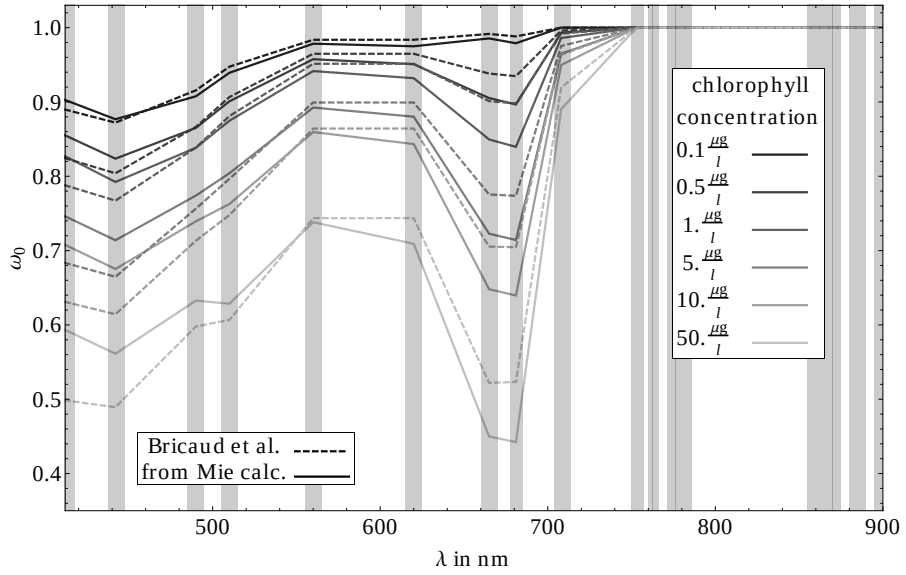

Figure 3.2.5: Single scattering albedo spectra from Bricaud 1998 (dashed lines), and best fit results with penalty terms using a log normal size distribution. The gray vertical columns indicate the position and the width of the OLCI channels in that spectral band.

Figure 3.2.6 shows the spectral dependence of all absorption coefficients in the bio-optical model. Data for the chlorophyll absorption is present where the symbols are drawn. For a given chlorophyll concentration in the *Bricaud 1989* data set, the absorption of CDOM can be calculated using the proposed exponential model:

$$a_{CDOM}(\lambda) = a_{CDOM}(440nm)e^{-S(\lambda-440nm)}, S = 0.011\frac{1}{nm}. \tag{3.2.36}$$

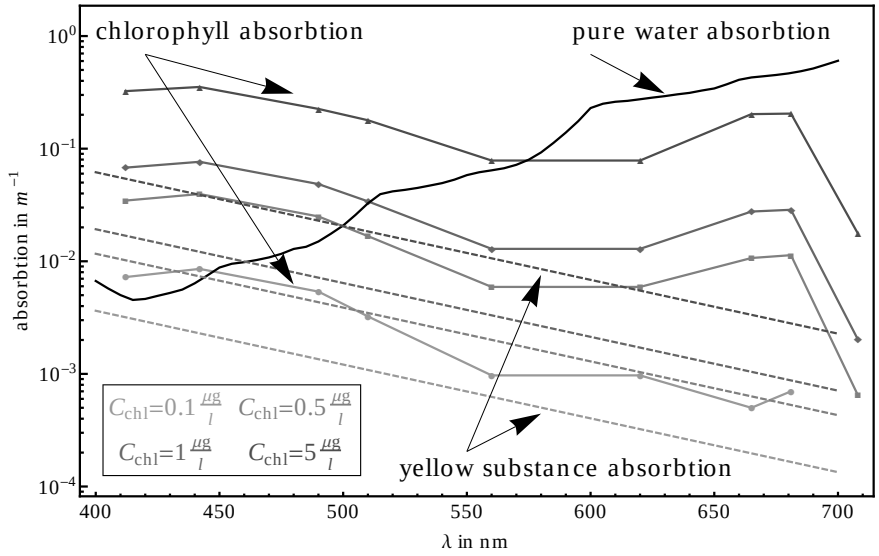

Figure 3.2.6: Absorption coefficients of the constituents of the bio-optical ocean model. The black solid line shows the absorption of pure water, the dashed lines show the absorption of CDOM and the straight lines the absorption of chlorophyll. Different gray tones represent different chlorophyll and associated CDOM concentrations.

3.2.7 Model Validation

The standard way of validating new implementations of RTE solvers is to compare results with independent implementations for common test cases. Tables containing numeric values of the polarized radiation field for special cases have been published by several authors [31, 68, 69, 70, 71, 32, 33]. We used data from Natraj *et al.* [32] and Kokhanovsky *et al.* [33] to validate MOMO. First, we compare Stokes vector tables for cases of pure Rayleigh scattering. Second, we compare light fields calculated with the SCIATRAN model [72] for scattering by three scattering matrices (including Rayleigh) over a black surface. At last we look at physical aspects of the light field.

3.2.8 Rayleigh Scattering

The tables for Rayleigh scattering by Natraj *et al.* [32] have been calculated using a numerically more stable approach to the solution of the X and Y functions of Chandrasekhar and Coulsen [29, 31]. The range of viewing angles in the tables is from 0° to 90° (16 values), solar positions range from 0° to 90° (7 values), and azimuth positions range from 0° to 180° (7 values). Surface albedos range from 0.0 to 1.0 (3 values) and Rayleigh optical depth range from 0.02 to 1.0 (5 values).

The main result of our comparison is shown in Figure 3.2.7. Panel (a) shows the relative differences with respect to viewing angle for every point in the table. Panel (b) is the same type of graph, but for significant differences. The significant difference of two numbers a and b is the difference of the significant in language independent arithmetic form of a and b divided by ten to the power of the exponent of a. The value shows the number of (nonzero) equal digits of the two numbers.

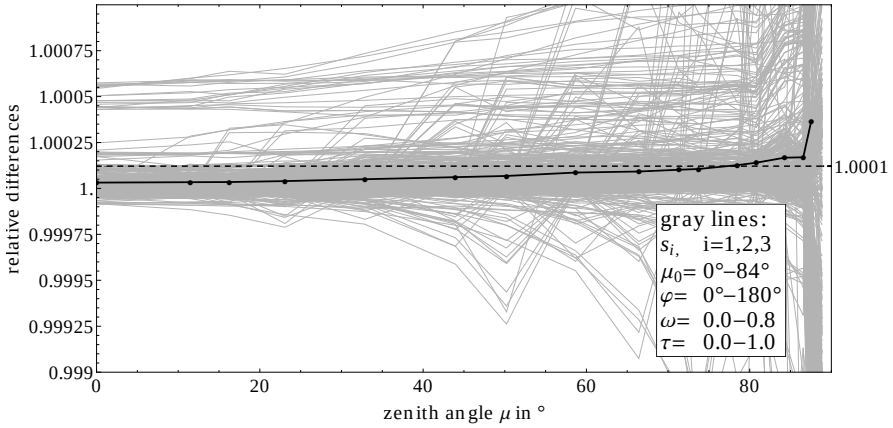

(a) Relative differences of the published tables and MOMO results.

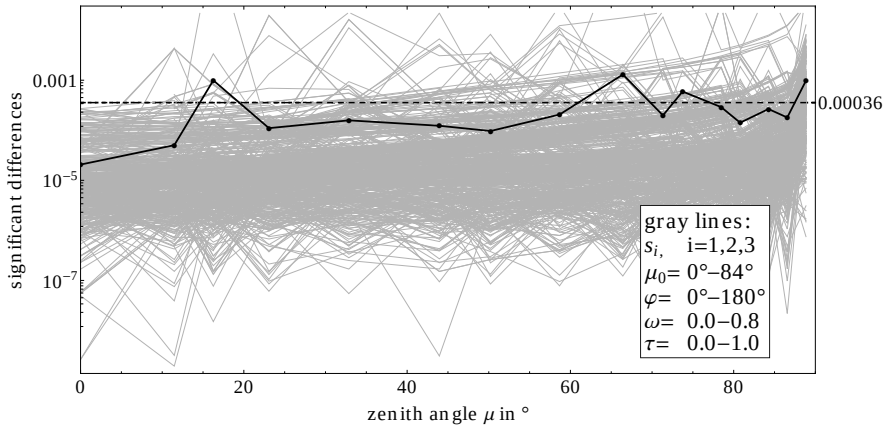

(b) Significant differences of the published tables and MOMO results. Significant differences indicates the number of equal digits of the compared numbers.

Figure 3.2.7: Difference of MOMO calculations and Natraj's tables [32]. All available cases are plotted in gray. The zenith resolved mean is shown in black, and the overall mean as number on the right scale.

3.2.9 Mie Scattering

Kokhanovsky *et al.* [33] have published results from the SCIATRAN model, where three scattering cases involve a homogeneous purely scattering layer over a black surface. As scatterers they have chosen the Rayleigh, an aerosol and a cloud type phase matrix. The components of the phase matrices under consideration are shown in Figure 3.2.8. Both phase functions (see m_1 and m_3 component) are strongly peaked in the forward direction. The other phase matrix elements m_5 and m_6 are rich in features and hence useful to test the accuracy of the models for given resolutions.

The mean relative deviations of MOMO and SCIATRAN results for all cases are shown in Figure 3.2.9. Results of MOMO calculations for the two cases together with the SCIATRAN results are shown in the Appendix in Figure 3.2.22. Our results agree very well with the results from SCIATRAN. The dashed lines in the figure represent cases in which the phase functions have been truncated and straight lines represent results for the original phase functions. This approximation cannot reproduce the intensity in the forward scattering direction, but reproduces the components Q,U,V in this region quite well and results can be reproduced with much less computational effort (see also Section 3.2.17 and Figure 3.2.22).

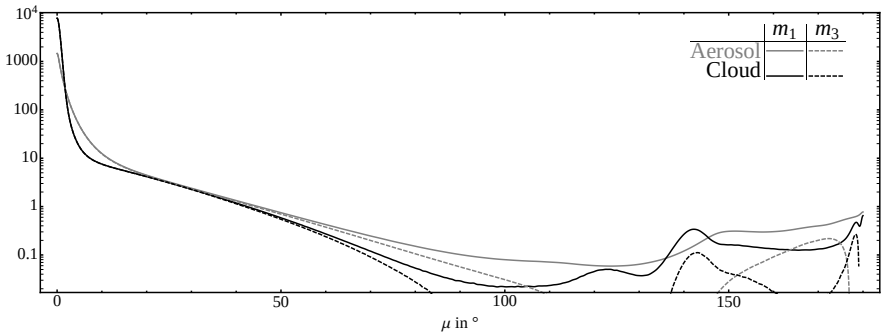

(a) M_1 and M_3 component.

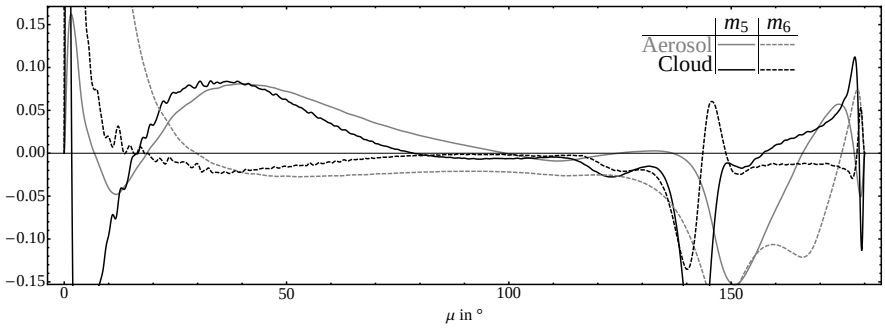

(b) M_5 and M_6 component.

Figure 3.2.8: Benchmark phase matrices from Kokhanovsky *et al.* [33].

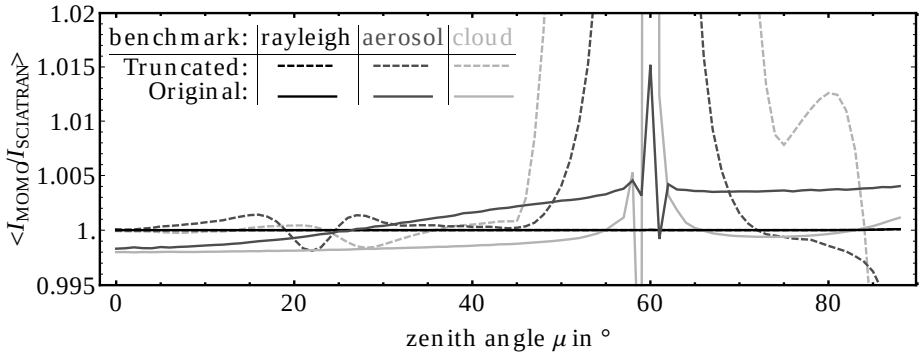

(a) Intensity.

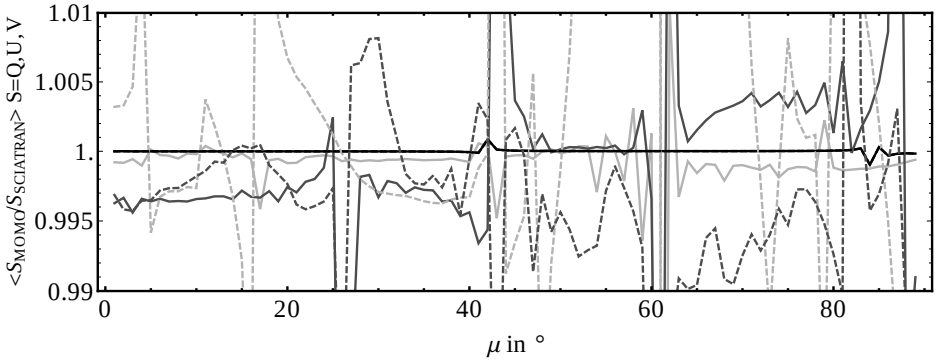

(b) Q, U and V parameter.

Figure 3.2.9: Mean of relative differences for MOMO and SCIATRAN results. The mean is taken over the azimuth values and up and downward direction. Scatter types are indicated with gray tones. Straight lines show results for the original phase matrices and dashed lines for the truncated phase matrices. Absolute values are shown in Figure 3.2.22.

3.2.10 Conservation of Flux

Elastic scattering conserves the radiance flux. To test only the effects of scattering, we calculated a number of test cases where the direct solar source is only present in the top of atmosphere layer. This layer is the only source of diffuse radiation that propagates through the system. With no internal sources and no absorption present, the outward directed fluxes from a single layer must balance the inward directed fluxes from the neighbor layers:

$$\epsilon = \underbrace{\left(F^{\uparrow}(\tau_n) + F^{\downarrow}(\tau_n)\right)}_{F_{out}} - \underbrace{\left(F^{\uparrow}(\tau_{n-1}) + F^{\downarrow}(\tau_{n+1})\right)}_{F_{in}}, \tag{3.2.37}$$

$$\delta = \frac{F_{out} - F_{in}}{\frac{1}{2}(F_{out} + F_{in})}. \tag{3.2.38}$$

The deficiency value ϵ should be small for all layers, and can serve as a proxy for the accuracy of the model for a given resolution. Here we use δ to describe the ratio of the deficiency to the mean of the two fluxes. To test the Fourier expansion, we calculate the fluxes from azimuthal resolved radiances at a layer boundary:

$$F^{\uparrow,\downarrow}(\tau) = \int d\mu d\phi \mu L^{\uparrow,\downarrow}(\tau, \mu, \phi). \tag{3.2.39}$$

A nonzero value of δ has two possible origins: first, due to errors in the implementation, and second, due to the numeric approximation of the integrals. Since it can be almost impossible to distinguish the two effects, δ must be small. For layers with Mie scattering, δ is smaller than 1% when choosing 30 atmospheric Gaussian points, 36 Fourier terms, and azimuthal output at every 30°. Using this procedure we can also test the atmosphere ocean interface and at the same resolution we find deficiencies smaller than 3%.

3.2.11 Ocean Surface Reflection

Tables of the radiation emerging from the ocean, to our best knowledge, have not been published yet.[7] In a paper by Mobley *et al.* [73], the authors showed a comparison of several models for oceanic waters. The scalar version of our model agreed well with the published values [39]. However, they do not include polarization or detailed radiance fields, and hence are not sufficient for a comparison. For this comparison, we consider an atmosphere with Rayleigh scattering with an optical thickness of 0.1, a rough sea surface as lower boundary, no ocean body, and the wind speed is set to $7m/s$. Via personal communication, the author of the NASA GISS radiative transfer model, Jacek Chowdhary, shared with us some results of his model [40, 74]. The compared model output was the upward directed vector radiance at the top of the atmosphere. In Figure 3.2.10 we show results for the upward directed radiance and degree of polarization for both models. The dashed lines represent Chowdhary's results, and the plot markers show the model resolution of 0.1 in terms of zenith cosines. Since for a given zenith resolution both of the models use different sampling points, we used MOMO with a high resolution of 60 zenith angles to be able to compare with Chowdhary's results. In both panels we show results for different solar angles indicated by different gray shades, and show solar positions with vertical dashed lines. The two models agree very well with each other, which holds for all other viewing geometries. A comparison in which we used the same zenith resolution produced similar results. The largest deviations are seen in the direction of the horizon near sun glint for low solar angles.

[7] An statement also given by Zhai *et al.* in 2010 [42].

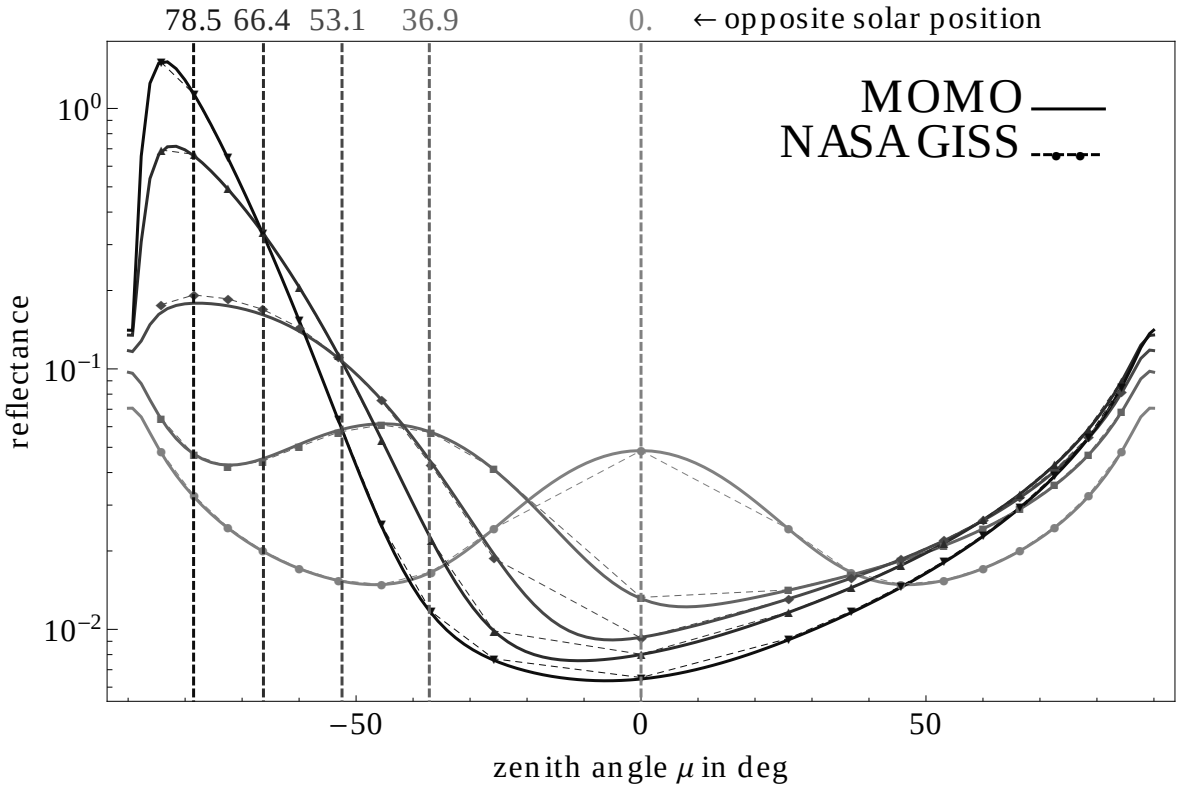

(a) Comparison of radiances in the principal plane for different solar positions.

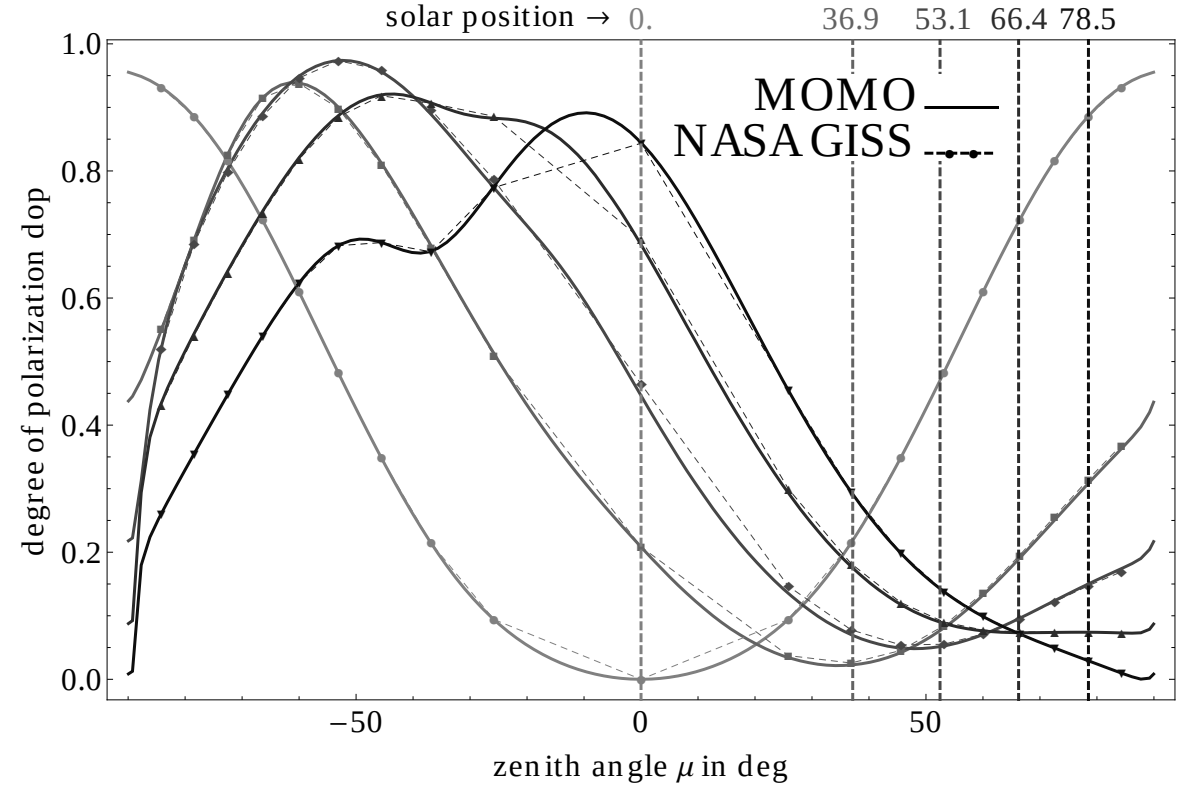

(b) Comparison of degree of polarization in the principal plane for different solar positions.

Figure 3.2.10: Comparison of radiances and degree of polarization computed with our and Chowdhary's model. The viewing geometry is the principal plane, and curves show the results for different solar positions.

3.2.12 Known Properties

To test if the radiative transfer model is physically correct, we look at special cases and verify if the model reproduces our expectations. The sun glints directed into the atmosphere and into the ocean are good proxies for the correct implementation of the reflection and transmission matrices of the interface. Both are dominant features, showing strong dependencies with the zenith and azimuth angles, and they are computed with the same matrices that are used for the diffuse reflection and transmission. In Figure 3.2.11 we show upward directed TOA radiances for a Rayleigh atmosphere with a black surface, and cases with an ocean surface with varying wind speed. The Rayleigh optical thickness for these cases was set to 0.1 ($\approx 545nm$) using a US standard atmosphere. As the wind speed becomes smaller, the sun glint becomes more narrow and stronger as one would expect if the surface roughness is changing from rippled to flat.

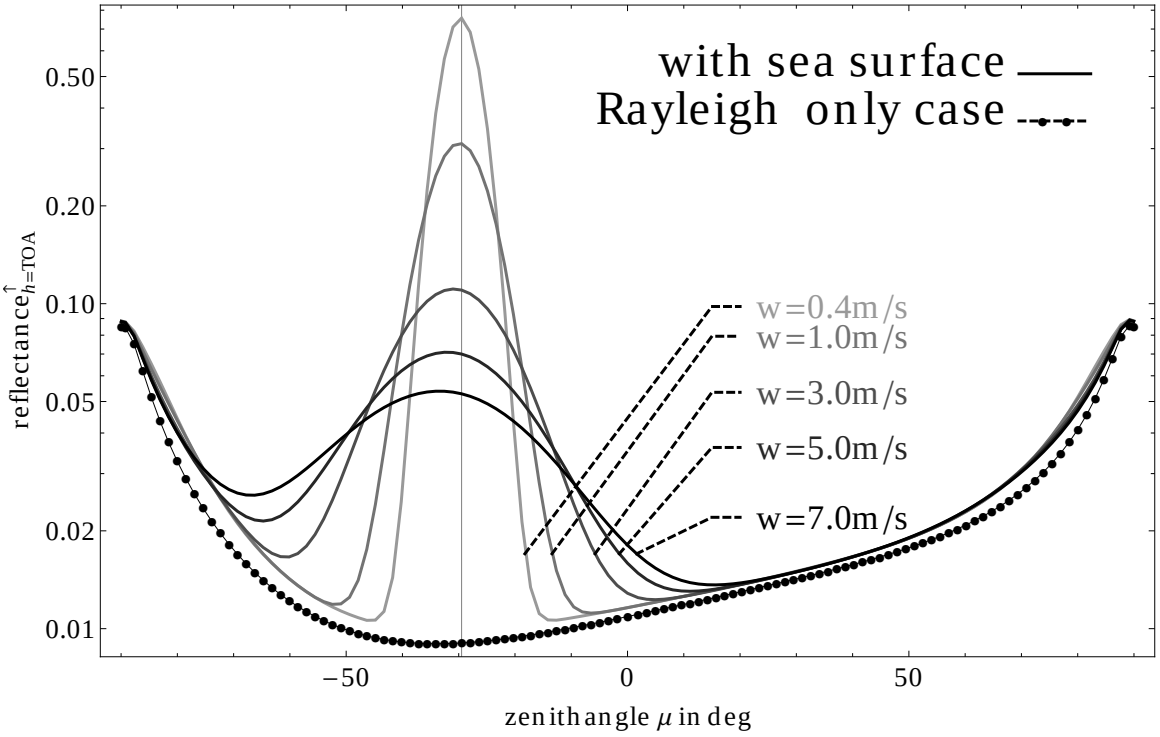

Figure 3.2.11: Upward directed radiance at the top of the atmosphere in the principal plane. Solar position is indicated with a vertical line. The black line with plot markers represents the result with a black surface and shows also the zenith resolution. Result for different surface wind speeds are shown as gray shaded lines. The solar constant was set to unity, so the unit represents reflection.

When the light field propagates into the ocean it is refracted according to Snell's law. In Figure 3.2.12 ($\tau = 0.1, w = 1m/s$) we show the upward and downward directed radiance just above and below the ocean interface. The directions are indicated by the signs of the radiances. We show the position of the sun, the critical angle, and the position of the refracted solar position with vertical lines. As expected, the glint into the ocean is refracted, and the sun glint has a steeper angle.

Another way to test the refraction in the model is to look at the downward directed radiance just below the ocean surface. We set the solar position to the zenith and chose a high water absorption so that there is no upward directed radiance that can contribute to the signal from reflection at the ocean surface. In Figure 3.2.13 we show the results of this simulation for

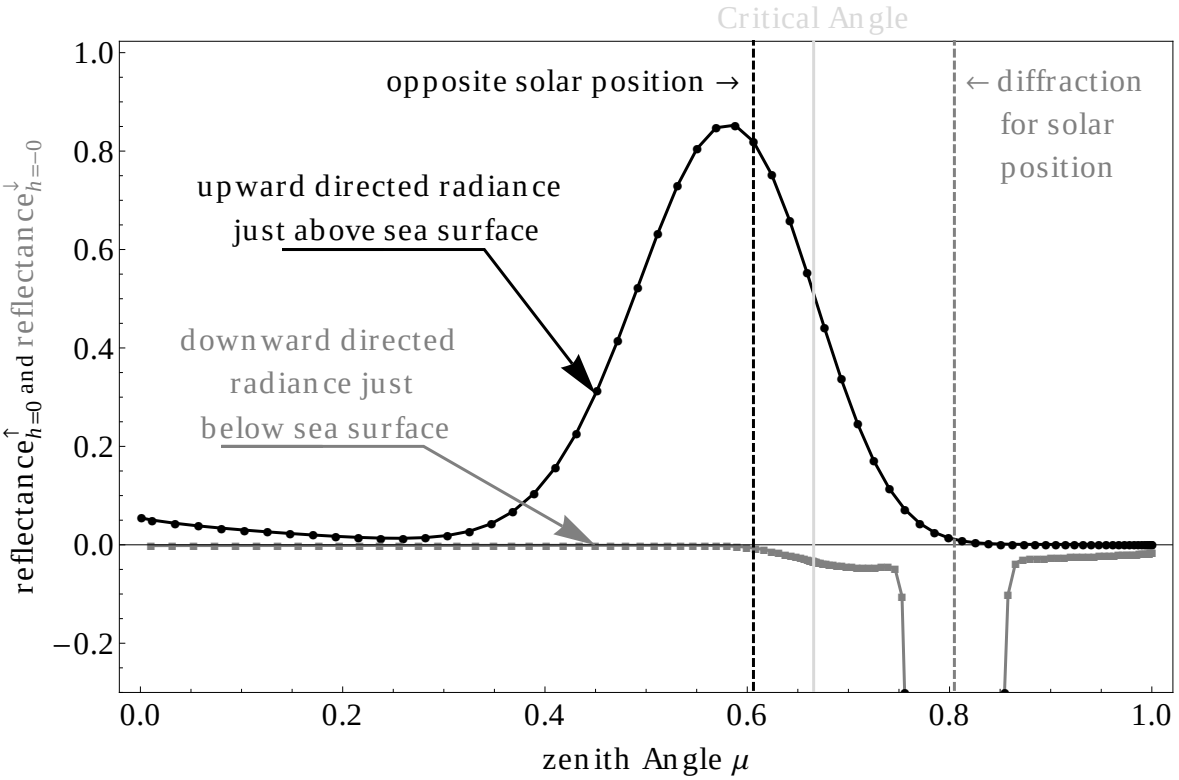

Figure 3.2.12: Upward (black) and downward (gray) directed radiances just above and below the ocean surface. The solar position and refracted solar position are shown with vertical dashed lines. The critical angle is shown by the gray vertical line.

different surface wind speeds. When looking at the lowest chosen wind speed of $0.1m/s$, we can clearly see that the transmitted diffuse radiance is almost entirely refracted into the Fresnel cone. At the boundary of the cone we can see the brightening of the underwater horizon. If the surface wind speed increases the boundary becomes more smooth and radiance is distributed to the outside of the Fresnel cone.

For a flat ocean surface the Fresnel cone has a sharp boundary and all transmitted radiance from the atmosphere is refracted into the cone. Upward directed radiance just below the ocean interface becomes total internally reflected if outside the Fresnel cone. In Figure 3.2.14 we show the downward directed radiance just below the ocean interface; the sun is in zenith, the sky is black, and the ocean is purely scattering. Different wind speeds are shown with different shades of gray and one can see how the sharp boundary of the Fresnel cone becomes smoother for rougher ocean surfaces.

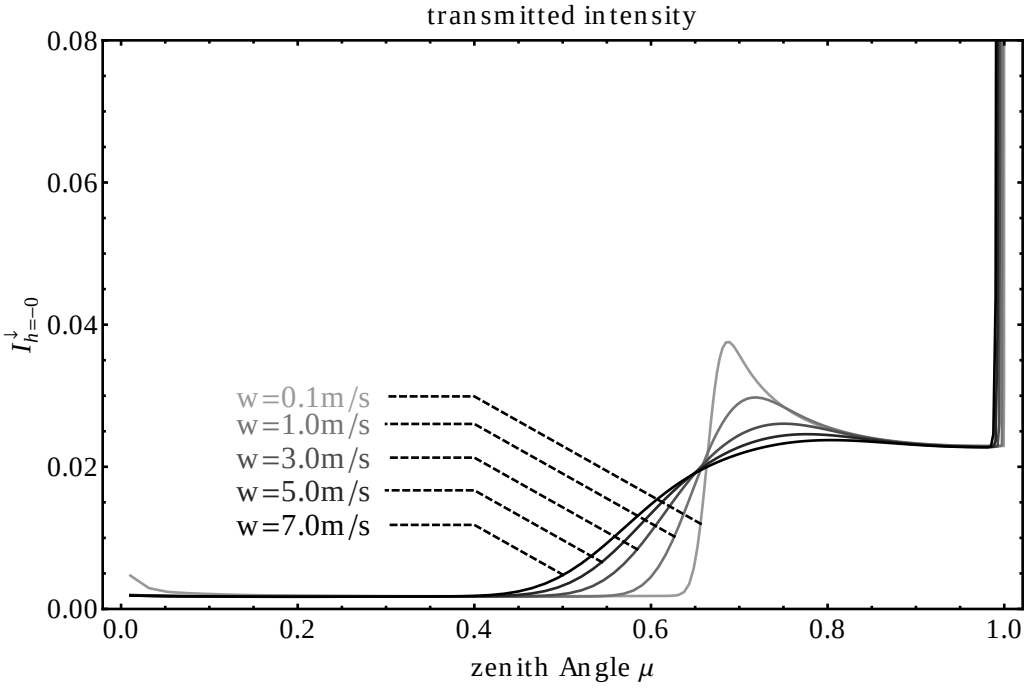

Figure 3.2.13: Downward directed radiance just below the ocean surface. The solar position is set to zenith and different surface wind speed cases are shown with different gray shades. The ocean is highly absorbing and reflection from upward directed radiance from the ocean is not contributing to the signal.

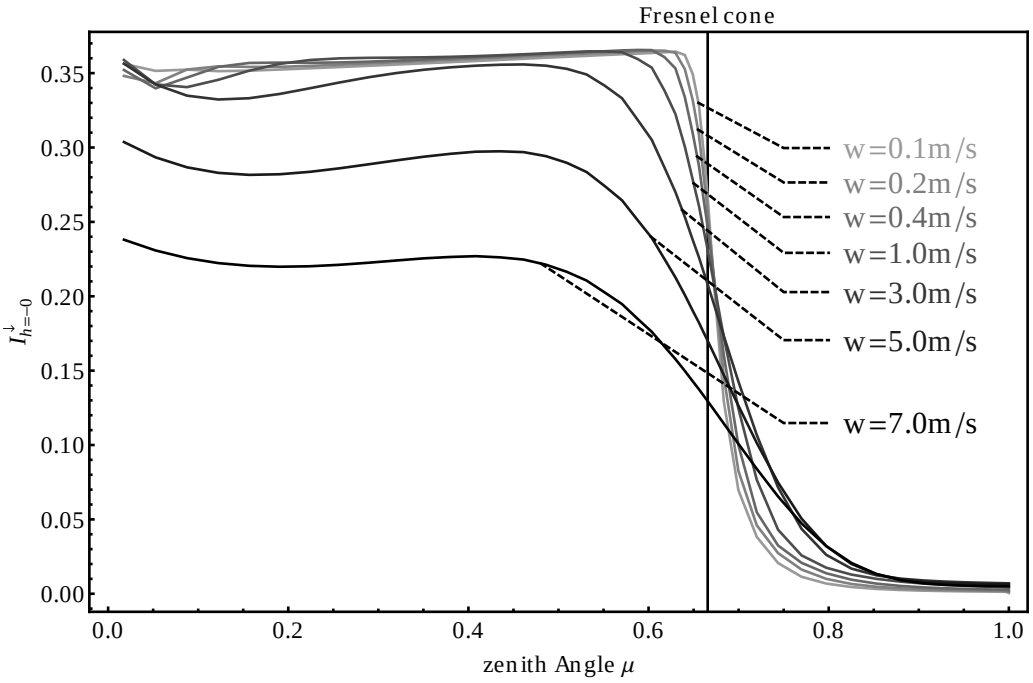

Figure 3.2.14: Downward directed radiance just below the ocean surface without contribution from transmitted radiance. Different surface wind speeds are indicated with different shades of gray.

3.2.13 First Applications

MOMO now accounts for polarization, sea water salinity, and sea water temperature, and all three effects can have a non-negligible impact on top-of-atmosphere and water-leaving radiance. In this section we discuss two applications of the model for top-of-atmosphere and water-leaving radiances, for channels from $412.5nm$ up to $900nm$ of the upcoming ocean color instrument OLCI (Ocean Land Color Instrument) onboard ESA's Sentinel 3 satellite.

3.2.14 Effects of Neglecting Polarization in Case One Waters

MOMO can be operated in a scalar mode that neglects polarization and therefore consumes less memory and is much faster than the vector mode. When switching from polarization to scalar mode, the difference in computing time and memory is slightly smaller than $1/(3 \times 3)$ for linear, or $1/(4 \times 4)$ for complete, Stokes vector calculations. The main reason for this effect is that higher order Fourier terms of the scattering matrices tend to contain more zero valued elements than those of lower orders (depending on the actual physical constituent) and that we use a sparse matrix multiplication approach, which is much faster for matrices containing zero valued elements. Using only scalar radiative transfer is usually much faster to compute and less difficult to implement, but resulting relative deviations from vector calculations can reach up to 20% for atmosphere ocean systems [42] and will in general depend on wavelength and scene. For a brief discussion we computed the effects of neglecting polarization for the $412nm$ OLCI channel where the sea water is most transparent. Figure 3.2.15 shows hemispheric plots with radiances calculated with the vector model (see top of each panel) and the relative difference $1 - \vec{I}/I$ with respect to the scalar mode (bottom of each panel). We call $1 - \vec{I}/I$ the relative polarization error, and if it is smaller then zero, the scalar calculations are underestimating the real value. Results are shown for the solar positions 25.9° (see Panel (a)) and 50.3° (see Panel (b)). The salinity is $35PSU$, the wind speed is $7m/s$, and the sea water temperature is $15°C$. For both cases combined, the relative polarization error is in the order of $\pm 8\%$. A change of sign occurs and the pattern of this change depends strongly on solar position. The highest relative polarization error can be found in the principle plane opposite to the solar position.

Figure 3.2.15 shows results for water-leaving radiances for the same case. The range of the relative polarization error increases from -2.5% to -5% to values from 1.5% to -6% for the higher solar angle. With increasing solar angle a sign change of the relative polarization error occurs.

We can conclude that the effects of neglecting polarization for a realistic atmosphere ocean system with case one waters depend strongly on viewing geometry and solar angle, and in the shown cases reached values up to $\pm 8\%$. The relative polarization error can show a rather complex pattern; therefore we see no easy way of correcting scalar radiative results without running a full vector model.

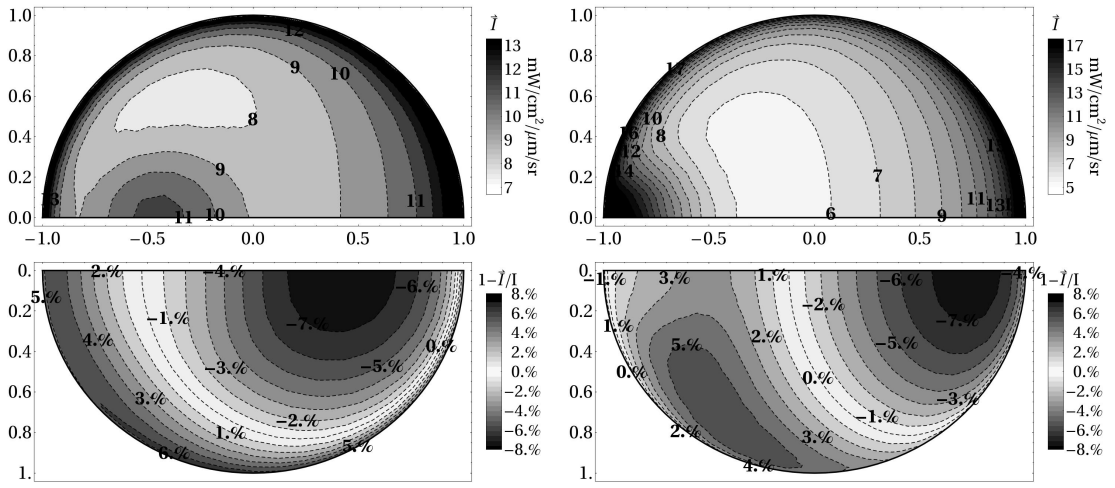

(a) Sun at 25.9°. (b) Sun at 50.3°.

Figure 3.2.15: Top-of-atmosphere vector radiance field in the 412.5nnm channel for an atmosphere ocean system with clear atmosphere and case one waters. The chlorophyll concentration is 0.1$\mu g/l$, the wind speed is 7m/s, and the salinity is 35PSU. In Panel (a) the sun is at 25.9° and in Panel (b) the sun is at 50.3°. The upper part of each panel shows the vector radiance where the radiance direction on the unit sphere has been projected to the equatorial plane. The gray colors indicate the value of the radiance in $W/m^2/nm/sr$. The lower part of the panel uses the same projection technique but shows the value of $1 - \vec{I}/I$ to show the relative difference of the two radiances in %.

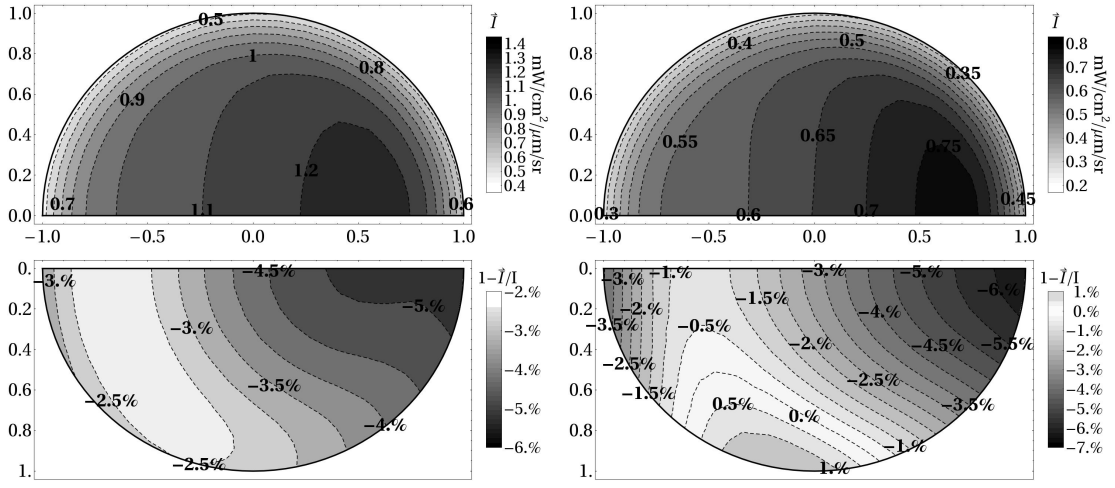

(a) Sun at 25.9°. (b) Sun at 50.3°.

Figure 3.2.16: Same case as in Figure 3.2.15, but for the water leaving radiance.

3.2.15 Salinity

The salinity of the ocean can vary from values as little as $5PSU$, as in the northern part of the Baltic sea, to a maximum of $40PSU$. A standard value of $35PSU$ for the open oceans can be assumed [75]. Figure 3.2.17 and 3.2.18 show the effects of a salinity change from $35PSU$ to $5PSU$ on top of atmosphere and water leaving zenith radiance: $1 - I_{5PSU}/I_{35PSU}$. The water leaving radiance is defined as the upward directed radiance just above the ocean surface, but without radiance contributions from diffuse and direct reflection from the ocean surface. It is the radiance directly emerging from the ocean and is an useful starting point for ocean color retrievals using radiative transfer results for the ocean alone.

Both figures show values for the sun at zenith (top value per cell), at 25.9° (bottom value per cell), and a chlorophyll concentration ranging from zero (pure sea water) to $50\mu g/l$. The atmosphere was modeled aerosol free, and gaseous absorption was taken into account. The root causes of the salinity effect are changes in the sea water absorption, the sea water bulk scattering coefficient, and the real part of the sea water refractive index. The results for the pure sea water case can be seen as upper limit to the salinity effect. Increasing chlorophyll concentration leads to additional absorption and scattering by ocean components that are independent from the salinity, therefore decreasing the salinity effect. A chlorophyll concentration of $0.1\mu g/l$ represents global mean value and for this concentration the salinity effect is in the order of 3.11% to 4.85%. For top-of-atmosphere radiances and channels up to $753.8nm$, the salinity effect is generally decreasing with increasing chlorophyll concentration, and remains almost constant for the channels with higher wavelength. This is caused by the increase in sea water absorption (see Figure 3.2.6). High sea water absorption renders the water body almost black and the remaining cause for effects are changes of the refractive index, and thus the reflectivity of the atmosphere ocean interface. When this effect dominates the signal, the salinity effect becomes independent from the chlorophyll concentration.

	413.	442.	490.	510.	560.	620.	665.	681.	709.	754.	761.	781.	863.	885.	900.
pure sea water	6.8	6.1	4.7	3.8	3.9	4.1	4.3	3.6	4.4	4.6	4.4	3.9	4.	4.	4.9
	6.6	*5.9*	*4.*	*2.5*	*2.2*	*2.*	*2.2*	*1.9*	*2.4*	*2.5*	*2.3*	*2.2*	*2.3*	*2.3*	*2.8*
C_{Chl}=0.1 $\frac{\mu g}{l}$	3.1	3.5	3.9	3.6	3.8	4.	4.3	3.6	4.4	4.6	4.4	3.9	4.	4.	4.8
	2.4	*2.6*	*2.8*	*2.3*	*2.2*	*2.*	*2.2*	*1.9*	*2.4*	*2.5*	*2.3*	*2.2*	*2.3*	*2.3*	*2.8*
C_{Chl}=0.5 $\frac{\mu g}{l}$	2.2	2.6	3.3	3.4	3.8	4.	4.3	3.6	4.4	4.6	4.4	3.9	4.	4.	4.9
	1.3	*1.5*	*1.9*	*1.9*	*2.1*	*2.*	*2.2*	*1.9*	*2.3*	*2.5*	*2.3*	*2.2*	*2.3*	*2.3*	*2.8*
C_{Chl}=1 $\frac{\mu g}{l}$	2.	2.4	3.1	3.3	3.7	4.	4.3	3.6	4.4	4.6	4.4	3.9	4.	4.	4.8
	1.	*1.2*	*1.6*	*1.7*	*2.*	*2.*	*2.2*	*1.9*	*2.3*	*2.5*	*2.3*	*2.2*	*2.3*	*2.3*	*2.8*
C_{Chl}=5 $\frac{\mu g}{l}$	1.7	2.2	2.9	3.1	3.5	4.	4.2	3.6	4.4	4.6	4.4	3.9	4.	4.	4.8
	0.7	*0.9*	*1.2*	*1.3*	*1.6*	*1.9*	*2.1*	*1.8*	*2.3*	*2.5*	*2.3*	*2.1*	*2.3*	*2.3*	*2.8*
C_{Chl}=10 $\frac{\mu g}{l}$	1.7	2.1	2.8	3.	3.4	3.9	4.1	3.5	4.4	4.6	4.4	3.9	4.	4.	4.8
	0.6	*0.8*	*1.1*	*1.2*	*1.5*	*1.8*	*2.*	*1.7*	*2.3*	*2.5*	*2.3*	*2.1*	*2.3*	*2.3*	*2.8*
C_{Chl}=50 $\frac{\mu g}{l}$	1.6	2.	2.5	2.7	3.	3.3	3.5	2.9	4.1	4.5	4.4	3.8	4.	4.	4.8
	0.5	*0.6*	*0.8*	*0.9*	*0.9*	*1.1*	*1.3*	*1.1*	*1.9*	*2.4*	*2.2*	*2.1*	*2.3*	*2.3*	*2.8*

λ in nm

Figure 3.2.17: Salinity effect ($1 - I_{35PSU}/I_{5PSU}$) for top-of-atmosphere zenith radiance in %. The top value per cell represents results with the sun in zenith position, and bottom values for the sun at 25.9°. Results are shown for the OLCI channel subset from $412.5nm$ to $900nm$, and a chlorophyll concentration range from pure sea water to $50\mu g/l$.

Figure 3.2.18 shows the salinity effect for the water-leaving radiance. For a chlorophyll concentration of $0.1\mu g/l$ the salinity effect is ranging from 4.85% to 16.84%. The effect is highest when the sea water absorption is lowest. For pure sea water, the effect is almost constant with variation from 17.59% to 19.26%, and with increasing chlorophyll concentration the salinity effect becomes smaller. For the channels in the NIR, due to the high sea water absorption, the chlorophyll signal dominates the water-leaving radiance, therefore the salinity effect becomes small.

We showed that the sea water salinity can have a significant effect on both, the top-of-

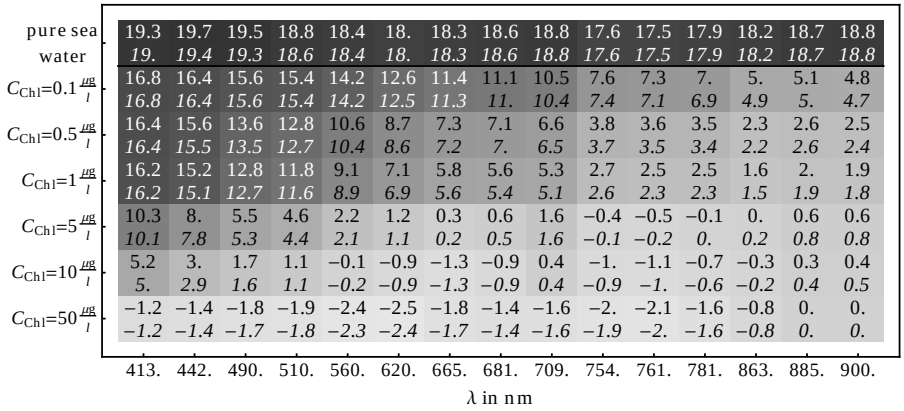

Figure 3.2.18: Salinity effect $(1 - I_{35PSU}/I_{5PSU})$ for zenith water leaving radiance in %. Top value per cell represents results with the sun in zenith position, and bottom values for the sun at 25.9°. Results are shown for the OLCI channel subset from $412.5nm$ to $900nm$, and a chlorophyll concentration range from pure sea water to $50\mu g/l$.

atmosphere radiance and the water leaving radiance. The effect is caused by changes of the sea surface reflection, sea water absorption and scattering. The changes for water-leaving radiance can reach up to 19.26%, and could have a significant effect for retrievals of ocean constituents if the actual value of the salinity is neglected.

3.2.16 Conclusion and Outlook

MOMO, now accounts for the polarization of radiation in the atmosphere-ocean system, and we are confident that our implementation is free of major errors. During the development of the vector version of the program, the latest stable scalar version was used to implement the treatment of inelastic Raman scattering. The result of merging the two versions would be an almost feature complete, one dimensional, radiative transfer system for atmosphere ocean systems.

Acknowledgments

We thank the DFG (*Deutsche Forschungsgemeinschaft*) with the SPP 1294 (HALO) and the ESA (European Space Agency) WATERRADIANCE project for providing funding for this research. We want to thank Jacek Chowdhary and Peng-Wang Zhai for sharing the results of their radiative transfer programs with us, and also appreciate the fruitful discussions with René Preusker during the implementation of this model. We also want to thank the two anonymous reviewers for their very much appreciated comments.

3.2.17 Appendix

Rough Atmosphere Ocean Interface

The model of the surface reflection matrix R and transmission matrix T is based on papers by Nakajima and Tanaka [36], Kattawar and Adams [35], and Sancer [76]. The surface is modeled as a Gaussian distribution of surface facet normals, which is caused by surface roughening due to the wind blowing over the surface [77, 78]. Shadowing effects of the surfaces facets are modeled using a shadowing function.

$$\epsilon(\mu) = 1 - \frac{1}{\mu}\int_0^1 d\mu' \int_0^{2\pi} d\phi \left(R(\mu,\mu',\phi) + T(\mu,\mu',\phi)\right). \tag{3.2.40}$$

The deviation of the deficiency term $\epsilon(\mu)$ from unity shows how the models conserve radiance flux. In Figure 3.2.19 we show the hemispheric reflection and transmission for wind speeds of 5,10, and $15 m/s$ for relative refractive indexes 1.33 and 1.33^{-1}. The top panel shows the values for light incident from the atmosphere and the bottom panel for incident light from the ocean. The window of total internal reflection (Snell's cone) can be clearly seen in Panel (b) of Figure 3.2.19. The deficiency is larger for larger wind speeds, which may be caused from multiple scattering and shadowing effects which are modeled by an shadowing function.

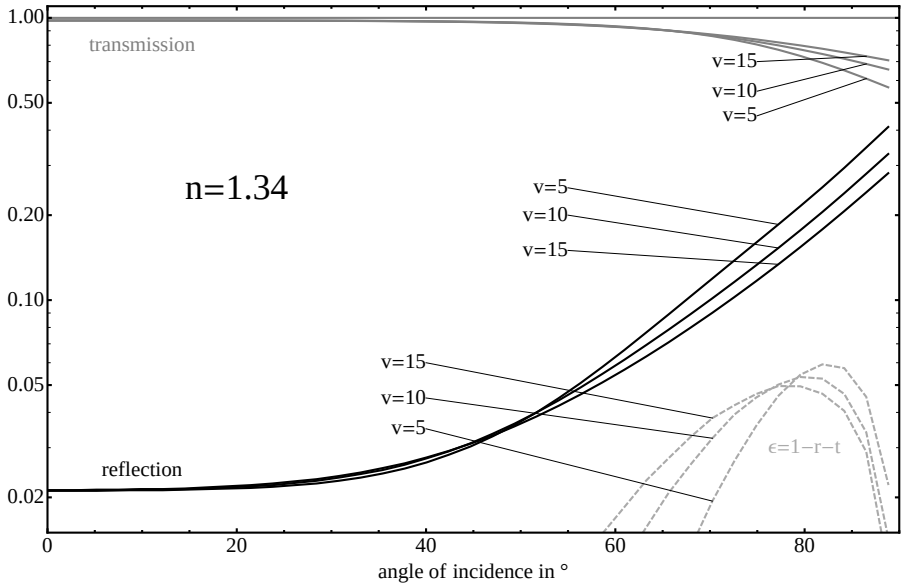

(a) Radiation incident from the atmosphere.

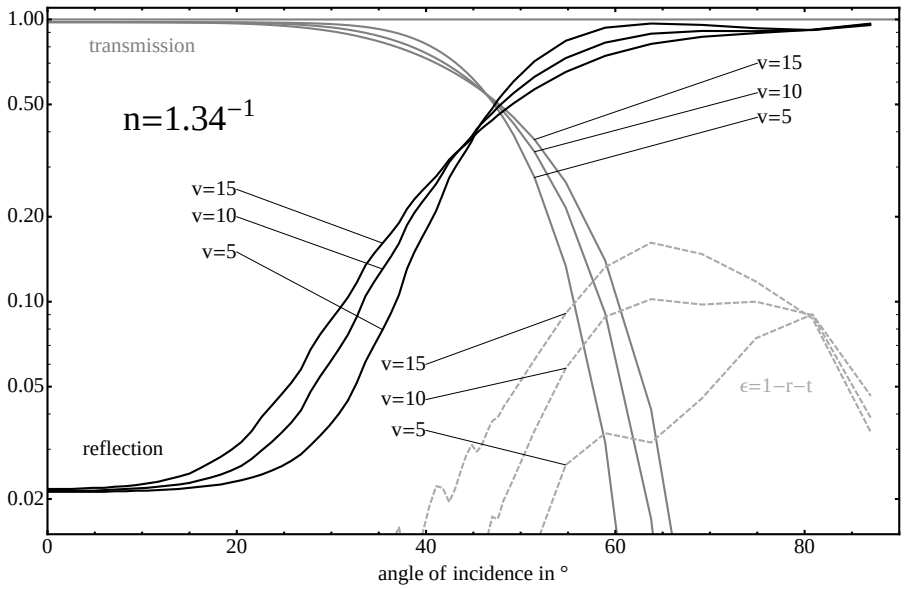

(b) Radiation incident from the ocean.

Figure 3.2.19: Hemispheric reflectivity and transmissivity for wind speeds 5,10,15 m/s for a relative refractive index of 1.34 (from atmosphere)and 1.34^{-1} (from ocean). The deficiency ϵ is shown in gray dashed lines for all three wind speeds.

Numerical Techniques: Phase Function Truncation

Phase function truncation is a widely used method to decrease the number of Fourier terms necessary for azimuthal radiative transfer calculations. The general procedure is shown in Figure 3.2.20. The strong forward peak of the original phase function (shown in black) is continuously replaced by a second order polynomial. To accurately represent the modified phase function, far fewer Fourier terms are necessary, but forward scattered radiation is effectively treated as unscattered. We show this effect in Figure 3.2.22 using the phase functions used in the comparison with SCIATRAN. We show results from the SCIATRAN model, and results from MOMO using the original and the truncated phase function. In Panel (b) we show the downward directed radiation. The strong diffuse forward scattering could not be reproduced, but away from this feature the results with truncated phase function agree well.

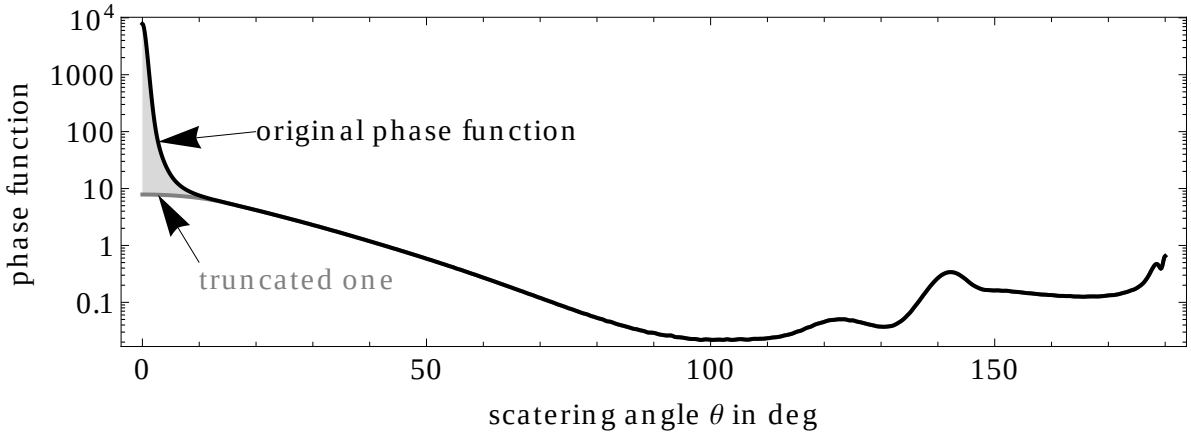

Figure 3.2.20: Phase function and truncated phase function. Truncation is performed from 15° on.

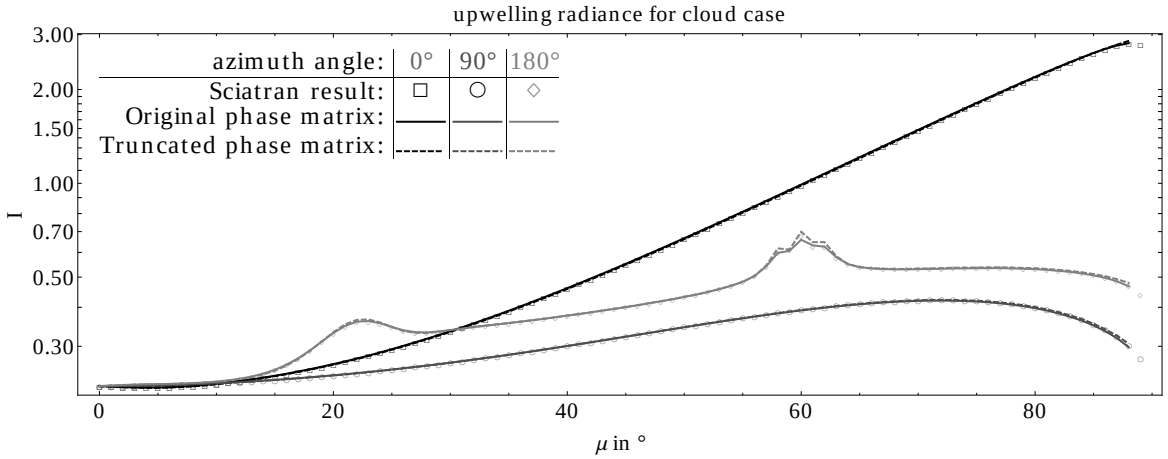

Figure 3.2.21: Detailed comparisons of MOMO and SCIATRAN results for the upward directed radiance for the aerosol case.

To keep the polarization properties of the original phase matrix, we rescale all other elements of the matrix with the ratio of the truncated and the original phase function [38].

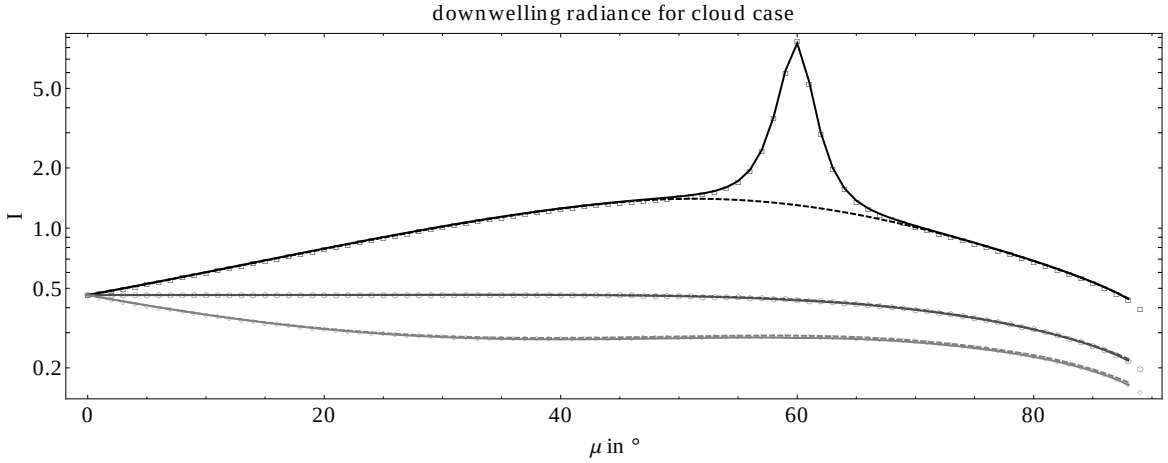

Figure 3.2.22: Same as Figure 3.2.21, but for the downward directed radiance for the aerosol case.

Numerical Techniques: Fourier Series Modification for the Conservation of Radiation

The conservation of intensity for scattering can become an issue if the zenith resolution of the RT computations is too low. Incident radiation $\vec{S}(\mu')$ is scattered to all other directions μ described by the phase matrix: $\vec{S}^{\mu'}(\mu) = M(\mu', \mu)\vec{S}(\mu')$. In Fourier space, the zeroth matrix $\tilde{M}_0$ describes the mean of the angular distribution and we therefore describe the energy conservation in Fourier space as:

$$I_{\mu'} = \int d\mu \vec{S}_0^{\mu'}(\mu) = \int d\mu (\tilde{M}_0(\mu', \mu)\vec{S}(\mu'))_0. \tag{3.2.41}$$

In the case of unpolarized incident solar radiation the matrix product simplifies, and the conservation of intensity can be written as:

$$\forall \mu' \rightarrow 1 - \int d\mu \tilde{M}_{11}(\mu', \mu)_0 = 0 \rightarrow \epsilon_{\mu'}. \tag{3.2.42}$$

Due to the limited number of zenith angles, the left hand side of Equation 3.2.42 may not vanish and is set to ϵ. Increasing the number of zenith angles would diminish this residual, but this may not be possible due to constraints in available computation resources. For this reason we modify the phase matrix:

$$\tilde{M}_{11}(\mu', \mu')_0 = M_{11}(\mu', \mu')_0 - \frac{\epsilon_{\mu'}}{g_{\mu'}}. \tag{3.2.43}$$

As described in Section 3.2.17, the phase matrix is then modified to keep the polarization state of the scattered radiation unaltered, and the rescalation factor δ becomes:

$$\delta_\mu = 1 - \frac{\epsilon_\mu}{g_\mu M_{11}(\mu, \mu)_0}. \tag{3.2.44}$$

The effect of these phase function modification for a cloud case is shown in Figure 3.2.23. The *highres* case was calculated using 180 zenith Gaussian points and the unaltered phase matrix. The *original* and *modified* were calculated using 60 zenith Gaussian points except the original and the modified phase matrix. The surface is black and the optical thickness of the cloud is 5. The *highres* case represents the truth. The *modified* version agrees very well with the *highres* results but needed significantly less computation effort. The usage of the *original* phase matrix leads to errors in the intensity and degree of polarization. The case was chosen so

that the effect of the discussed procedure becomes visible; for standard cases the effect wouldn't be as pronounced, since real droplet size distributions tend to dilute the pronounced features of such special cases.

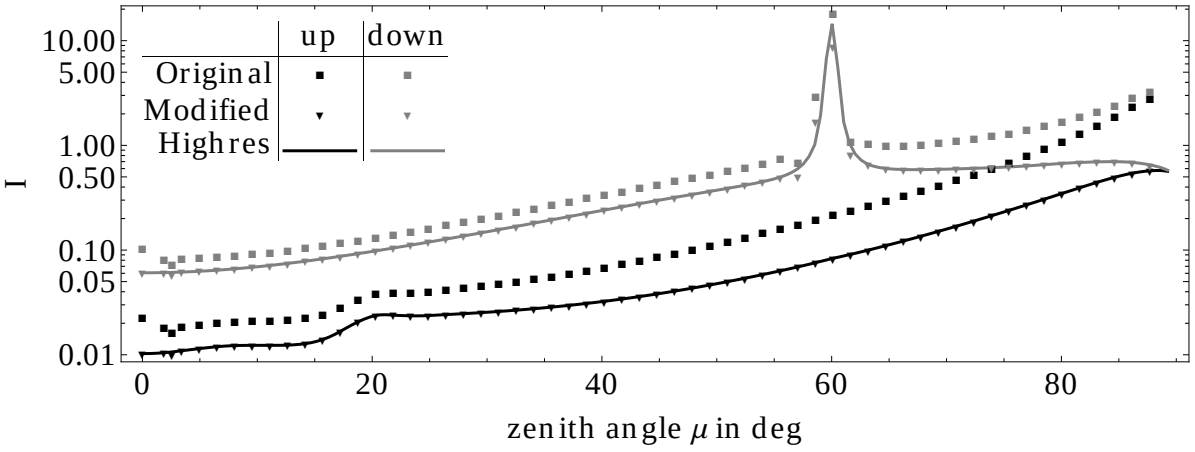

(a) Comparison of upward and downward azimuthal averaged intensity.

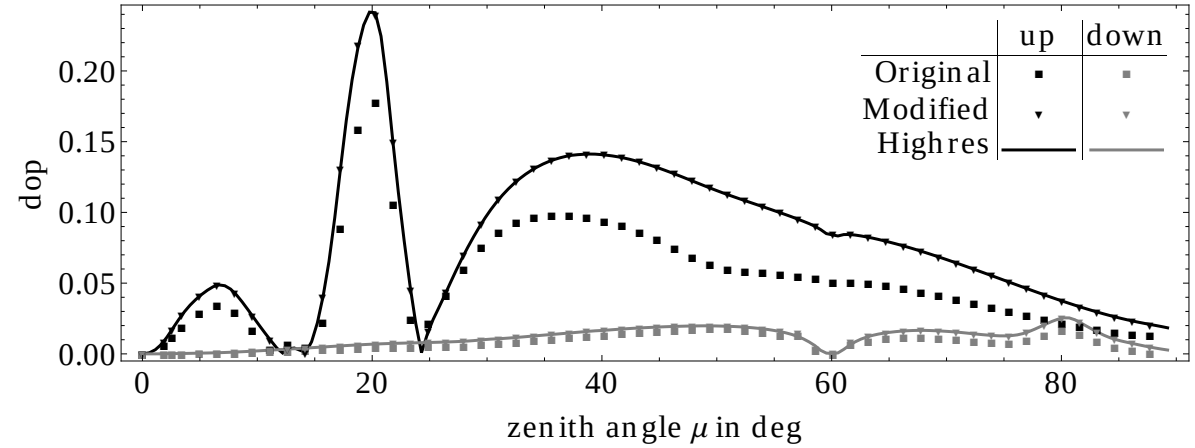

(b) Comparison of upward and downward azimuthal averaged degree of polarization.

Figure 3.2.23: Effect of diagonal balancing of residuals to better conserve the total intensity of the system. Comparing intensity and degree of polarization for the original and balanced case using a cloud model with optical thickness 5 and a black underlying surface. Azimuthal averaged calculations were done using 180 (high res) and 60 zenith angles. For the cases with lower resolution, the original and the modified cases were calculated and the high resolution is seen as truth.

3.3 Verification of Radiative Transfer Results by Inserting them into the RTE: A Demonstration for Rayleigh Scattering

3.3.1 Abstract

The verification of a new or updated radiative transfer model (RTM) is one of the important steps in its development; this is usually achieved by comparisons with real measurements or published tables of generally accepted radiative transfer results. If such tables do not exist, verification becomes more complicated and an external review of the implementation is often unpractical due to the sheer amount and complexity of the code. The presented verification approach is to "simply" insert results of radiative transfer (RT) calculations into the radiative transfer equation (RTE). The evaluation of the RTE consists of numerically calculating partial derivatives and integrals, which is much simpler to implement than a solution of the RTE. Presented is a demonstration of this approach for a case of Rayleigh scattering in a plane parallel atmosphere, which showed only very small deviation from the radiative transfer equation.

This approach has two key benefits. First, its implementation into a high level computer language can be very short ($\approx$ 60 lines in MATHEMATICA) and clear compared to a full RTM; and such code is much more easy to review. Second, this approach can be easily extended to cases where no other independent RT implementation is available for validation. The proposed implementation and data are provided with this paper[8].

3.3.2 Motivation

One of the important steps in implementing a radiative transfer model (RTM) is verification of the technique. Two commonly used techniques are comparisons with real measurements [79] and with results from independent models [80, 42][9]. During the past, a number of radiative transfer results have been published that are commonly used for verification. Examples are vector light field results for a Rayleigh scattering atmosphere [31, 32], cases of Mie scattering [70, 33], or atmosphere-ocean cases [73]. These results can be used to verify certain aspects of the RTM, such as scattering and surface reflection, but since further benchmark results are often lacking, other features are more complicated to verify. Prominent examples of such features are the atmosphere-ocean system, effects of the sphericity of the earth, and inelastic scattering in the atmosphere and ocean.

Error sources of RTM's can originate in the understanding of the problem, as well as the complexity of their implementation. The code of published RTM models can be easily spread over a large number of source files and thousands of lines of code (e.g. libradtran [81]). The main idea of this approach is that it is much more complicated to solve the radiative transfer equation (RTE), than to verify that a particular light field is in fact a solution to it. For verification, the integro-differential equation does not have to be solved and only a partial derivative and two integrals have to be computed. Secondly, such verification does not need to be as fast as possible, hence instead of inherently fast low level languages such as FORTRAN or C, high level languages such as SAGE [82], or MATHEMATICA [83] can be used. The results of this paper are based on an implementation in MATHEMATICA for the plane parallel atmosphere, which is all in all about sixty lines of code long. The source code as well as the data are provided with this paper.

[8] The data is hosted by JQSRT and can be obtained from: `http://dx.doi.org/10.1016/j.jqsrt.2012.06.006`.
[9] This is true for almost any paper describing a radiative transfer model; the references shall only provide some examples.

3.3.3 RTE in Differential and Integrated Forms

The RTE for a plane parallel atmosphere is an integro-differential equation, which states that the change of the radiance field L with optical thickness τ is proportional to the radiance field itself and the combined sources:

$$\mu\partial_\tau L + L - (J_E + J_S) = 0. \tag{3.3.1}$$

The cosine of the viewing zenith angle is denoted by μ, the relative azimuth angle with ϕ, and $\partial_\tau L$ denotes the partial derivative of L with respect to τ. Here, two sources due to elastic scattering are considered. The source due to single scattered incident solar irradiance is called[10] J_E and the source due to scattering of diffuse radiance is called J_S:

$$J_E(\tau,\mu,\phi) = \omega_0 P(\tau,\mu,\phi,\mu_E,\phi_E = 0)e^{-\tau/\mu_E} S_0, \tag{3.3.2}$$

$$J_S(\tau,\mu,\phi) = \int d\mu' d\phi' P(\tau,\mu,\phi,\mu',\phi')L(\tau,\mu',\phi'), \tag{3.3.3}$$

where P is the scattering matrix, S_0 the solar constant, which for this paper is set to unity, ω_0 the single scattering albedo, and μ_E, ϕ_E the position of the sun. The Rayleigh phase matrix along with the rotation matrices are used [35]. To make the solutions unique, additional boundary conditions for the top, bottom, and if considered, interfaces must be set.

The differential form of the RTE from equation 3.3.1 can be integrated with respect to the optical thickness such that the partial derivative of the radiance field is replaced by a difference for the optical thickness and the other terms by their integrals:

$$\mu(L(\tau_2) - L(\tau_1)) + \int_{\tau_1}^{\tau_2} d\tau \left(L(\tau) - J_E(\tau) + J_S(\tau)\right) = 0. \tag{3.3.4}$$

3.3.4 Demonstration for Rayleigh Scattering

The methodology employed is straightforward. A radiance field is inserted into the RTE and then one has to verify that the left hand sides of Equations 3.3.1 and 3.3.4 equals zero. Hence, the RTM must be capable of simulating the light fields at all spacial and angular points. The vector radiative transfer model MOMO [5] was used to calculate the radiance field in a purely Rayleigh scattering atmosphere. To achieve small errors of the numerically calculated partial derivative and the integrals, the light field was calculated using a rather high resolution for optical thickness (80 layers), zenith angles (80 angles), and azimuth angles (40 angles). A total optical thickness of the atmosphere of 0.1 was used. The evaluation of both formulations of the RTE from Equations 3.3.1 and 3.3.4, as well as a boundary value condition were implemented in MATHEMATICA. The lower boundary is a Lambertian reflector with reflectivity of 0.2. The calculations of the two integrals are based on the inbuilt integration capabilities using *InterpolationFunction* objects. For these the discrete radiance field calculated with MOMO is used to create a continuous model of the light field by using a third order interpolation scheme. The calculations of the two integrals are based on the inbuilt integration capabilities and a third order interpolation scheme of the radiances calculated with MOMO.

Results of inserting the calculated radiances into both RTE equations from Equations 3.3.1 and 3.3.4 are shown in Figures 3.3.1 to 3.3.2b. Figures 3.3.1 and 3.3.2a show results for the differential form of the RTE and Figure 3.3.2b shows results for the integrated form. The left panel of each figure shows the terms of the RTE with respect to viewing direction. Figure 3.3.1 shows results for averaged azimuth viewing angle and three optical thicknesses, while the Figure 3.3.2a and 3.3.2b show results for the Stokes parameters I, Q, and U. The right panel

[10] E for external.

shows the balance of the four terms in the same units as the left panel, but with a magnification factor, which is shown above the arrows. The azimuth angle in Figure 3.3.2a and 3.3.2b is $\pi/4$.

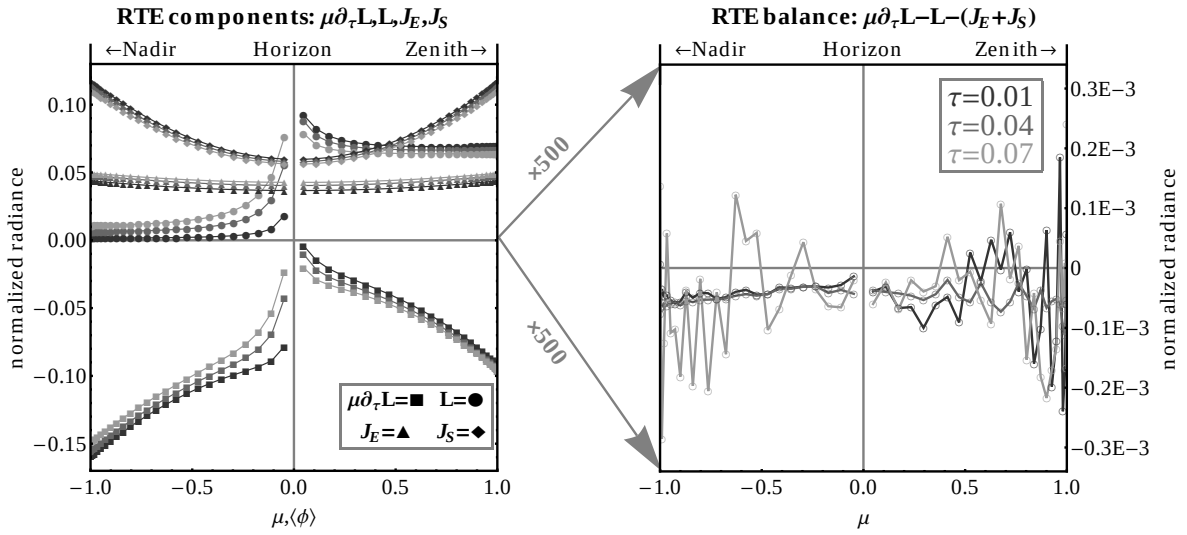

Figure 3.3.1: The four contributing terms of the RTE are shown with respect to viewing zenith angle. Results for three optical thicknesses are shown with different shades of gray. The top of the atmosphere is at $\tau = 0$ and at the bottom of the atmosphere $t = 0.1$. The results are averaged about the full azimuth angle. The right part of the plot shows the balance of the four contributions, with a scale magnification of 500.

All three figures show small residual values, which are around 1000 times smaller than the shown RTE contributions. Such residual values are caused by potential errors in the model, inherent shortcomings of the model, the discretization of the problem in terms of viewing direction and optical thickness, and interpolation and integration errors from the verification scheme. Especially calculating the integrals could become more diffucult for arbitrary cases; but it should be possible to reduce this error by increasing the spacial and angular sampling of the light field by the RTM. Errors of the radiative transfer model could be caused by implementation errors, numerical errors, and inherent shortcomings of the model.

The model used is based on the matrix operator technique, which has two limitations. First, the reflection and transmission properties of atmospheric layers are based on the doubling method, which itself is based on calculated optical properties of an elementary layer for which the single scattering approximation holds. The optical thickness of this layer is set to a small number, for which this assumptions holds, but which is still large enough to not cause numeric under flows in double-precision arithmetic. Second, a matrix inversion is used, which is inherently prone to numerical errors. In the model used, this inversion is calculated using a truncated series of matrix multiplications. These possible error sources make it difficult to decide weather the residuals can be explained by the uncertainty of both models, or not. Previous comparisons with tables for Rayleigh scattering showed an average agreement of four decimal places, while the author of the tables claimed that these are correct within six decimal places [5, 32]. These former results, together with residuals that are smaller than three orders of magnitude than the contributing terms, lead to the conclusion that the model is correct and that the verification was successful. The lower boundary condition was also tested and showed similar results.

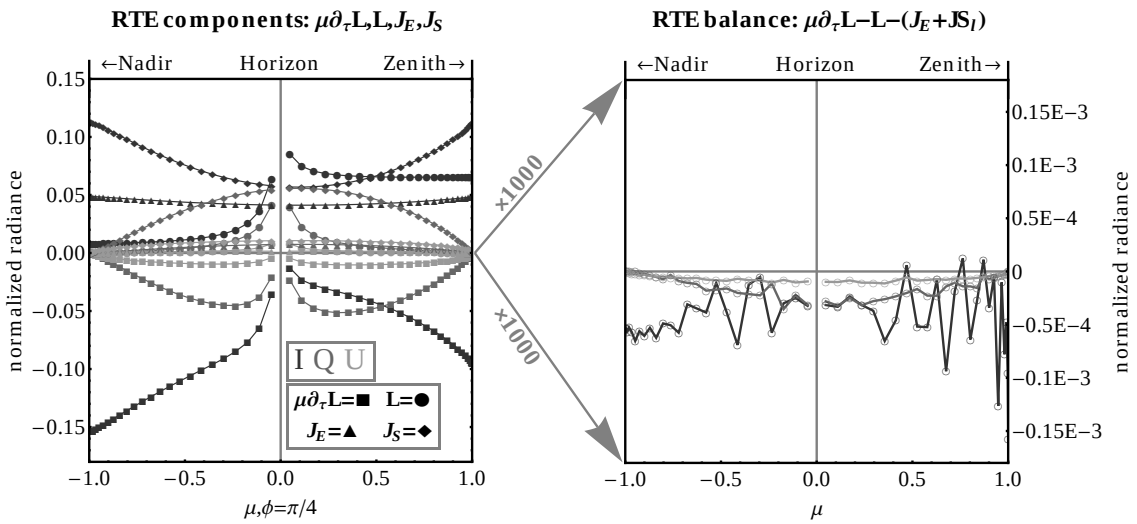

(a) Same as Figure 3.3.1, but for optical thickness of 0.05, azimuth angle of $\pi/4$, a magnification of 1000, and the Stokes parameters I, Q, and U.

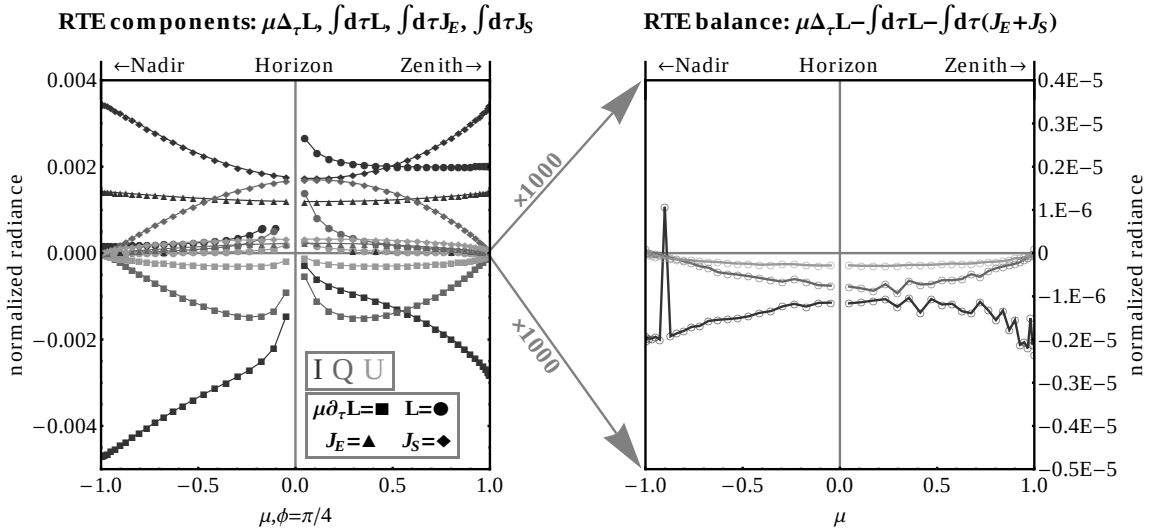

(b) Same as Figure 3.3.2a, but for the integrated form of the RTE. The integration was done from 0.02 to 0.05.

Figure 3.3.2:

3.3.5 Conclusion

The discussed validation through verification approach showed very good results for the case of Rayleigh scattering in a plane parallel atmosphere. Since the model was already validated, this also validates the short and clear implementation of the verification scheme. This tool can now be extended to account for more general geometries, more complex physical effects, and cases where no tables or analytic solutions are known. Of special interest are the coupled atmosphere-ocean system with rough interface, inelastic effects such as Raman scattering in the atmosphere and ocean, and effects of thermal emission. Accounting for these effects makes the solution of the RTE more complicated, whereas such a verification scheme can stay simple and clear.

Acknowledgments

I would like to thank René Preusker for fruitful discussions about this manuscript.

CHAPTER 4

APPLICATIONS TO REMOTE SENSING

Contents

While Chapter 3 was concerned with introducing tools that can be used to solve the radiative transfer equation for the atmosphere-ocean system, this chapter is devoted to the description of quite different applications of these tools in the field of the remote sensing of aerosols and hydrosols. Aerosols and hydrosols are particulate mater, which in case of the aerosols are suspended in the atmosphere and for the hydrosols in the ocean. Figure 4.1.1 provides visual reference of some examples of aerosols and hydrosols. They exist on rather different size scales, have very different couplings and interactions with their surroundings, but in terms of radiative transfer can be described using the same methods, namely their phase matrices, bulk scattering coefficients, and absorption coefficients.

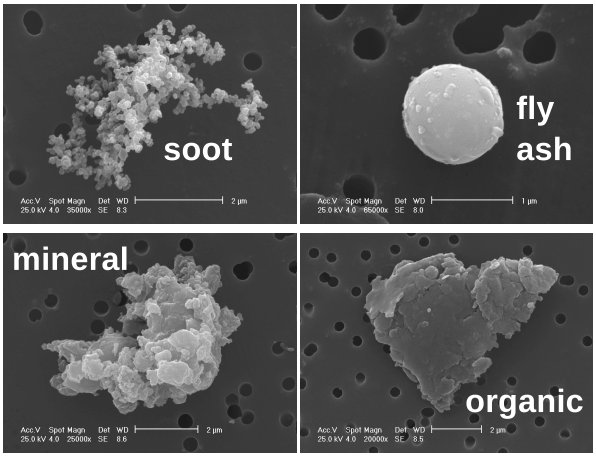

(a) Images of different aerosol types, including soot, fly ash, mineral, and dust. Reproduced from [84].

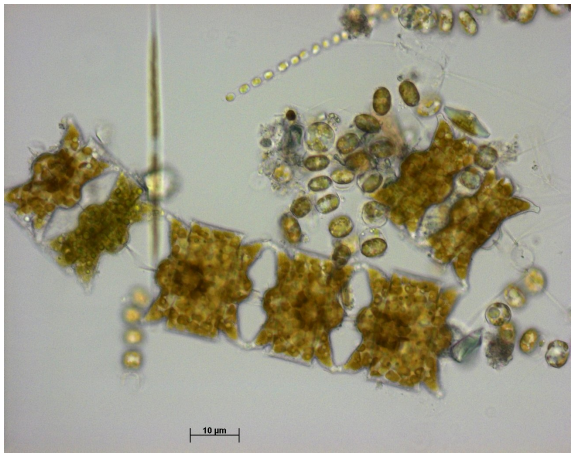

(b) Mixed population of phytoplankton. Field sample from Long Island [85].

Figure 4.1.1: Images of aerosol and hydrosol particles. Due to the large variability of aerosols and hydrosols in nature, these images are rather not representative, but an almost random sample. Both images show a size scale that highlights that these particles differ not only in shape and inner structure, but also in size.

The remote sensing of hydrosols delivers important information for both researchers and policy makers, and is itself a large field of research. An introduction and reviews about its state and achievements so far can be found in references [86, 87] and references therein. In general, its results can be used to observe the state of the oceans, potential harmful algae blooms, the net primary productions of the ocean body, and hence its carbon balance. Figure 4.1.2 shows a nice and detailed result of ocean color research for the Baja Peninsula (Mexico). The left part of the figure shows the scene as seen from space using semi-natural colors. The slightly green colors indicate the presence and structure of the chlorophyll in the upper parts of the ocean. Ocean color algorithms can then process the satellite data and, by using a combination of multiple spectral channels, convert the subtle changes in visible color to quantitative concentrations of chlorophyll particles and other optically active in water constituents. Large parts of the used algorithms are based on the inversion of radiative transfer simulations and hence the appropriate description of the optical properties of the in water constituents is one major key for their successful retrieval by means of remote sensing techniques.

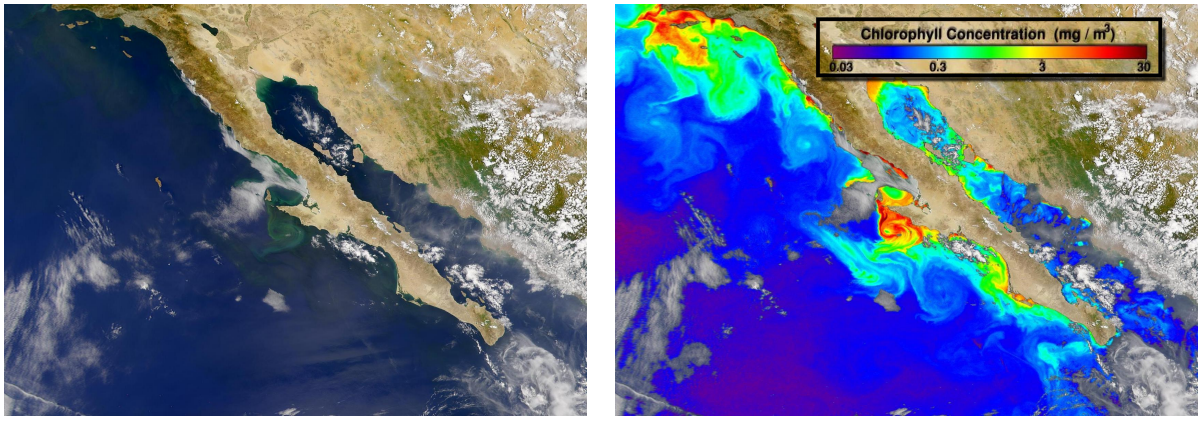

(a) View of the Baja Peninsula (Mexico) as seen from space on August 10, 2003 using a semi-natural color scheme.

(b) Same scene as the left image, but false colors are used to show the chlorophyll concentration, which has been derived from spectral resolved measurements.

Figure 4.1.2: Both images with modification from `http://oceancolor.gsfc.nasa.gov`. Both images are without copyright restrictions.

A part of the scientific problem that has often been neglected in the past, are the effects of salinity, temperature, and polarization on top-of-atmosphere and water-leaving radiances, which is discussed in detail in Section 4.2. Although it is known that the inherent optical properties of sea water depend not only on wavelength, but also on salinity and temperature, in the past these dependencies were often neglected. A good example are the ocean color reference models for the MERIS [88] and MODIS [89] instruments, in which for example radiative transfer using a constant salinity is applied. For the case of salinity, it is for large parts of the globe not problematic to neglect it, since for open oceans the salinity is almost constant at $35PSU$ (practical salinity units) with only minor seasonal variation [75]. However, strong salinity variations occur if fresh water inflow from melting water, large rivers, or rainfall is present. The global variation of salinity is shown in Figure 4.1.3(a). Similar to salinity, the temperature of the ocean water is mainly neglected in ocean color retrievals, with the main difference that the temperature varies strongly with region and season. A global map of the annual mean sea surface temperature is shown in Figure 4.1.3(b). Not accounting for salinity and temperature made the problem of retrieving ocean constituents from top-of-atmosphere radiance measurements two dimensions less complicated, which reduces the numeric effort in developing and applying ocean color remote sensing algorithms.

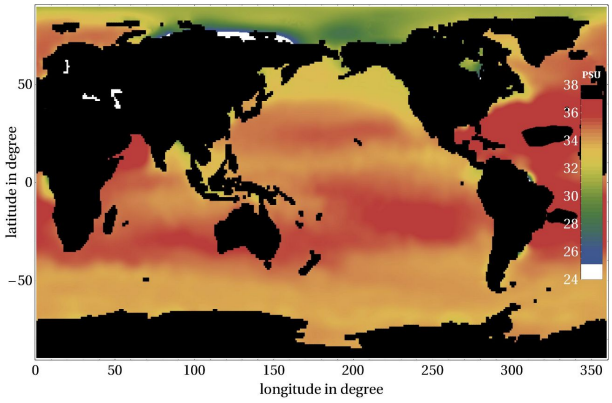

(a) Global map of sea surface salinity using climatology data from the World Ocean Atlas 2009 [75].

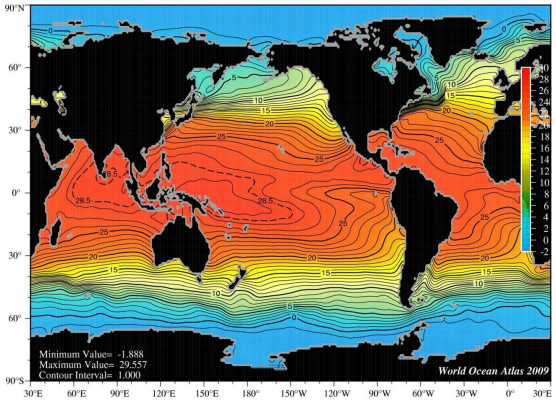

(b) Global map of the annual mean sea surface temperatures from the World Ocean Atlas 2009 [90].

Figure 4.1.3:

The research presented in Section 4.2 was part of the ESA WATERRADIANCE project[1] and was published in the peer-reviewed Journal *Applied Optics* as:

> *André Hollstein and Jürgen Fischer. Effects of salinity, temperature, and polarzation on top of atmosphere and water leaving radiances for case one waters.* Applied Optics*, 10 2012. doc. ID 169561, accepted 10/17/2012.*

It was also presented at the *IRS2012* conference as:

> *IRS2012-9: Salinity, Temperature and Polarization Effects for Simulated Radiances in a Case One Waters Atmosphere Ocean System, A. Hollstein and J. Fischer.*

Section 4.3 deals with the possibilities for the remote sensing of the aerosol vertical extinction profile using the passive imaging and space borne instrument FLORIS on board the FLEX satellite. At the time of publication of this thesis, the FLORIS instrument was selected by ESA as candidate for the Earth Explorer 8 mission and accepted for phase A/B1. FLORIS features high spectral measurement capabilities in the oxygen A and B band, in which radiation reflected from Earth into space is sensitive to aerosol height. A retrieval of aerosol vertical distribution from space using such an imaging instrument with its high spacial and temporal resolution could be used to produce a much more detailed representation of the global three-dimensional aerosol field. The retrieval of aerosol height from space is currently only operational from the LIDAR CALIOP on board the CALIPSO satellite. It is an active instrument, which emits short laser pulses and measures the back scattered light with high temporal resolution. Using a time of flight approach, the data from the temporal domain can be converted to the spacial domain of the aerosol vertical profile. The main downside of this approach is the sparse temporal and spacial coverage of the globe, since the LIDAR pulse is only sent downwards, which results in 100m footprints along the path of the satellite, but no measurement to the left and right of this point.

Spaceborne imaging instruments can feature swath widths in the order of hundreds or thousands of kilometers. Hence, if the retrieval of aerosol vertical extinction profiles would be possible using such a type of instrument, a much more detailed state of the three-dimensional structure of the aerosols could be obtained. This information could be used to increase the level of scientific understanding of the role of aerosols in Earth's climate and climate change as stated

[1] ESA contract AO 1-5859/08/NL/CT.

by the *Intergovernmental Panel on Climate Change* in its *IPCC Fourth Assessment Report: Climate Change 2007*. Figure 4.1.4 shows an overview about anthropogenic contribution to the radiative forcing of climate between 1750 and 2005. The largest negative effects are those caused by aerosols. The direct and indirect aerosol effects show also the largest uncertainties and lowest levels of scientific understanding. The larger of the two uncertainties is associated with the cloud albedo effect, which includes the aerosol cloud interactions which affect cloud albedo. The contributing aerosol cloud interactions are shown in Figure 4.1.5. Hence, the vertical distribution of the aerosol is, next to their total optical thickness and type, a key parameter to decrease the large uncertainty associated to its radiative forcing in Earth's climate.

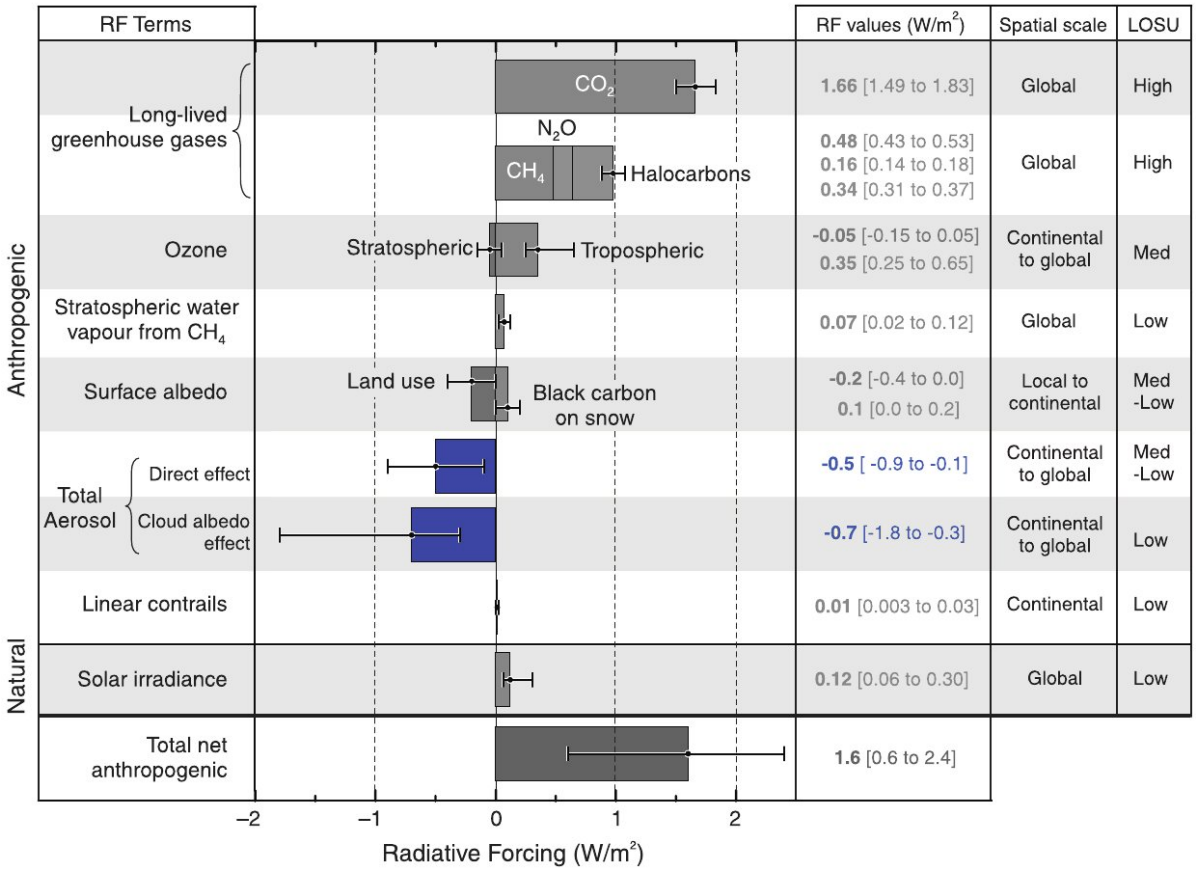

Figure 4.1.4: Various anthropogenic contributors to the radiative forcing on Earth's climate between 1750 and 2005. Reproduced from the fourth IPCC report [91].

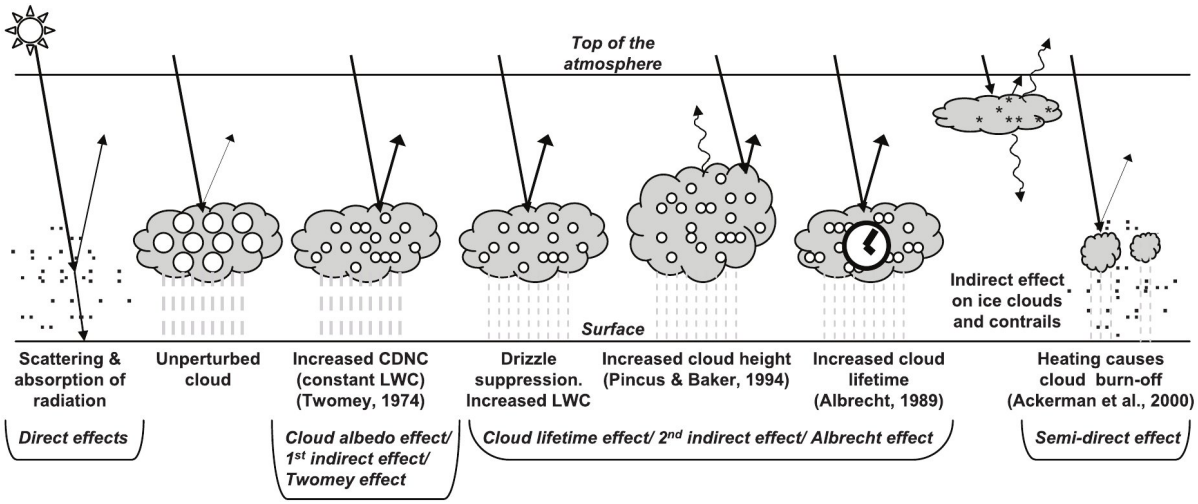

Figure 4.1.5: Aerosol cloud interactions, which contribute to the aerosol cloud albedo effect as shown in Figure 4.1.4. Edited version from reference [91], originally from reference [92].

The research described in Section 4.3 was carried out as part of the FLUSS[2] project by ESA. The aim of this part of the project was to explore the possibilities for a potential retrieval of aerosol vertical structure using measurements of the FLORIS instrument. Its key parameters for this application are a spectral resolution of $0.3nm$ in the oxygen A and B band, a signal to noise ratio of above 500, and the high spacial resolution provided by the $300m \times 300m$ ground pixel size. The swath of the instrument is expected to be $390km$, hence the instrument features a much larger spacial and temporal resolution as it is provided by CALIOP. Large parts of this research were presented at the *IRS2012* conference in Berlin:

> *André Hollstein and Jürgen Fischer. Possibilities for remote sensing of aerosol vertical structure using the O_2A band: A sensitivity study concerning polarization, spectral resolution, instrument level, and various scenes over land. IRS2012-65, 8 2012*,

and some key results have been submitted to the proceedings of the *IRS2012* conference:

> *André Hollstein and Florian Filipitsch. Possibilities for the retrieval of aerosol vertical profiles from space using hyper spectral radiance measurements in oxygen absorption bands. submitted to the Proceedings of IRS2012, 8 2012.*

In Section 4.4, the developed techniques are applied to a data set of hyperspectral measurements of top-of-atmosphere radiance in the O_2A band. The measurement were made by the instrument TANSO-FTS on board the Greenhouse Gases Observing Satellite (GOSAT), which is in orbit since January 2009. The data is characterized by high spectral resolution, but poor spatial and temporal resolution, if compared to the previously discussed FLORIS instrument. A single measurement is shown in Figure 4.1.6. Additionally shown is the solar constant in adjusted units. This example shows that the shape of the measurements is governed not only by the oxygen absorption, but also by the solar constant and its Fraunhofer lines. Further driving parameters are the surface reflectance, surface pressure, and aerosol optical parameters.

[2] ESA project number: TEC-EEP/2011.698/MB

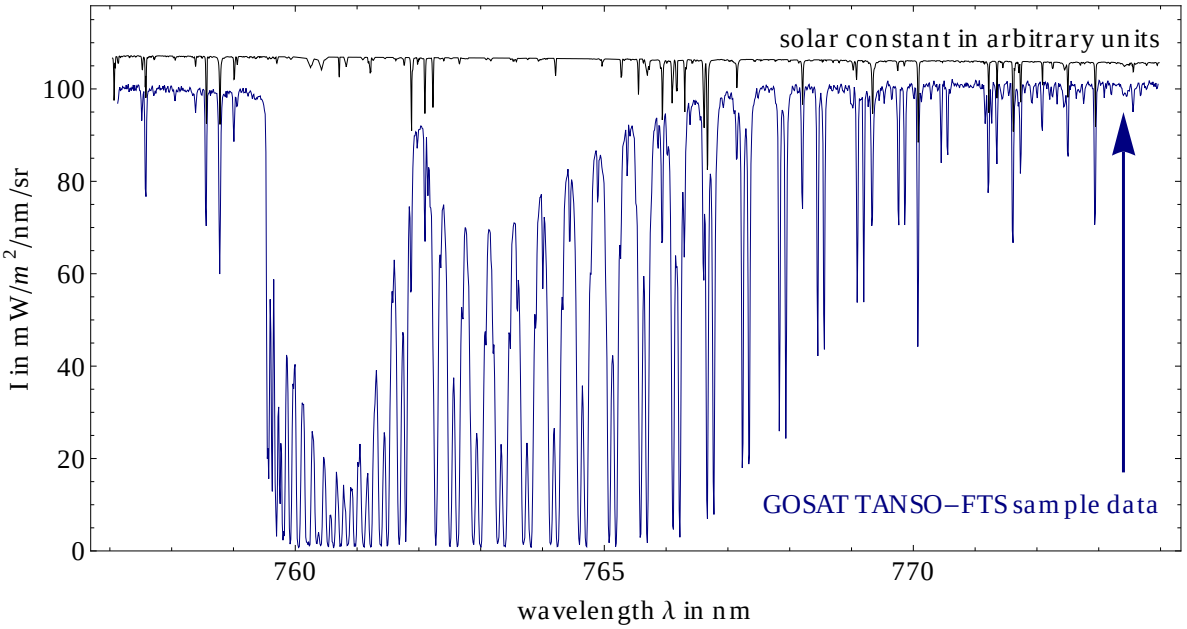

Figure 4.1.6: A single measurement made by the TANSO-FTS instrument on board the GOSAT satellite. Additionally shown is the solar constant, which was scaled such that both spectra can be shown together. This allows to differentiate between features due to oxygen absorption or Fraunhofer lines.

The radiative transfer forward operator that is described in Section 4.3.5 is applied to the TANSO-FTS instrument. The results are used to set up a forward operator, which is based on a lookup table approach and a mix of linear and quadratic interpolation. Then, an inversion scheme based on the method of differential evolution (DE) was set up. The data set includes 104 measurements over land, which were used as input for the inversion. Although systematic residuals between measurements and simulations are present, the inversion results were in general of very good quality. Although no cloud screening algorithm was used, a fail of the inversion was in the majority of cases most likely caused by contamination of the scene by clouds. All remaining systematic residuals can be explained by shortcomings of the spectroscopy, absorption calculation, or variations of the temperature profile.

The results can be used as proof of concept for the derivation of aerosol vertical structure from spaceborne radiance measurements. They also show, which effects need to be accounted for in the future development of the applied absorption model.

The limitations, posed by the spatial and temporal resolution of the instrument, limit the applicability of a possible aerosol vertical distribution product, but the data can serve as viable test case and proof of concept for future instruments that are better suited for this kind of retrieval.

4.2 Effects of Salinity, Temperature, and Polarization on Top-of-Atmosphere and Water-Leaving Radiances for Case One Waters

4.2.1 Abstract

The effects of polarization, sea water salinity, and temperature on top-of-atmosphere radiances and water-leaving radiances are discussed using radiative transfer simulations for MERIS channels from $412nm$ to $900nm$. A coupled system of an aerosol-free atmosphere and an ocean bulk containing chlorophyll and colored dissolved organic matter (case one waters) was simulated. A simple, but realistic, bio-optical model was set up to relate chlorophyll concentration and wavelength to scattering matrices and absorption coefficients for chlorophyll and colored dissolved organic matter. The model of the optical properties of the sea water accounts for the salinity, temperature, and wavelength dependence of the relative refractive index, as well as the absorption and the bulk scattering coefficient. The results show that the relative difference of water-leaving radiances at zenith for a salinity of $5PSU$ and $35PSU$ can reach values of 16% in the $412nm$ channel, decreasing to 4% in the $900nm$ channel. For the more realistic case of $25PSU$ compared to $35PSU$, the effect is reduced to 5% for the $412nm$ channel and decreasing to 2% for the $900nm$ channel. The effect on radiance caused by changing sea water temperature is dominated by changes of sea water absorption and shows strong spectral features. For water-leaving radiances, a change of $10°C$ can cause relative changes of above 3%. The effects of neglecting polarization in the radiative transfer depends strongly on direction and wavelength, and can reach values of $\pm 8\%$ for the $412nm$ channel. The effect is discussed for MERIS channels, viewing geometry, and chlorophyll content.

4.2.2 Introduction and Motivation

Monitoring oceans and lakes on a global basis is highly important for both, researchers and policy makers. Remote sensing of oceans from space using ocean color instruments such as MERIS, MODIS, or SeaWIFS [87] provides information on the biogeochemical properties required to quantify marine biology, as well as the ocean uptake of carbon. Most of their products are based on the inversion of radiative transfer models, which relate biological quantities such as chlorophyll concentration and atmospheric state to the top-of-atmosphere radiance. The success of such schemes depends on the quality of the measurements, as well as the modeling and the applied inherent optical properties of the atmosphere-ocean system. For the pure sea water body, these depend on wavelength, temperature, and salinity. For open oceans, a standard salinity value of $35PSU$ (practical salinity units) can be used as standard value [75], although strong regional gradients can be found in the Baltic sea [93], in areas influenced by melting water [94, 95], or fresh water discharge by rivers. The absolute global variation ranges from $5.1PSU$ to $40.3PSU$ [96, 97], and the inter annual variation depends on location and is in the order of $\pm 0.28PSU$ [98, 99]. On a global scale, the sea water temperature varies from $-1.8°C$ to $29.5°C$ [90] and depends strongly on region and season.

The main goal of this research was to quantify the effects of variations in salinity and temperature on top of atmosphere (TOA) radiances and water-leaving radiances[3] (WLR). This is of special interest, considering that in the present reference model for the MERIS level 2 processing [88], a constant salinity of $35PSU$ and temperature of 12° is assumed.[4] The

[3] Which is defined as the upward directed radiance just above the ocean surface, but without contributions from surface reflection. [4] In the MODIS ATBD [89] for case two waters, the salinity is also assumed to be constant. However, the authors discuss that a drop in salinity, caused by melting waters in northern parts of the globe, may have caused deviations of the retrieval and in situ measurements.

second aim was to quantify the errors when polarization is neglected in the radiative transfer calculations.

To address these questions, the MOMO [5, 39] radiative transfer model (RTM) was used to simulate radiances for a parameter grid composed of sea water salinity, sea water temperature, surface wind speed, chlorophyll concentration with associated colored dissolved organic matter (CDOM), wavelength (using the MEdium Resolution Imaging Spectrometer (MERIS) channels [86]), and various viewing geometries. Some of the MERIS channels are inherited from former ocean color instruments and similar channel settings are widely used in the ocean color community. The instrument OLCI [100] on ESA's upcoming satellite Sentinel-3 will also inherit these channel settings. The applied sea water and bio-optical model is described in Sections 4.2.3 and 4.2.4, while the results of the case study are discussed in Section 4.2.5.

4.2.3 Ocean Optical Model

Ocean water is modeled as a mixture of pure water with salt ions and is implemented as a scattering and absorbing medium. Its optical properties are the absorption coefficient $a(\lambda, S, T)$, the volume scattering coefficient $\beta(\lambda, S, T)$, and the phase matrix $p(\mu, \phi, \mu', \phi')$. These quantities depend on wavelength λ, salinity S, temperature T, zenith angle μ, and azimuth angle ϕ. The absorption coefficient of pure sea water was taken from reference [55], where several[5] data sets where consistently merged. Its dependency with respect to wavelength, sea water salinity, and temperature was modeled using an uncoupled linear relationship. The basis absorption spectra was measured at $T_0 = 20°C$ and $S_0 = 0PSU$, and the spectral dependent temperature $\Psi_T(\lambda)$ and salinity coefficients $\Psi_S(\lambda)$ complete the model:

$$a_w(T, S, \lambda) := a_w(T_0, S_0, \lambda) + \Psi_T(\lambda)(T - T_0) + \Psi_S(\lambda)(S - S_0). \tag{4.2.1}$$

The physical rationale behind the linear behavior as given in Equation 4.2.1 remains unclear, but an explanation has been given by Max and Chapados [63]. Their idea is that the solution of salt ions in pure sea water leads to the formation of an additional type of water, which is formed as a stable ion pair complex. Increasing the salinity concentration leads to a decrease of the pure water fraction, and an increase of the salty water fraction. A similar idea is used to explain the temperature behavior. They assume that the water is composed of two types of water: one type close to boiling, and one type close to freezing. With changing temperature, the fraction of these two types of water is altered. The absorption change with temperature seems to originate from frequency shifts of the three main $oxygen - hydrogen$ mode vibrational states.

Figure 4.2.1 shows the sea water absorption coefficient (top), and its dependence with changing salinity and temperature (bottom) for a reference point of $35PSU$ and $35°C$. In the spectral range from $300nm$ to $1100nm$, the sea water absorption coefficient covers a range of more than three magnitudes, hence the differences due to salinity and temperature changes are shown using scaling factors. The difference of salinity and temperature was chosen such that with the same scaling factor the absorption changes are within $\pm 1/m$, which results in a salinity delta of $25PSU$ and a temperature delta of $2°C$. This means that a change of $25PSU$ in salinity causes roughly the same effect as a change of $2°C$ in temperature.

This dependency is controlled by the temperature and salinity coefficient as defined in Equation 4.2.1. Figure 4.2.2 shows their spectral dependency. Black lines show the salinity coefficient, gray lines the temperature coefficient, and the experimental error of both coefficients is shown with dotted lines. Both coefficients show strong spectral variation, and in most cases the absolute temperature coefficient is almost one magnitude larger than the salinity coefficient. The experimental error is large, especially for the visible region, which is mainly due to the very low water absorption in that spectral region.

[5] See references [58, 59, 60, 61, 62, 63, 64].

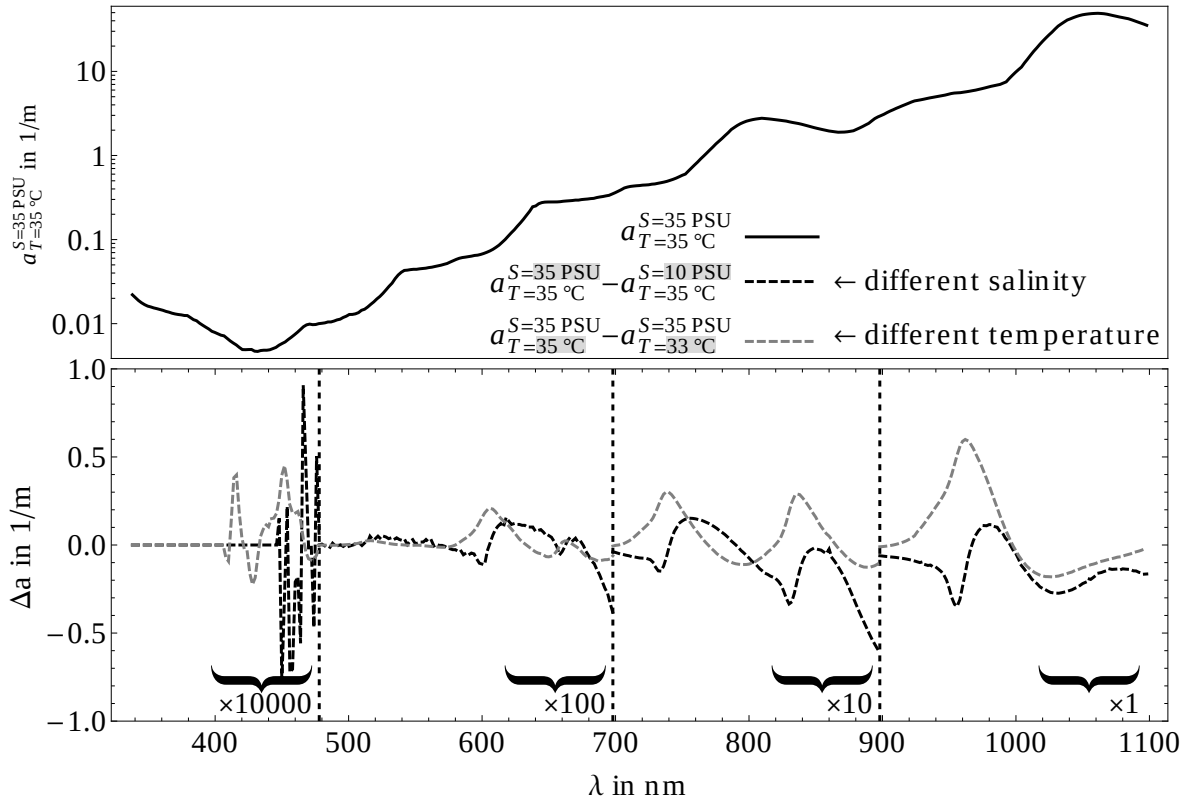

Figure 4.2.1: Absorption coefficient of sea water (top panel) for a salinity of $35PSU$ and temperature of $35°C$. The bottom panel shows the difference of the absorption coefficient for decreased salinity ($35PSU$ vs. $10PSU$,dashed black line) and lower temperature ($35°C$ vs. $33°C$, dashed gray line). The differences have been scaled such that the scaled absorption difference varies between $\pm 1/m$.

Smoluchowski and Einstein [101, 102] explained the scattering by sea water using its thermodynamic density fluctuations. As a result, a Rayleigh phase matrix $P_\delta(\theta)$ [103, 104, 29] with depolarization factor δ can be used. The bulk scattering coefficient depends on salinity, temperature, and wavelength, and has been discussed in detail by Zhang [56]. It is built from the sum of two independent pairs of scattering; β_{df} due to density, and β_{cf} due to concentration fluctuations:

$$\beta_{sw}(\lambda, T, S) = \beta_{df}(\lambda, T, S) + \beta_{cf}(\lambda, T, S). \tag{4.2.2}$$

The two functions depend on several coefficients, which can be found in Zhang's paper. The complete scattering matrix of sea water is then given by:

$$\beta_{sw}(\lambda, S, T, \theta) = \beta_{sw}(\lambda, S, T) P_\delta(\theta). \tag{4.2.3}$$

Figure 4.2.3 shows the ratio of the scattering contributions from density and concentration fluctuations. For a salinity of $10PSU$, the contribution from density fluctuation is almost one order of magnitude larger than those from concentration fluctuations. With increasing salinity, this ratio decreases, which shows that the relative impact of temperature decreases with increasing salinity. Ratios of these bulk scattering coefficients and those from the widely used model[6] by Morel [105] are varying from $+6\%$ to -16% for the VIS to SWIR spectral region [5].

[6] $\beta(\lambda) = 0.00288(\lambda/500nm)^{4.32}$

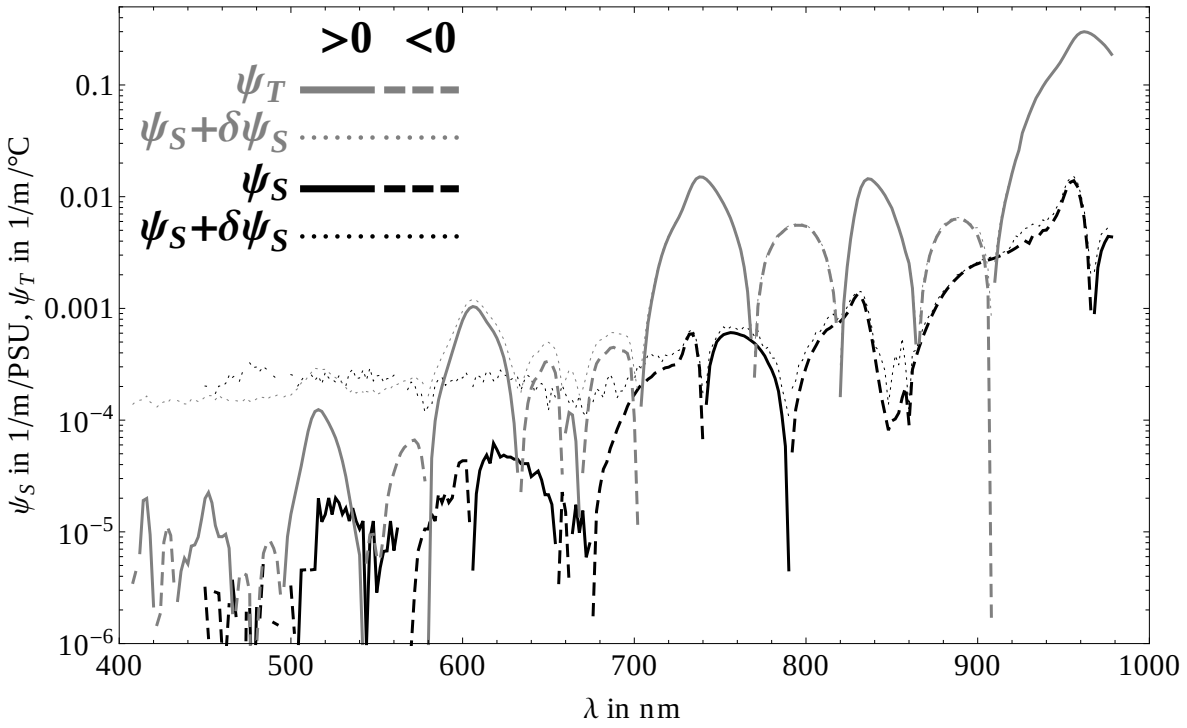

Figure 4.2.2: Salinity and temperature absorption coefficients ψ_S and ψ_T. Negative values are indicated using dashed lines. The experimental error for both coefficients is shown using dotted lines.

The reflection and transmission properties of the ocean surface are driven by the wind speed and the relative refractive index,[7] and were modeled according to results of Sancer [76], Nakajima [36], and Kattawar [35]. Changes in temperature and salinity affect the sea water absorption and hence[8] refractive index, which was calculated using two models from references [61, 55]. In the visible, the model is based on a set of parameters which fits the measurements from reference [61]. From $800nm$ onward, the salinity and temperature effects at $800nm$ are used as a constant offset for the whole spectral region up to $4000nm$. The refractive index and its relative variation for a change in salinity ($24.5PSU \rightarrow 35PSU$) and temperature ($5°C \rightarrow 25°C$) are shown in Figure 4.2.4. The salinity change was chosen such that the relative change of the refractive index is comparable with a temperature change of $20°C$. While the temperature was decreased, the salinity was increased to cause a similar effect on the refractive index.

[7] From now on refractive index. [8] These are closely coupled by the Kramers-Kronig relations; an application to water ice can be found in reference [106].

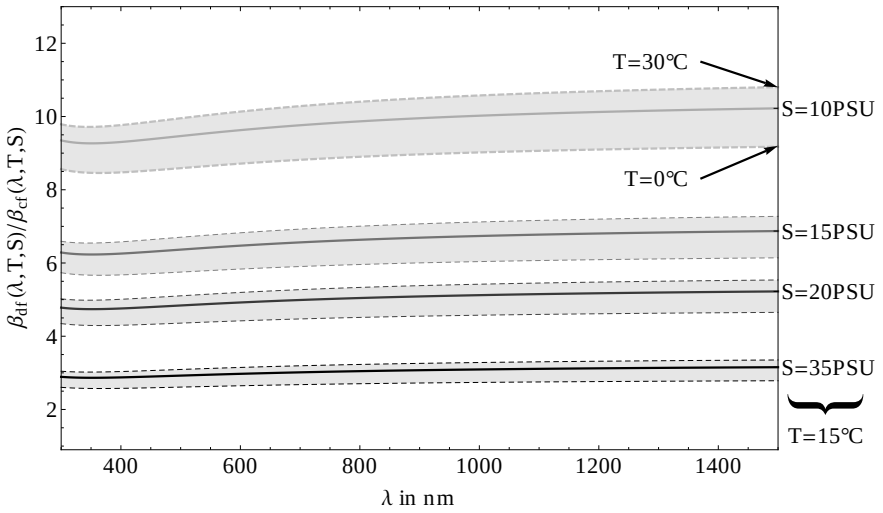

Figure 4.2.3: Relative values β_{df}/β_{cf} of the bulk scattering contributions due to density and concentration fluctuations. The middle line of each group is for a temperature of $15°C$ and varying salinity. The gray shaded range is bounded by temperatures of $0°C$ and $30°C$.

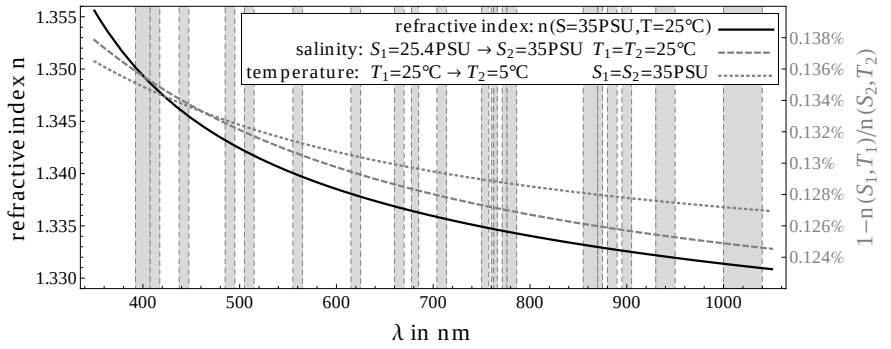

Figure 4.2.4: Refractive index n of sea water (black line, left scale) and its relative variation with a change in salinity (gray dashed line, right scale) and temperature (gray dotted line, right scale). The salinity change was chosen such that the relative change of the refractive index is comparable to a temperature change of $20°C$. The gray vertical rectangles show the position and width of the MERIS channels.

4.2.4 Bio-Optical Model

To our best knowledge, there are no published and complete measurement sets available that describe all bio-optical properties needed for vector radiative transfer. This is especially true for scattering matrices of chlorophyll and other in-water constituents. As a solution, a simple yet realistic bio-model was set up, which depends on chlorophyll concentration and wavelength.

While there are published phase function measurements (e.g. from Petzold [107]), measurements of the other elements of the phase matrix are rare. Some published phase matrices can be found in the papers from Voss and Fry [108, 109], by Volten et al. [110], or Gogoi et al. [111]. They discuss the great variability of possible scattering matrices and conclude that Mie theory was not able to reproduce all occurring features of scattering matrices. Various authors used different approaches of setting up such a model, and descriptions of their bio-optical models can be found in papers by Morel [66], Chowdhary [40], or Chami [38]. Here, the focus is not so much the biological diversity, but rather the effects of polarization, salinity, and temperature. Mie theory was applied to reproduce the known scalar properties of Petzold measurements to the best extent possible.

The model is based on the latest available set of measurements from Bricaud et al. [65], which include spectral resolved measurements of the chlorophyll single scattering albedo ω_0 and the absorption coefficient a_{chl} for the MERIS channels from $412.5nm$ to $900nm$. The absorption coefficient was converted into the imaginary part of the refractive index of the scattering particle using [65, 67]:

$$n_i(\lambda) = \frac{a_{chl}(\lambda)\lambda}{4\pi}. \tag{4.2.4}$$

This simple model can be derived[9] by assuming that the chlorophyll particle is a semi-infinite bulk and the electric field is an evanescent wave; hence this value is only used as a first guess of the true value.

For a given chlorophyll concentration, the absorption of CDOM can be calculated using an exponential model proposed by Bricaud et. al.:

$$a_{CDOM}(\lambda) = a_{CDOM}(440nm)e^{-S(\lambda-440nm)}; S := 0.011\frac{1}{nm}. \tag{4.2.5}$$

Figure 4.2.5 shows the spectral dependence of the absorption due to pure water (black lines), chlorophyll (gray lines), and CDOM (gray dashed lines).

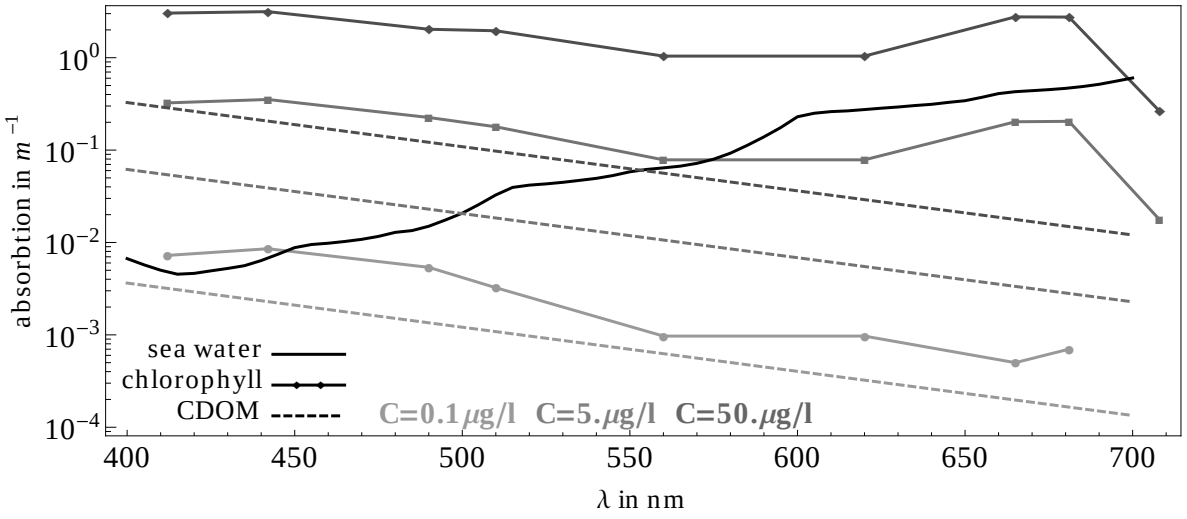

Figure 4.2.5: Absorption spectra of pure sea water (black line), chlorophyll (solid curves), and CDOM (dashed curves). Different chlorophyll concentrations are shown with different gray tones.

When measured size distribution parameters, refractive index and absorption coefficients are used as input for Mie calculations, one must think of scattering by optically equivalent spheres, which scatter light like the real chlorophyll particle. The measured data was used as a first guess for the Mie calculations. To find the best optically equivalent spheres, the input was optimized using a Levenberg Marquard[10] optimization scheme to retrieve physically consistent phase matrices. The dashed lines in Figure 4.2.6 show the spectral variation of the chlorophyll single scattering albedo from the data set and results from the optimization scheme.

The free parameters of the optimization scheme were the size distribution (Junge and log normal), its parameters, the real part of the refractive index, and a scaling parameter for the

[9] Assuming an evanescent wave $\vec{E}(\vec{x}) = \vec{E}_0\, \mathrm{e}^{i(\omega * t + \vec{k}\vec{x})}$, which propagates through the particle, where $\vec{x}$ is the position vector and $\vec{k} = \frac{\omega}{c}(n_r + i \cdot n_i)$ is the complex wave vector, which depends on the speed of light c, its angular frequency ω, and the complex refractive index $n = n_r + i \cdot n_i$ of the particle. The intensity of the field inside the particle is then given by the scalar product $\vec{E}\vec{E}^*$ and Equation 4.2.4 can be obtained by comparing the result with Beer's law: $\vec{E}\vec{E}^* = E_0^2 e^{-2n_i x\omega/c + i(2n_r x\omega/c - 2t\omega)} := \underbrace{E_0^2 e^{-a_{chl}x}}_{\text{Beer's law}} e^{i(2n_r x\omega/c - 2t\omega)}$. [10] Using an IDL implementation from Markwardt [112].

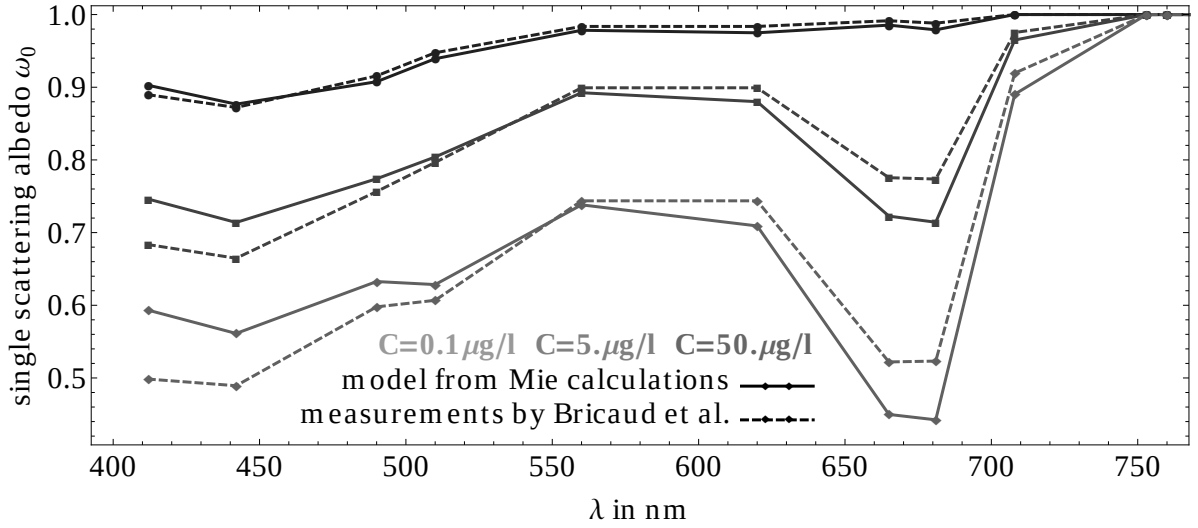

Figure 4.2.6: Spectral variation of chlorophyll single scattering albedo ω_0 for various chlorophyll concentrations. Dashed lines show data from Bricaud's data set, and solid lines show results of the bio-optical model.

absorption spectra, assuming that the spectral shape of the first guess represents the real spectral shape up to an unknown factor. Without applying further conditions, the optimization yields almost perfect fits to the single scattering albedo spectrum, but the resulting size distribution becomes nonphysically narrow, which leads to highly oscillating phase functions. Morel et al. [66] proposed to apply Mie theory for spheroids to avoid such features, but also stated that this does not mean that chlorophyll is necessarily of spheroidal shape. This approach can be adopted to avoid the rainbow features of the phase function, but also introduces additional free parameters.

It is evident that accurate measurements of chlorophyll phase matrices are needed, and could improve bio-optical models used in radiative transfer. Such measurements could replace this kind of bio-optical modeling, and thus the inherently unknown uncertainty associated with it. Since the introduction of additional free parameters for more complex scattering models is likely of unknown physical meaning, a different approach was chosen to address this issue. The parameter space was restricted to exclude very narrow solutions and a penalty term was introduced. The penalty term increases if the backward direction of the resulting phase function is either to small or shows strong oscillations. This procedure was motivated from a comparison of Mie calculation results and the measurements of turbid San Diego harbor water by Petzold [107] (see also Figure 4.2.7). By assigning weight to a physical shape of the phase function, the deviation of the results and the measured ω_0 spectrum becomes significantly larger, but is still acceptable for this application. The advantage of this approach is that it combines the simple use of Mie theory, additional knowledge from Petzold's measurements, and results from in situ measurements.

As shown in Figure 4.2.6, the model reproduces the ω_0 spectrum quite well. Log normal and Junge type size distributions were both tested and it was found that the overall agreement was better for the log normal type, but other authors like Chami and Chowdhary [38, 40] use Junge type size distributions. Figure 4.2.7 shows Petzold's measured phase function of San Diego harbor water [107], and phase function results from the bio-optical model for both size distributions types. The log normal type phase functions are smooth and do not show the steep increase in backward scattering, but lack the correct representation of the strong forward scattering. Using the log, normal size distribution leads to a better representation of the backward scattering, but the forward scattering is weaker. For the Junge size distribution,

the forward peak is better represented, but the backward scattering direction shows stronger features. The deviation in the forward direction is acceptable, since it is of lesser importance for accurate simulations of the upward directed water-leaving radiance. The reduced scattering in backward direction is welcome, since our group [47] experienced that when using Petzold's phase function the retrieved chlorophyll concentration can become too large in some cases.

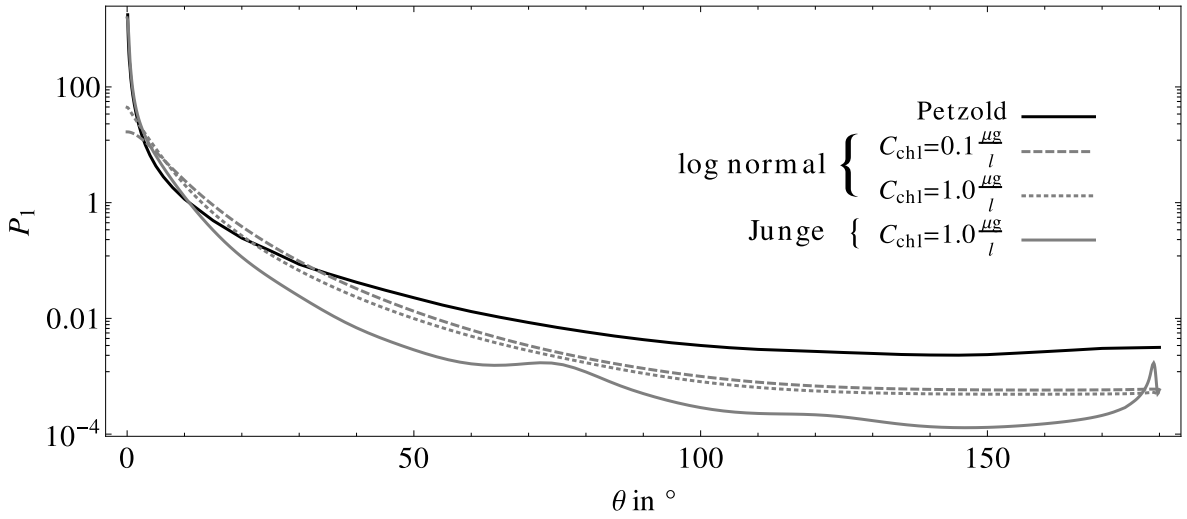

Figure 4.2.7: Phase functions versus scattering angle; Petzold's (black line), and from the bio-optical model with log normal (gray dashed line) and Junge size distribution (gray line).

4.2.5 Sensitivity Study

The sensitivity study consists of radiative transfer simulations for the MERIS [86, 100] channels from $412.5nm$ to $900nm$. Varied parameters were the ocean's[11] salinity S, temperature T, chlorophyll concentration C_{chl}, and surface wind speed W. The complete parameter set is shown in Table 4.2.1. The one dimensional radiative transfer model MOMO [5, 39], which is based on the matrix operator scheme, was used and an aerosol free *midlatitude summer* [113] atmospheric profile was chosen. The ocean depth was set to $100m$ with a black bottom and the hydrosols were evenly distributed throughout the ocean body. Atmosphere and ocean are coupled using a rough surface model, which is briefly described in Section 4.2.3 and reference [5]. Molecular absorption from H_2O, CO_2, O_3, N_2O, CO, CH_4, and O_2 was accounted for using the HITRAN [114] database and a modified k-distribution approach [44]. The introduced bio-optical model describes a case one waters scenario [57], which is a good model for open ocean waters. The model does not consider sea water Raman scattering or chlorophyll fluorescence, since the implementation of these features into the vector version of the RTM is not yet complete. However, the model is well suited for studying the effects of salinity, temperature, and polarization.

study parameter	grid values	unit
salinity S	0,5,15,25,35	PSU
temperature T	10,15,20	$°C$
chlorophyll concentration C	0,0.1,0.5,5,10,50	$\mu g/l$
wind speed W	2,6,7,8,10	m/s

Table 4.2.1: Parameter grid of the sensitivity study.

[11] Salinity, temperature, and chlorophyll concentration are always used for the ocean body.

In the following sections, the effects of salinity, temperature, and polarization are discussed in terms of relative changes for top of atmosphere (TOA) radiance and water-leaving radiance (WLR). The *salinity effect*:

$$s_\Delta = 1 - I(S = \Delta)/I(S = 35PSU), \tag{4.2.6}$$

is defined as one minus the radiance ratio for a salinity of Δ and standard sea water with a salinity of $35PSU$. In this paper S_5 and S_{25} will be used to discuss the effect. The value of S_5 describes the expected maximum relative error one could encounter due to errors in the chosen salinity. This can happen if an open ocean model, which does not account for salinity, is applied to almost fresh water cases. Low salinity values such as $5PSU$ can be found in the Baltic sea, which is in fact better modeled as case two water, but the *salinity effect* highlights the possible maximum error one can expect from incorrect salinity values. The value of S_{25} describes a more realistic scenario, which represents seasonal and regional salinity variations [95, 75].

Analogously defined is the *temperature effect*:

$$t = 1 - I(T = 10C^\circ)/I(T = 20C^\circ), \tag{4.2.7}$$

which describes the relative error that is caused by a $10^\circ C$ sea water temperature change at $20^\circ C$. Such variation can be easily caused by regional or seasonal changes [90].

As described in Section 4.2.3, all inherent optical properties of sea water depend on salinity and temperature, and changes of their values cause changes of the light field in the atmosphere ocean system. Two different types of effects can be distinguished. First, inside the optically thick ocean body, absorption and scattering are competing processes that determine the WLR, and for its accurate simulation the radiative transfer model must treat multiple scattering correctly. Second, the salinity and temperature dependence of the refractive index directly affects the reflection and transmission of the atmosphere ocean interface [35]. Ergo even with negligible WLR, changes of the salinity and temperature of the ocean can affect TOA radiances.

The *polarization error* is defined as:

$$p = 1 - I/\vec{I}, \tag{4.2.8}$$

where I is the radiance that results from a scalar radiative transfer model run and $\vec{I}$ the simulated radiance from a vector run of the model. Radiance differences come about because a scalar model neglects all elements apart from the phase function from the scattering matrix (see discussion in Section 4.2.5). This effect is known, and several aspects of it have been discussed by other authors in the past [115, 116, 117, 42]. The main cause of such deviations originates from ocean surface reflection and single scattering from air molecules. In Section 4.2.5, this error is discussed with respect to solar angle, MERIS channels, and chlorophyll concentration, which makes the results suitable for the discussion of MERIS, and MERIS band related instruments and their application for ocean color retrieval algorithms. Its spectral signature can be of interest for the algorithm development when polarization has been neglected in the past.

Directional Effects in the 412nm MERIS Channel

The directional salinity and temperature effect for TOA radiances in the $412.5nm$ channel are shown in Figure 4.2.8. Both effects show a similar pattern, where the absolute maxima are located at the sun glint position and in absolute terms decreasing with increasing distance from that point. As defined in Equation 4.2.6, the salinity effect s_Δ describes the relative radiance change for a drop in salinity from $35PSU$ to $\Delta = 5PSU$ (S_5) or $\Delta = 25PSU$ (S_{25}). Likewise defined was the temperature effect in Equation 4.2.7, which describes the relative radiance change for a temperature drop from $20^\circ C$ to $10^\circ C$. In that respect, the salinity effects are both more pronounced than the temperature effect. A change of $10PSU$ causes an effect that

is approximately twice as large as the temperature effect. The mean relative difference of both shown salinity effects is 3.4 ± 0.07. This is roughly 12% larger than the factor of three, which corresponds to the simple ratio of the salinity differences. For TOA radiances, the salinity effect is slightly non linear.

For the case shown, the temperature effect is negative while the salinity effect is positive. If $35PSU$ and $20°C$ are seen as the standard reference, and $5PSU$ as the salinity anomaly and $10°C$ as the temperature anomaly, then a positive salinity effect implies that the radiance for the anomaly is smaller than for the reference. Hence, the decrease in salinity leads to a decrease in radiance. In the $412nm$ channel the sea water absorption is not affected by the salinity decrease (see Figure 4.2.1), but the bulk scattering coefficient decreases by about 25%. The refractive index decreases by about 4%, which slightly increases the ocean surface transmission. This also counterbalances to some extent the decrease in scattering by the sea water.

The negative temperature effect indicates an increase in radiance with decreasing temperature. This is caused by a sea water absorption decrease of 1.3% and an increase in the bulk scattering by 2.3%. The refractive index remains almost constant with only a change of 0.7%. In this case, the positive salinity effect is mainly due to the increase of the sea water scattering, while the negative temperature effect is mainly caused by the decrease of sea water absorption and the increase of sea water scattering.

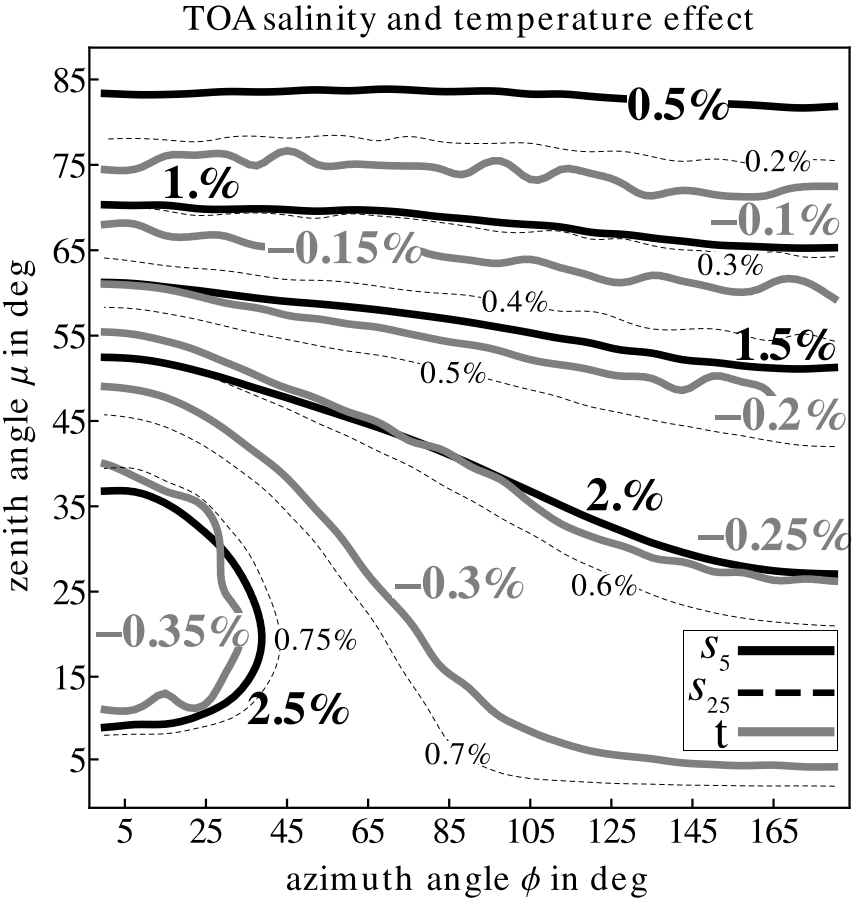

Figure 4.2.8: Directional salinity (black lines show S_{25}, thin dashed black lines show S_5) and temperature (gray lines) effects for top-of-atmosphere radiance in the $412nm$ channel. The effects were defined in Equation 4.2.6 and 4.2.7. The surface wind speed is $10m/s$, the solar position is 12.8°, and the chlorophyll concentrations is $1\mu g/l$.

For water-leaving radiances, the directional dependence of the salinity and temperature

effect is almost isotropic, which is shown in Figure 4.2.9 (similar to Figure 4.2.8, but for the water leaving radiance). Both salinity effects are much larger than for the TOA case, but the variation with direction is less pronounced. The mean of s_{25} is $16.6\% \pm 0.2\%$, while the mean of s_5 is $4.73\% \pm 0.07\%$. The mean value of the ratio of both salinity effects is 3.509 ± 0.007, which is similar to the TOA case. This almost isotropic behavior highlights that the directional dependence of both effects for TOA radiance is mainly caused by the change of surface reflection and transmission, which is caused by the change of the refractive index. The mean value of the temperature effect is $-1.72\% \pm 0.06\%$, and both effects show the same sign as the TOA case.

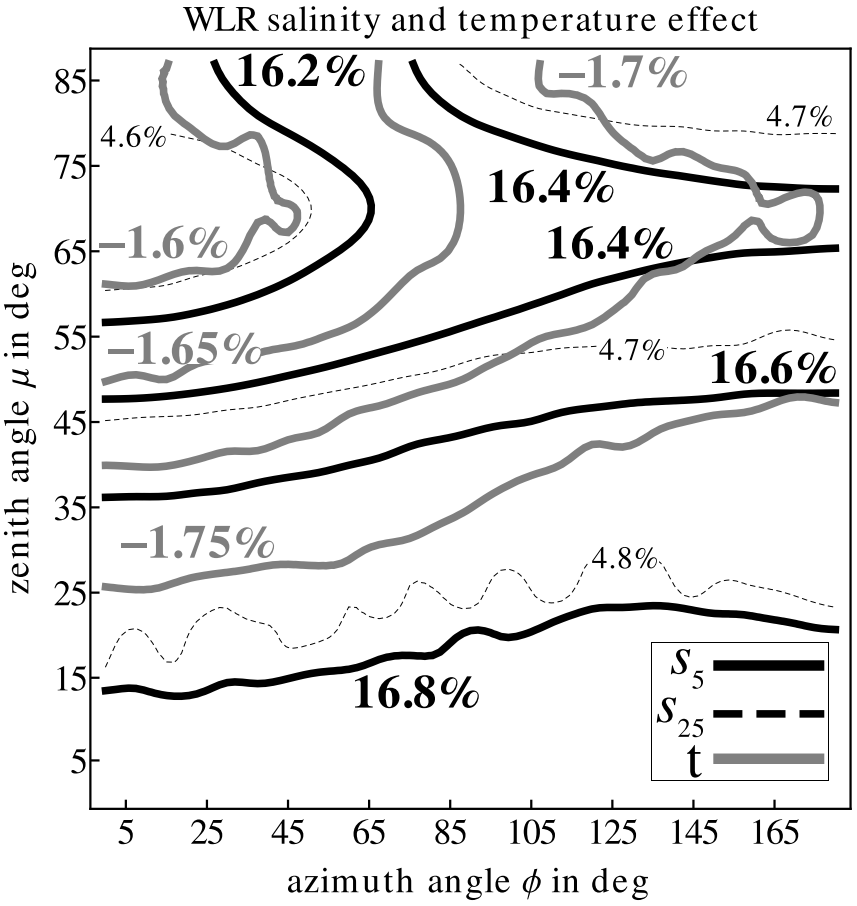

Figure 4.2.9: Same as in Figure 4.2.8, but for the water-leaving radiance.

The maximum of the TOA salinity and temperature effect is found in the principal plane. Figure 4.2.10 highlights this dependency, and combines it with the TOA and WLR radiance for two solar positions. With increasing solar angle (measured from zenith), the maximum of the salinity and temperature effect is shifted towards the horizon like the sun glint and is at the same time decreasing. Again, this shows how the surface reflectivity is a major contribution to both effects. With further increasing the solar angle, the maximum salinity effect for s_{25} becomes smaller, from above three percent for the sun in zenith, to about two percent for the sun at 50°. Towards the horizon, the salinity effect for s_{25} becomes smaller and is under one percent for zenith angles above ±70°. The WLR case shows only little variation with the solar angle, which is also the case for the temperature effect.

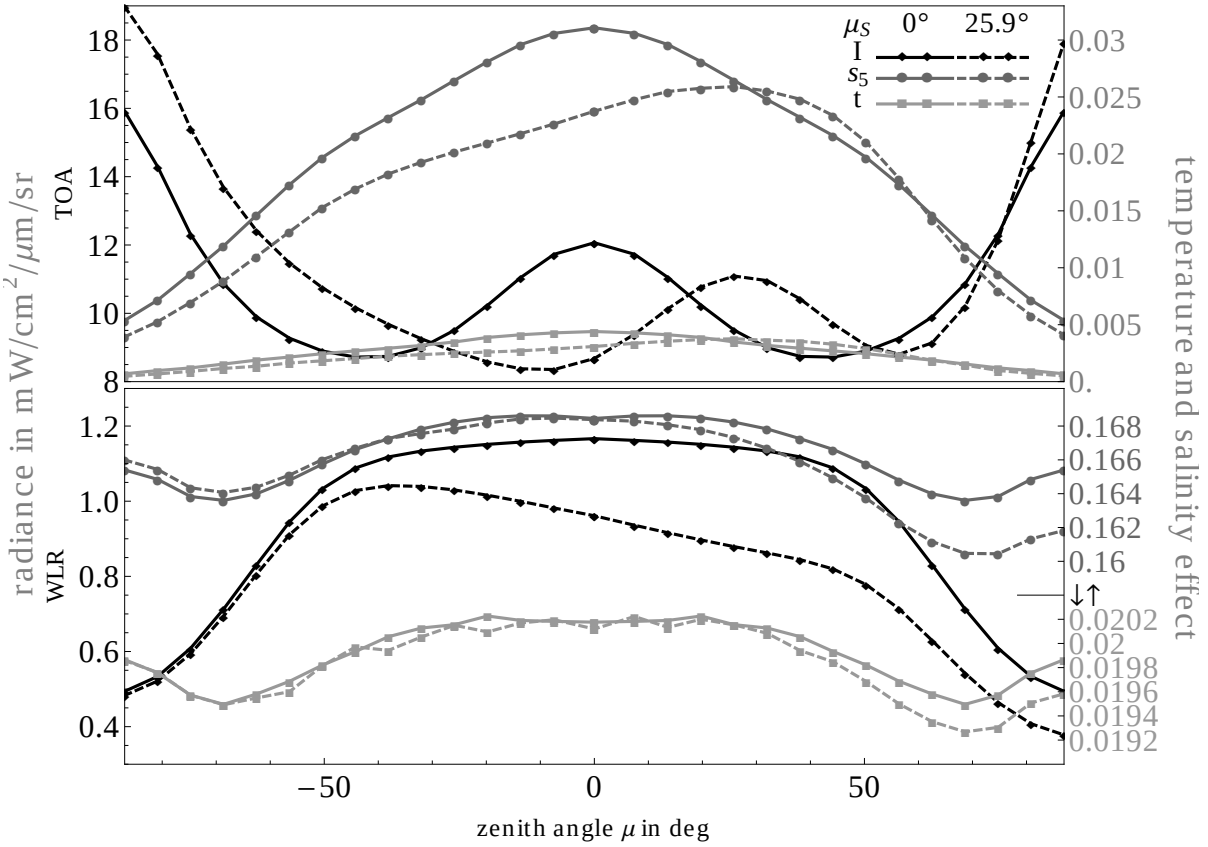

Figure 4.2.10: TOA (top panel) and WLR (bottom panel) radiance (I, black lines) in the principle plane for a case with a salinity of $5PSU$, temperature of $15°C$, wind speed of $7m/s$, chlorophyll concentration of $0.1\mu g/l$, and sun in zenith (solid lines) and at 25.9° (dashed lines). The gray lines and right scale show the temperature and salinity effect (S_5). The viewing zenith angle μ is measured from zenith and negative values indicate an azimuth angle of 180°.

In general, both effects become smaller with increasing chlorophyll concentration. For the TOA case, s_5 reaches its maximum for pure sea water with about 7.06%, s_{25} with 2.04%, and the temperature effect with 1.13%. The decrease of the effects with increasing chlorophyll concentration is shown in Figure 4.2.11. With increasing chlorophyll concentration, the TOA salinity effect s_5 decreases, but the maximum keeps its position and is least strongly affected. The increasing chlorophyll concentration starts to dominate the signal due to increasing scattering and absorption in the water bulk, hence decreasing the salinity effect. For a chlorophyll concentration above $5\mu g/l$, almost only the surface contribution remains as a source for the salinity effect. This saturation is less pronounced for the temperature, since the change of the refractive index is smaller. For the more absorbing sea water of the SWIR region, it becomes the dominant source of the TOA salinity effect. The contribution of the surface to the salinity and temperature effect is also present for more complex waters, as e.g. coastal waters or the Baltic sea. The optical properties of such water types are determined by a larger number of hydrosols and the relative effects caused by the variation of the sea water inherent optical properties will be less pronounced. This will decrease the salinity and temperature effect. However, to derive the WLR from TOA radiances, correct values of the ocean surface reflectivity and transmissivity must be used. The effects might be non-negligible for the associated radiative transfer calculations for these types of waters. For WLR, the salinity effect also decreases with increasing chlorophyll concentration, since the signal from the chlorophyll becomes increasingly important with rising concentration. The temperature effect shows the same behavior,

and decreases with increasing chlorophyll concentration.

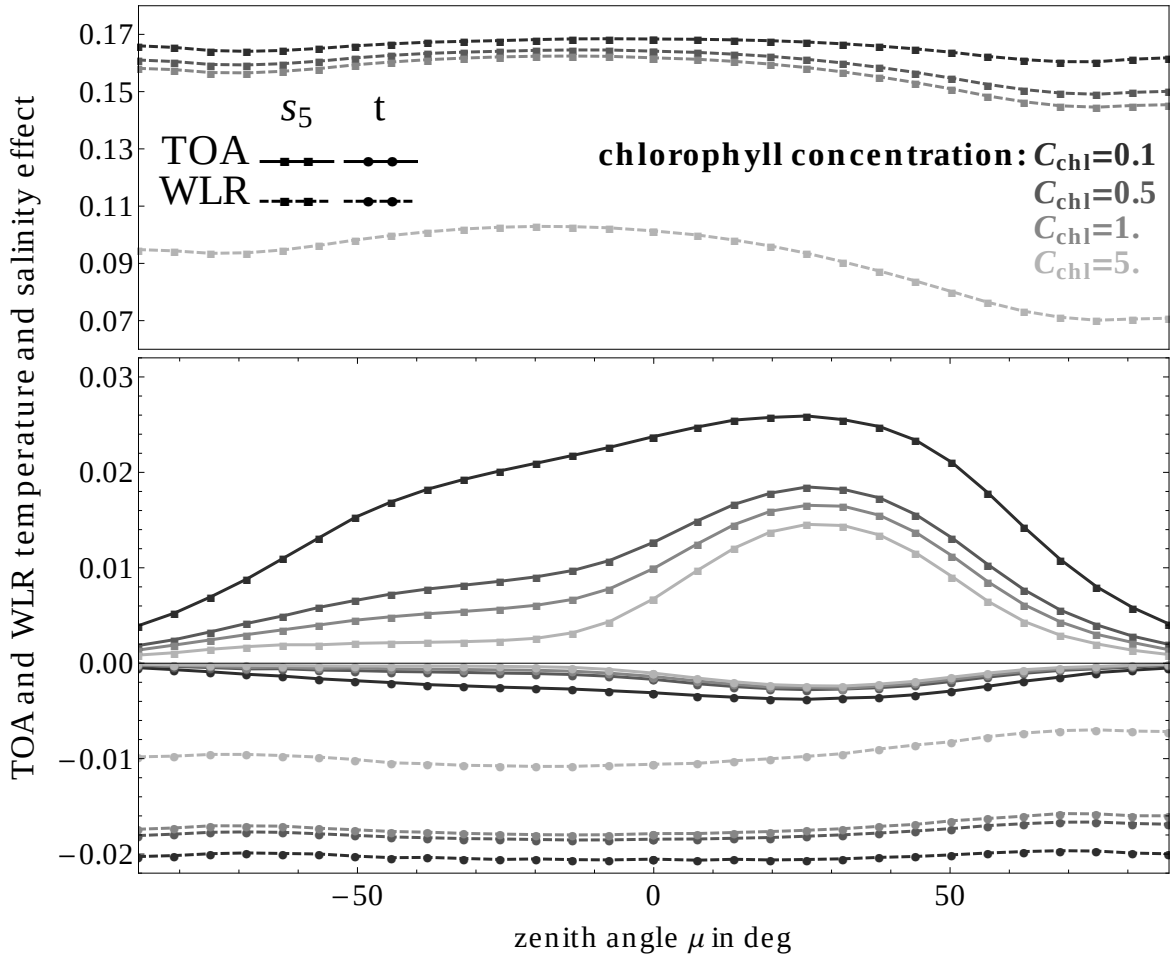

Figure 4.2.11: Salinity (squares) and temperature (circles) effect in the principal plane for TOA (solid curves) and WLR (dashed curves). The viewing zenith angle μ is measured from the zenith and negative values indicate an azimuth angle of 180°. Shown are results for a case with a wind speed of $7m/s$, solar angle of 25.9°, and chlorophyll concentration ranging from $0.1\mu g/l$ to $5\mu g/l$. To show the variability of s_5, the scale was split between 0.03 and 0.07.

Spectral Effects for MERIS/OLCI Channels

The discussion in the previous section was centered on the $412nm$ channel and the directional dependencies of the temperature and salinity effect. In this channel the sea water absorption has a strong minimum (see Figure 4.2.1) and for the range of wavelengths considered, both effects are pronounced. Figure 4.2.12 shows the zenith water-leaving radiance for the complete channel set for pure sea water and chlorophyll concentrations up to $50\mu g/l$. The variation of the radiance signal is dominated by the sea water absorption, the solar spectrum, and gaseous absorption (e.g. as in the O_2A band at $760nm$). Two regimes can be distinguished. Below $560nm$, the increasing chlorophyll concentration decreases the signal, since additional absorption is introduced. Above the hinge point at $560nm$, the water absorption is much stronger compared to chlorophyll, but its strong scattering and the minimum in its absorption is leading to an increase of the signal. This figure is mainly shown to put the relative quantities into the perspective of the common signal, which covers several orders of magnitude for the analyzed range of wavelengths.

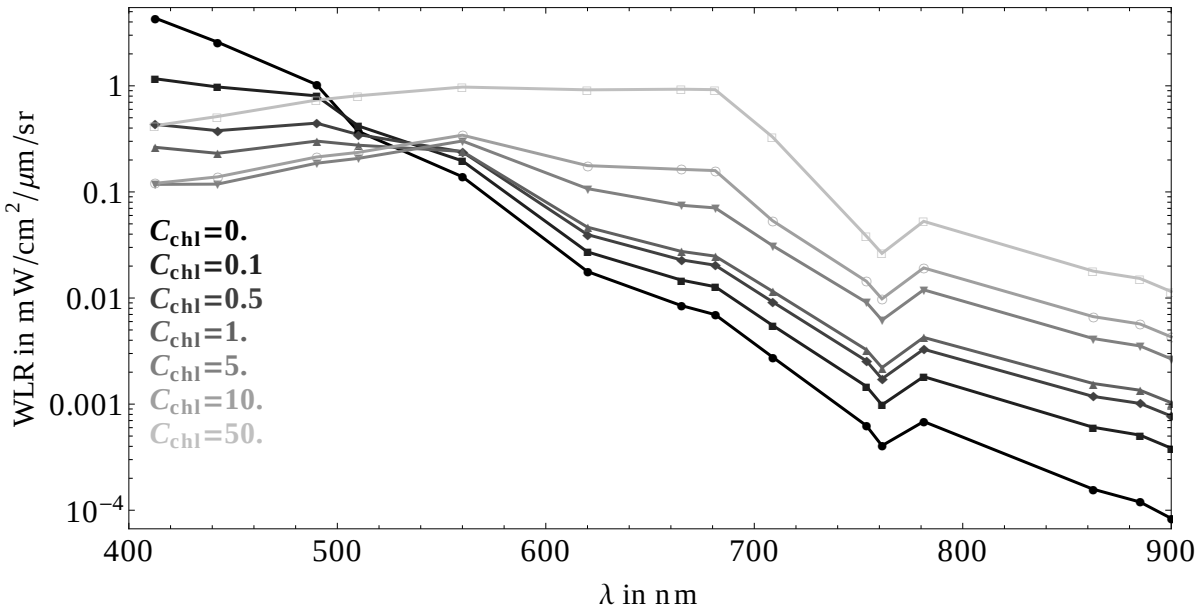

Figure 4.2.12: Zenith water-leaving radiances for MERIS channels from 412.5nm to 900nm. The chlorophyll concentration ranges from zero (pure sea water, black line) to 50$\mu g/l$ (light gray line). The surface wind speed is 7m/s and the solar position is 25.9°.

Figure 4.2.13 shows both the salinity and temperature effects for zenith water-leaving radiances over the whole spectral region and with chlorophyll concentrations ranging from zero to 50$\mu g/l$. The pure sea water salinity effects are almost independent from wavelength, since the effect is dominated by changes in the bulk scattering coefficient (compare with Figure 4.2.3). The remaining spectral variation is caused by the spectral dependency of the salinity absorption parameter Ψ_S, which was shown in Figure 4.2.2. The pure sea water temperature effect shows spectral variations, which corresponds to the spectral variation of the temperature absorption coefficient Ψ_T (compare with Figure 4.2.2). If chlorophyll is introduced, both salinity effects decrease since the scattering and absorption of the hydrosols become more dominant in determining the WLR.

The temperature effect is smaller than the salinity effects. Its maximum is below -5%, and decreases with increasing chlorophyll concentration. For some of the longer wavelength channels, such as 781.25, this behavior changes so that an increase in chlorophyll increases the temperature effect. Here the water leaving radiances increase by almost one order of magnitude with increasing chlorophyll concentration (see Figure 4.2.12). This is caused by the scattering of chlorophyll, which is counterbalancing the strong water absorption. The WLR is in those cases very sensitive to even small changes in absorption, and this channel almost coincides with a local maximum of Ψ_T.

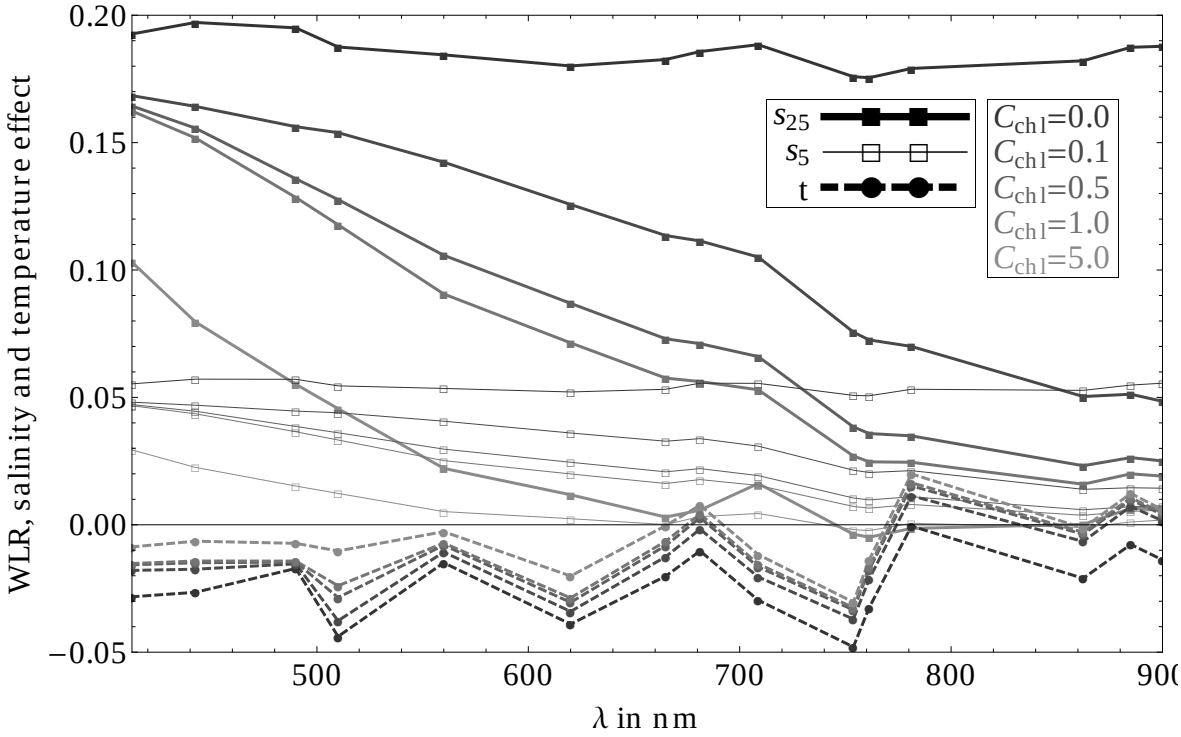

Figure 4.2.13: Zenith salinity and temperature effect for water-leaving radiance, chlorophyll concentrations from zero to $5.0\mu g/l$, and MERIS channels from $412.5nm$ to $900nm$.

Polarization Error

The polarization of the TOA radiance has two major consequences. It could be used as additional source of information and can lead to measurement errors of radiometers that are sensitive to polarization. The TOA degree of polarization is sensitive to both changes in salinity and chlorophyll concentration, as is shown for the $412nm$ channel in Figure 4.2.14. The figure shows the difference in TOA degree of polarization for changing salinity and chlorophyll concentrations with respect to a salinity of $35PSU$ and chlorophyll concentration of $0.1\mu g/l$. The patterns of both effects are quite similar. The decrease in salinity leads to an increase of the TOA degree of polarization. The reason is the decreasing bulk scattering coefficient, which decreases the TOA radiance contribution from the ocean, which increases the radiance fraction that has been scattered only by air molecules, which increases the degree of polarization. Also, the refractive index is decreasing, which decreases the highly polarized ocean surface reflection. The increase in TOA degree of polarization is much stronger for increasing chlorophyll concentration, where the increasing chlorophyll scattering increases the TOA radiance contribution from the ocean bulk.

Neglecting polarization in radiative transfer calculations can lead to radiance errors. This strongly depends on viewing geometry, scene, and spectral channel. The reason for this effect is that in scalar RT schemes, scattered radiance I' is modeled as a multiplication of the phase function $p(\theta)$ with the incident radiance I : $I' = p(\theta)I$, where θ is the scattering angle. Vector radiative transfer schemes treat the polarized nature of light by using a four vector $\vec{I} = (s_1, \ldots, s_4)^T$ and real 4×4 scattering matrices $\mathbf{p}(\theta)$ to model the scattering: $\vec{I'} = \mathbf{p}(\theta)\vec{I}$. In general, the non $(1,1)$ elements of $\mathbf{p}$ are nonzero and the matrix multiplication couples the $s_2, \ldots, s_4$ elements with the s_1 element of $\vec{I}$, which in the Stokes formalism is just the radiance. This coupling is completely neglected in scalar radiative transfer schemes, and leads to a radiance error that was defined in Equation 4.2.8 as *polarization error*: $1 - I/\vec{I}$. This effect and several of its aspects have been discussed in the past (see references: [115, 116, 117, 42]).

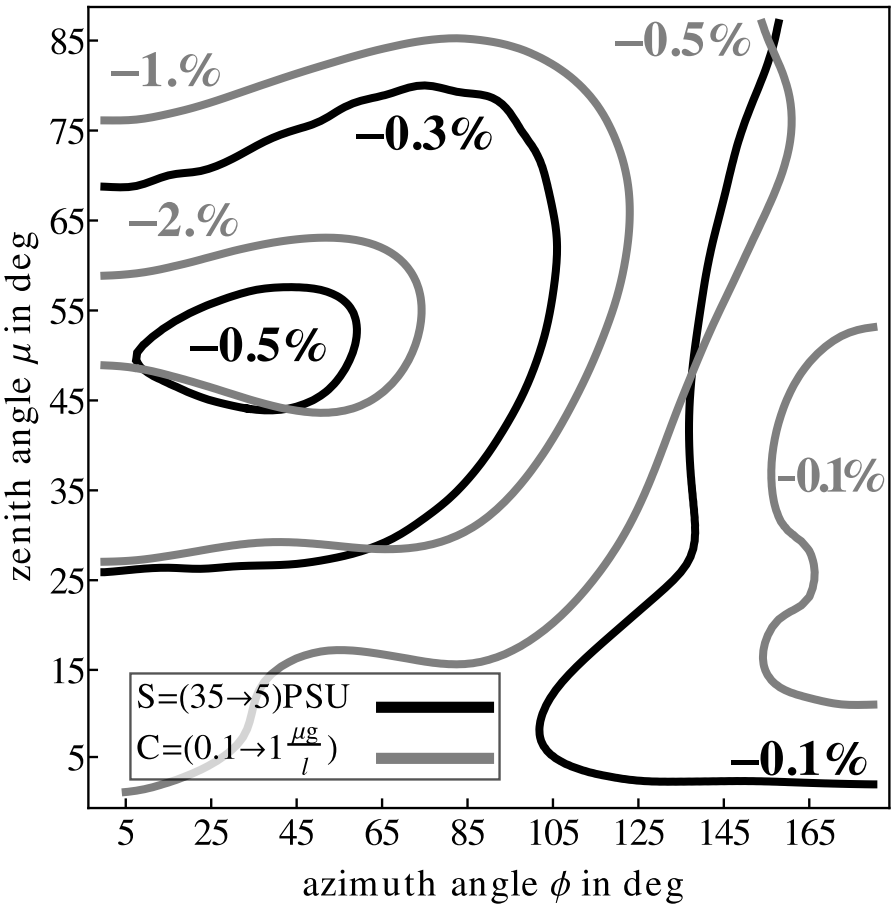

Figure 4.2.14: Difference of TOA degree of polarization in the 412.5nm MERIS channel with respect to a salinity of 35PSU, a chlorophyll concentration of 0.1$\mu g/l$, a wind speed of 7m/s, and a solar zenith angle of 25.9°. The black lines show the differences for a decreased salinity of 5PSU and the gray lines for an increased chlorophyll concentration of 1$\mu g/l$.

In the following, the effect's directional dependence for the 412nm channel and its spectral variation for MERIS channels up to 900nm is discussed. In Section 4.2.5, a comparison of all three effects is provided and discussed.

Figure 4.2.15a and 4.2.15b show the radiance field at TOA and for WLR, together with the polarization error as defined in Equation 4.2.8. For the TOA case, the polarization error varies between ±8%, with strong dependence on geometry and solar position (not shown here). The principal plane contains the minimum and maximum of the polarization error. A sign change occurs for the polarization error, which shows that scalar radiative transfer will both over- and underestimate the true radiance field. The shape of the line of zero polarization error depends strongly on solar position. The WLR case is shown in Figure 4.2.15b, which is similar to Figure 4.2.15a. The polarization error varies between −3% and −6%. Again, the maximum error is found in the principal plane and the directional variation of the error depends strongly on the solar position (not shown). A sign change occurs only for larger solar zenith angles. Results for higher solar zenith angles and lower chlorophyll are given in reference [5].

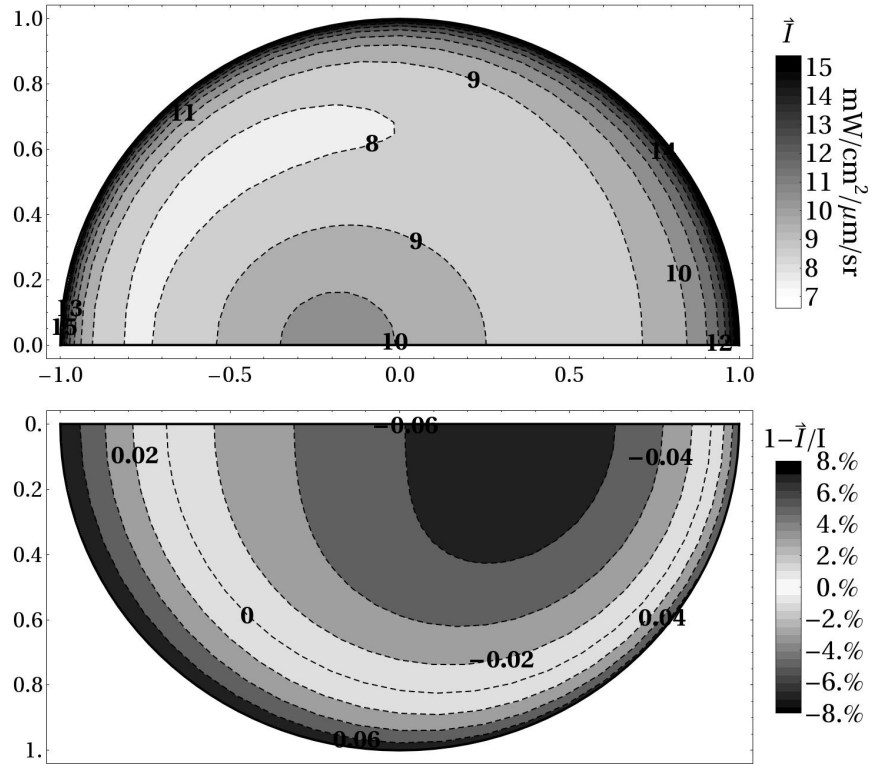

(a) Top-of-atmosphere case.

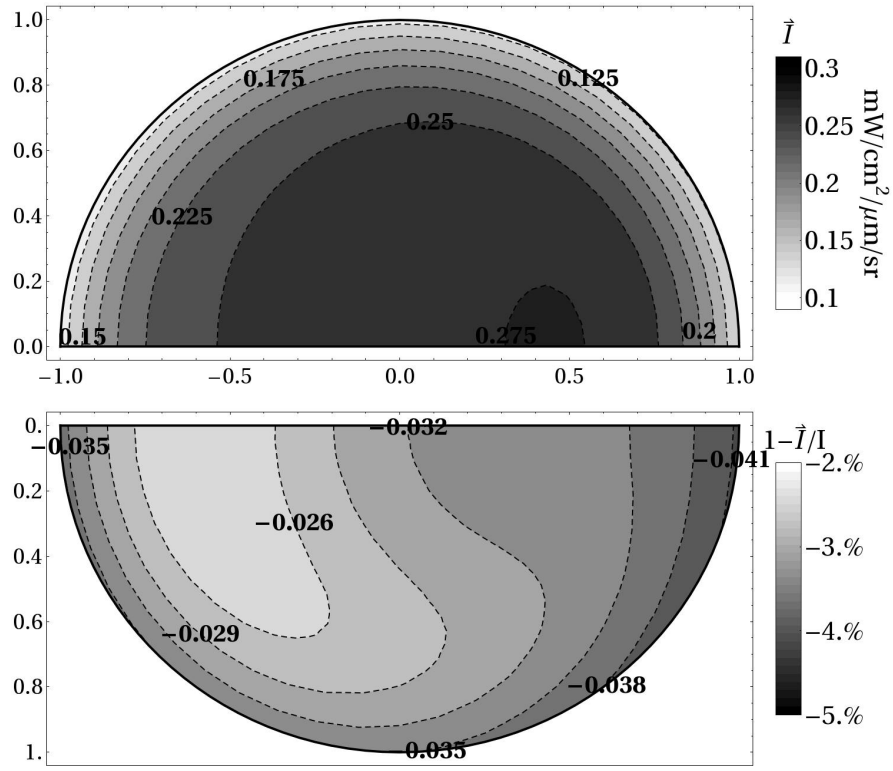

(b) Water-leaving radiance case.

Figure 4.2.15: Directional TOA radiance and WLR in the $412nm$ channel (top panel) and polarization error (bottom channel) as defined in Equation 4.2.8. The sun is at 25.9°, the wind speed is $7m/s$, and the chlorophyll concentration is $0.1\mu g/l$.

The spectral variation in the polarization error depends on the amount of scattering, absorption, and ocean surface reflection and transmission. Scattering depends on the optical thickness of the atmosphere[12] and the ocean. The spectral variation of the TOA polarization error for several solar zenith angles and chlorophyll concentrations is shown in Figure 4.2.16. The mean absolute polarization error,[13] the maximum polarization error with respect to viewing geometry, and the relative variation of the polarization error for an increase of chlorophyll concentration from $0.1\mu g/l$ to $1\mu g/l$ are shown for various solar zenith angles. The mean polarization error decreases with increasing wavelength, (i.e. with Rayleigh optical thickness) and has a prominent minimum in the 0_2A absorption band. The maximum polarization error depends much more strongly on solar position than the mean absolute polarization error does. It depends only slightly on the chlorophyll concentration, which is shown by the dotted lines.

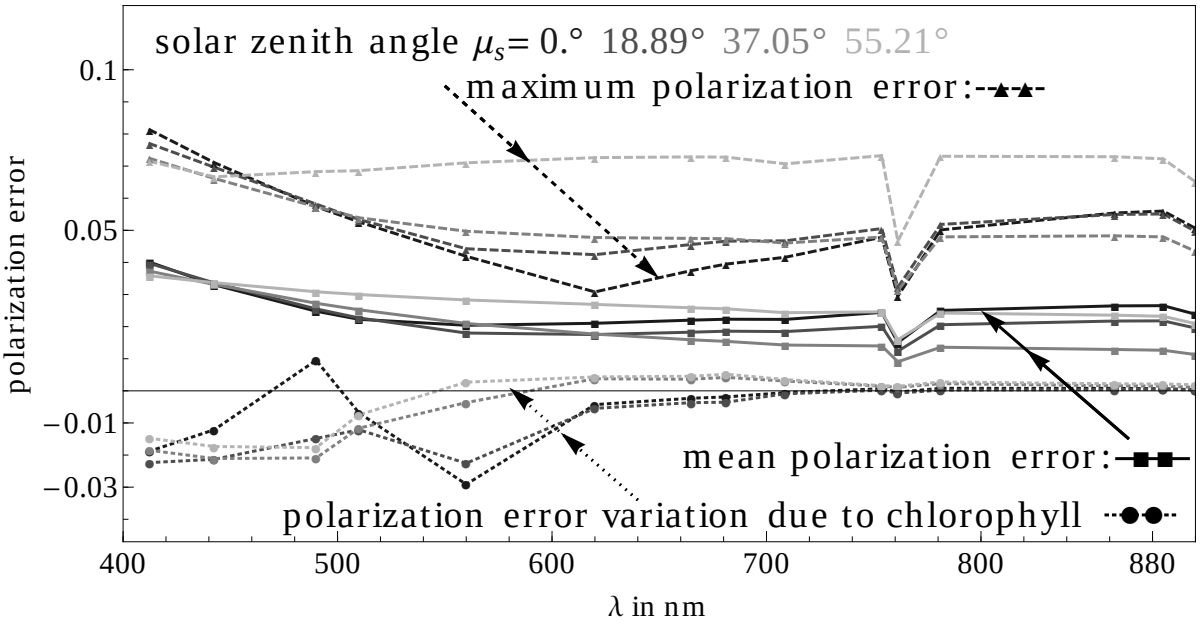

Figure 4.2.16: Mean TOA polarization error [13] (gray solid curves) for MERIS channels from $412.5nm$ to $900nm$, for solar angles from 0° to 50.32°, wind speed of $7m/s$, and chlorophyll concentration of $0.1\mu g/l$. The gray dashed lines show the maximum polarization error with respect to zenith and azimuth angle. The dotted lines show the relative variation of the mean polarization error with respect to a chlorophyll change, which was calculated according to: $1 - \langle p(c = 1\mu g/l)\rangle / \langle p(c = 0.1\mu g/l)\rangle$.

Overview

The effects of salinity, temperature and polarization have been separately discussed in Sections 4.2.5 to 4.2.5. For a better comparison, all three effects have been compiled in Figure 4.2.17. Results are shown for WLR, chlorophyll concentration of $0.1\mu g/l$ and $1.0\mu g/l$, zenith viewing direction, and a solar zenith angle of $25.9°C$. The salinity effect s_5, which indicates a salinity drop from $35PSU$ to 5, is the most pronounced effect and decreases with wavelength and chlorophyll concentration. The more realistic salinity effect s_{25} is much smaller, with the same characteristics with respect to wavelength and chlorophyll concentration.

Although it is discussed in detail here, the surface wind speed is an important parameter in ocean color retrieval schemes and is also shown. The wind speed effect has been defined as:

[12] Rayleigh optical thickness were calculated according to reference [118]. [13] The mean absolute polarization error has been calculated using $\langle p\rangle = 1/(4\pi)\int_0^{2\pi} d\varphi \int_0^{\mu} d\phi \left|1 - I(\varphi,\mu)/\vec{I}(\varphi,\mu)\right| \sin(\mu)$.

$$w = 1 - I(W = 10m/s)/I(W = 2m/s). \tag{4.2.9}$$

The s_5 effect is comparable in size with the effect from changing the wind speed from $2m/s$ to $10m/s$. The wind speed effect has a maximum for which the spectral position depends on the chlorophyll concentration. The wind speed mainly changes the reflection and transmission of the atmosphere ocean interface. Increasing the wind speed increases the reflection, and therefore decreases the transmission of radiation into the ocean. The positive wind speed effect shows that increasing the wind speed decreases the WLR. It depends strongly on chlorophyll content and the spectral variation of the chlorophyll absorption.

The s_{25} salinity effect, the temperature effect, and the polarization error are comparable in absolute size but not in their spectral variation. In particular the spectrum of the temperature effects shows the strong impact of the temperature on the sea water absorption.

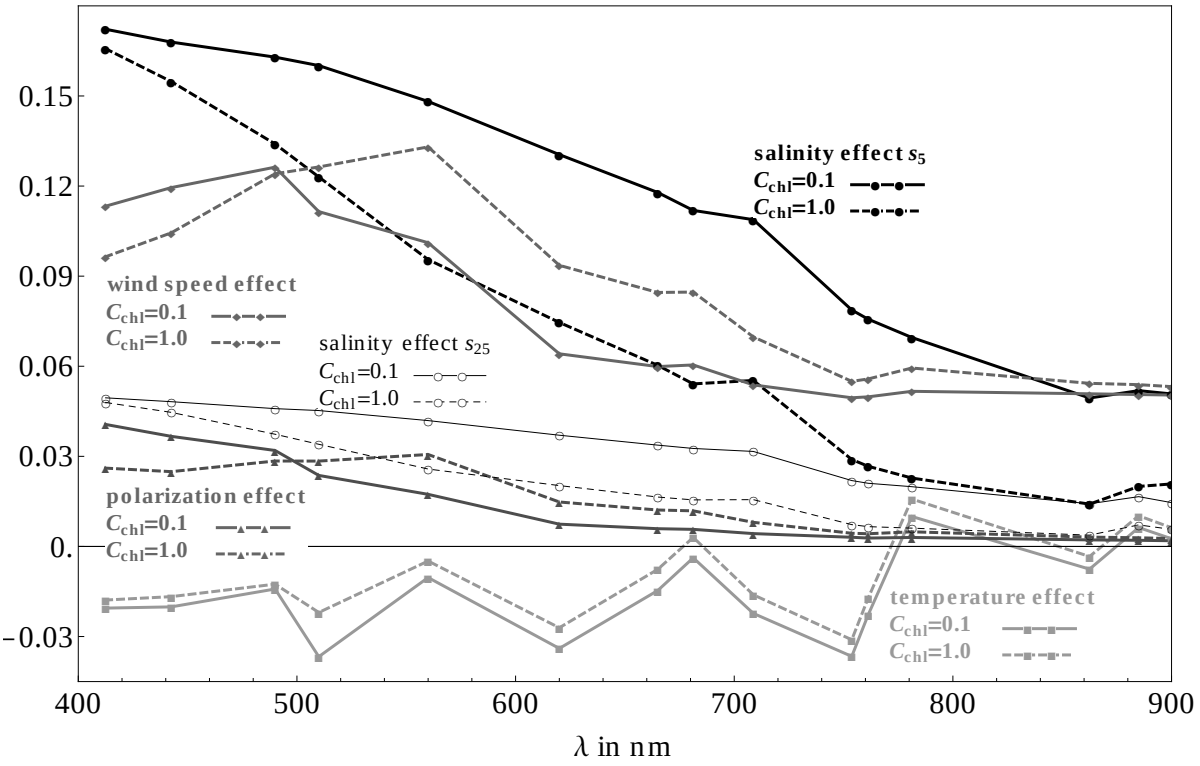

Figure 4.2.17: Zenith WLR salinity effect s_5 and s_{25}, temperature effect, polarization error, and wind speed effect for MERIS channels from $412.5nm$ to $900nm$. All effects are shown for chlorophyll concentrations of $0.1\mu g/l$ and $1\mu g/l$. The solar zenith angle is $25.8°$ and the wind speed $7m/s$.

4.2.6 Conclusion

A simple but realistic bio-optical model was presented and applied for a sensitivity study concerning the effects of salinity, temperature, and polarization. The bio-optical model combines in situ optical measurements of chlorophyll, basic assumptions about the phase function, and Mie theory to deliver a consistent set of phase matrices. The model would benefit if more detailed bio-optical data would be available. Most essential are measurements of scatter matrices at high spectral resolution. Finer spectral resolution could be used for more accurate modeling of given instrument channels, since the spectral behavior within the channel could be taken into account more accurately. Additional spectral information could also aid the modeling of the scattering properties of water constituents.

Raman scattering and chlorophyll fluorescence effects have not been considered in this study. From results of the scalar version of the model, which accounts for it, we know that Raman scattering can lead to significant contributions to water-leaving radiances. Its inclusion into the vector radiative transfer scheme would then lead to even more precise modeling results.

Radiative transfer simulations have shown that salinity, temperature, and polarization can have significant effects on top-of-atmosphere radiances and water-leaving radiances. The effects of salinity and temperature are most pronounced for the clearest waters, and are reduced when chlorophyll is added to the water body. Even in cases where the water leaving radiance contribution is negligible for the top of atmosphere radiance, a sensitivity to salinity and temperature is caused by changes of the reflectivity of the ocean surface.

Polarization plays an important role in radiative transfer simulations of atmosphere ocean systems, and neglecting it can lead to the over and underestimation of radiance by scalar codes in the order of $\pm 8\%$ for top of atmosphere radiances. This result shows explicitly that the polarization has to be taken into account for simulation of coupled atmosphere ocean systems. The error for top of atmosphere radiances and water leaving radiances depends strongly on geometry, and probably cannot be reduced without performing vector radiative transfer simulations.

The results indicate that errors in the temperature and salinity can affect ocean color retrieval schemes, which disentangle atmospheric and oceanic constituents using spectrally dependent differences of their inherent optical properties. If such a scheme is based on the inversion of radiative transfer simulations, an inversion using incorrect salinity and temperature values can produce meaningful results, but might introduce additional error and biases. Increased retrieval errors can be caused by the errors made in the modeling of the sea water, which might be *absorbed* by the retrieval by changing the concentration of other in water constituents. For this reason, even if the simulated spectra and measurements show only small systematic deviations, some parts of the retrieval error may be caused by errors in salinity, temperature, or the use of scalar radiative transfer. Quantifying this error was beyond the scope of this paper. A possible improvement of ocean color retrievals would inherently lead to an increase of the computational effort of the radiative transfer simulations, since two additional dimensions for salinity and temperature would be needed. Using vector radiative transfer increases the computation time and also increases the complexity of the atmosphere and ocean model. While scattering matrices of aerosols can be computed using Mie or T-Matrix theory, computing scattering matrices of ocean constituents is more complex and this part of the bio-optical modeling could benefit if more measurements would be available.

Acknowledgment

This research was funded by the ESA support to science project WATERRADIANCE (AO/1-5859/08/NL/CT). I would like to thank Rüdiger Rötgers, Roland Dörfer, and Jonas von Bismarck for many fruitful discussions.

4.3 Possibilities for the Retrieval of Aerosol Vertical Profiles using Satellite Hyperspectral Radiance Measurements in Oxygen Absorption Bands

4.3.1 Abstract

Future spaceborne instruments such as OCO2, FLORIS, and CarbonSat offer possibilities to retrieve the vertical aerosol extinction profile over land using their hyperspectral radiance measurement capabilities in oxygen absorption bands. Based on forward modeling of FLORIS measurements, an inversion scheme was set up and a synthetic retrieval algorithm was developed. The forward model is based on coupled local interpolation of the full radiative transfer simulations, which were performed using the MOMO model. The expected retrieval uncertainty for a FLORIS-like instrument is discussed for varying surface types, aerosol optical thickness, single scattering albedo, and surface inhomogeneities. The global applicability of a retrieval algorithm is assessed based on global data of surface reflectance, surface homogeneity, and aerosol loading. As a main result, the spectral resolution of FLORIS of $0.3nm$ in the oxygen A and B band and the SNR of above 500 would allow a retrieval with an uncertainty of approximately 30% for mono modal aerosol vertical structures. Using the two oxygen absorption bands together includes a higher range of possible surface reflectances for each spectrum, which can improve the retrieval. Next to the instrument specification itself, the retrieval uncertainty is mainly influenced by aerosol optical thickness, surface reflectance and surface inhomogeneity, and is decreasing with increasing aerosol optical thickness and increasing surface homogeneity.

4.3.2 Motivation

Multiple fields of research can benefit from more detailed knowledge about the global variation of the vertical distribution of aerosols. Weather aerosols are a net cooling or warming agent, for the climate system depends not only on the aerosol type, but also their height [119], as well as their interactions with clouds [120, 119]. Aerosol height has a main influence on its impact on human health and pollution [121, 122] and on the retrieval of total aerosol optical thickness [123] from passive spaceborne measurements. Such errors can affect atmospheric correction schemes [124], which are widely used in remote sensing to derive properties of the oceans [87] or land surfaces [125].

On local scales, the aerosol vertical profile can be derived using LIDAR measurements (e.g. EARLINET [126]), airborne experiments [127], or balloon ascents [128]. On global scale, the only instrument currently providing such information is the back scatter LIDAR CALIOP, which is on board the satellite CALIPSO [129]. Its main downside is the sparse spatial temporal resolution [130], which could in principle be overcome by using passive imaging instruments. Figure 4.3.1 shows the CALIPSO satellite as part of NASA's A-Train and how its data forms a curtain in the atmosphere. No data across the satellite track can be acquired, which leads to sparse spatial and temporal coverage of the globe. Imaging instruments can feature swath widths in the order of tens to thousands of kilometers. Using such type of instruments would dramatically increase the spatial and temporal coverage the measurements.

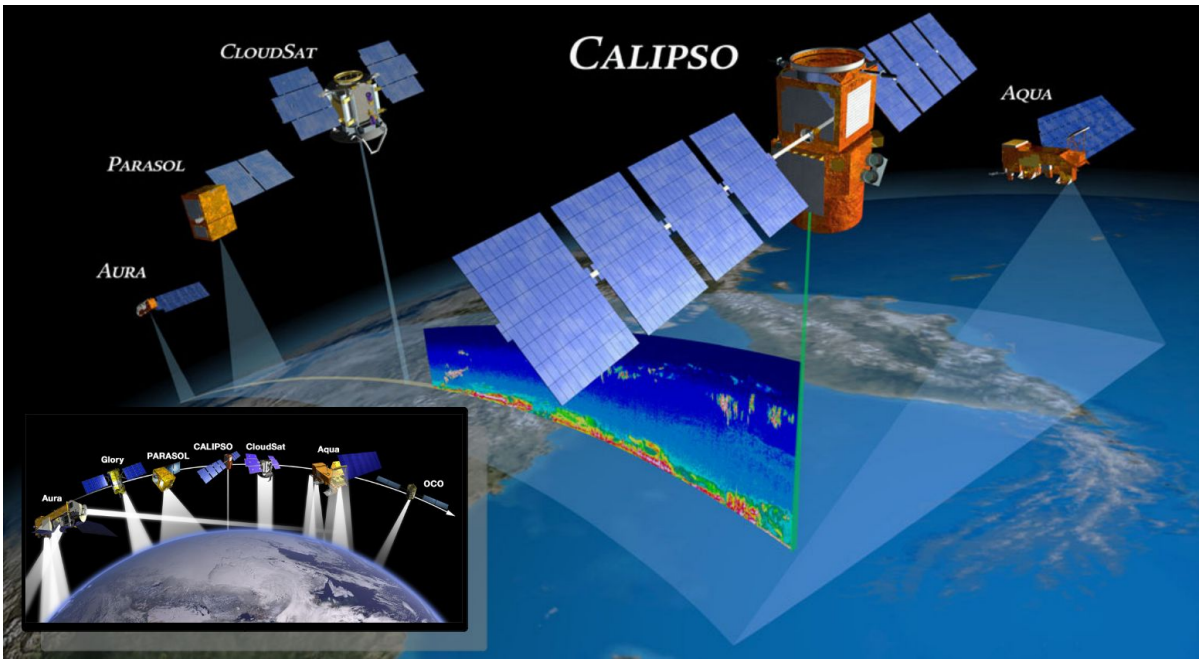

Figure 4.3.1: CALIPSO satellite as part of NASA's the A-Train. The LIDAR back scatter signal can be used to acquire vertical resolved data about the atmosphere in form of a curtain. Also shown is that in contrast to passive imaging instruments, no measurements across track are performed. Image source is NASA without copyright.

Attempts to use the oxygen absorption bands to derive aerosol- [131, 132, 133, 134, 133, 135, 136] or cloud-height [137] have been published in the past, but for aerosol over land no operational data product exists. For a case study, the aerosol mean height over oceans was derived using data from MERIS and POLDER [138, 124]. The authors used the reflectance ratio from two channels inside and outside the O_2A band. Sanghavi et al. discussed about using the O_2A and O_2B band to derive aerosol vertical distribution from SCIAMACHI data and applied the technique to a scene for Kanpur (India). This approach is limited by the coarse spatial resolution of SCIAMACHI, its calibration accuracy [139], and its sensitivity to polarization [140, 141]. Limitations due to coarse spatial resolution also apply to GOSAT [142, 143], which can lead to problems ascribed to inhomogeneities of the aerosol and the land surface, which is discussed in more detail in Section 4.3.10 and 4.4.

The future instruments OCO2 [144, 145] and the two competing ESA Earth Explorer missions [146, 147] FLEX [148, 149, 150] and CarbonSat [151] offer opportunities to derive the aerosol vertical structure, since they include hyperspectral measurements in oxygen absorption bands. None of those projects is primarily an aerosol mission, hence the design of the instruments was driven by other requirements. Some of their key aspects relevant to aerosol remote sensing are compiled in Table 4.3.1. While having all comparable signal to noise (SNR) levels, the main differences are the trade-offs made between spatial and spectral resolution. FLORIS has the smallest spectral resolution, but includes the O_2B band and offers the highest spatial resolution. CarbonSat and OCO2 offer both much higher spectral resolution, but have much coarser spatial resolution. From those instrument specifications it is not obvious which of the missions is suited best for the remote sensing of aerosol vertical distribution. While this section covers mainly the FLORIS instrument and is therefore theoretic, Section 4.4 is devoted to the inversion of radiative transfer simulations for a set of measurements made by the instrument TANSO-FTS on board the GOSAT satellite.

mission:	FLORIS [152, 153]	CarbonSat [154]	OCO2 [144, 155]	GOSAT [156, 143, 157]
SR[a] at O_2A	$0.3nm$	$0.03nm$	$0.045nm$	$0.03nm$
SNR[b] at O_2A	$> 500nm$	> 500	> 310	> 300
SR[a] at O_2B	0.3	–	–	–
SNR[b] at O_2B	$> 500nm$	–	–	–
swath width:	$390km$	$500km$	$10km$	$3 \times 88km$[d]
footprint[c]:	$300 \times 300m^2$	$2 \times 2km^2$	$2.25 \times 1.19km^2$	$10km$

[a] Spectral resolution using the full width at half maximum definition.
[b] SNR is usually a function of the signal and integration time, hence these values provide only a proxy for the real SNR spectrum.
[c] Footprint for a single measurement/pixel: along×cross track.
[d] GOSAT's instrument TANSO-FTS is a Fourier transform spectrometer with a pointing device to achieve cross track resolution. The number of cross track points can be set by JAXA to 1,3,5, or 7.

Table 4.3.1: Key instrument features of future missions suitable for the remote sensing of aerosol vertical structure using passive hyperspectral radiance measurements in oxygen absorption bands.

Discussed in the following sections are the possibilities for a retrieval of aerosol vertical structure from FLORIS hyperspectral measurements in the O_2A and O_2B band. The theoretical analysis is based on the inversion of radiative transfer calculations that where used to simulate FLORIS measurements. The forward modeling is described in Section 4.3.5. Discussed in the subsections are the aerosol vertical model, the aerosol optical model, the surface reflectance model, and the radiative transfer scheme. The inversion algorithm is discussed in Section 4.3.9, and its results for a set of test cases in Section 4.3.10. The discussion includes the inversion error depending on the surface type and homogeneity, the aerosol optical thickness and absorption, and the neglecting of polarization in the radiative transfer. An estimation about to be expected error and global applicability is given in Section 4.3.12 and Section 4.3.13.

4.3.3 Measurement Principle

Top-of-atmosphere (TOA) radiance is sensitive to aerosol height and vertical distribution if scattering and absorption in the atmosphere are competing processes. In general, absorption reduces the TOA radiance while scattering tends to increase it. In fact, if inter atmospheric light sources[14] are not present, scattering and surface reflectance are the only sources for diffuse TOA radiance. Absorption can be measured in $1/m_{absorber}$, where $m_{absorber}$ is a meter of the absorber mass.[15] This means that the light field becomes smaller if the absorbing medium becomes geometrically thicker. Scatterers within the absorbing medium effectively decrease the light path in the absorber and hence increase the TOA radiance. The closer the scatterer is located to the top of the absorber, the higher the radiance increase will be. A sketch of this general principle is shown in Figure 4.3.2.

[14] E.g. thermal emission, Raman scattering in the atmosphere or ocean, or fluorescence from plants or phytoplankton. [15] Assuming a constant density of the absorber.

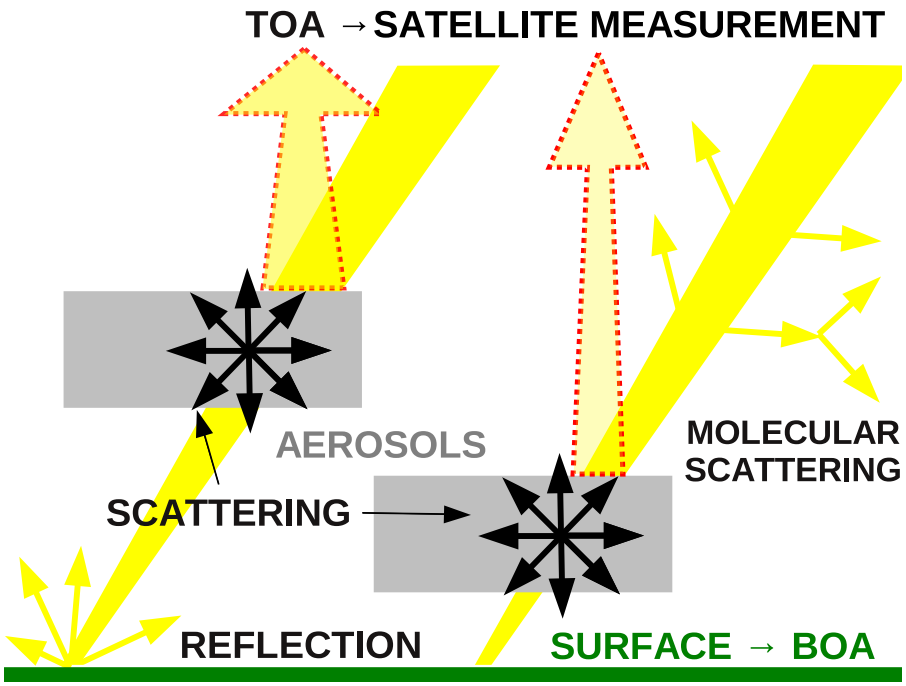

Figure 4.3.2: Basic principle of the remote sensing of aerosol vertical structure using TOA radiance measurements in atmospheric absorption bands. The higher the aerosol pack is located, the less absorption takes place before the radiation is scattered towards the top of the atmosphere. This increases the radiance if compared to a scenario where the aerosol pack is located closer to the bottom of the atmosphere.

Competing processes means that the scattering process needs to have the chance to increase the radiance, which can only happen if radiance is left to be scattered. If the absorption is so strong that all radiance is absorbed before scattering happens, it cannot increase the radiance.

To employ this effect for the remote sensing of aerosol vertical distribution, the amount and vertical profile of the absorber and other scatterers should be well known. This greatly decreases the number of unknown parameters, which simplifies the inversion of radiative transfer simulations. Since FLEX is a land surface only mission, the subject of this research are cloud free cases over land. This means that next to aerosol, the only scattering source is molecular scattering, which can be described by Rayleigh scattering and depends in general only on the temperature profile of the atmosphere and the surface pressure.

The O_2A band is very well suited to apply this principle, since oxygen is considered to be a well-mixed gas. Its absorption then depends in general only on the atmospheric temperature profile and the surface pressure. In the spectral window of the O_2A band, no other major atmospheric absorbers have to be considered. Also, the aerosol optical thickness, which tends to decrease with increasing wavelength, is large enough to have an non-negligible effect.

The O_2B band offers similar options to remote sensing, but is at its borders affected by water vapor absorption. In contrast to oxygen, water vapor is not well mixed and its amount and vertical structure is itself subject to retrievals by remote sensing algorithms. This means that either the affected spectral region should be excluded from a retrieval, or the results of a water vapor retrieval are needed as additional input. Whether this is possible depends on the used platform, instrument, and available prior knowledge.

4.3.4 The FLORIS Instrument

The FLORIS [148] instrument on board the FLEX [149, 150] satellite is currently in development at ESA and contractors and was accepted for phase A/B1 of the Earth Explorers program. If selected, the mission could be launched in the year 2017. The FLORIS instrument features a spatial resolution of $300m \times 300m$, a swath width of $390km$, and a spectral resolution of $0.1nm$ inside and $0.3nm$ outside the oxygen absorption bands. A sketch of the viewing geometry is shown in Figure 4.3.3b and a drawing of the instrument and its platform in Figure 4.3.3a. Its main mission is the retrieval of fluorescence from vegetation and one candidate for a retrieval algorithm is based on an accurate atmospheric correction scheme, which can benefit from the additional characterization of aerosol vertical distribution. Although aerosol characterization is not the main mission goal and instrument requirement driver, with the current specifications of SNR and spectral resolution (see reference [153] and Table 4.3.1) the retrieval of aerosol vertical distribution could be possible and could contribute to the overall success of the mission.

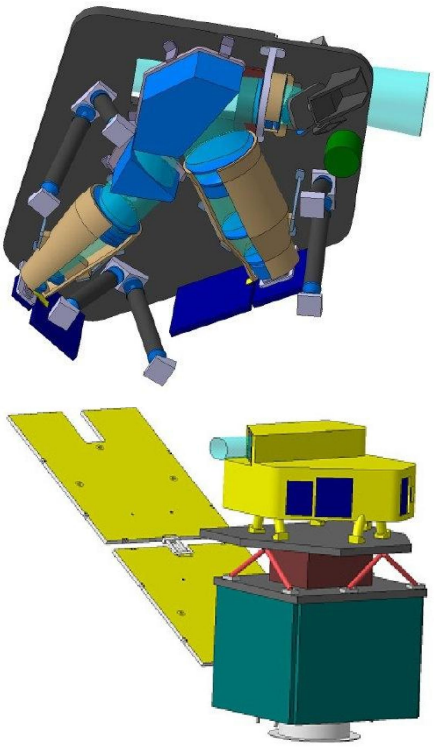

(a) Top: sketch of the FLORIS instrument. Bottom: FLORIS mounted on the MYRIADE micro satellite platform [158].

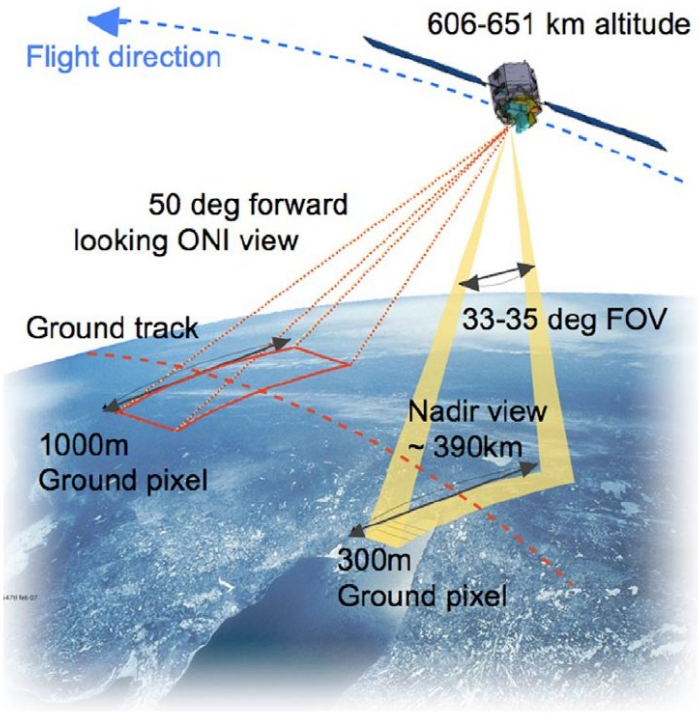

(b) FLEX/FLORIS viewing geometry. FLORIS is a nadir looking imaging spectrometer with high spectral and spatial resolution.

Figure 4.3.3:

Figures 4.3.4a and 4.3.4b show simulated reflectance spectra at the spectral resolution of the radiative transfer simulations (HighRes) and the FLORIS instrument, as well as the GOAL SNR model. Shown are only the oxygen absorption bands. The complete spectral range of FLORIS is $500nm$ to $800nm$.

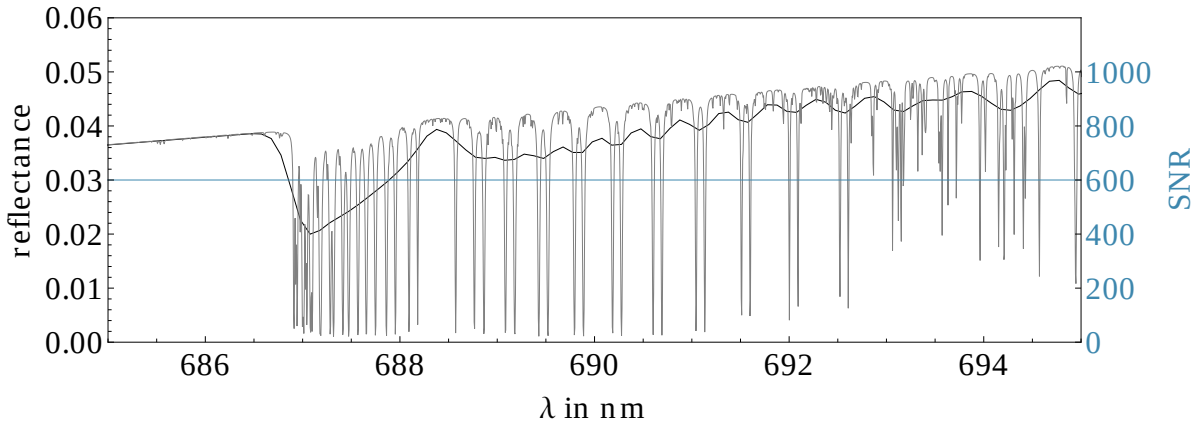

(a) Oxygen B band.

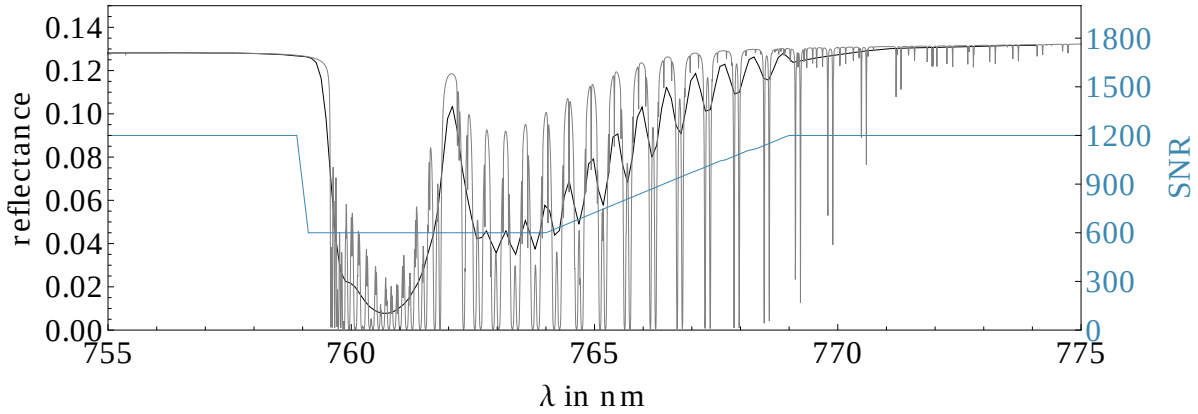

(b) Oxygen A band.

Figure 4.3.4: Example reflectance spectra for the O_2A and O_2B band. The gray line represents the high resolution reflectance spectra from the radiative transfer simulations and the black line represents results for the FLORIS resolution. The blue line shows the SNR of the GOAL model (see also references [153, 159] and Figure 4.3.18).

4.3.5 Forward Modeling

Radiative transfer simulations are used to simulate measurements of a theoretical instrument and for the inversion of the atmospheric state. The setup of the simulations is described in the following subsections. Discussed is the aerosol vertical model, the aerosol optical model, the surface reflectance model, and the radiative transfer scheme.

Aerosol Vertical Model

The radiative transfer model MOMO accepts the aerosol fraction per layer and the total aerosol optical thickness as input. This means that the internal aerosol vertical model has $(n_l-1)+1 = n_l$ degrees of freedom, where n_l is the number of atmospheric layers used for the simulation. This high number of parameters is likely unpractical for an inversion, since the numeric effort increases with the number of free parameters. The number of parameters can be reduced with a vertical distribution model with fewer parameters than n_l, which makes the retrieved profile independent of the internally used number of layers. A reduced number of free parameters can also lead to a more robust inversion and more meaningful physical parameters, such as mean height and width for every retrieved vertical aerosol mode.

The assumption of an exponential, rectangular, or log normal distribution is widely used in

radiative transfer models. To investigate which model is a suitable candidate, CALIOP [129] nighttime aerosol extinction profiles[16] were analyzed and compared with model fits. The used model is defined as:

$$\rho(h) = \sum_{i=1}^{n_a} \frac{\tau_i}{h \log(\sigma_i)} \, \mathrm{e}^{\frac{(\log(h)-\log(h_i))^2}{2\log(\sigma_i)^2}}, \tag{4.3.1}$$

where h is height, n_a is the number of used log normal modes, τ_i the optical thickness of mode i, h_i the mean height of mode i, and σ_i the width of mode i. The data was processed and provided by Florian Filipitsch,[17] Figure 4.3.5 shows an example of a seasonal averaged aerosol extinction profile for the Naples (Italy) area and three attempts to model the data using the sum of one, two, and three log normal functions. Results for the Berlin (Germany) area are shown in Figure 4.3.6. Both results show that a model using a sum of three log normal functions can quite accurately represent the measured structure. The separated bi-modal structure from the Naples example is of course badly represented by the model using only a single log normal function, but this model provides a good representation for the Berlin case. The applied models are only able to represent the main features of the extinction profile. Features on a small scale are not captured, which can be an issue if these type of features are important for the analysis. Using such type of model represents in fact a type of data reduction algorithm, which can simplify the analysis of large data sets. For a small local region, it may be useful to characterize the aerosol vertical structure on vertical small scales, but for regional to global data sets, the smoothed representation by a model provides much easier access to the data.

[16] CALIOP level 2 version 3.01 data from 1. December 2009 to 31. December 2010 was used. Regional and seasonal averages are discussed and shown. [17] *Freie Universität Berlin*, Institute for Space Sciences

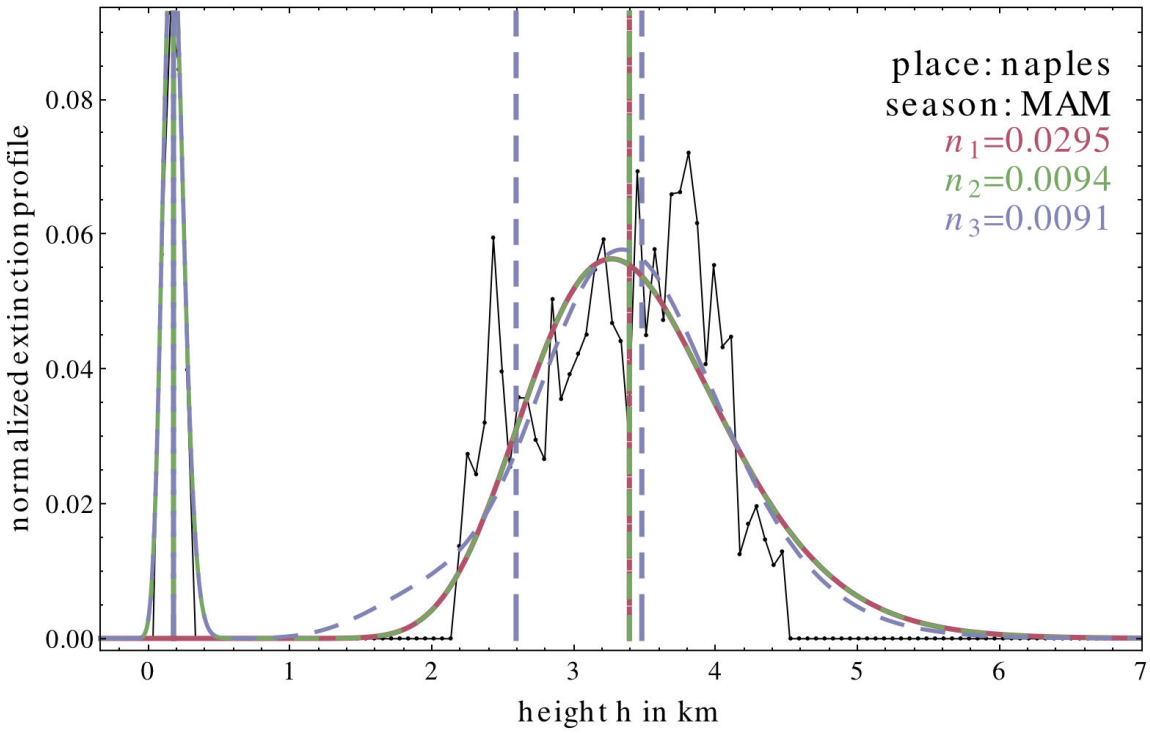

Figure 4.3.5: Seasonal averaged (March, April, and May) vertical aerosol extinction profile (black lines) for the Naples (Italy) area. The red line shows a fit using a single log normal function, the green line a fit using the sum of two log normal functions, and in blue a fit using the sum of three log normal functions. The dashed vertical lines show the position of the detected mean heights. The sums of least squares for each model is shown in the plot legend.

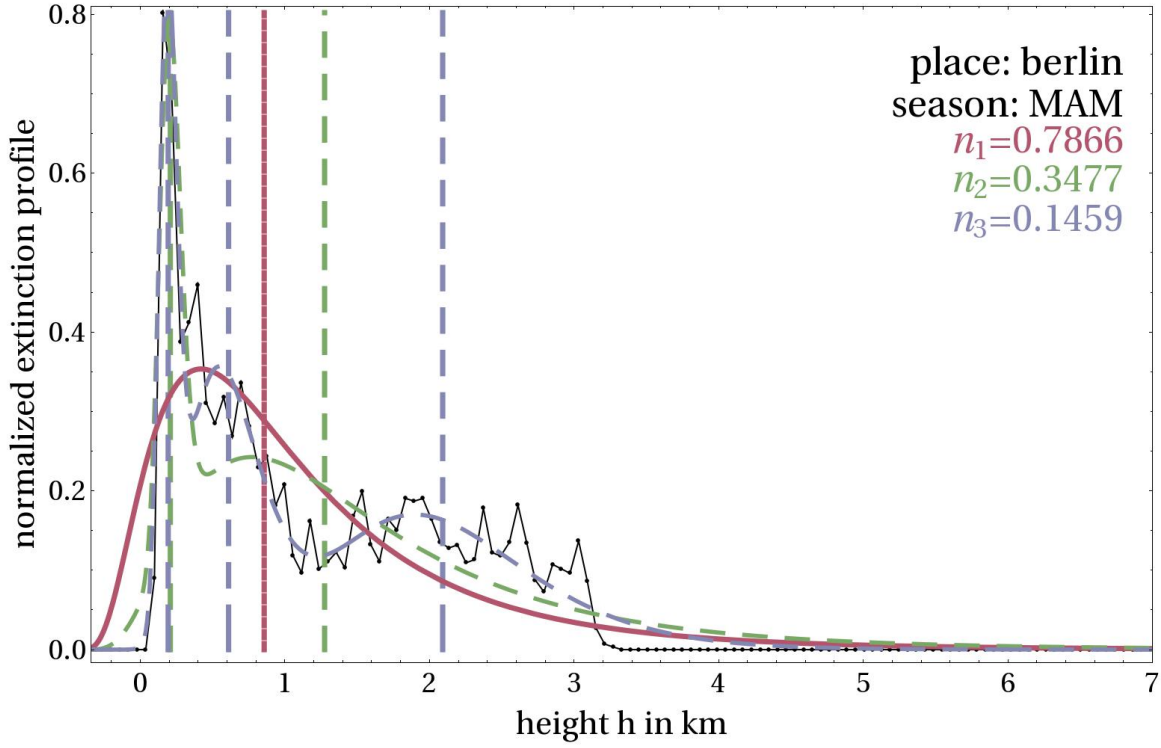

Figure 4.3.6: Same as Figure 4.3.5, but for the Berlin (Germany) area.

An overview about results for the complete data set is shown in Figure 4.3.7. It becomes apparent that a sum of two log normal functions is the best candidate of the three, in terms of accuracy and complexity. In all cases but one, the fit with two log normal functions provides significantly better results than the model using a single log normal function (see caption of Figure 4.3.7). In most cases, the increase to a sum of three log normal functions leads only to a slight increase in the representation of the real profile.

The residuals for the complete data set are slightly higher than the possible optimum, because the normalization parameter τ_i were bound to positive values to represent optical thickness. Allowing negative values could in some cases lead to a better result, but it would be unphysical in the sense of aerosol modes and would not be usable in an RTM.

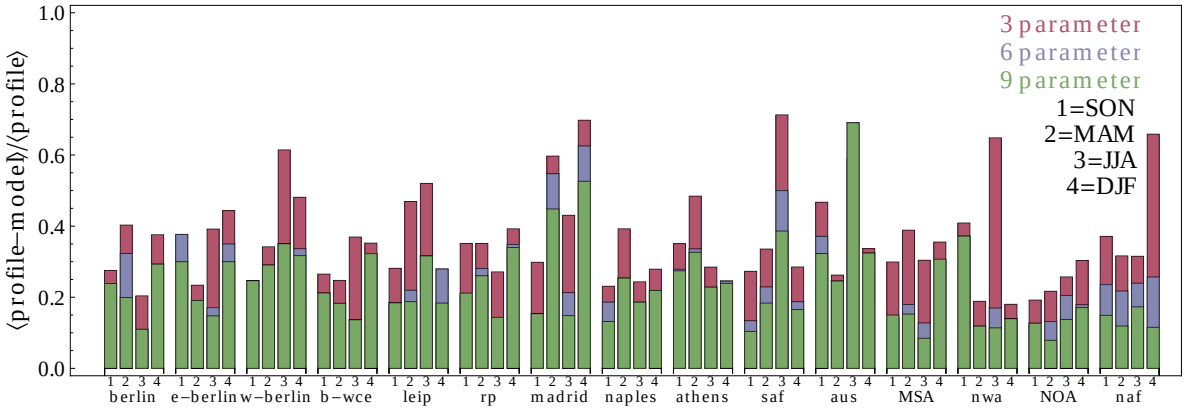

Figure 4.3.7: Overview of best fit results for the complete CALIOP nighttime data set for regional and seasonal means. Shown is the mean of the absolute residuals divided by the mean of the profile to make the numbers comparable. Shown in red are results for a single log normal distribution, in blue for the sum of two log normal distributions, and in green the sum of three log normal distributions. If the parameter increase was not leading to a better result, the result with fewer parameters is used. As a result, if areas with red color are visible, then an increase to two or three log normal distributions was leading to a better result. If blue colored areas are visible, an increase to the sum of three log normal distributions lead to a better result.

The conclusion of the analysis is that a retrieval of a bimodal log normal aerosol model would be a good representation of the true aerosol extinction profile on regional to global scales. Even a single log normal distribution is in many cases able to represent the true aerosol vertical profile reasonably well. This means that at least three parameters (τ_i, h_i, σ_i) for each aerosol mode have to be retrieved from the measurements. This number increases if additional aerosol optical parameters such as aerosol model or single scattering albedo are to be included in the retrieval.

acronym	description	area type
berlin	Berlin (Germany)	urban
b-wce	Greater Berlin area	
leip	Leipzig (Germany)	
rp	Ruhr Valley (Germany)	
madrid	Madrid (Spain)	
naples	Naples (Italy)	coastal
athens	Athens (Greece)	
e-berlin	Eastern Berlin	rural
w-berlin	Western Berlin	
saf	South Africa	
aus	Australia	forest
MSA	Middle Central Africa	
nwa	Northwest Africa	desert
NOA	Northeast Africa	
naf	North Africa	

Table 4.3.2: Acronyms as used in Figure 4.3.7.

Aerosol Optical Model

A continental, maritime, and biomass burning aerosol model based on OPAC [160] data was used within the FLUSS project and was defined by Rasmus Lindstrot. The following discussion is based on results for the continental aerosol, since results for the other models are very similar. Absorption of aerosols was included by modifying the imaginary part of the refractive index using a scaling factor. This approach is likely over simplistic, since the scaling factor only modifies the bulk absorption of the particle and leaves the size distribution unchanged. In a more realistic aerosol model, the parameters' absorption, scattering, and size distribution are not independent and can be constrained (see e.g. reference [161]). A more realistic model could be based on a larger set of models, facilitate the optical thickness as key parameter for other optical properties [162], or use more free parameters (e.g. complex refractive index, its spectral complex slope, and size distribution parameters). Such an elaborate model is beyond the scope of this discussion. However, the simple model includes next to the chosen model itself, the two free parameters' optical depth and single scattering albedo. This, is a good first step without overcomplicating the analysis.

The aerosol single scattering albedo, extinction, and phase function were computed using a Mie code [163]. The resulting single scattering albedo of the aerosol ω_0 was expressed as a function of the scaling parameter that was used as free parameter in the inversion scheme. The conversion model between the scaling factor and ω_0 is based on a fit assuming a quadratic model and is shown in Figure 4.3.8. Shown are fit results for a linear and a quadratic model, using all results (straight lines) and the three points (dashed lines) that are used in the fast model (see Section 4.3.7). The quadratic model works very well and its parameters are almost independent of the chosen data points.

The scaling parameter modifies the scattering and the absorption of the aerosol model. The relative change with respect to a scaling factor of one is shown in Figure 4.3.9. The scaling factor ranges from one to ten, which results in a relative absorption change of 0.5% and a much more pronounced change of 25% for relative scattering. Increasing the scaling factor decreases the single scattering albedo, which is caused by a slight reduction of absorption and a more pronounced reduction of scattering.

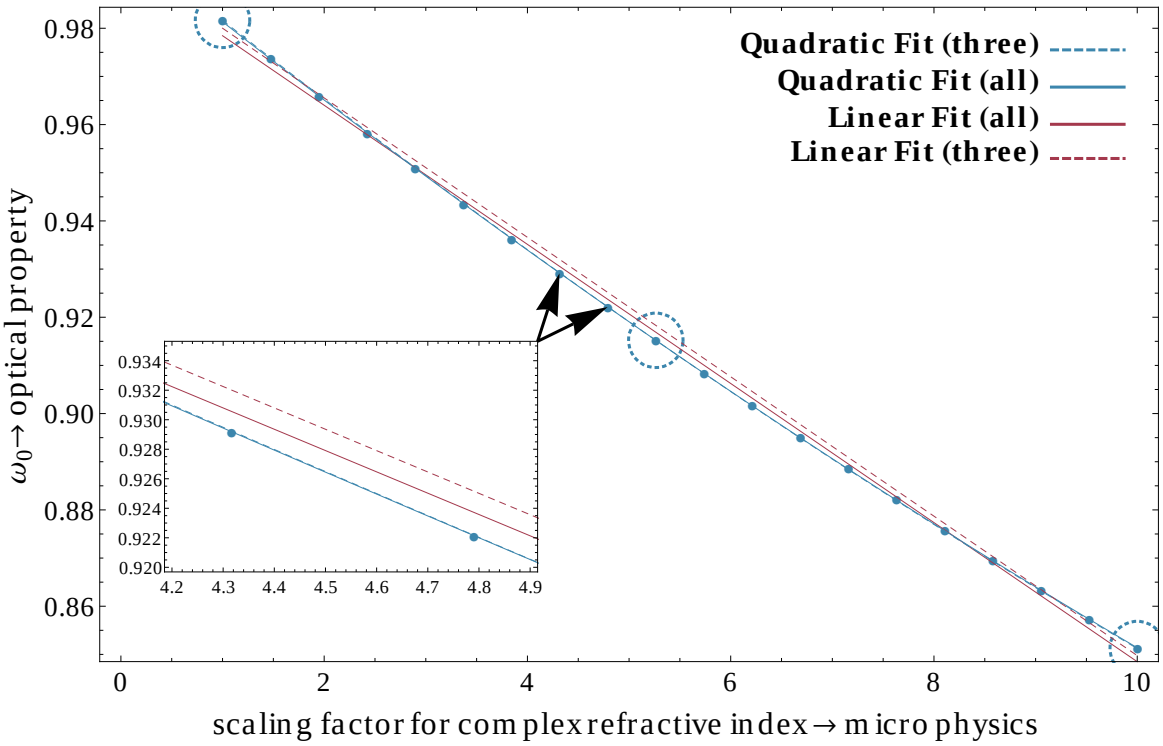

Figure 4.3.8: Aerosol single scattering albedo with respect to the scaling parameter. Blue and red lines show fit results using a linear and a quadratic model. Results where only the three highlighted data points were used are shown with dashed lines.

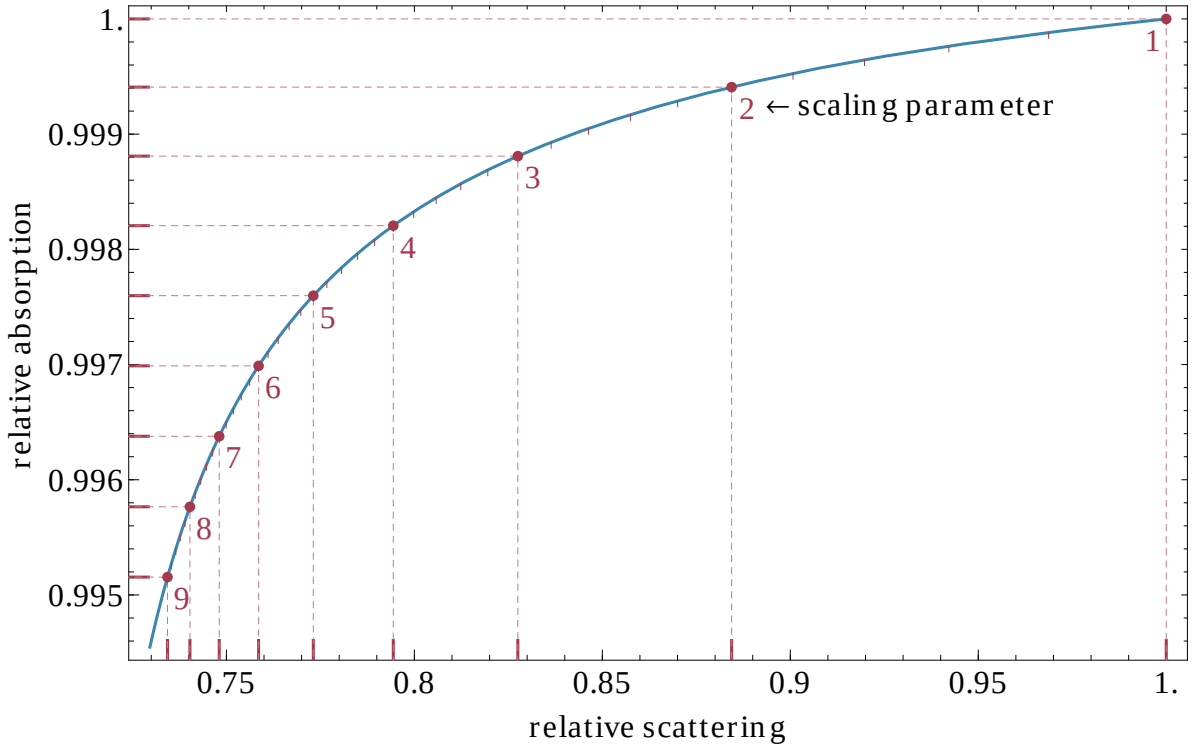

Figure 4.3.9: Aerosol scattering and absorption with respect to the scaling parameter. Both parameters are shown as relative values for a scaling parameter of one, which represents the unmodified OPAC model.

Surface Reflectance Spectrum Model

Among other parameters, the surface reflectance of the scene has to be retrieved as well. In the visible, the surface reflectance spectra are highly correlated. For narrow bands, simple models can be used to represent the surface reflectance spectrum using only a few parameters. An example with spectra for a soil and a vegetation case is shown in Figure 4.3.10. Additional spectra are shown in Figure 4.4.6 on Page 124.

It is sufficient to model the surface reflectance in the O_2A band with a linear model:

$$\alpha_A(\lambda) = a\lambda + b, \quad \alpha_1 = \alpha_A(\lambda_1), \alpha_2 = \alpha_A(\lambda_2), \tag{4.3.2}$$

$$a = \frac{\alpha_1 - \alpha_2}{\lambda_1 - \lambda_2}, \tag{4.3.3}$$

$$b = \frac{\alpha_2\lambda_1 - \alpha_1\lambda_2}{\lambda_1 - \lambda_2}, \tag{4.3.4}$$

where $\lambda_1 = 759nm$ and $\lambda_2 = 780nm$ denote the boundaries of the spectral band and α_1 the reflectivity at λ_1 and α_2 the reflectivity at λ_2. Defining the offset a and slope b this way makes the model slightly more complicated to define, but the parameters α_1 and α_2 represent both reflectivities, share the same unit, and are of similar size. A quadratic model for the O_2B can be set up the same way:

$$\alpha_B(\lambda) = a\lambda + b + c\lambda^2, \quad \alpha_1 = \alpha_B(\lambda_1), \alpha_2 = \alpha_B(\lambda_2), \alpha_3 = \alpha_B(\frac{\lambda_1 + \lambda_2}{2}), \tag{4.3.5}$$

$$a = \frac{\lambda_1(\alpha_1 + 3\alpha_2 - 4\alpha_3) + \lambda_2(3\alpha_1 + \alpha_2 - 4\alpha_3)}{(\lambda_1 - \lambda_2)^2}, \tag{4.3.6}$$

$$b = \frac{\lambda_1\lambda_2(\alpha_1 + \alpha_2 - 4\alpha 3) + \alpha_1\lambda_2^2 + \alpha_2\lambda_1^2}{(\lambda_1 - \lambda_2)^2}, \tag{4.3.7}$$

$$c = \frac{2(\alpha_1 + \alpha_2 - 2\alpha 3)}{(\lambda_1 - \lambda_2)^2}, \tag{4.3.8}$$

$$\tag{4.3.9}$$

where α_3 is the reflectivity in the middle of the band and the notation from Equation 4.3.2 is used. To reduce the numeric burden, a linear model was also used for the O_2B band.

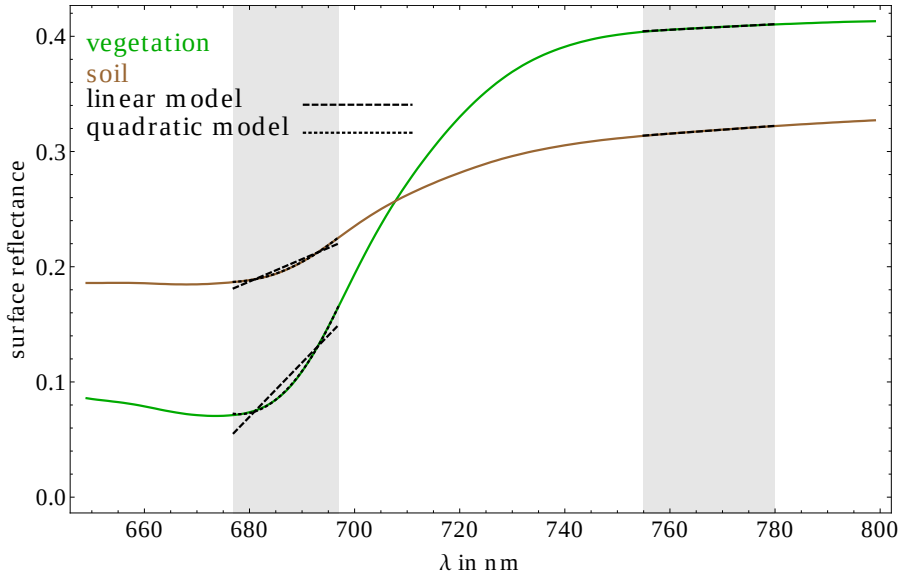

Figure 4.3.10: Spectra of surface reflectivity for bare soil (brown color) and vegetation (green color). The data was provided by ESA's FLUSS project and has been prepared using the SAIL and PROSPECT model [164, 165] (work made by Luis Alonso and Jochem Verelst, Image Processing Laboratory (IPL) Universitat de Valencia, Spain). The O_2A and O_2B bands are marked and the representation using a linear and a quadratic model is shown.

Radiative Transfer Setup

The radiative transfer model MOMO [43, 39, 5] was used to simulate the spectral intervals $650nm - 680nm$ and $760nm - 780nm$ with a spectral resolution and sampling of $0.005nm$. FLORIS spectra were generated by convolving the signal with Gaussian channel response functions. This approach offers great flexibility if the instrument specifications were to be changed, or the inversion scheme should be applied to a different instrument.[18] Two results of the radiative transfer simulations were already shown in Figure 4.3.4. Gaseous absorption due to oxygen and water vapor was treated using a modified k-binning approach [44] and the HITRAN 2008 [114] database.

MOMO itself is a single treated program and was written in the FORTRAN 77/90 language. A single spectrum of the two bands at $0.005nm$ spectral resolution consists of 7244 simulations/MOMO runs. A single FLORIS spectrum consists of 252 channels, which means that 252 convolutions of the used Gaussian response function and the high resolution data have to be calculated. Even for today's modern desktop computers,[19] this poses a large numeric burden. The computing facility at the Institute for Space Sciences is a heterogeneous cluster of standard PCs running different flavors of Linux based operating systems.[20] To use these resources efficiently, a robust forward operator (FO) was implemented in FORTRAN. Its input is the atmospheric state and the result is the simulated spectrum for the complete set of viewing geometries. A sketch of the setup is shown in Figure 4.3.11. The FO runs on a master node, which distributes the work throughout the network. The workload is shared between the nodes so that all nodes should finish after the same run time. The results are transferred via the *ssh* protocol and the protocol overhead is minimized by keeping the ssh connections open, so that the protocol is initialized only once. To make use of today's multi-core CPUs, multiple MOMO instances per node are executed. The parallelization and scheduling is realized using

[18] Which is described in Section 4.4, where the same forward operator was applied to the TANSO-FTS instrument on board the GOSAT satellite. [19] The authors desktop computer is a Intel i7 quad core with 16GB of RAM. [20] Different versions of Fedora, Ubuntu, Open SUSE, CentOS, and Scientific Linux.

the OpenMP [166] standard. The convolution is calculated entirely on the master node, since in principle the complete spectra are needed. This step is also parallelized using OpenMP. The FO is robust against non-responding nodes or network failures. If a node is not responding, it is excluded from the work share and a separate process tries to reestablish the node, so that it can be reintegrated in the set of working nodes.

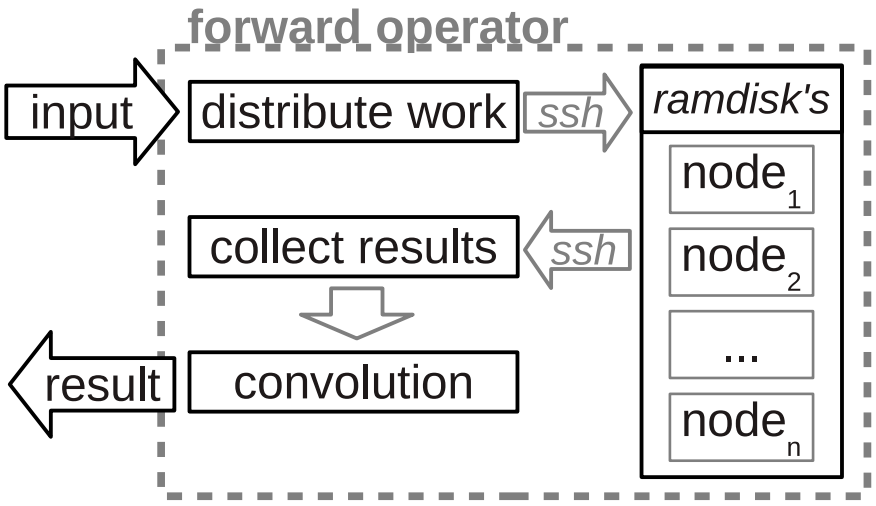

Figure 4.3.11: Operating scheme of the implemented forward operator. Parallelization on each node is realized using the OpenMP standard, which is also used for the convolution step.

Figure 4.3.12 shows scaled Jacobeans for the aerosol width σ, mean height h, and aerosol optical thickness τ for the FLORIS instrument and the initial spectral resolution. The sensitivity of the reflectance with respect to aerosol optical thickness is smaller inside the absorption band than outside. The opposite is true for aerosol mean height and width. For them, almost no sensitivity outside the absorption band is visible.

Figure 4.3.13 shows the resulting reflectance change for a change of aerosol optical thickness τ of 0.05, aerosol mean height h of $100m$, and aerosol width σ of 1 where the Jacobeans from Figure 4.3.12 were used. The reflectivity change with respect to the aerosol vertical distribution is higher in the oxygen A-band than in the B-band, which is due to the stronger absorption in the A-band. In the B-band, the change due to aerosol optical thickness dominates.

Figure 4.3.14 shows how the Jacobeans are related to each other. Shown is the aerosol width Jacobean normalized to its maximum, versus the other three Jacobeans, which are also normalized. The scatter plot of the Jacobeans of width and height shows a clear twofold linear relationship, which is much less pronounced for the intercomparison of the aerosol optical thickness Jacobean. This almost twofold linear relationship shows how closely related both parameters are, and that a retrieval might have difficulties to disentangle both parameters.

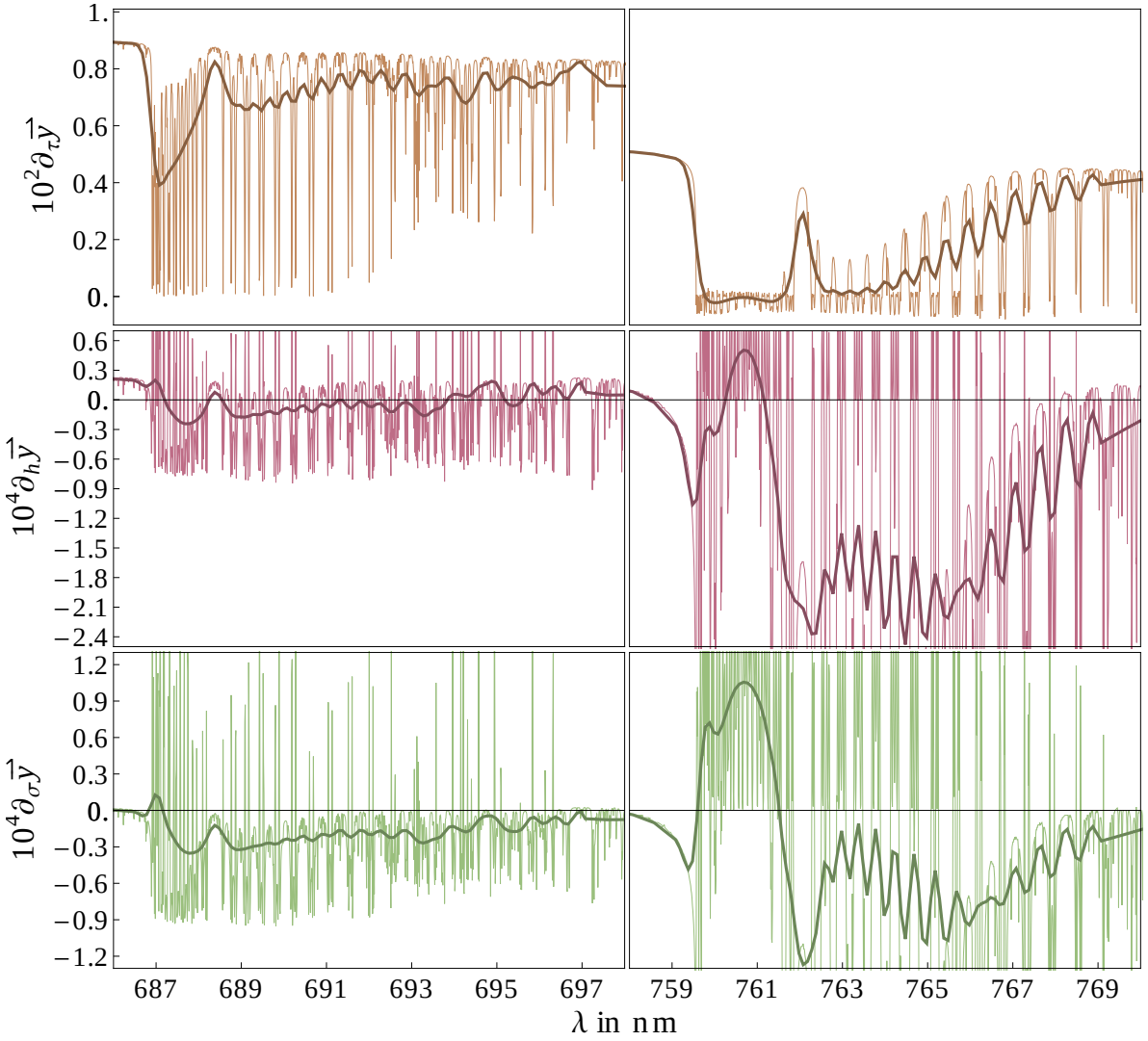

Figure 4.3.12: Jacobeans in the O_2B (left) and O_2A (right) band for aerosol width σ (green, bottom panel), height h (purple, middle panel), and optical thickness τ (orange, top panel). Light colors represent high spectral resolution and the normal color represents FLORIS spectral resolution. The surface reflectivity in the band center is 0.2 for O_2B and 0.4 for the O_2A band.

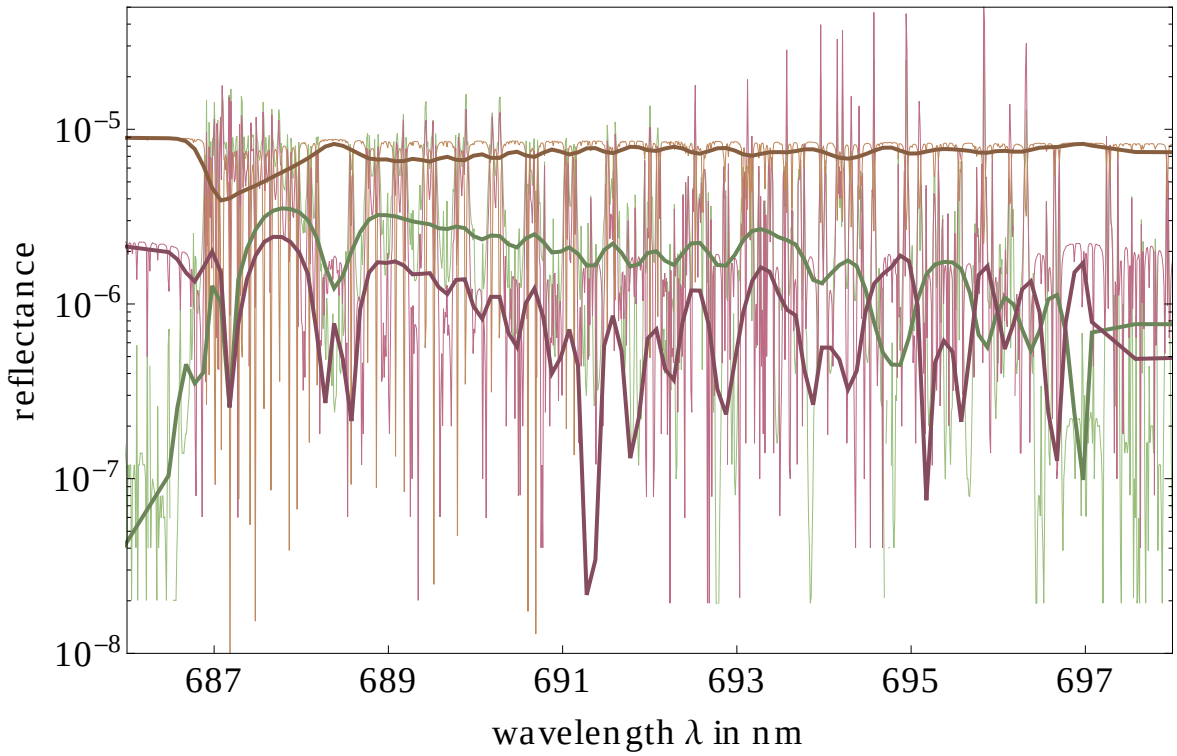

(a) O_2B band.

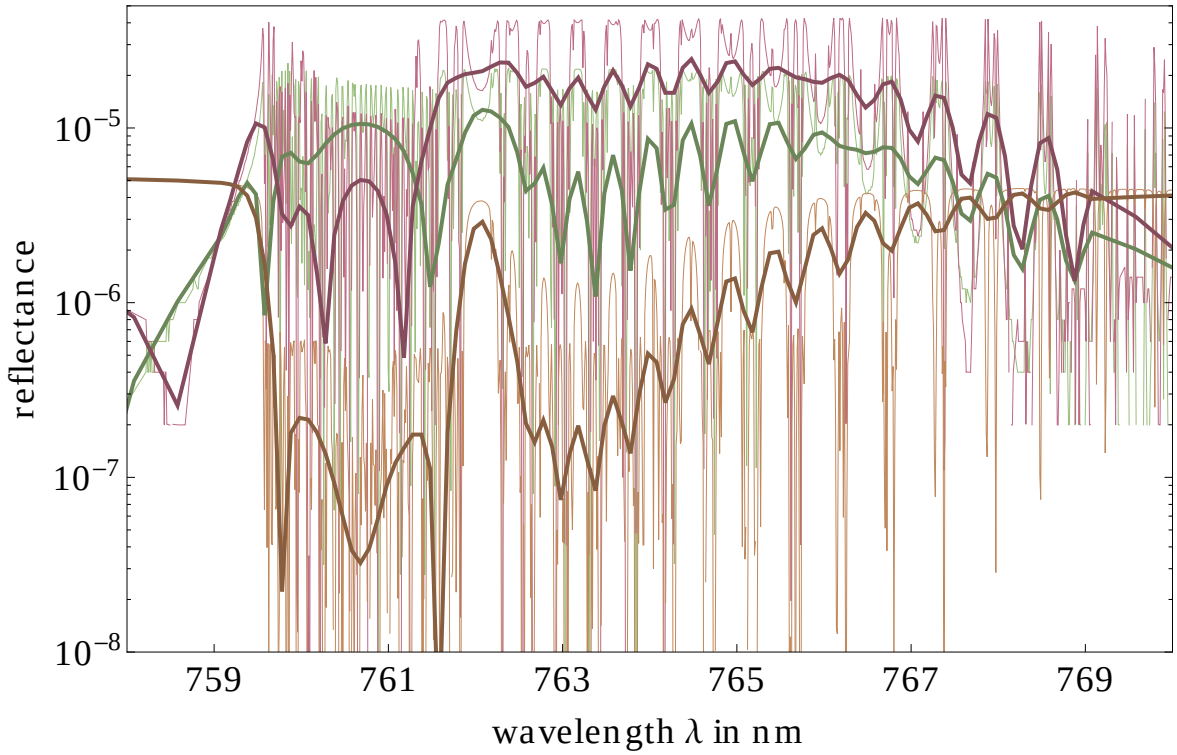

(b) O_2A band.

Figure 4.3.13: Reflectance change for aerosol optical thickness change of 0.05 (orange), height change of $100m$ (purple), and width change of 1 (green). The Jacobeans as shown in Figure 4.3.12 were multiplied with the given parameter change. The same color scheme and parameter values as in Figure 4.3.12 are used.

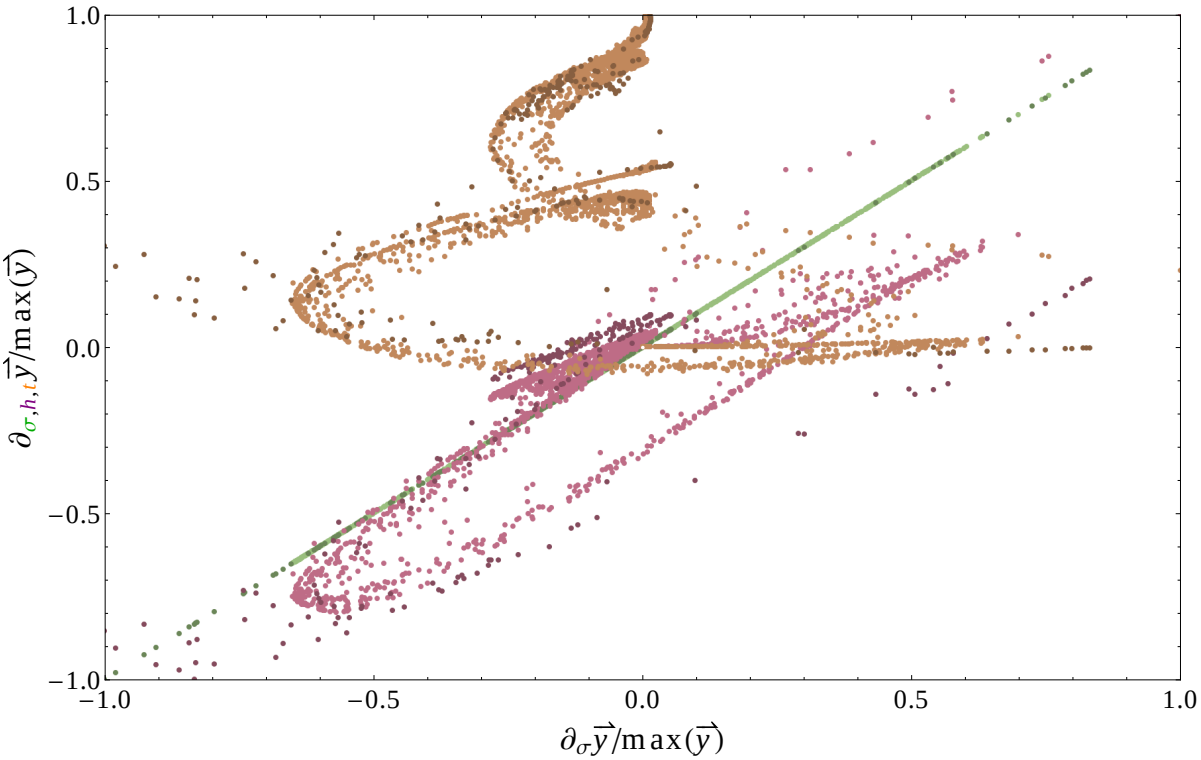

Figure 4.3.14: Jacobeans from Figure 4.3.12 in a scatter plot with respect to the width Jacobean. The Jacobeans are scaled using their mean value and the mean value of the width Jacobean. The same color scheme and parameter values as in Figure 4.3.12 are used.

4.3.6 Rapid Prototyping of the Remote of Sensing Algorithm

A tool for the rapid prototyping of remote sensing algorithms was set up and extensively tested and used. The design of this system allows to start the development of a retrieval scheme without the need of a precomputed lookup table, which may take long time to compute. The guiding principle behind this scheme is based on the assumption that the real forward operator exists, but its run time is too long to use it directly for the inversion. In this application, the run time of a single FO evaluation is approximately $3.5s$ when using 60 cores and would increase if polarization[21] or more zenith angles [22] are used. A commonly used approach to solve this issue is to precalculate tables and use interpolation in the table as forward operator. The defining parameters of this approach are the dimension of the table, the gridding of the table, and the kind of interpolation used in between tabulated grid points. The proposed scheme can be seen as a similar approach, but the way it is implemented guarantees more flexibility. The components of the scheme are shown in Figure 4.3.6.

The FO and its input is denoted with $f(x)$ and the resulting spectrum with $\vec{y}$. The FO results are stored in a local database and restored if a formerly calculated parameter set $\vec{x}$ is called again. The applied fast model is described in the next Section 4.3.7. The only assumption is that the fast model $f_{\sim}(\vec{x})$ is a local model around an area of $\vec{x}$, which is based on a set of FO evaluations and that the area is defined by a given metric function. The set of FO results and supplementary data is stored in a similar database as the FO results. It resides on HDD storage, where storage limitations can be neglected but the trade of is relatively slow data access. The fast model uses a second data layer in the RAM memory of the master node. This

[21] Run time increase with respect to scalar simulations is approximately ×9 for on linear, or ×16 for complete polarization. [22] The total run time scales approximately quadratic with the number of zenith angles.

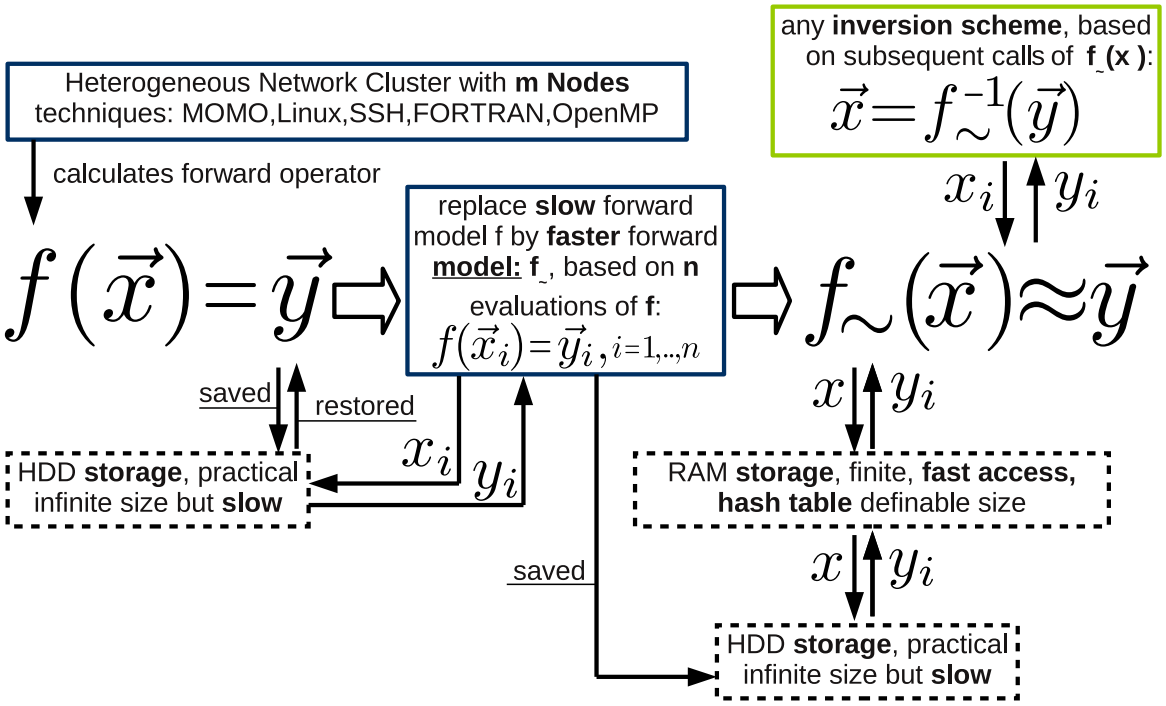

Figure 4.3.15: Operating scheme of the FO approximation scheme. The function f denotes the forward operator, x the state vector, and y the measurement vector. The fast model $f_{\sim}$ is based on precalculated FO evaluations around points x_i. Computed results for both models are stored in a local database and are only computed once.

data layer is implemented as hash table with a definable size. Data that has been loaded from the HDD is stored in this layer and, if needed, read from there. If the storage capacity of the hash table is exceeded, older data is removed to make room for actual data. This intermediate data access layer increases the execution speed of the fast model drastically.

As a result, one can start to test the fast model and the retrieval scheme right away. At the beginning it starts slowly, but when the needed corridor in the input space has been charted by the FO, the inversion becomes reasonably fast. The scheme allows great flexibility. In the early stages of the development, the fast model and the inversion scheme can undergo frequent changes and one gets fast feedback to the changes made. Also, the amount of needed RAM is independent from the size of the table.

4.3.7 Local RT Approximation

The fast radiative transfer is defined as the function $f_{\sim}(\vec{x})$ with $\vec{x}$ as the state vector and the resulting spectrum as $\vec{y}$: $f(\vec{x}) = \vec{y} \approx f_{\sim}(\vec{x})$, where $f(\vec{x})$ is the FO. It is implemented as a local functional expansion scheme:

$$f_{\sim}(\vec{x}) = f(\vec{x}_0) + \sum_{j=1}^{m} \tilde{f}_j(\vec{x}). \tag{4.3.10}$$

The local approximation $f_{\sim}$ is represented by the sum of several functions $\tilde{f}_i$ and f at $\vec{x}_0$. The point $\vec{x}_0$ depends on $\vec{x}$ and is calculated using a gridding function: $\vec{x}_0 = g(\vec{x})$. The definition of the functions $\tilde{f}_j$ is based on a notation of index sets. The state $\vec{x}$ is represented in a basis $\vec{e}_i, i = 1 \ldots p : \vec{x} = \Sigma_{i=1}^{p} x_i \vec{e}_i$. The coefficients e_i are the physical parameters, such as surface pressure or aerosol mean height. All indices are collected in the index set $\tilde{p}$:

$$\tilde{p} = \{1, \ldots, p\} \tag{4.3.11}$$

This set is subdivided into subsets $\tilde{p}_i, i = 1, \ldots, m$, where each index is only member of a single subset: $\tilde{p} = \bigcup\{\tilde{p}_1, \ldots, \tilde{p}_m\}, \quad \tilde{p}_i \bigcap \tilde{p}_j = \emptyset \quad \forall i \neq j$ and $i, j \in \tilde{p}$. The number of elements in a subset is denoted by the norm of this set: $|\tilde{p}_j| = p_j$. The gridding function g determines the resolution of the table and a box type form is used: $g(\vec{x}) = \vec{x}_0^g + \vec{x}_\Delta^g \left\lfloor \frac{\vec{x} - \vec{x}_0^g}{\vec{x}_\Delta^g} \right\rfloor$, where vector division is executed as element wise division and $\lfloor . \rfloor$ denotes the floor function. Values of the offset vector $\vec{x}_0^g$ and interval length vector $\vec{x}_\Delta^g$ are given in Table 4.3.3.

	ρ_{surf}	α_i	τ_j	h_j	σ_j
x_0^g	1008	0.01	0.05	150	1.01
$\vec{x}_\Delta^g$	5	0.2	0.3	300	0.25

Table 4.3.3: Gridding function parameters. All surface reflection parameters α_i share the same settings and are only mentioned once. The same is true for every aerosol mode that is denoted with the index j.

For compact notation: $\vec{e}_{j,i} = \vec{e}_{\{\tilde{p}_j\}_i}$, $\Delta_{j,i} = \vec{x}_\Delta^g \vec{e}_{j,i}$, and $\vec{\Delta}_{j,i} = \Delta_{j,i} \vec{e}_{j,i}$. An analysis of the interpolation error and numeric experiments with a Levenberg-Marquardt inversion scheme lead to a setup of two distinct interpolations methods. Employed are an uncorrelated quadratic (m=1), and linear correlated (m=2) interpolation scheme.

The first model $\tilde{f}_1$ is a quadratic interpolation for the parameters in the set $\tilde{p}_1$: $\tilde{f}_1(\vec{x}) = \sum_{i=1}^{p_1} (\vec{x} - \vec{x}_0) \vec{e}_{1,j} (\alpha_{1,i} + (\vec{x} - \vec{x}_0) \vec{e}_{1,j} \beta_{1,i})$. The coefficients $\alpha_{1,i}$ and $\beta_{1,i}$ are solved for the conditions that $\forall j \in \tilde{p}_1 : \tilde{f}_1(\vec{x}_0 + \vec{\Delta}_{1,j}) - f(\vec{x}_0) = f(\vec{x}_0 + \vec{\Delta}_{1,j})$ and $\tilde{f}_1(\vec{x}_0 + 2\vec{\Delta}_{1,j}) - f(\vec{x}_0) = f(\vec{x}_0 + 2\vec{\Delta}_{1,j})$. These points are located at $\vec{x}_0$ and the half and full distance in each basis direction to the next interpolation cell.

The second model $\tilde{f}_2$ is a coupled linear interpolation for three parameters and is used for the aerosol parameters: τ, h, and σ. The function is defined as: $\tilde{f}_2(\vec{x}) = \sum_{i=1}^{3} (\vec{x} - \vec{x}_0) \vec{e}_{2,i} \alpha_{2,i} + \sum_{i=1}^{3} \prod_{j=i}^{i+1} (\vec{x} - \vec{x}_0) \vec{e}_{2,j} \beta_{2,j} + \prod_{i=1}^{3} (\vec{x} - \vec{x}_0) \vec{e}_{2,i} \gamma_2$, and an index ring is used. When an index is higher than possible for the set, the index overflows and starts from the beginning. The coefficients $\alpha_{2,i}$,$\beta_{2,j}$, and γ_2 are solved using the conditions $\forall j, k \in \tilde{p}_2$:

$$\begin{aligned}
\tilde{f}_2(\vec{x}_0 + \vec{\Delta}_{2,j}) - f(\vec{x}_0) &= f(\vec{x}_0 + \vec{\Delta}_{2,j}), \\
j \neq k : \tilde{f}_2(\vec{x}_0 + \vec{\Delta}_{2,j} + \vec{\Delta}_{2,k}) - f(\vec{x}_0) &= f(\vec{x}_0 + \vec{\Delta}_{2,j} + \vec{\Delta}_{2,k}), \\
\tilde{f}_2(\vec{x}_0 + \sum_{i=1}^{p_j} \vec{\Delta}_{2,1}) - f(\vec{x}_0) &= f(\vec{x}_0 + \sum_{i=1}^{p_j} \vec{\Delta}_{2,1}).
\end{aligned}$$

This model is the most complex of the two interpolation methods used. It reduces the interpolation error, but more importantly it streamlines the inversion. The cost function (l_2 norm) variation is rather weak (see Figure 4.3.19 and the discussion in the section) and for a purely uncoupled interpolation an inversion attempt may converge at steps. The effect of coupled and uncoupled interpolation is shown in Figure 4.3.16. The variation of the fast FO for aerosol height and width are shown in the left Panel 4.3.16a, while the same result for a coupled interpolation is shown in the right Panel 4.3.16b. Clearly visible are the various points $\vec{x}_0$ and the range of each interpolation cell. The uncoupled (linear interpolation) approach shows kinks and steps as one would expect. The coupled approach (f_2, Figure 4.3.16b) is much smoother.

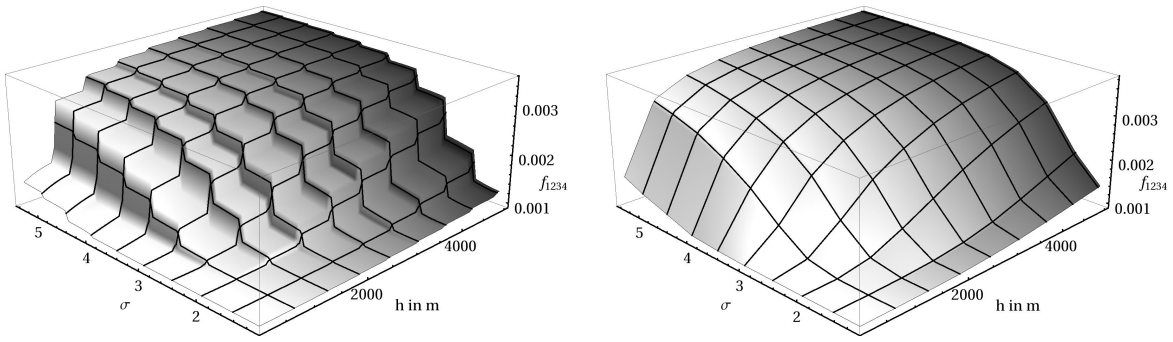

(a) No parameter coupling. Uncoupled linear expansion.

(b) Linear coupling of aerosol optical thickness, height and width.

Figure 4.3.16: Results for channel 1234 with respect to aerosol width and height.

Higher order coupled interpolation is also possible, but not necessary for this application. This approach is a mixed approach of coupled and uncoupled, linear and quadratic interpolation. It reflects results from numeric experiments in which the interpolation error was minimized, while also trying to keep the numeric effort as small as possible.

4.3.8 Definition of Test Cases

A number of representative test scenarios is used to discuss the result of the retrieval algorithm. The vertical distribution is based on the log normal distribution that was defined in Equation 4.3.1 on Page 88. Figure 4.3.17a shows the definition of six vertical distributions, which consists of three localized and three less-localized distributions. Two typical test cases of bimodal vertical distributions were selected and are shown in Figure 4.3.17b. These were inspired by the analysis discussed in Section 4.3.5. One profile consists of the sum of two log normal distributions and a scaling factor n_r, which defines the normalization ratio between the two. Scaling factors of 2 and 0.5 are considered, so that an optically thicker mode is placed above and below the thinner mode.

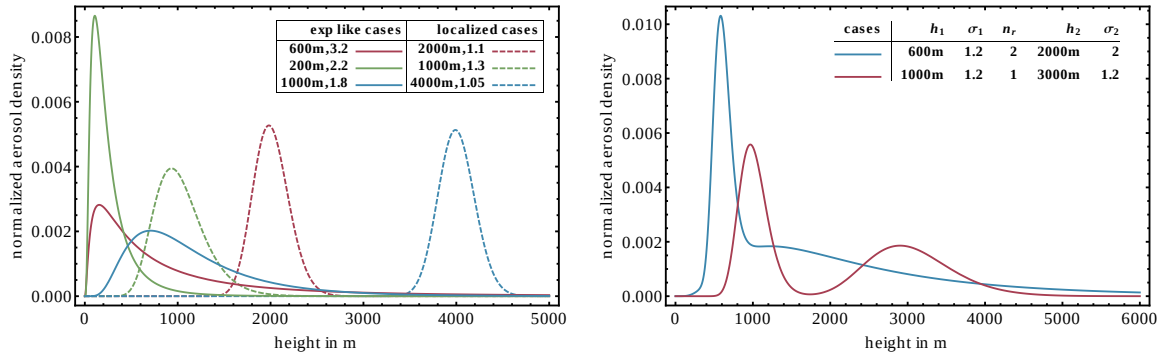

(a) Selected vertical aerosol distribution test cases. Three localized and three distributed test cases.

(b) Selected test cases for a bimodal aerosol vertical distribution.

Figure 4.3.17: Aerosol vertical distribution test cases.

The surface reflectivities as shown in Figure 4.3.10 on Page 94 are representative spectra for a surface with vegetation and soil and are used as test case. For both cases, the reflectivity in the O_2B band is significantly lower than in the O_2A band. The figure shows that the surface reflectance in the O_2A can be accurately modeled by using a linear model, but that for the O_2B band a quadratic model would be the significantly better option. Further analysis was

performed using a linear surface reflectivity model, which should be sufficient to asses the potential benefit of including the O_2B band.

The SNR of the final instrument depends on many factors. Several synthetic SNR spectra were defined within the FLUSS project to model possible scenarios and are shown in Figure 4.3.18. For one of the two ongoing FLEX industry studies, a more realistic SNR model, which is close to the GOAL model, became available at the end of this study [153].

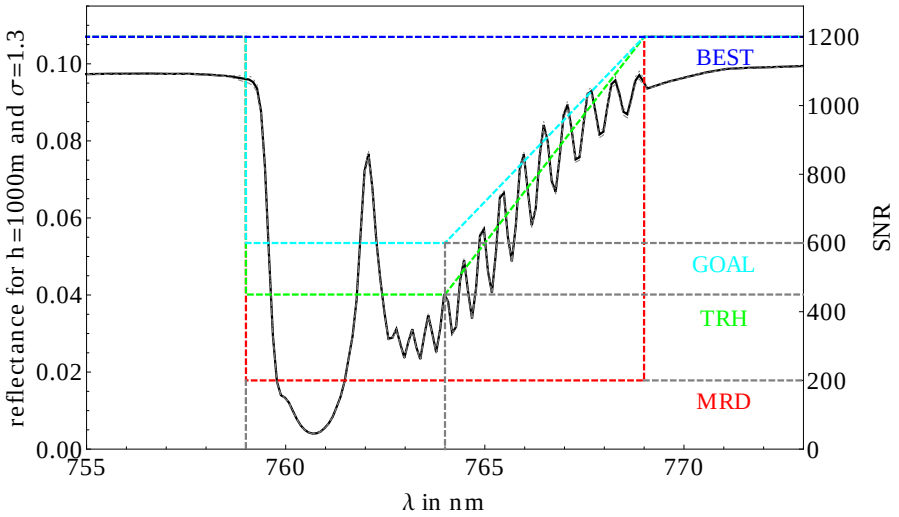

Figure 4.3.18: Signal to noise ratio definitions for FLORIS instrument in the O_2A band.

4.3.9 Inversion Algorithm

The inversion is approached as minimization problem of a multidimensional cost function $\delta(\vec{x})$ for the state vector $\vec{x}$. The l_2 norm of a simulated measurement and the forward operator result $f_{\sim}(\vec{x})$ was chosen as cost function. Figure 4.3.19a shows the cost function with respect to aerosol mean height and width for a true height of $2000m$ and a width of 1.2. No pronounced minimum is visible. The cost function steeply increases for increasing mean height h and aerosol width σ, but not so for decreasing values. A pronounced minimum is only visible in the logarithmic plot, which is shown in Figure 4.3.19b. Both Figures show that the sensitivity of the measurement with respect to aerosol vertical distribution, which is expressed by the cost function, is weak.

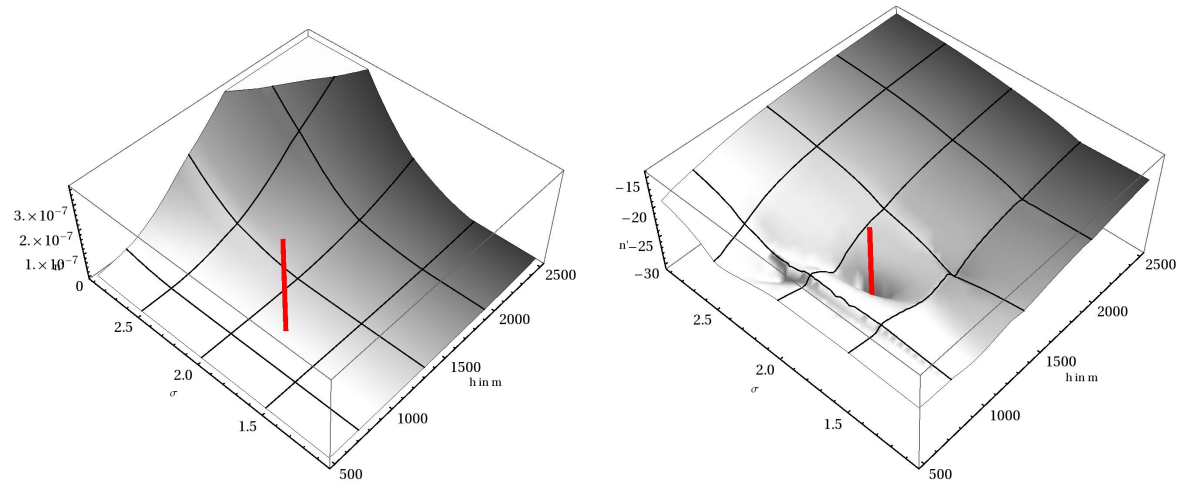

(a) Cost function value.

(b) Logarithm of the cost function.

Figure 4.3.19: Cost function with respect to aerosol mean height and aerosol width. Truth values are $2000m$ for height and 1.2 for width and are marked with a red line. A pronounced minimum is only visible in the right panel, which shows the logarithm of the cost function for the same case.

Prior knowledge and its uncertainty is used in many remote sensing problems to constrain the solution and to modify the cost function using the optimal estimation technique [30]. This approach would not add much value for the vertical distribution retrieval, since there is no suitable prior information for the aerosol vertical distribution available. It can be used for the parameters surface pressure ρ, surface reflectance α, and aerosol optical thickness τ, since for those parameters prior knowledge is in general available.

It is however not used here, since their retrieval poses not the main difficulty. Instead, an inversion space constraint of 10% on τ and α is used. For surface pressure, a uncertainty of $\pm 1hPa$ is assumed. This is justified, since the FLEX mission is planned to fly in tandem with Sentinel 3 [167, 100], so that remote sensing products from OLCI and SLSTR can be used as prior information for FLEX. Those two instruments are the successors of ENVISATS's MERIS and AATSR instruments and should deliver aerosol optical depth with uncertainties below 15% [168, 169, 170, 171]. Prior information about surface pressure can be used from numerical weather prediction (NWP) models such as ECMWF [172] and digital elevation models (DEM) [173]. Their accuracy can be expected to be in the order of $\pm 1hPa$ [174, 175].

Minimization of the cost function is performed using the Levenberg-Marquardt (LM) minimization scheme [176] and an implementation in IDL [112]. The algorithm needs a starting point and iterates from there until it converges or the maximum of allowed iterations is reached. Each iteration is based on the local linearized problem using its Jacobean matrix and a damping factor, which is its main difference from the Gauss-Newton algorithm. Convergence of the algorithm is not guaranteed if the starting point is too far away from the truth. Neither guaranteed is the convergence to the global minimum, so that local minima can lead to inversion errors. Advantages of the algorithm are its speed and its robustness.

Figure 4.3.20a shows results (green points) of a number of inversion runs with randomly selected starting values (red dots) using the LM algorithm. Both points are connected by a gray line. If the norm of the result lies below a certain threshold, orange color is used. The cost function is drawn in the background of the figure. The figure shows that the final result of a inversion attempt strongly depends on the starting value and that local minima exist that can lead to inversion biases.

The lesson that can be learned from Figure 4.3.20a is that good starting values are needed

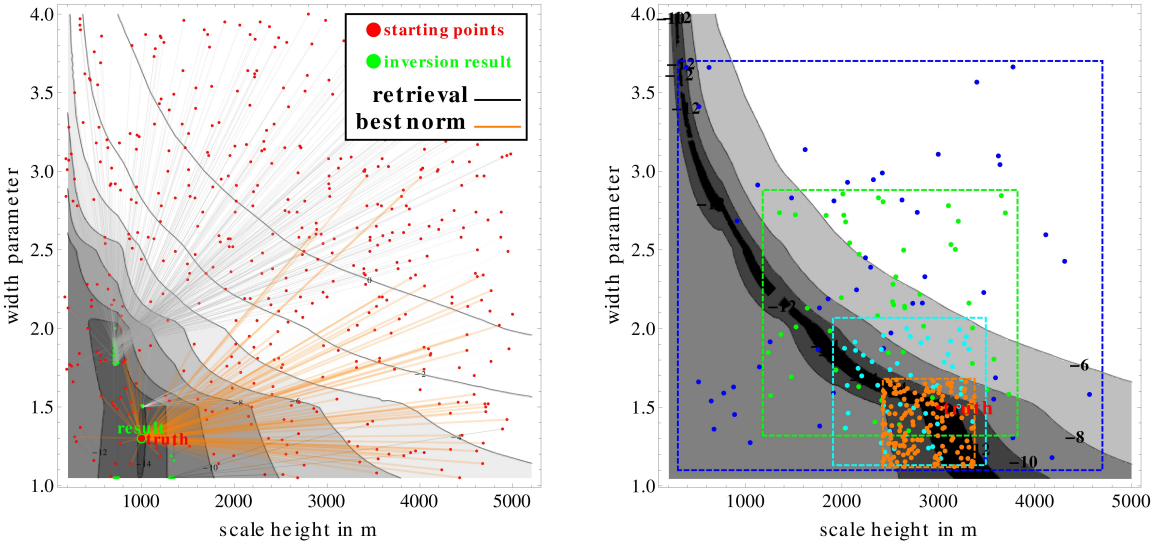

(a) Inversion results (green) and their initial value (red) with respect to aerosol mean height and width. Several local minima lead to a convergence bias from the true value. The orange line indicates results that converged close to the true value.

(b) Monte Carlo approach as provider for suitable starting values. A number of n_{mc} randomly selected points within the search region is tested for their norm. The best candidate is the new center of a shrunk search region and the procedure starts over and is repeated n_s times.

Figure 4.3.20: Monte Carlo Approach of the retrieval algorithm. The background of both panels show the logarithm of the cost function for the marked truth.

and that convergence to local minima can cause errors. This issue was approached by using a simple and fixed step Monte Carlo approach as provider for suitable starting values. In each step, the fast FO is called n_{MC} times with randomly selected values within the given search region. The point with the smallest norm is used as the new center of a shrunk search region. The reduction is implemented by using a scaling factor of 0.6 on each parameter range. This procedure is repeated n_s times and the best candidate is used as starting value for the LM algorithm. This can be repeated and the best result is returned as result. The algorithm is robust and delivers reliable results. Its run time is likely not fast enough to be applied to large data sets. However, run time was not the driving factor. For a theoretical study it is more important that the inversion is good and reliable, so that uncertainties are due to the problem itself and not due to the inversion algorithm.

The aerosol optical depth and the surface reflectance are the most important background parameters for a successful retrieval of the aerosol vertical distribution. The optical depth generates the signal for the vertical distribution in the first place. The surface reflectivity and its spectral behavior is the other main source of TOA radiation. Figure 4.3.21 shows the cost function for a localized aerosol distribution case for two aerosol optical thicknesses of 0.3 and 0.1 and surface reflectance of 0.4 and 0.2 in the middle of the O_2A band. The minimum is most pronounced for the case of high aerosol optical thickness and low surface reflectance. Increasing surface reflectivity leads to more pronounced ambiguity in the width parameter (compare Figure 4.3.21b with 4.3.21a). With decreasing aerosol optical thickness the minimum becomes broader and takes the form of a valley. The behavior is likely caused by the almost linear relationship of the width and height Jacobean, which was shown in Figure 4.3.14 on Page 98.

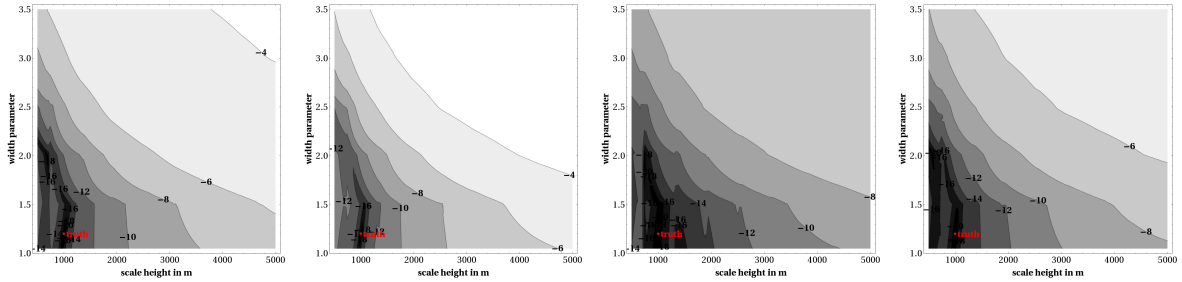

(a) $\tau = 0.3$ $\alpha \approx 0.4$ (b) $\tau = 0.3$ $\alpha \approx 0.2$ (c) $\tau = 0.1$ $\alpha \approx 0.4$ (d) $\tau = 0.1$ $\alpha \approx 0.2$

Figure 4.3.21: Cost function for a localized aerosol distribution case and varying aerosol optical thicknesses and surface reflectance for the O_2A band.

Instrument noise is a key parameter that will affect the inversion scheme. Figure 4.3.22 shows the cost function for continental aerosol with aerosol optical thickness $\tau = 0.1$ and surface reflectivity in the O_2A band of $\alpha = 0.4$. The cost function minimum is most pronounced in the error free case and with increasing SNR the minimum becomes broader and less pronounced. This effect will effectively limit the success of the inversion scheme. Figure 4.3.22d is for the MRD noise level and shows that there is almost no contrast left around the truth value. The situation slightly improves when the TRH noise level (Figure 4.3.22c) is used, but still the area around the truth is of poor contrast.

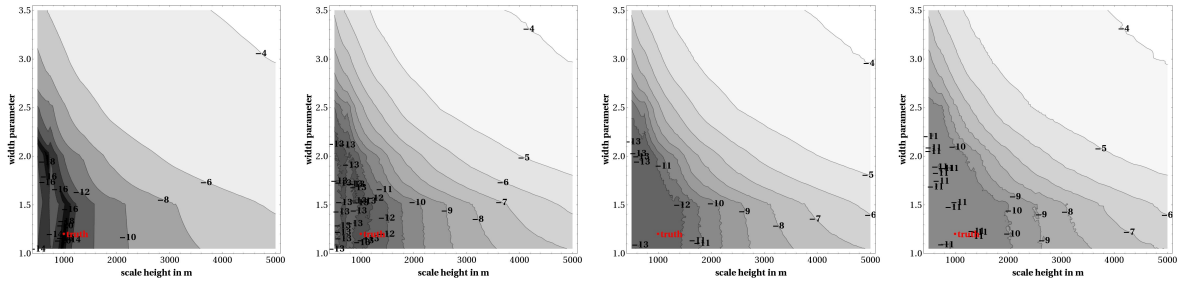

(a) Error free (b) GOAL (c) TRH (d) MRD

Figure 4.3.22: Cost function for the different levels of SNR for the FLORIS type spectra as shown in Figure 4.3.18.

4.3.10 Retrieval Results

One can expect that the success of a retrieval of aerosol vertical distribution not only depends on aerosol optical thickness, but also on the distribution itself and external parameters such as surface reflectance. The sensitivity of the measurement with respect to aerosol height will decrease with decreasing aerosol optical thickness since the total signal caused by the aerosol becomes smaller. Figure 4.3.23 shows retrieval results for the FLORIS and HighRes cases for two aerosol optical thicknesses. The HighRes case is defined by the spectral resolution and sampling of the underlying radiative transfer simulations. It can be seen as proxy for the amount of retrieval accuracy that is lost by reducing the spectral resolution to the FLORIS definition. Figure 4.3.23a shows results for a case with aerosol optical thickness of 0.1 and Figure 4.3.23b for an increase to 0.3. In fact, both values are realistic and not on the high side of possible scenarios. As shown in Figure 4.3.36c on Page 117, which shows a yearly mean of aerosol optical thickness on a global map, average values are in the order of 0.1, while much higher values can be seen for Sahara dust outbreaks or the densely populated areas of India

and China. The detailed picture is of course much more complicated since the variation of the aerosol model itself is not discussed here.

Both figures show that the retrieval using the HighRes data yields much better results in terms of error and bias. The biases are likely caused by the similarities of the parameter Jacobeans as shown in Figure 4.3.14 on Page 98. Most HighRes cases are retrieved very well. Error and bias increase slightly for lower aerosol mean height and decrease slightly with increasing aerosol optical thickness. The FLORIS retrieval for low aerosol optical thickness shows large errors for mean aerosol height and width. The results are right, in that the true value for all cases lies within the uncertainty, but have failed in the sense that the different test cases become indistinguishable. Such errors would only allow to distinguish between high and low, and localized and distributed aerosol vertical distributions, which still is, of course, valuable information. The case with higher aerosol optical thickness shows a clear decrease of the retrieval error and more test cases become distinguishable. One can expect that for higher aerosol optical thickness the error will become smaller.

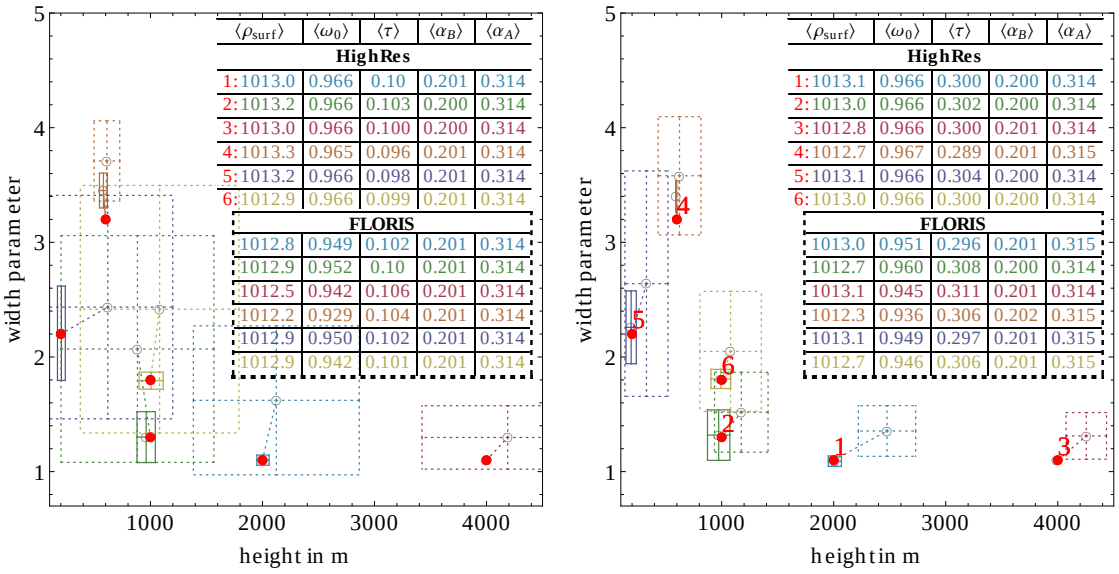

	$\langle\rho_{surf}\rangle$	$\langle\omega_0\rangle$	$\langle\tau\rangle$	$\langle\alpha_B\rangle$	$\langle\alpha_A\rangle$
HighRes					
1:	1013.0	0.966	0.10	0.201	0.314
2:	1013.2	0.966	0.103	0.200	0.314
3:	1013.0	0.966	0.100	0.200	0.314
4:	1013.3	0.965	0.096	0.201	0.314
5:	1013.2	0.966	0.098	0.201	0.314
6:	1012.9	0.966	0.099	0.201	0.314
FLORIS					
	1012.8	0.949	0.102	0.201	0.314
	1012.9	0.952	0.10	0.201	0.314
	1012.5	0.942	0.106	0.201	0.314
	1012.2	0.929	0.104	0.201	0.314
	1012.9	0.950	0.102	0.201	0.314
	1012.9	0.942	0.101	0.201	0.314

(a) Aerosol optical thickness τ of 0.1.

	$\langle\rho_{surf}\rangle$	$\langle\omega_0\rangle$	$\langle\tau\rangle$	$\langle\alpha_B\rangle$	$\langle\alpha_A\rangle$
HighRes					
1:	1013.1	0.966	0.300	0.200	0.314
2:	1013.0	0.966	0.302	0.200	0.314
3:	1012.8	0.966	0.300	0.201	0.314
4:	1012.7	0.967	0.289	0.201	0.315
5:	1013.1	0.966	0.304	0.200	0.314
6:	1013.0	0.966	0.300	0.200	0.314
FLORIS					
	1013.0	0.951	0.296	0.201	0.315
	1012.7	0.960	0.308	0.200	0.314
	1013.1	0.945	0.311	0.201	0.314
	1012.3	0.936	0.306	0.202	0.315
	1013.1	0.949	0.297	0.201	0.315
	1012.7	0.946	0.306	0.201	0.315

(b) Aerosol optical thickness τ of 0.3.

Figure 4.3.23: Inversion results for aerosol vertical distribution for the HighRes and FLORIS cases using the GOAL SNR model. Red dots show the true mean height and width of the aerosol. Circles and error boxes show the retrieval result and error. Straight lines show results for the HighRes case and dashed lines show results for the FLORIS case. Tables in both figures show results for the background parameters surface pressure ρ_{surf}, aerosol single scattering albedo ω_0, aerosol optical thickness τ, and surface reflectivity in both bands: α_B and α_A. Both reflectances values show the mean value of the two underlying reflectance parameters at the band borders and represent the reflectance value in the middle of the band.

Figure 4.3.24 and Figure 4.3.25 show how the retrieval error was computed and how successful the inversion was for each case. Every result and error box was computed using the mean and the standard deviation of 50 inversion attempts, each with different random multiplicative noise according to the GOAL SNR model. This is an experimental propagation of the instrument noise to the inversion error. A standard *1-sigma* filter with respect to the retrieved aerosol optical thickness was applied to filter outliers. Both figures show histograms of the mean height and width for the HighRes- and FLORIS cases, which was shown in Figure 4.3.23b. First of all, the histograms show that the resulting probability density functions (PDF) for mean height and width are non-Gaussian, which means that the mean value of the results

may not represent the true expectation value of the PDF. Since the PDF is unknown, using the mean value is a good guess. The same reasoning is true for all other retrieved parameters.

The PDFs for the HighRes results are in general more narrow and centered closer to the truth than the FLORIS results. Even for the HighRes results outliers and biases for the width parameters are visible. The results are in general worse for the set of FLORIS results. This is not surprising, since the shown inversion results are characterized by non-negligible biases and errors.

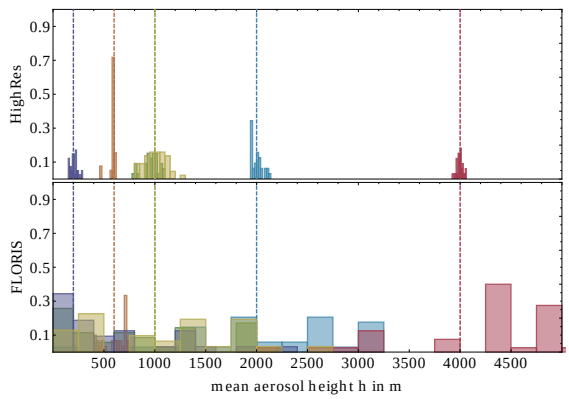

(a) Aerosol mean height. The top panel shows results for the HighRes case and the bottom panel for the FLORIS case.

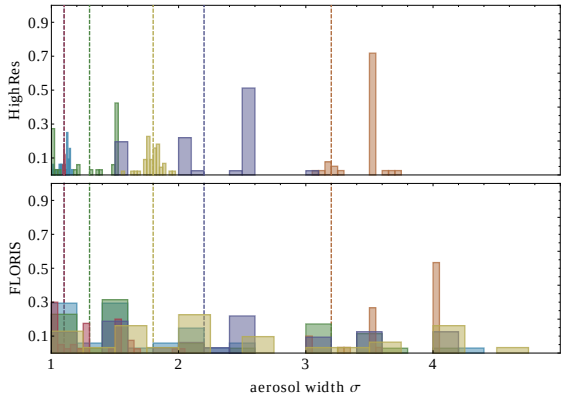

(b) Aerosol width. The top panel shows results for the HighRes case and the bottom panel for the FLORIS case.

Figure 4.3.24: Histogram for aerosol mean height and width for the HighRes and FLORIS results as shown in Figure 4.3.23b. Each result and error box was calculated using the mean value and standard deviation of 50 inversion results with different random multiplicative noise as defined by the GOAL SNR model. The same color scheme as in Figure 4.3.23b is used.

Figure 4.3.25 shows histograms of the ratio of the norm of the inversion result and the norm of the truth. The inversion tries to minimize the norm of the forward simulation and a simulated measurement. In general, the global minimum is not known, since the measurement is affected by noise. A retrieval is a success if the residuals are smaller than the error of the measurements. In this synthetic retrieval, the random error is known and the norm of the truth, with and without error, can be calculated. This is a proxy for the lower bound of the norm. This value was not used in the inversion, since it is unknown for real cases, but can be used here to discuss the performance of the inversion algorithm. Values below one indicate that the found norm is larger than the norm caused by the error alone. Values higher than one imply that the found norm is even smaller than the norm caused by the error, which can be called *overfitting*. This effect occurs only for the HighRes case. The figure shows that the inversion performs better for the HighRes case, since the histograms are very narrow and closely centered at one. In the FLORIS case, the algorithm in general converges to a norm that is within 5% of the norm caused entirely by noise.

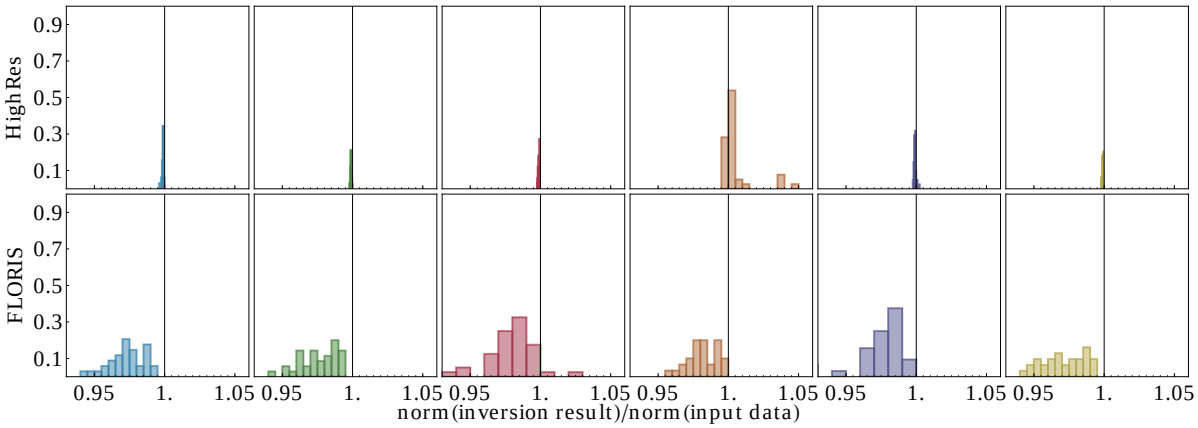

Figure 4.3.25: Histograms of the ratio of the norm of the inversion result and the norm of the truth. The top panels show results for the HighRes case and the bottom panel for the FLORIS case. The same color scheme as in Figure 4.3.23b is used.

Figure 4.3.26a shows a comparison of inversion results for a soil-like and a vegetation-like surface reflectance spectrum. The vegetation case is brighter in the O_2B band and darker in the O_2A band compared to the soil case. Although rather small, some differences are visible. This means that for both surface types a similar inversion error can be expected.

The shown inversion results were using both oxygen absorption bands, and Figure 4.3.26b shows results where only the O_2A band was used. For most cases, the inversion result is slightly better with reduced bias and error, but there is no drastic improvement when using both bands. The improvements are higher for aerosol nodes closer to the surface where the error and bias is largest. The results are not a clear argument for using both bands. The retrieval shows slightly better results, but at least three more free parameters must be considered for the inversion. Also, the aerosol optical model must be suitable to reproduce aerosol optical properties consistently for both bands. One could either introduce additional parameters, or let the inversion choose different optical thicknesses for both bands. Either way, the inversion becomes more complicated, since additional parameters need to be retrieved. The possible gains are slightly smaller errors for aerosols located closer to the surface.

The aerosol single scattering albedo ω_0 as a free parameter in the inversion and Figure 4.3.27a shows inversion results for two different values of ω_0. The results are very similar for both cases. The table inside the figure shows that the inversion was able to retrieve the parameter with an accuracy of approximately 3%, which means that both cases could be very well distinguished. Although the inversion of the aerosol vertical profile shows minor differences, the general retrieval performance has not changed much. These results show that additional aerosol microphysical parameters are accessible for this type of retrieval.

Figure 4.3.27b shows a comparison of an inversion with fixed and free parameter ω_0. The results with fixed ω_0 are slightly better, especially those for the higher aerosol. The main result of this exercise is that additional aerosol microphysical parameters can be retrieved without compromising the retrieval of the aerosol vertical structure. The converse argument is that the true optical aerosol model can be retrieved together with its vertical structure and must not be known in advance.

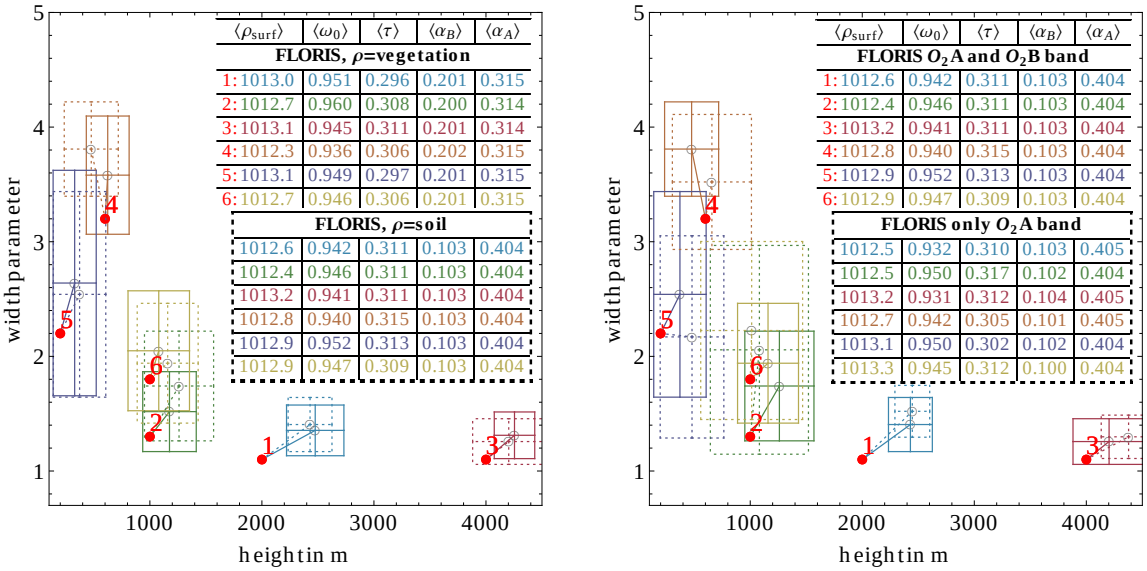

(a) Comparison of FLORIS inversion results for a vegetation- and soil-like surface reflectance.

(b) Comparison of FLORIS inversion results when using only the O_2A band or both bands.

Figure 4.3.26:

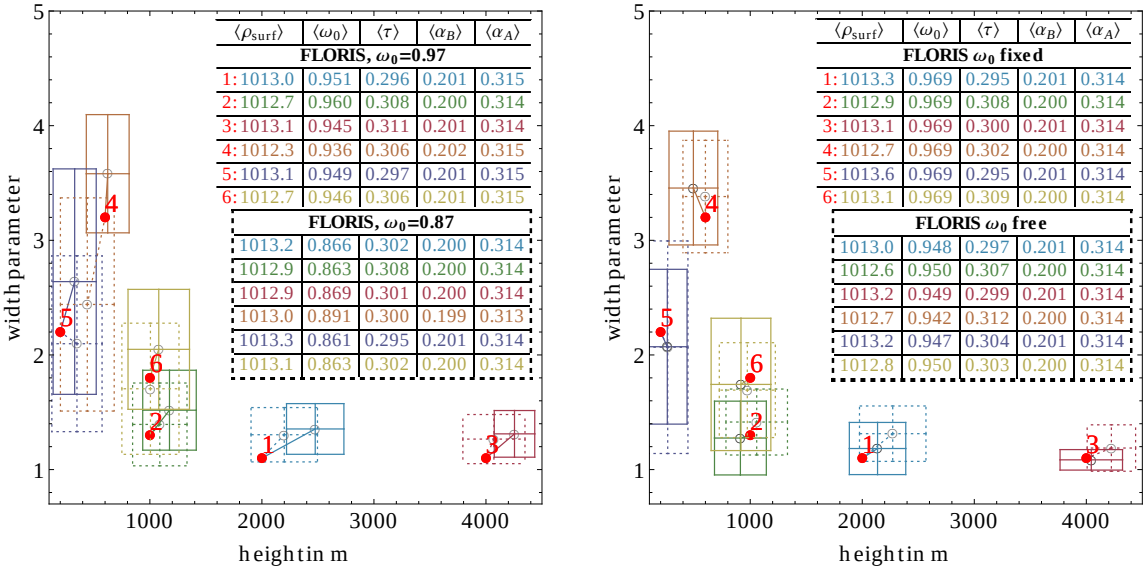

(a) Comparison of FLORIS results for two different values of aerosol single scattering albedo.

(b) Comparison of FLORIS results for a inversion with fixed and free aerosol single scattering albedo.

Figure 4.3.27:

Monomodal Inversion with Bimodal Truth

The analysis from Section 4.3.5 showed that a bimodal model is a good choice for an aerosol vertical distribution model if small scale aerosol features can be neglected. Shown in the previous section were results where the truth and the inversion scheme used the same aerosol vertical profile. This implies that the inversion has the chance to perfectly reproduce the simulated measurement with residuals smaller or equal than the measurement error. In a real world application, the underlying vertical aerosol distribution is very likely not part of the inversion scheme. Shown in this section are the effects if the true vertical profile is bimodal, but the inversion includes only a monomodal distribution. The bimodal test cases as shown in Figure 4.3.17b on Page 101 are used to asses the results of a monomodal retrieval.

Figure 4.3.28 shows results for two cases with $n_r = 2$, which means that the optically thicker aerosol mode is placed above the thinner mode. In both cases, the inversion result is placed between the two real modes and the retrieval error is in the same order as discussed in the previous section. This result shows that the result of a monomodal inversion scheme represents a intermediate aerosol height and width of the true distribution.

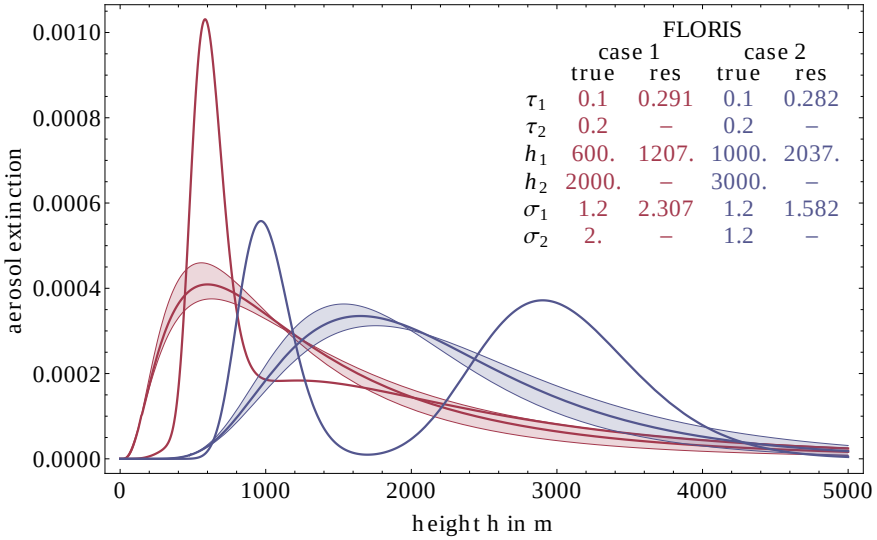

Figure 4.3.28: Monomodal inversion result for a bimodal true aerosol vertical profile using the TRH SNR model. The shaded area shows the variability of the result with respect the the error of mean aerosol height and width. The table in the top right corner shows the input data and the retrieval result.

Surface Inhomogeneities

In a single run of the radiative transfer simulation a homogeneous surface is assumed. Whether this assumption is valid for a measurement depends on the ground size of the footprint of a measurement and the observed area itself. The reflectivity for typical surfaces can vary on almost any scale from cm to km, while the typical spatial resolution of spaceborne remote sensing instruments is in the order of $100m$ to many km. As an example, the MERIS instrument provides data with $250m$ spacial sampling, the TANSO-FTS instrument on board GOSAT has a footprint of $10km$, the FLORIS instrument is planned to have a spatial sampling of $300m \times 300m$, while CarbonSat will have a spatial resolution of $2km \times 2km$. Figure 4.3.29 demonstrates the effects of spatial sampling for FLORIS and CarbonSat. Panel (a) shows a MERIS full resolution scene, which is a good proxy for FLEX, and Panel (b) shows the same scene, but with spatial resolution reduced to $2km$ as it is the case for CarbonSat. The general

features of both scenes are similar, but much detail is lost in the reduced resolution scene. Panels (c) and (d) show the surface homogeneity on both scales. The fraction of homogeneous pixels is smaller for the reduced resolution. Also, areas are marked as homogeneous, which are clearly not in the high resolution image (e.g. lower left corner). This example just shows that it is difficult to asses the true homogeneity of a scene without using external data sources. This can be assessed using external surface reflectance data such as ALBEDOMAP from MERIS [125] or MODIS products [177, 178].

(a) MERIS full resolution image from the O_2A channel with $250m$ spatial resolution.

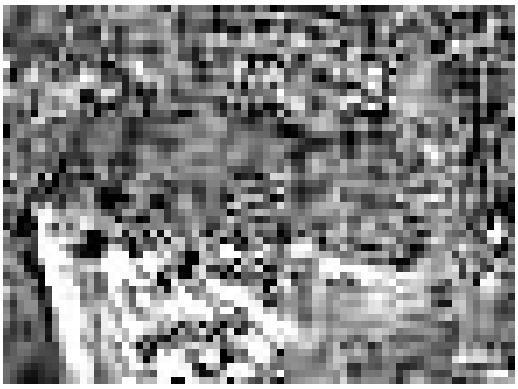

(b) Same scene as in panel (a), but with spatial resolution reduced to 2km.

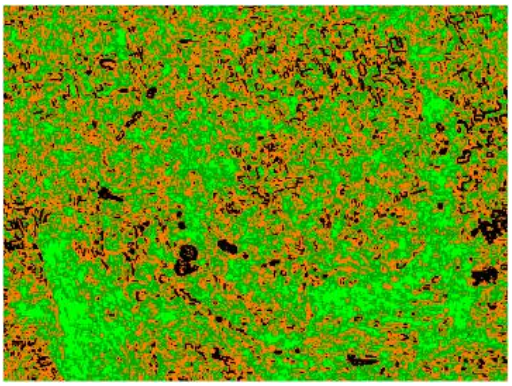

(c) Same scene as in Panel (a) but shown is the surface homogeneity. Colors indicate that the ratio of the standard deviation and mean value δ_h of the reflectance of a pixel and its 8 neighbors: $0<\delta_h<0.05$, $0.05<\delta_h<0.1$, $0.1<\delta_h<0.2$, and $0.2<\delta_h$

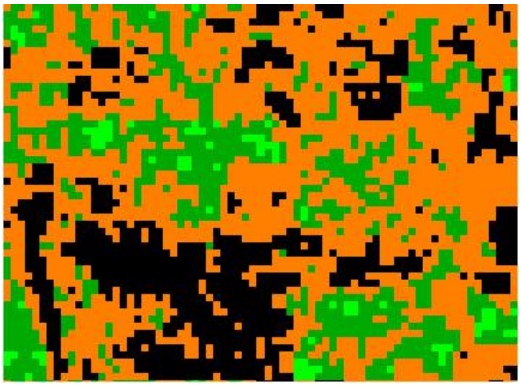

(d) Same scene as shown in Panel (c), but with a reduced spatial resolution of $2km$. The same color scale as in Panel (c) is used. The lower left corner of this panel shows much higher homogeneity than Panel (c).

Figure 4.3.29: Random MERIS image from south Russia, near the city of Stavropol.

If the observed scene contains a mixture of different surfaces, which are not taken into account by the inversion, the inverted surface reflectance can only represent an average surface reflectance. A possible realization of a mixed scene is the weighted average of independent simulations. Figure 4.3.30 shows the effects on the retrieval if the simulated measurement is the mean value of simulations made for the soil and vegetation case. Figure 4.3.30a shows results for the HighRes case and Figure 4.3.30b for the FLORIS case. In the HighRes case, effect of surface homogeneity leads to a strong increase of biases and a medium increase of the inversion error. A similar, but more pronounced effect is visible in the FLORIS case. A conclusion of this numeric experiment is that surface inhomogeneities can introduce additional biases and errors to the inversion.

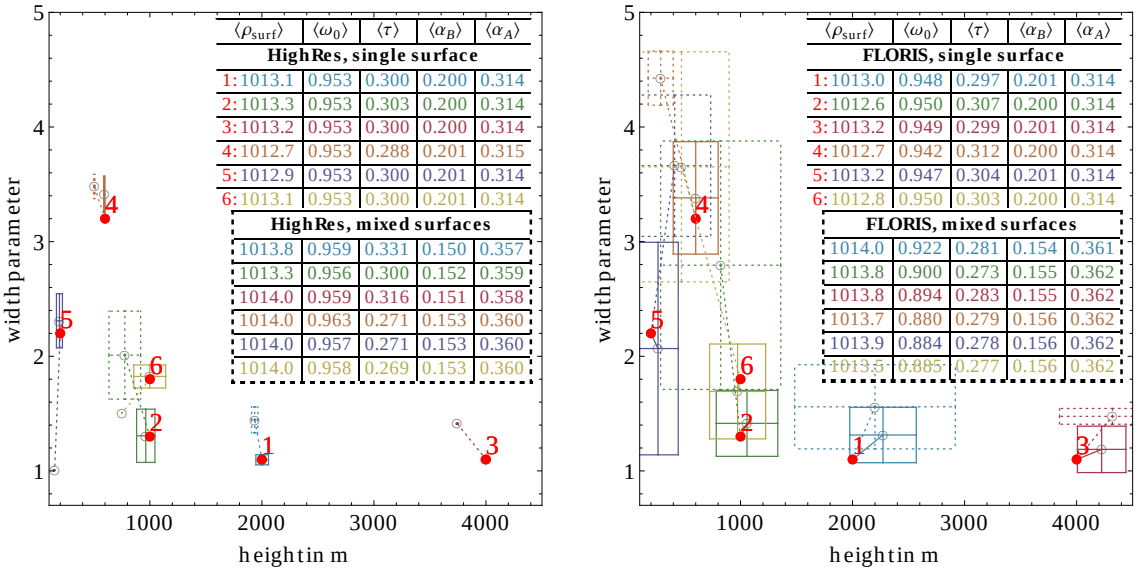

$\langle\rho_{surf}\rangle$	$\langle\omega_0\rangle$	$\langle\tau\rangle$	$\langle\alpha_B\rangle$	$\langle\alpha_A\rangle$
HighRes, single surface				
1: 1013.1	0.953	0.300	0.200	0.314
2: 1013.3	0.953	0.303	0.200	0.314
3: 1013.2	0.953	0.300	0.200	0.314
4: 1012.7	0.953	0.288	0.201	0.315
5: 1012.9	0.953	0.300	0.201	0.314
6: 1013.1	0.953	0.300	0.201	0.314
HighRes, mixed surfaces				
1013.8	0.959	0.331	0.150	0.357
1013.3	0.956	0.300	0.152	0.359
1014.0	0.959	0.316	0.151	0.358
1014.0	0.963	0.271	0.153	0.360
1014.0	0.957	0.271	0.153	0.360
1014.0	0.958	0.269	0.153	0.360

(a) HighRes case.

$\langle\rho_{surf}\rangle$	$\langle\omega_0\rangle$	$\langle\tau\rangle$	$\langle\alpha_B\rangle$	$\langle\alpha_A\rangle$
FLORIS, single surface				
1: 1013.0	0.948	0.297	0.201	0.314
2: 1012.6	0.950	0.307	0.200	0.314
3: 1013.2	0.949	0.299	0.201	0.314
4: 1012.7	0.942	0.312	0.200	0.314
5: 1013.2	0.947	0.304	0.201	0.314
6: 1012.8	0.950	0.303	0.200	0.314
FLORIS, mixed surfaces				
1014.0	0.922	0.281	0.154	0.361
1013.8	0.900	0.273	0.155	0.362
1013.8	0.894	0.283	0.155	0.362
1013.7	0.880	0.279	0.156	0.362
1013.9	0.884	0.278	0.156	0.362
1013.5	0.885	0.277	0.156	0.362

(b) FLORIS case.

Figure 4.3.30: Comparison of a standard inversion for the vegetation type surface reflectance case (straight lines) and a inversion where the simulated measurement was the mean value of simulations for both surface types (dashed lines).

4.3.11 Neglecting Polarization in the Radiative Transfer

The scalar radiative transfer approximation can lead to errors for simulated radiances of several percent, depending on scene and viewing geometry. Figure 4.3.31a shows a spectrum of relative deviations in the O_2A band for an exemplary case. The relative error varies strongly with the reflectance spectrum and is similar to the surface reflectance and the oxygen absorption spectrum. The error is below 1%, which for this scene holds also for other viewing geometries. Figure 4.3.31b shows absolute differences in the spectrum for simulations with and without polarization. The differences are compared with those caused by a small change of the aerosol vertical distribution. Both vertical distributions have a mean height of $600m$, but have different widths of 3.2 and 4.2. The effect of changing the aerosol width is about five times as large as the effect caused by neglecting polarization.

Figure 4.3.32 shows the effects on the inversion if polarization is neglected in the radiative transfer. Inversion results are shown for the regular case where the inversion as well as the simulation of the measurements are based on scalar radiative transfer. These results are compared with results where the simulated measurement was simulated including polarization, but where the inversion was based on scalar radiative transfer. Figure 4.3.32a shows results for the vegetation type surface spectra and Figure 4.3.32b shows results for the soil-like spectra. For both cases, errors and biases increase slightly, which is more pronounced for the vegetation type surface reflectance.

The results of this numeric experiment are unclear. Neglecting polarization can introduce additional biases and errors, but on the other hand simplifies the radiative transport simulations, since they need much less computation time. With unlimited resources available, polarization should clearly be included. If only limited resources are available, the tradeoff made for the inclusion must be carefully analyzed.

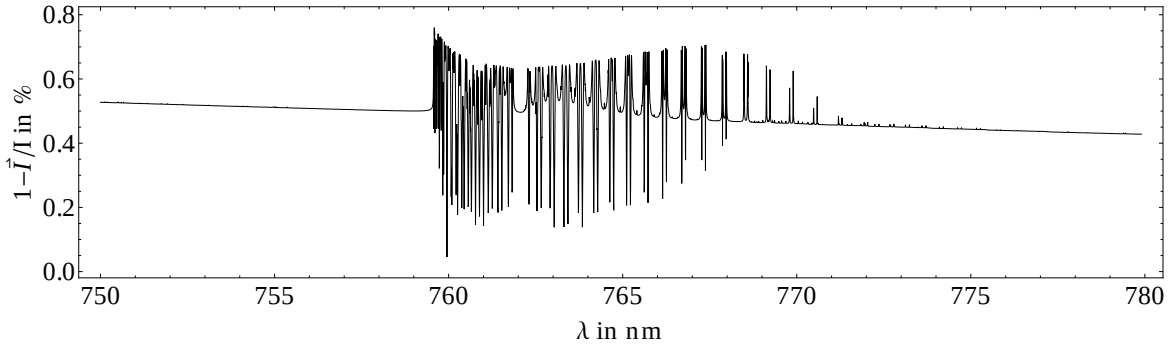

(a) Relative polarization error for the exemplary reflectance spectra. The error follows the oxygen absorption spectrum, the surface reflectance spectrum, and the aerosol optical thickness spectrum. It varies strongly between 0% and 0.7%.

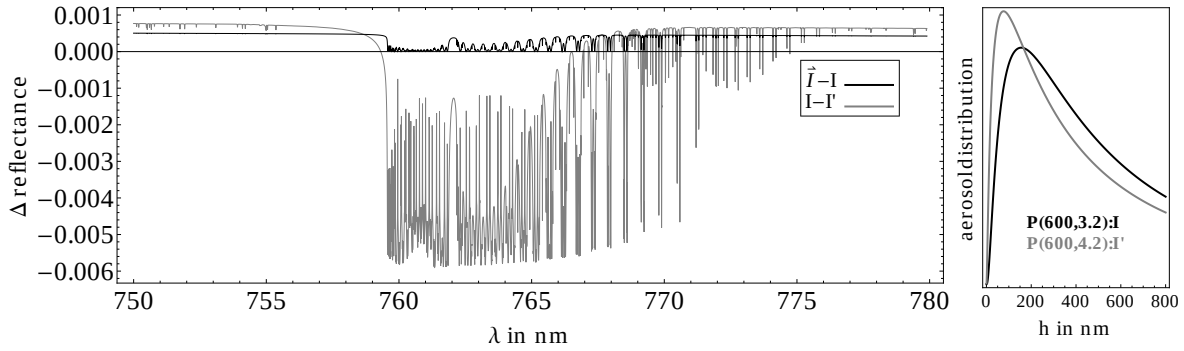

(b) The black line shows the reflectance error caused by the scalar radiative transfer approximation. The gray line shows the deviation caused by a small change in the aerosol vertical profile as shown in the small subfigure.

Figure 4.3.31:

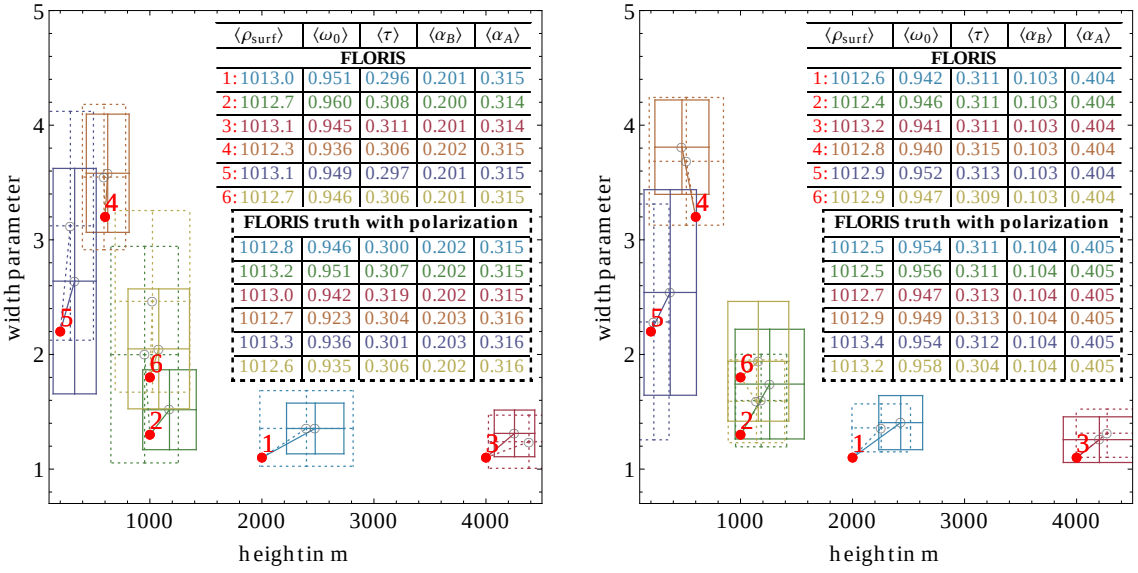

(a) Vegetation type surface reflection case.

(b) Soil type surface reflection case.

Figure 4.3.32: Comparison of the effects caused by neglecting polarization in the radiative transfer. Straight lines show the regular case, where the inversion and the simulation of a measurement are both based on scalar radiative transfer. The dashes lines show inversion results where the simulated measurements was simulated using vector radiative transfer.

Bimodal Inversion

It was shown in Section 4.3.5 that a bimodal aerosol vertical distribution is the best candidate to model the real aerosol distribution on regional to global scales. The discussion in the previous sections was centered at various aspects of a retrieval using a monomodal inversion. Figures 4.3.33 and 4.3.34 show inversion results for the bimodal test cases, which were defined in Section 4.3.8 on Page 101. The test case from Figure 4.3.33 is characterized by a localized mode close to the surface and a more distributed mode further up. In the case where the optically thicker mode is placed above the thinner mode (see Figure 4.3.33a) the inversion was able to reproduce the general features of the scene, although with large error and bias for the width parameter. This quite successful retrieval breaks down if the optically thicker mode is placed below the optically thinner mode. However, this behavior is not systematic. Figure 4.3.34 shows results for the same setup as Figure 4.3.33, but this time both aerosol modes are of the localized type. In both shown cases, the retrieval error and bias is so large that the two modes become indistinguishable.

This inversion scheme is more demanding than the previously discussed scheme, since three additional parameters need to be retrieved. With the FLORIS specifications, it seem quite unlikely that a successful retrieval of two aerosol modes is feasible. A conclusion is that an inversion attempt using FLORIS data should use a single aerosol mode only. As a result, one might be able to only retrieve the total aerosol mean height and width.

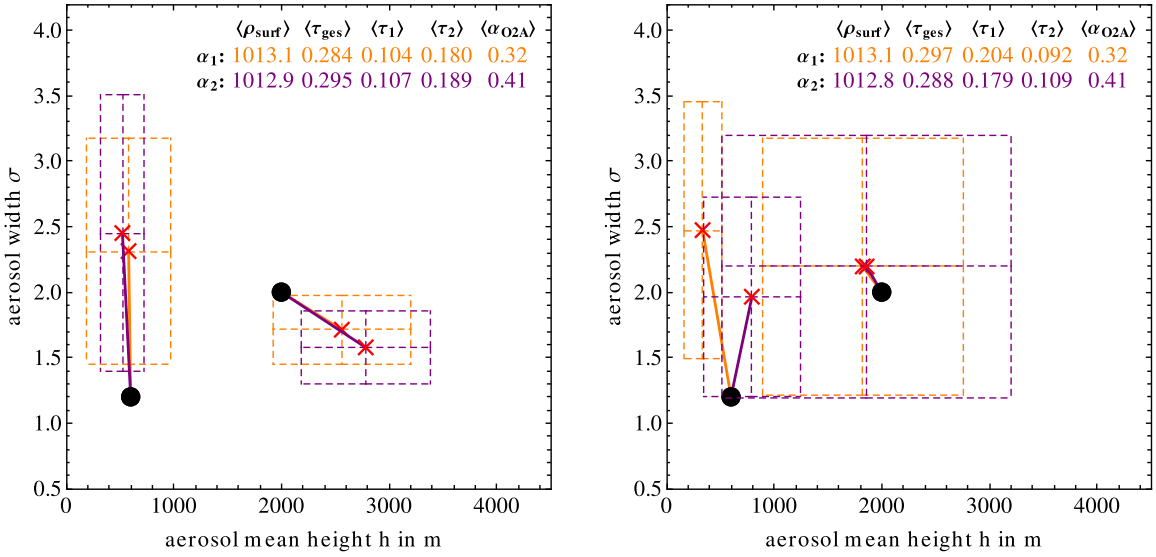

(a) Optically **thicker** aerosol mode placed above the thinner mode.

(b) Optically **thinner** aerosol mode placed above the thicker mode.

Figure 4.3.33: Inversion of a bimodal aerosol vertical distribution. Shown with different colors are the results for the two surface reflectance spectra.

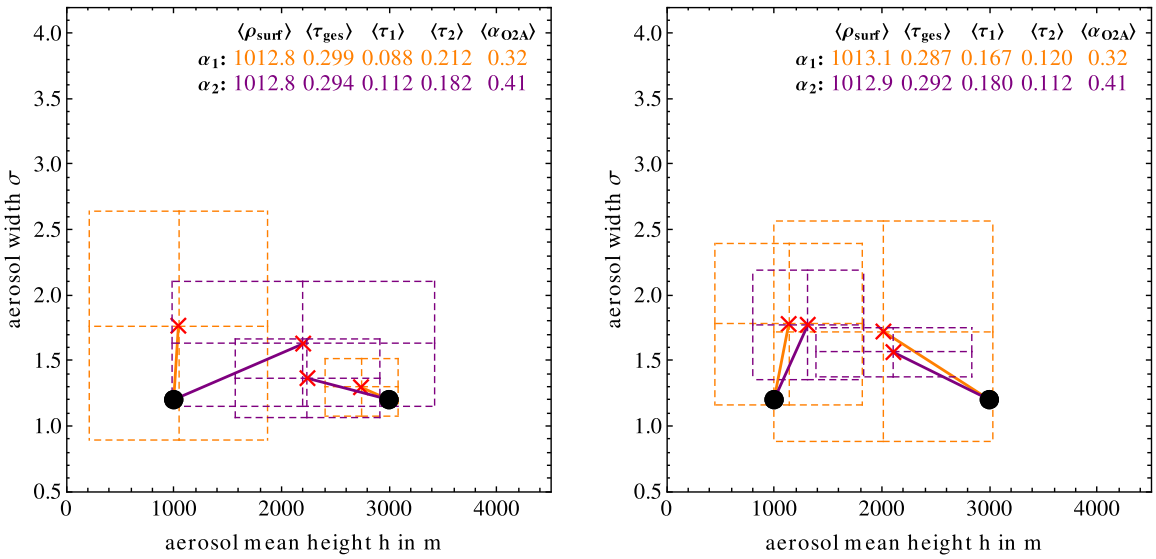

(a) Optically **thicker** aerosol mode placed above the thinner mode.

(b) Optically **thinner** aerosol mode placed above the thicker mode.

Figure 4.3.34: Same setup as shown in Figure 4.3.33, but for a different test case. Both aerosol modes are of the localized type.

4.3.12 Expected Retrieval Uncertainty

It is not straightforward to estimate the expected accuracy of an aerosol vertical distribution retrieval from FLEX hyperspectral data, since the retrieval success depends on all major parameters, such as aerosol height, aerosol width, aerosol optical thickness, and surface reflectance. One approach to reduce the complexity is to split the parameter space into two distinct sets, then to average out the effects of the first set, and then to model the error for the second set. To quantify the global applicability of a retrieval, it is feasible to model the expected error with respect to aerosol optical thickness and surface reflectance at $760nm$. The results discussed in Section 4.3.10 were used and the errors for the test cases one to six were averaged for the given aerosol optical thickness and surface reflectance. From the two aerosol optical thicknesses and surface reflectances, a coupled linear model for the expected relative error was constructed:

$$\epsilon_h = 1.07 \pm 66\% - 2.30 \pm 71\%\alpha + (8.86 \pm 56\%\alpha - 3.24 \pm 62\%)\tau, \tag{4.3.12}$$

$$\epsilon_\sigma = 1.16 \pm 42\% - 2.36 \pm 48\%\alpha + (11.38 \pm 40\%\alpha - 4.46 \pm 41\%)\tau, \tag{4.3.13}$$

were ϵ_h is the expected relative error for height and ϵ_σ is the expected relative error for the width parameter. The parameter α is the surface reflectance at $760nm$ and τ the aerosol optical thickness at $550nm$. The errors of the model parameters were estimated using the mean value $\pm$ the standard deviation for the set of scenes. The model is likely valid only for the shown parameter range. Results for the two models are shown in Figures 4.3.35a and 4.3.35b. The model shows a decrease of the error with respect to aerosol optical thickness. With increasing surface reflectance, this behavior is changed and the error starts to increase with increasing aerosol optical thickness. The error of the error model is large for all cases.

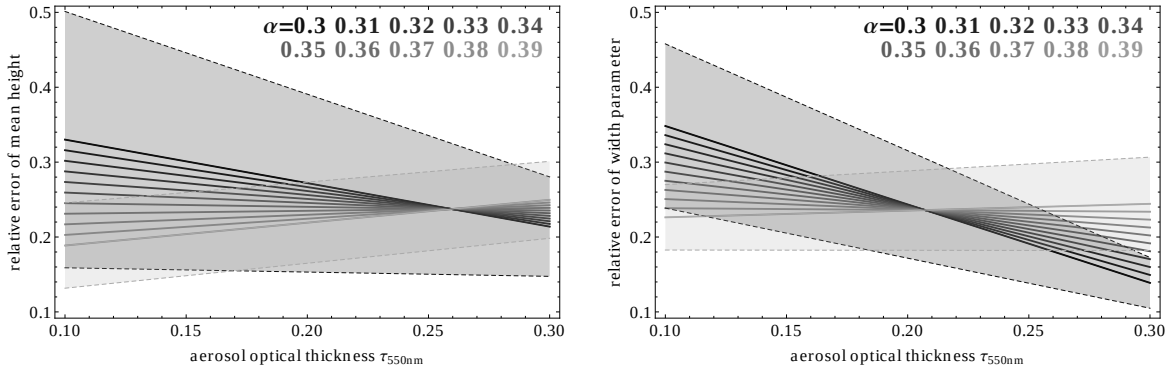

(a) Expected error for the aerosol mean height.

(b) Expected error for the aerosol width parameter.

Figure 4.3.35: Expected error for aerosol mean height and width with respect to aerosol optical thickness. Different shades of gray show curves for different surface reflectivities at the center of the O_2A band. The error of the model is shown for the darkest and brightness surface reflectivity case using dashed lines.

One can conclude that the expected error will depend on the scene, but in general a retrieval error for FLORIS of about 30% for both aerosol vertical parameters can be expected. This error model is valid only if the true scene is characterized by a monomodal aerosol distribution; hence the true error might be larger. This also means that the presented error model can be seen as lower boundary for the true error.

4.3.13 Global Applicability

The presented error model makes it feasible to globally asses the potential applicable area of the algorithm. In principle, areas with low surface reflectance variation, with not too high surface reflectance, and with not too small aerosol loading are the best candidates for the retrieval. To find such areas, ALBEDOMAP[125] and CALIOP data was combined and analyzed.

Figure 4.3.36a shows the albedo in the the MERIS O_2A channel and is based on mean values of ALBEDOMAP data for the years 2003 to 2005. The data was provided by Rene Preusker. Figure 4.3.36b shows the albedo variation for this data set. Shown is the ratio of the standard deviation and the mean value of the surface reflectance of the eight nearest neighbors of a pixel and the pixel itself. These areas would be candidates where an increase of the SNR ratio could be achieved through pixel binning and where surface inhomogeneities would be smallest. The global data set is based on a 0.05° grid and does not reflect the higher spatial resolution of FLORIS, but is useful to globally asses the areas where binning might be used.

The global distribution of aerosol optical thickness can be assessed using CALIOP data[23] and is shown in Figure 4.3.36c. Not shown is the rich variety of different aerosol types and their variation on shorter timescales.

[23] Using the same data set as in Section 4.3.5.

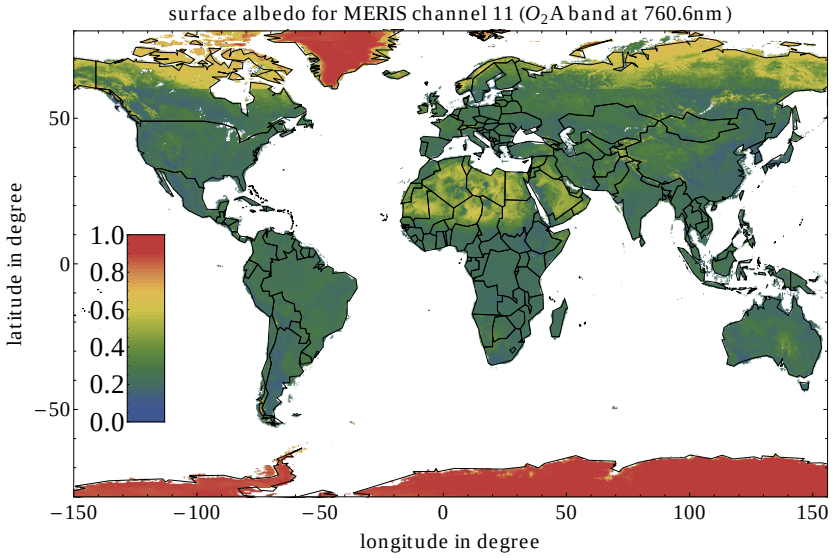

(a) Multi-year mean of surface reflection in the O_2A band. ALBEDOMAP data from MERIS from the years 2003 to 2005 was used.

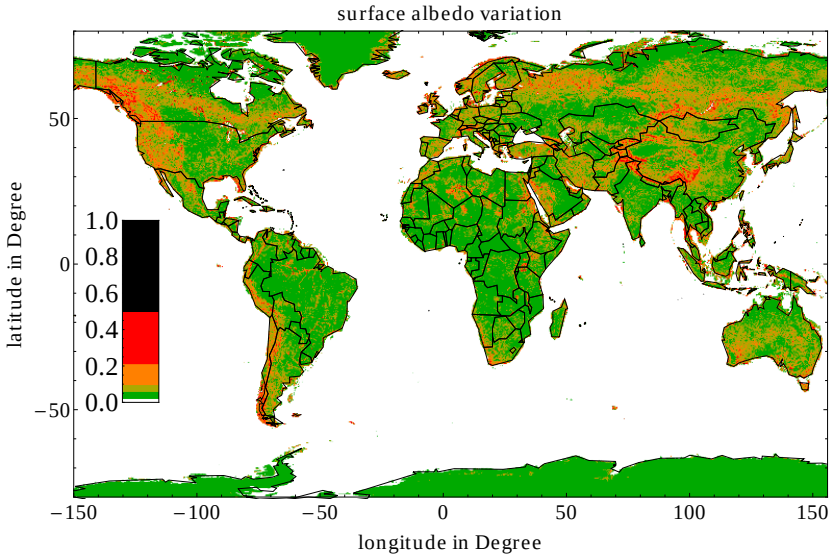

(b) The data from Panel (a) is used to asses global surface homogeneity. The color scale shows the ratio of the standard deviation and mean value of a surface reflectivity pixel and its eight neighbors.

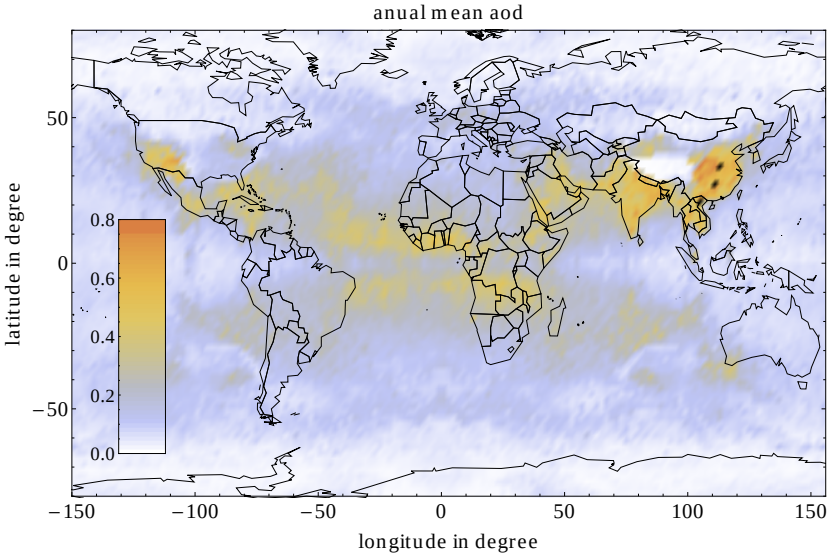

(c) Yearly mean of aerosol optical depth from CALIOP data. The same data set as discussed in Section 4.3.5 was used.

Figure 4.3.36:

These three parameters are not able to describe the complexity of the real situation, but they can be used to roughly asses the applicability of the algorithm that is shown in Figure 4.3.37. Land masses were colored using a *traffic light* like scheme. Dark green colored areas have a surface albedo variation below 7.5%, surface albedo below 0.5, and mean aerosol optical thickness above 0.2. Light green colored areas have the same properties, but their mean aerosol optical thickness is below 0.2. The yellow and red areas have an albedo above 0.5 and dark red areas have surface albedo variation above 7.5%. The map shows that in case of a cloud and snow free scene, the greater part of the landmasses are suitable candidates for the retrieval of aerosol vertical structure.

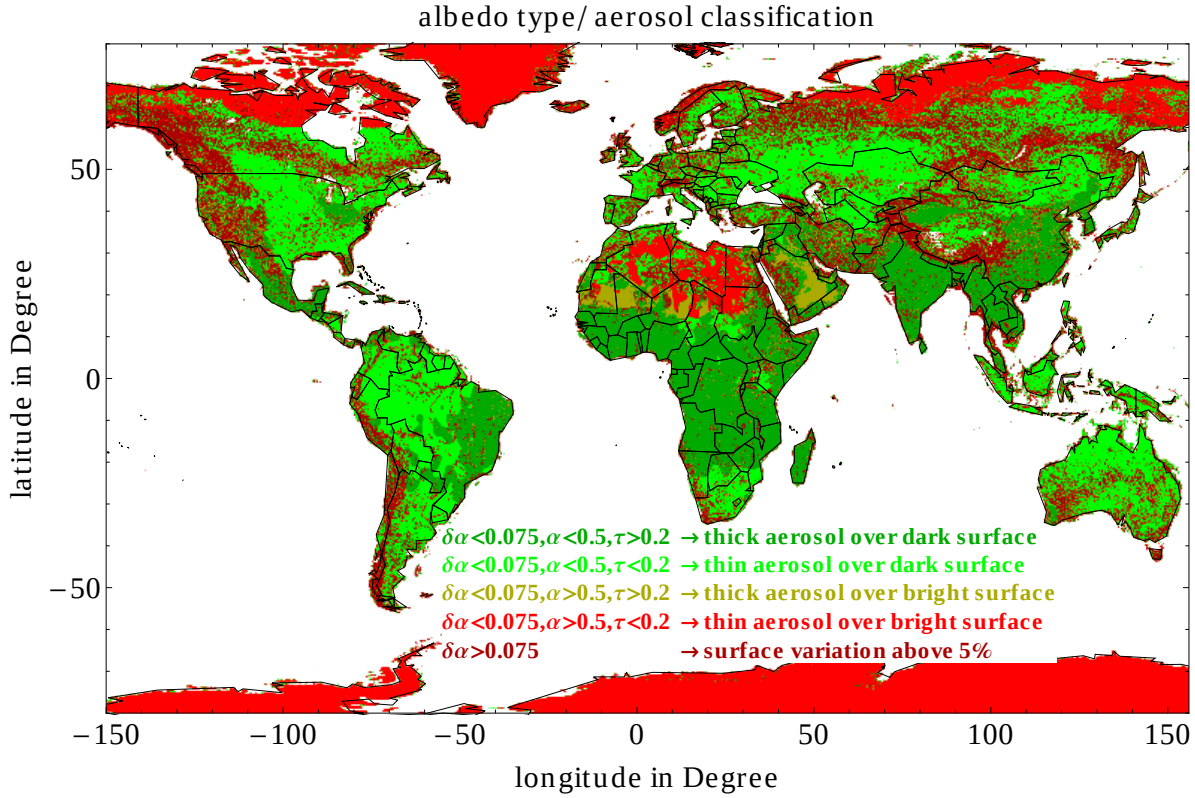

Figure 4.3.37: Global assessment of areas that are good candidates for a retrieval of aerosol vertical structure using FLORS measurements. Green areas are most homogeneous and the surface reflectivity is below 0.5 in the O_2A band. Red and yellow areas are either too inhomogeneous, have too high surface reflectivities, or their mean aerosol loading is to low.

4.3.14 Conclusion

A number of conclusions can be drawn from the presented analysis:

- Spectral high resolution top-of-atmosphere radiance measurements in the O_2A band can be a viable tool for the remote sensing of aerosol vertical distribution.
- On regional to global scales, the vertical distribution is accurately modeled using a bimodal log normal distribution.
- The inversion error is affected by the scene itself. It is decreasing for higher aerosol optical thicknesses and darker surfaces.
- The inversion error for a bimodal inversion approach is strongly affected by spectral resolution. At FLORIS spectral resolution the results shows only very limited capability of retrieving two aerosol modes.
- Inversion of bimodal aerosol vertical distribution cases with a monomodal algorithm lead to intermediate results for the aerosol vertical distribution.
- Including measurement in the O_2B band into the retrieval increases the complexity by as least three parameters and leads to small improvements of the inversion result for cases with low aerosol optical thickness.
- A large fraction of land covered areas are, if snow and cloud free, suitable targets for the retrieval of aerosol vertical structure. A retrieval uncertainty of 30% for monomodal distributions can be achieved using FLORIS data.
- The high spatial resolution of FLORIS has major benefits. The effects from surface inhomogeneities are reduced, contamination from subpixel clouds are more easy to avoid, and SNR can be increased by binning several pixels.

Acknowledgments

This research was funded by the ESA project FLUSS (AO/1-6485/10/NL/LvH). I also thank Rene Preusker for providing ALBEDOMAP data, Florian Filipitsch for processing CALIOP data, Rasmus Lindstrot for providing his data for the FLUSS aerosol model, and the whole FLUSS team for many fruitful discussions.

4.4 Simulating Hyper Spectral Measurements in the O_2A Band As Observed by the GOSAT Satellite: A Proof of Concept for Deriving Aerosol Vertical Distribution

4.4.1 Abstract

It was demonstrated in Section 4.3 that, in principle, aerosol vertical distribution information over land surfaces can be derived from top-of-atmosphere hyperspectral radiance measurements in oxygen absorption bands. It was shown that the success of a possible retrieval in general depends on the scene itself, the instrument's spectral resolution, spatial resolution, and signal to noise ratio. In this section, the aerosol retrieval techniques developed in Section 4.3 are applied to a sample of 104 hyperspectral measurements observed by the Fourier transform spectrometer TANSO-FTS on board the Greenhouse Gases Observing Satellite (GOSAT). Shown is that the radiative transfer model MOMO is well able to reproduce most cases of the measurements. All remaining systematic residuals between measurements and simulations can be explained by cloud contamination, effects of the temperature profile, uncertainties in the HITRAN database, and limitations of the used Voigt line shape model to calculate the oxygen absorption. The successful application of the developed techniques to a real world example explicitly shows their value for the retrieval of aerosol vertical structure. However, a thorough validation of the retrieval results was beyond the scope of the presented work. The main limitation of using GOSAT data is its low signal to noise ratio and poor spacial and temporal resolution. Nevertheless, it can serve as viable test case until data from better suited instruments such as OCO2, FLORIS, or CarbonSat will become available.

4.4.2 GOSAT (IBUKI) and the TANSO-FTS Instrument

The *Greenhouse Gases Observing Satellite* (GOSAT),[24] as shown by a sketch in Figure 4.4.1a, was launched on the 23rd of January, 2009 by the *Japan Aerospace Exploration Agency* (JAXA) [179]. Its main instrument is the *Thermal And Near-infrared Sensor for carbon Observation* (TANSO). The instrument consists of the two subunits TANSO-FTS (Fourier Transform Spectrometer) and TANSO-CAI (Cloud Aerosol Imager). A sketch of the optical system is shown in Figure 4.4.1b. The key optical properties of TANSO-FTS are shown in Figure 4.4.2. Measurements of the two instrument are used to derive CO_2 and CH_4 columns (level 2 data) and their global distribution and temporal variation (level 3 data) [180].

The TANSO-FTS instrument measures polarized radiance in the S and P direction, from which the radiance spectra can be calculated as the mean value of both measurements. The spectral sampling within the O_2A band is approx. $0.012nm$, which is one magnitude larger than for the previously discussed FLORIS instrument (see Section 4.3.4). The spectral resolution of $0.5/cm$ (see Figure 4.4.2) at the O_2A band (spectral band 1) results in a spectral resolution of $0.029nm$ at $760nm$.

In contrast to the high spectral resolution, the spacial resolution of the instrument is poor when compared to the $300m \times 300m$ footprint of a single FLORIS pixel. The TANSO-FTS is not an imaging instrument such as FLORIS, and spacial resolution across track is acquired using a pointing mechanism. The acquisition time for an interferogram depends on the chosen gain settings and is in the order of a second. A sketch of the pointing procedure is shown in Figure 4.4.3b. The number of cross track points can be changed between 1, 3, 5, and 7 by JAXA and the resulting measurement point grid is shown for one orbit in Figure 4.4.3a. The Figure additionally shows the corresponding TANSO-CAI image.

[24] GOSAT is the international name of the satellite. The Japanese name is *IBUKI*, which means breath.

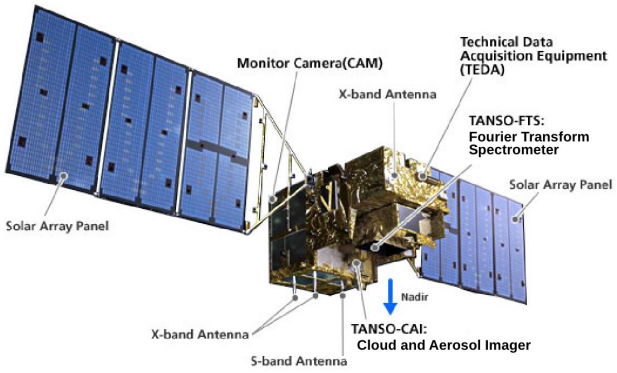

(a) Sketch of the GOSAT (IBUKI) satellite. Main Instruments are TANSO-FTS and TANSO-CAI. Image credits: JAXA.

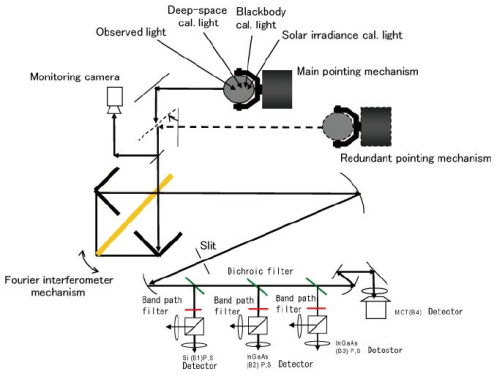

(b) Sketch of the TANSO-FTS optical system. It consists of the pointing mechanism, the Fourier interferometer, and specialized detectors. Reproduced from reference [157].

Figure 4.4.1:

Ground Pointing Mechanism and Fore optics	Configuration	2-axes scanner (fully redundant)				
	Scanning	Cross Track (±35 deg) Along Track (±20deg)				
	Field of view	IFOV 8 km 88 km (Interval) 790 km (scan width) (latitude of 30 deg)				
Fourier Transform Spectrometer	Speed	0.7 1 (Interferogram)/sec				
	Spectral band	1	2	3	4	5
	Coverage (cm^{-1})	12900-13200	5200-6400	4800-5200	2000-2500	660-2000
	resolution (cm^{-1})	0.5	0.2	0.2	0.1	0.1
	Detector	Si	InGaAs	InGaAs	InSb	PC-MCT
	Calibration	Solar Irradiance, Deep Space, Moon			Blackbody, Deep space	

Figure 4.4.2: Main optical specifications of the TANSO-FTS instrument. Reproduced from reference [157].

The field of view of the TANSO-FTS is $15.8mrad$, which results in a $10.5km$ footprint when the satellite is at its nominal height of $660km$. This relative poor spacial resolution limits the application of aerosol vertical distribution retrieval from GOSAT data. A TANSO-FTS spectrum with the given footprint can be easily contaminated by clouds, which makes the retrieval almost impossible. As a result, the interaction of aerosols with clouds at their surrounding, which is strongly affected by aerosol height, cannot be studied in detail. For this application, the spacial resolution of the aerosol vertical distribution product must be better than the spacial scale on which a cloud typically changes.

On the other hand, the measurements by GOSAT can be used as a real world test case and proof of concept of the methods developed in Section 4.3. The main idea of this section is to test whether the TANSO-FTS spectra can be explained using the MOMO radiative transfer model, while using realistic input parameters with realistic boundaries. Whether the retrieved parameters such as surface pressure, aerosol optical thickness, and aerosol vertical distribution have physical meaning is not discussed in this section. To do so, a large scale validation with CALIOP [129] data or Aeronet [19] data would be necessary, which is beyond the scope of this section.

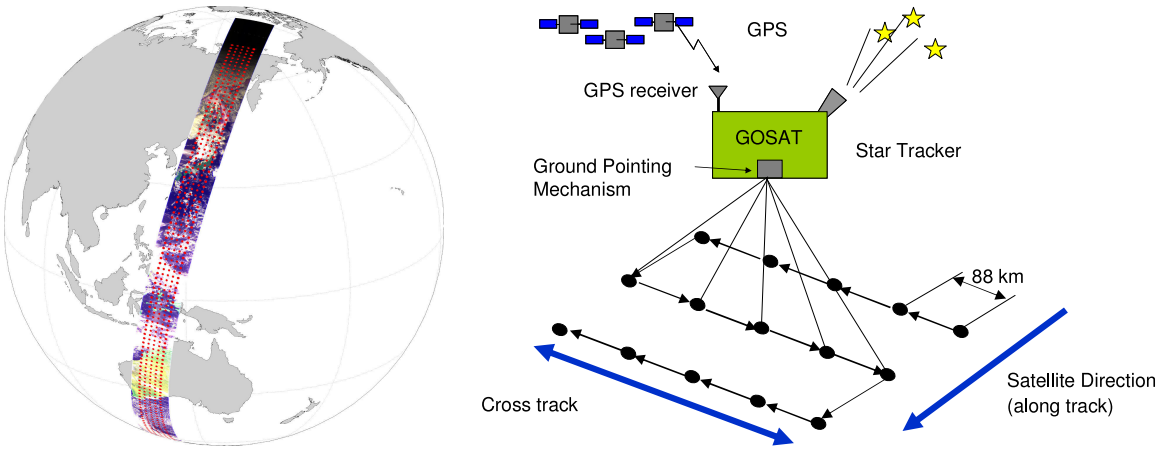

(a) TANSO-FTS measurements for an orbit combined with the corresponding TANSO-CAI images. In this example, 5 cross track observation points were used. Reproduced from [179].

(b) Sketch of the TANSO-FTS viewing geometry. A pointing mechanism is used to acquire spatial resolution across track. Shown is a scenario with 5 cross track points with $88km$ distance between each across track point. Reproduced from [157].

Figure 4.4.3:

4.4.3 Available GOSAT TANSO-FTS Data Set

A set of GOSAT TANSO-FTS measurements was provided by Luis Guanter, who is the principal investigator (PI) of the GOSAT project: *Space-based analysis of the relationship between vegetation functioning and atmospheric CO_2 and CH_4 greenhouse gases.* The data set consists of 250 spectra acquired in summer 2010 for the east coast of North America. A subset of the spectra acquired in the O_2A band is shown in Figure 4.4.4. Additionally shown is the solar constant [181] in arbitrary units. The general shape of the spectra is determined by the solar constant, the position and shape of its Fraunhofer lines [182], and the oxygen absorption. The solar constant is shown, so that the effects of Fraunhofer lines on the measurements can be distinguished from oxygen absorption features.

The data points are distributed over the east coast of North America and their positions are shown in Figure 4.4.5. The region was chosen such that a high number of cloud free days can be expected. The mean surface albedo in the O_2A band is shown in Figure 4.4.5a. A yearly mean of Albedomap [125] data was used to prepare the figure. Since the surface albedo depends strongly on the season, the shown values are only a rough estimate of the true value for a single measurement. The topography of the area is shown in Figure 4.4.5b, where data from a digital elevation model (DEM) [183, 184] was used. Such data could in principle be used to estimate the surface pressure of the data point. However, for the shown inversions this data was not used, since to convert surface height to surface pressure, knowledge about the atmospheric temperature profile is generally necessary. In principle, such data could be taken from numerical weather prediction (NWP) models or radiosonde data, but this was not available for this study. In an operational retrieval it can be used as prior knowledge for surface pressure and atmospheric profile.

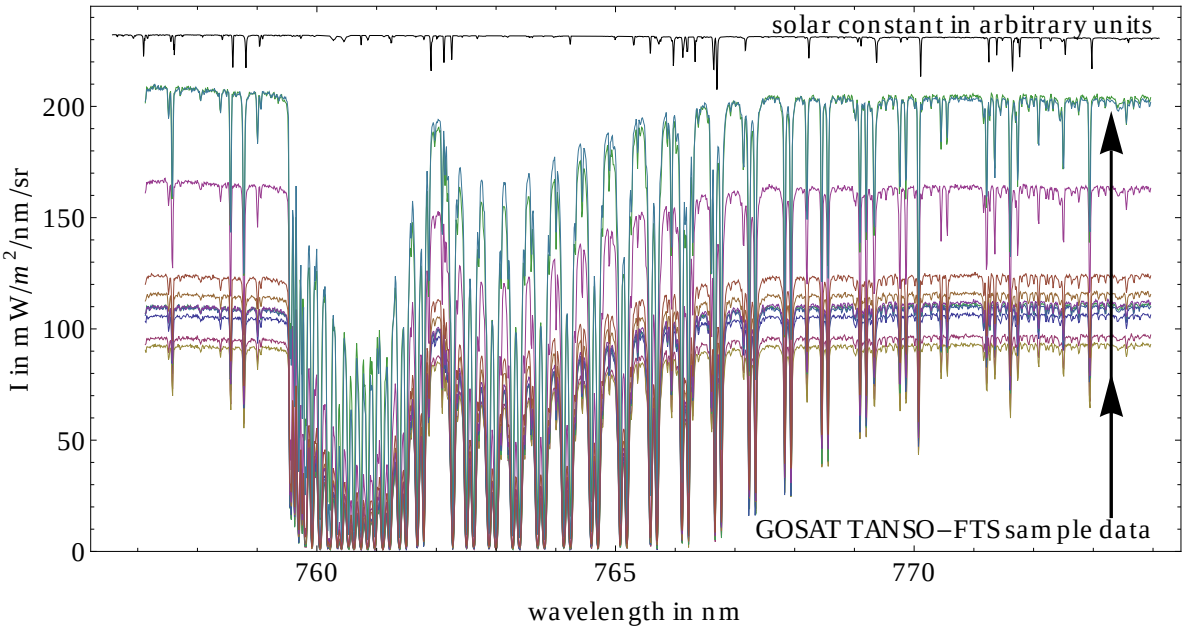

Figure 4.4.4: Shown is a subset of TANSO-FTS spectra from the data set provided by Luis Guanter. The black line shows the solar constant [181]. It is scaled such that it can be displayed together with the shown data. Clearly visible in the measurements is the oxygen A band and features caused by the Fraunhofer lines of the solar constant.

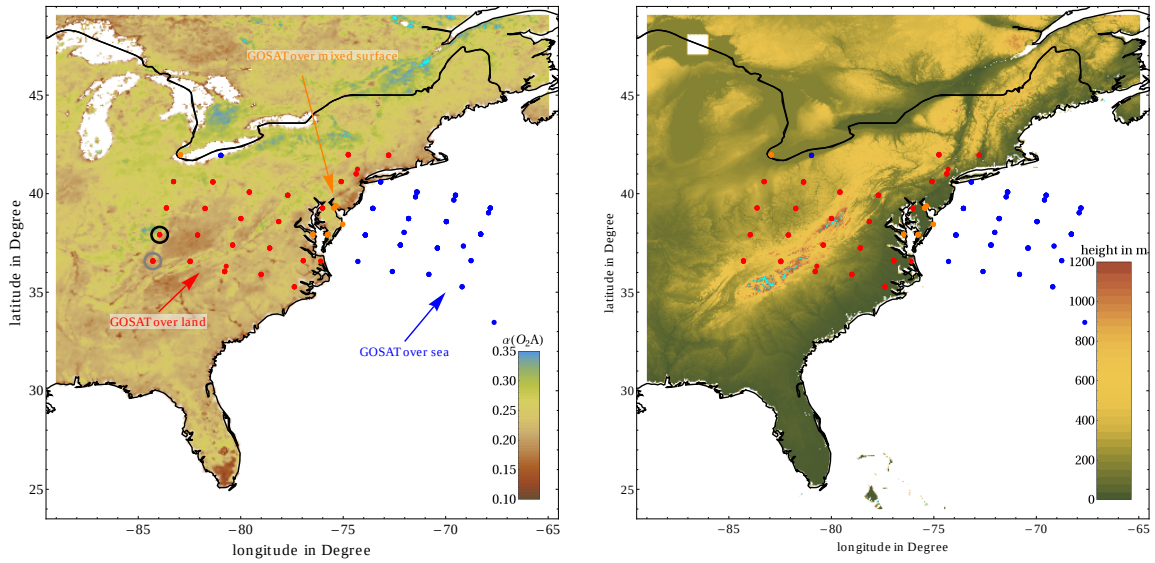

(a) GOSAT data positions together with the mean surface albedo in the O_2A band. Albedo was taken from Albedomap data [125] and represents a yearly mean value. The black circle indicates the position of the measurements shown in Figure 4.4.7 and the gray circle is for Figure 4.4.8.

(b) GOSAT data positions together with ground height from a digital elevation model (DEM) [183, 184]. The white rectangle is caused by a gap in the DEM data sat. Water surfaces were not especially marked.

Figure 4.4.5: Distribution of TANSO-FTS data points for the discussed data set. Colored points indicate data positions. Red points show that data has been acquired over land, blue points over sea, and orange points indicate a mixed scene.

4.4.4 Inversion Setup of Forward Radiative Transfer Simulations

The general radiative transfer setup as described in Section 4.3.5 was reused and applied to TANSO-FTS measurements. Results of this RT operator were used to set up a forward operator (FO) based on a lookup table approach. The free input parameters of the FO are the surface pressure ρ_0, the type of atmospheric profile, surface reflectivity (α_1, α_2) at the band borders, and aerosol parameters such as aerosol-model, -optical thickness τ, -mean height h, and -width σ. A linear spectral model of the surface reflectivity within the O_2A band is assumed and described by the reflectivity at the lower (α_1) and upper (α_2) spectral boundaries of the band as defined in Equation 4.3.2 on Page 93. A wide variety of possible surface reflectivities for a broader spectral range is shown in Figure 4.4.6. The data shows that a linear model should be well able to represent the data. For this study, the atmospheric profile was set to a mid-latitude summer atmospheric profile [113] and the aerosol model was set to a continental aerosol model.

To reduce the amount of additional implementation effort, a simple lookup table approach was chosen to construct the forward operator. The parameter grid for the lookup table is shown in Table 4.4.1. The numeric burden was reduced by choosing a rather large grid with two to four values per parameter. All in all, the physical parameter space is composed of $4_\rho * 3_\tau * 3_{\alpha_1} * 3_{\alpha_1} * 3_h * 2_\sigma = 648$ distinct states. The radiative transfer calculations were performed using 5 zenith angles, 5 Fourier terms, and 3 angles of azimuthal sampling, which is likely not enough for accurate simulations but was necessary to reduce the numeric burden. A single spectrum per state consists of 3501 data points distributed between $756.6nm$ and $774.1nm$ with a spectral sampling of $0.005nm$ and a spectral resolution of $0.005nm$. This means that an oversampling ratio of approximately $0.03/0.005 = 6$ is achieved. A higher oversampling ratio could reduce the error of the numeric convolution of the instrument line shape (ILS) function and the radiative transfer result, but would at the same time increase the numeric burden; hence this number is a reasonable compromise.

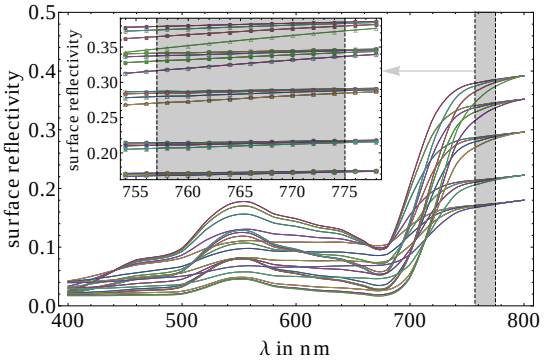

Figure 4.4.6: Sample set of surface reflectance spectra for soil and vegetation cases. The data was simulated using the PROSPECT and SAIL models [165, 164] and was provided by ESA's FLUSS project.

parameter state $\vec{x}$:	ρ in hPa	τ	α_1	α_2	h in m	σ
minimun value:	900	0.1	0.1	0.1	500	1.1
maximum value:	1050	2.1	0.7	0.7	4500	4.1
gridding value:	50	1.0	0.3	0.3	2000	3.0
number of values:	4	3	3	3	3	2

Table 4.4.1: Parameter grid of the lookup table.

In total, $3501 * 648 = 2.268.648$ radiative transfer simulations were performed to fill the lookup table. The simulated spectra were convolved with the TANSO-FTS ILS, which were provided with the sample data. The solar constant as a provided by Robert L. Kurucz [181] was used. The constructed forward operator FO_{TANSO} has an additional parameter $\delta\lambda$ to model wavelength shifts that occur for TANSO-FTS. The shift depends on orbit, and has to be inverted as well. In combination, FO_{TANSO} is expressed as:

$$FO_{MOMO}(\lambda, \vec{\mu}, \vec{x}) = \int d\lambda' ILS_\lambda(\lambda') \times S_0(\lambda') \times FO_{MOMO}(\vec{x}, \vec{\mu}, \lambda'), \tag{4.4.1}$$

$$FO_{TANSO}(\lambda, \delta\lambda, \vec{\mu}, \vec{x}) = FO_{MOMO}(\lambda + \delta\lambda, \vec{\mu}, \vec{x}), \tag{4.4.2}$$

where $\vec{\mu}$ is the vector defining the viewing geometry, $\vec{x}$ is the state vector as defined in Table 4.4.1, S_0 is the solar constant, and $ILS_\lambda(\lambda')$ is value of the TANSO-FTS ILS function at wavelength λ' for a channel centered at wavelength λ.

The whole setup was implemented using Mathematica and its interpolating object functionality. As a first step, the integrand of Equation 4.4.1 was pre-tabulated while keeping the original wavelength grid at $0.005nm$ spectral sampling, but with TANSO-FTS spectral resolution. Then, linear interpolation with respect to $\vec{x}$ and $\vec{\mu}$ is used to calculate a spectrum suitable for TANSO-FTS, but at much higher spectral resolution (six times oversampling). In a second step, quadratic interpolation and the wavelength shift parameter $\delta\lambda$ is used to sample the spectrum according to the TANSO-FTS wavelength grid. The implementation easily allows to add further spectral distortion parameters if necessary.

In a proof-of-concept phase, such type of implementation can be realized rather fast and with small amounts of code if compared to an implementation in low-level computer languages such as FORTRAN and C. The downside of this approach is that the execution time and memory use of Mathematica is generally worse when compared to an efficient implementation in one of the mentioned low-level languages, which only matters if large data amounts have to be processed.

For the inversion the *NMinimize* function with a maximum of 150 iteration steps was used. The minimization method *Differential Evolution* (DE) was chosen [185, 186]. The method itself is a parallel direct search method. A fixed number of states, a population, is updated according to a scheme of mutation, crossover, and selection. DE is in fact a simple but effective type of genetic minimization algorithm. In initial tests, it performed much better than the Nelder-Mead [187] method. The DE algorithm aims to find a global minimum with respect to the parameter bounds and its populations members are able to escape from local minima. This makes the algorithm especially suited for the problem (see discussion in Section 4.3.9). The inversion itself takes up to $30min$ per spectra on an Intel $i7-2600@3.4GHz$ CPU and consumes about $9GB$ of system memory. It is therefore too slow to be applied to a global data set. To do so, the algorithm should be implemented as parallel running algorithm in FORTRAN or C and could possibly make use of the processing capabilities of today's graphic cards using the CUDA or Open-ACC standards.

4.4.5 Inversion Results

From the 250 provided spectra, 104 were classified as measurements over land, which is the area of interest for this application (compare with Figure 4.4.5). An overview about inversion results for two successful cases is shown in Figure 4.4.7 and Figure 4.4.8. An overview about the fit quality for the complete data set is given in Figure 4.4.10 and Figure 4.4.11.

Figure 4.4.7 shows a detailed overview of a single TANSO-FTS measurement and the corresponding inversion result. It shows the measurement as a red line, the inversion result as a black line, the residual as a gray line, and for reference of features caused by Fraunhofer lines, the scaled solar constant as an orange line. The solar constant is shown so that the identification of solar Fraunhofer lines becomes straight forward. The box in the lower left corner of the top panel shows the inverted state, the mean absolute relative deviation $\langle \delta_{\%} \rangle$ and the mean absolute deviation $\langle \delta \rangle$ of the result:

$$\begin{aligned} \langle \delta \rangle &= \langle |\vec{M} - \vec{F}| \rangle, \\ \langle \delta_{\%} \rangle &= \langle \delta \rangle / \langle \vec{M} \rangle, \end{aligned} \tag{4.4.3}$$

where $\vec{M}$ is the TANSO-FTS measurement, $\vec{F}$ the result of the forward operator, and $\langle . \rangle$ denotes the mean value of all vector components.

Without knowing the surface pressure at time and location of the measurements, it is hard to judge whether the retrieved surface pressure is close to the real value. What can be said is that the range of the retrieved surface pressure values is reasonable. The same can be said for aerosol optical thickness, aerosol mean height, and aerosol width.

The temperature profile and the aerosol model were kept constant throughout the inversion. This means that the retrieved aerosol optical properties resemble effective optical properties that explain the measurements best. To determine the true aerosol type, a broader range of measurement windows in the visible spectrum, as well as in the infrared would be needed.

The result shown in Figure 4.4.7 is of similar quality as was shown in Figure 4.4.7, but the retrieved aerosol optical thickness of 0.9 is much higher.

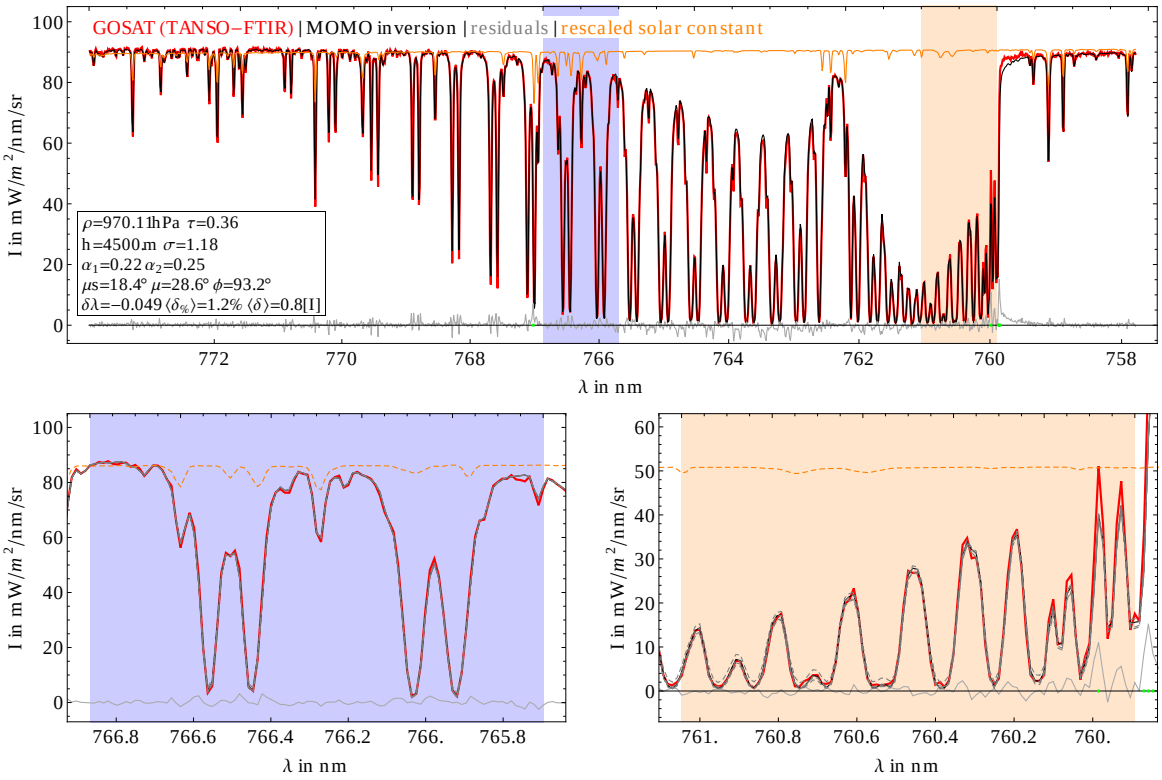

Figure 4.4.7: Overview of the inversion result for a single TANSO-FTS spectrum. The top panel shows the total spectral region which was used for the inversion. The red line shows the TANSO-FTS spectrum, the black line the final result of the forward operator, the gray line the residual, and the orange line shows the scaled solar constant. The solar constant is scaled such that its maximum is above the TANSO-FTS spectrum and that the Fraunhofer lines are clearly visible. The box in the lower left corner shows the inverted parameter state and the inversion quality parameters: $\langle \delta_{\%} \rangle$ and $\langle \delta \rangle$ (see Equation 4.4.3). The two lower panels show details of the top panels, as indicated by the light blue and light orange color bar. The solar constant is scaled for all three panels. The dashed lines in the two lower panels show the maximal range of the signal due to variation of aerosol height and width. The position at which the measurement was taken is shown by a **black circle** in Figure 4.4.5a.

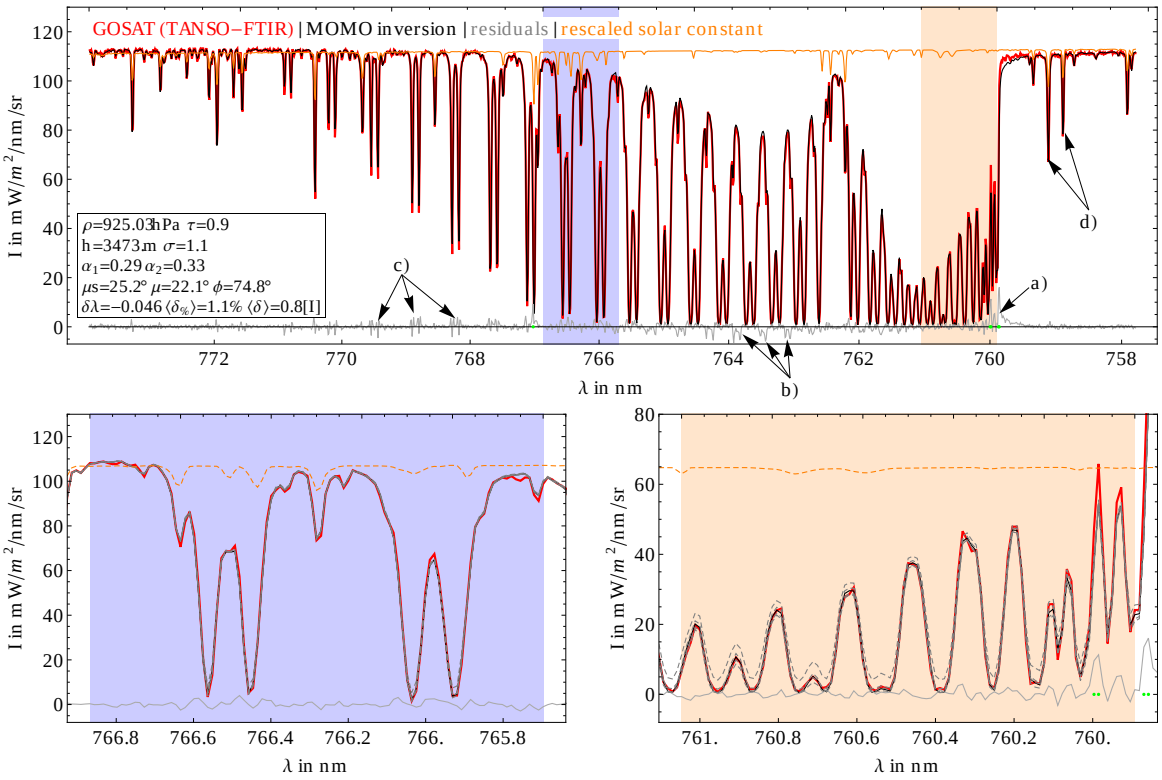

Figure 4.4.8: Same as Figure 4.4.7, but for a different measurement. The position at which the measurement was taken is shown by a **gray circle** in Figure 4.4.5a. Several features of the residuals (a,b,c,d) are highlighted and discussed in detail on Page 127. This type of residuals is also present in Figure 4.4.7 and are representative for the complete data set.

The results are generally of very good quality. The mean absolute relative deviation is at just $\langle \delta_{\%} \rangle = 1.1\%$ and the mean absolute deviation is at just $\langle \delta \rangle = 0.8 mW/m^2/nm/sr$. Fraunhofer lines and oxygen absorption features are spectrally very well represented. Especially the lower left panel shows in detail that the oxygen absorption and Fraunhofer lines are very well represented. There is no systematic residual that is only associated to a single feature and the residual spectrum shows only few distinct features. The most important of them are marked in Figure 4.4.8 and discussed here.

An obvious source of possible errors is the convolution of the radiative transfer results with the ILS function. Errors can be caused by a too small oversampling ratio or errors in the ILS function itself. From the presented results, it seems that this effect is negligible. The label *d)* highlights two Fraunhofer lines outside the oxygen absorption band. The residual for these two lines show no special feature when compared to the near spectral surrounding, which implies that the ILS of the instrument is well represented by the simulations.

This argument also implies that the Ring effect [188] for the scene is smaller than the residual, or has been absorbed by other parameters of the inversion. One of the largest contributions to the effect is Raman scattering, which was not included in the simulations. In the O_2A band, the effect could be as high as $\pm 2\%$ with strong spectral variation [189].

The largest systematic residuals are located at the lower edge of the absorption band at $760nm$ and are marked by *a)*. At the top of this decrease, the forward operator systematically underestimates the measurement, and hence overestimates the oxygen absorption. This residual is systematic for the results of the whole data set. Until the forward operator is able to reproduce this effect an explanation is speculation, but there is strong evidence that this effect is related to errors of absorption line positions in the used HITRAN database and effects of

line mixing as described by Tran and Hartmann [190]. Figure 4.4.9a reproduces Figure 1 from their paper and shows the same type of residual. They also state that using only the Voigt line shape model to calculate the oxygen absorption can lead to such errors. They propose a different algorithm, which is not yet implemented in the MOMO k-binning program [44].

The markers *c)* and *b)* show systematic residuals, which are associated with oxygen absorption line maxima (*c)*) and minima (*d)*). These are typical residuals due to deviation of the real temperature profile and the one used for the simulations. An example is shown in Figure 4.4.9b. These residuals could be reduced if variations in the temperature profile were included in the forward operator. As proposed by the authors of reference [191], a principal component-based approach could be applied. The general idea is to incorporate the global variability of possible temperature profiles by describing them with a truncated series of their principal components and proper weights. The accuracy needed for the simulations defines then the number of used principal components. As suggested by the authors, four to six components could be used to greatly reduce the error caused by deviations in the temperature profile. This would of course increase the numeric burden, since the size of the lookup table would scale with the number of principal components. This increase of only four to six should be manageable with modern computer systems. The main additional burden is posed on the inversion itself, since the parameter space would increase by four to six parameters. This will almost certainly increase the run time of an inversion operator, but again this should be feasible using a modern computer system. The increased run time could be simply compensated by using additional CPU cores and nodes in parallel.

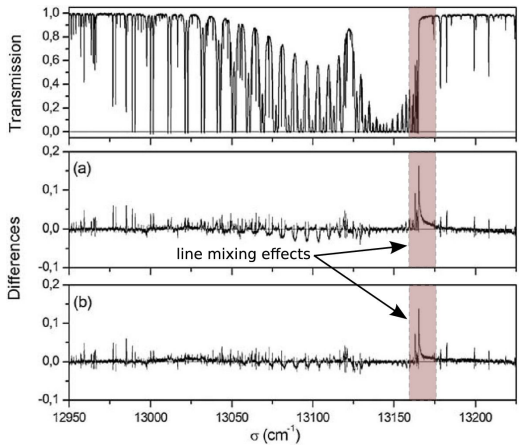

(a) Reproduced Figure 1 with modification from reference [190]. The top panel shows a measured atmospheric transmission spectrum and the two bottom panels show the residual with respect to two older simulation models proposed by the authors of the paper. The models are based on the HITRAN database and the Voigt line model and show the same type of residuals as seen in Figure 4.4.7 and Figure 4.4.8.

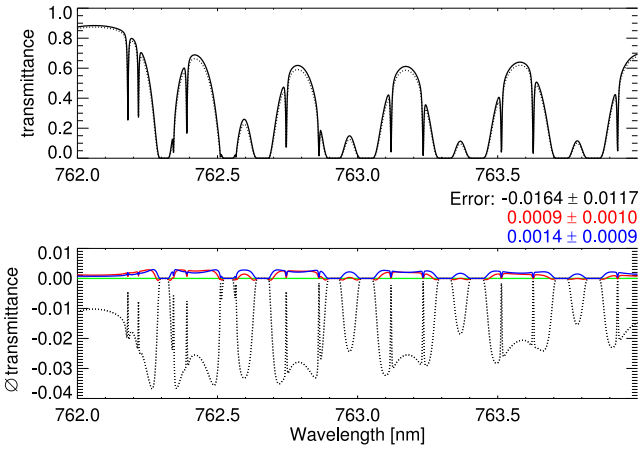

(b) Reproduced Figure 8 with modification from reference [191]. The top panel shows the transmission spectra located in the O_2A band. The bottom panel shows residuals if the same simulation were performed using a mean temperature profile (black dotted line). The blue and red line show the results if the used temperature profile is reconstructed using four principal components that describe the temperature profile. For this spectral window the largest residuals are found for transmittance maxima.

Figure 4.4.9:

An overview about the inversion results for the complete data set is shown in Figure 4.4.10. Shown is the mean absolute relative residual $\langle\delta\rangle$ and the mean absolute relative residual $\langle\delta_{\%}\rangle$. The data points were sorted according to $\langle\delta_{\%}\rangle$, and hence $\langle\delta_{\%}\rangle$ is strictly monotonic rising. This is not and must not be the case for $\langle\delta_{\%}\rangle$. For the lowest residuals and therefore the best inversion results $\langle\delta_{\%}\rangle$ rises also monotonically but starts to show jumps for inversions with higher residuals. The reason for this behavior is that small residuals for low values can cause high relative residuals. The position of the results shown in Figure 4.4.7 is indicated with a

dashed line and that from Figure 4.4.8 with a dotted line. The majority of the dataset can be explained with the forward operator and the residuals only start to strongly increase from index 80 on.

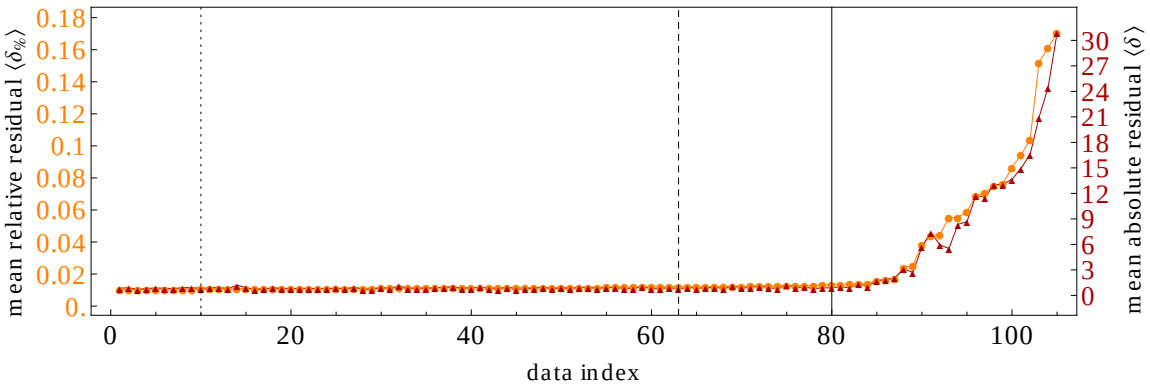

Figure 4.4.10: Overview about the inversion quality for the complete data set. The data set was sorted with respect to $\langle\delta_{\%}\rangle$. Additionally shown is $\langle\delta\rangle$. The dashed line represents the result shown in Figure 4.4.7 and the dotted line the results shown in Figure 4.4.8.

An inversion could be called a *fail* if the residuals exceed a certain limit, which can be defined by the instrument's SNR, or the inversion hits the boundaries for one or more parameters. Figure 4.4.11 shows an overview of the retrieved parameters with respect to the mean residuals as shown in Figure 4.4.10. In other words, the retrieved physical parameters are shown and sorted with respect to the quality of the inversion. This type of analysis can help to define the key parameters that govern the inversion success.

The first Panel 4.4.11a shows clearly that the inversion quality decreases for brighter measurements. The figure shows the mean value of the measurements in units of radiance and the ratio of the mean of the brightest and darkest 20%. This is a very strong indicator that measurements with high residuals were contaminated by clouds or cirrus. This assumption is supported by the results for the surface reflectance as shown in Figure 4.4.11b. For those results with higher residual, the inversion tries to increase the surface reflectance beyond physical limits. If the scene is cloud free, values in the order of 0.3 and below would be reasonable (compare Figure 4.4.6 and 4.4.5a). Since clouds are not included in the forward operator, the inversion tries to increase the radiance by increasing the surface reflectance.

Figure 4.4.11c shows that the surface pressure often hits the lower boundary of $900hPa$, which is a limitation in the calculated table. This happens for successful inversions as well as for failed inversion attempts. In a general retrieval scheme, the surface pressure could be bound by prior knowledge from NWP models and the table can be easily extended.

The retrieved aerosol optical thickness as shown in Figure 4.4.11c is quite high for many cases. Such high values could be caused by aerosol dust outbreaks or by contamination of the measurements by thin clouds and cirrus. This shows that effective cloud flagging is essential for the retrieval. This could be done by using data from the TANSO-CAI instrument, which is an imaging spectrometer, or by utilizing a cloud screening algorithm using the water vapor absorption in the $5150cm^{-1} - 5179cm^{-1}$ band as suggested by Guerlet et al. They suggested that under clear sky condition the radiance in the deepest absorption lines should be in the order of the instrument noise. Clouds and cirrus would effectively decrease the effective photon path length, which decreases the absorption and increases the signal. A threshold could then be used to classify a measurement as cloud free. The main advantage of this approach is that only data from TANSO-FTS are needed, and additional processing of TANSO-CAI data is avoided.

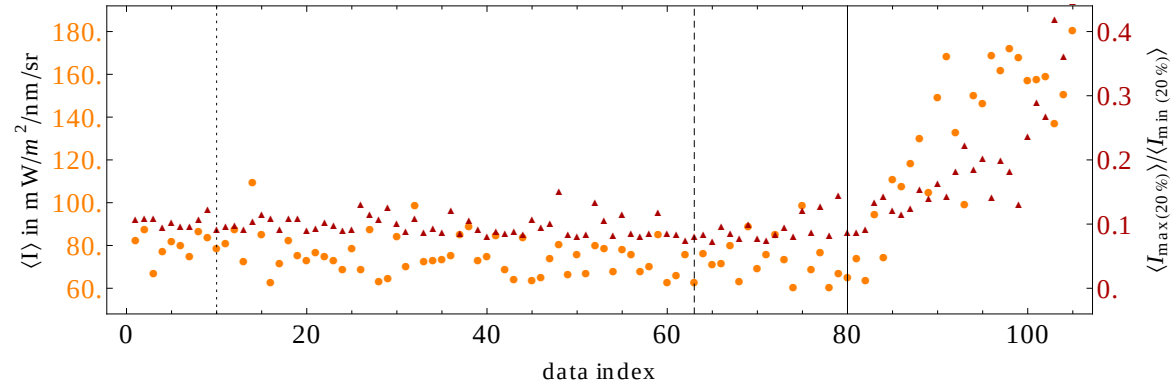

(a) Mean of the measurement $\langle \vec{M} \rangle$ and $\langle min_{20\%}(\vec{M}) \rangle / \langle max_{20\%}(\vec{M}) \rangle$.

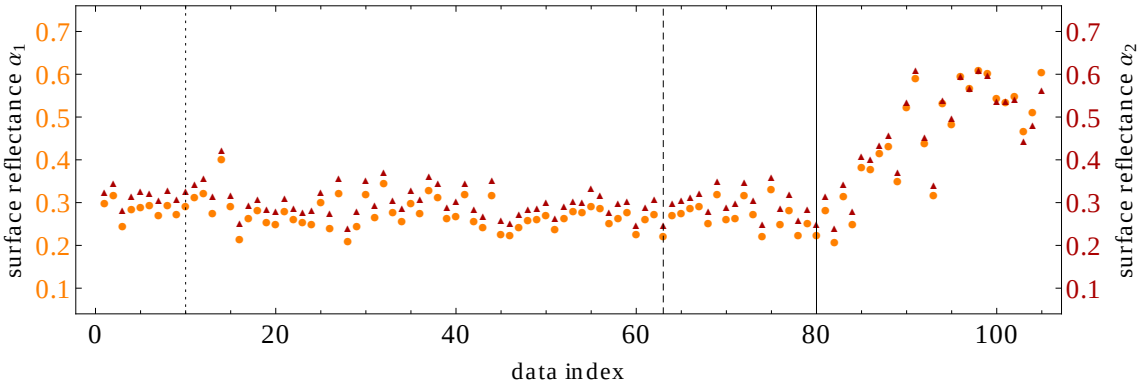

(b) Surface reflectance parameter α_1 and α_2.

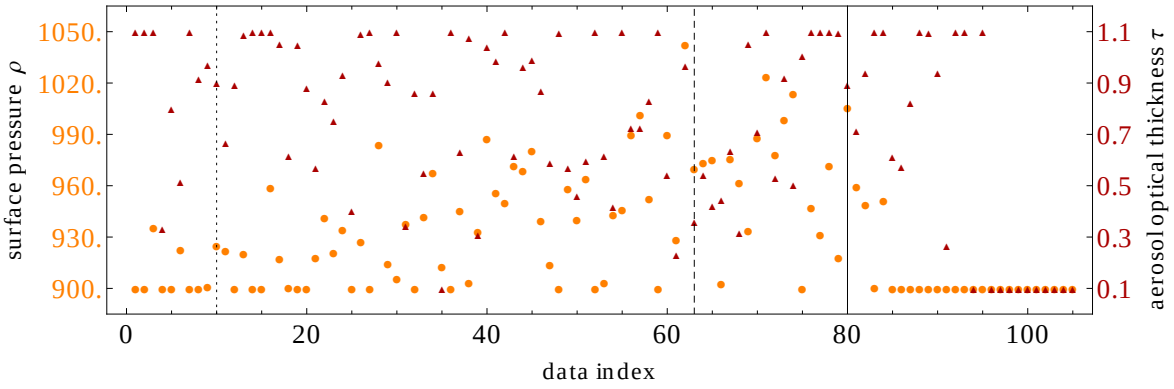

(c) Surface pressure ρ and aerosol optical thickness τ.

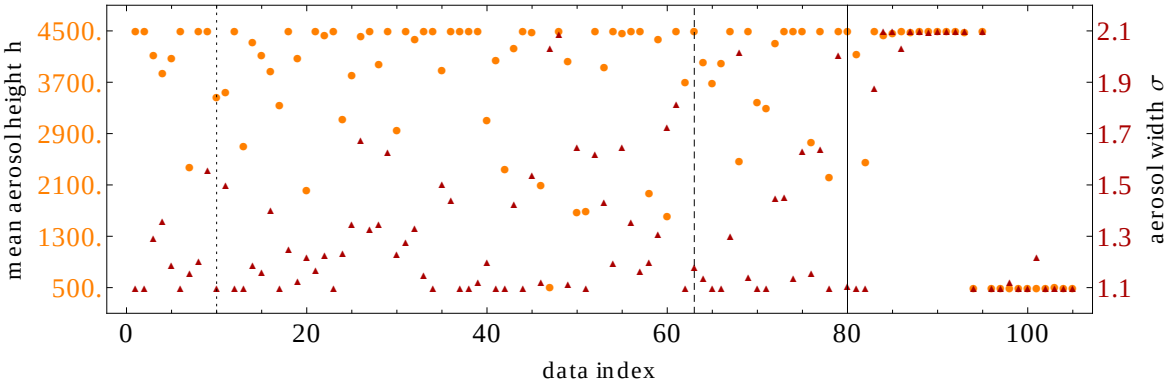

(d) Mean aerosol height h and aerosol width σ.

Figure 4.4.11: Overview of the TANSO-FTS measurements and inverted parameters. The results were sorted with respect to the mean absolute relative residual $\langle \delta_{\%} \rangle$ of the inversion result as shown in Figure 4.4.10. The dashed line represents the result shown in Figure 4.4.7 and the dotted line the results shown in Figure 4.4.8.

4.4.6 Conclusion

The presented results show clearly that the constructed forward radiative transfer operator is able to reproduce the hyperspectral measurements of top-of-atmosphere radiance in the O_2A band made by TANSO-FTS over land. The physical meaning of the retrieved parameters can be established after validating the product. An operational retrieval system should take a representative variability of aerosol optical properties and the variation of the temperature profile of the atmosphere into account. Also, prior knowledge of surface pressure from NWP should be introduced.

From the presented results it is difficult to judge whether an attempt of retrieving aerosol vertical distribution from TANSO-FTS measurements would be a goal worthwhile to follow. The question can be split into two distinct parts. First, what are the scientific questions related to aerosol height that could benefit from an aerosol height product with the spacial and temporal resolution of TANSO-FTS. Second, is it possible to retrieve aerosol vertical information from TANSO-FTS measurements with sufficient accuracy?

Both questions are closely related and can be answered for a specific field of research. If aerosol cloud interactions are to be studied, the possible benefit is likely low. Most interesting is the aerosol height close to horizontal borders of clouds and to study the entrainment effects [192, 193] (also compare Figure 4.1.5). If a measurement is affected by a cloud, then the aerosol vertical retrieval is not possible, although the cloud top pressure could possibly be derived. The next closest GOSAT measurement point is at least tens of kilometers away, which is also the scale at which aerosol properties typically vary. Hence, the use of a hypothetical GOSAT product is limited.

That being said, there might be enough research questions that could accept the spacial and temporal limitations of the product. However, such type of research could likely be also conducted using the data products provided by CALIOP [129].

The accuracy of a hypothetical product can only be established after validation with ground truth measurements, such as AERONET data for total aerosol optical thickness and EARLYNET [126] data for aerosol vertical distributions, which are beyond the scope of this work. However, the inversion quality indicates promising results. The results are merely a proof of concept for deriving aerosol vertical distribution from spaceborne radiance measurements. The limitations posed by the coarse spacial and temporal resolution of GOSAT could be overcome by future imaging instruments such as OCO2 [194], FLORIS [150], or CarbonSat [147].

Acknowledgments

I would like to thank Luis Guanter for providing the GOSAT data, and also for many helpful discussions about the retrieval results. I also thank Christian Frankenberg, who pointed out that the research of Tran et al. explains most of the systematic residuals that are not caused by the temperature profile.

CONCLUSION

The presented dissertation deals with some selected aspects that are important for the successful application of remote sensing techniques for the atmosphere and ocean. The sections of each chapter can be read independently and are with the exception[25] of Section 4.3 and Section 4.4 published in peer-reviewed journals. The subsections are written in the style of research papers, so that textbook knowledge of the subject area is required. A very brief introduction into the research area is given at the beginning of each chapter. The following is a brief summary of the main findings of the individual research results.

In the Chapter **Polarimetry**, results are presented that allow the construction of optimal multispectral polarimeters, which are based on the use of polarizing filters and waveplates. An analytical solution for the optimal positioning of polarizing filters and waveplates for a polarimeter with four optics was found and discussed. Moreover, a numerical minimization approach is used to derive an optimal polarimeter configuration, which further minimizes the measurement error for the most commonly anticipated measurements. Waveplates, which act as a converter of linear and circular polarization, are a central optical element for the discussed class of polarimeters. Their optical properties are critical for the design of a polarimeter and for deriving the polarization state from the measurements of the polarimeter. A robust method for determining their optical properties is introduced, discussed, and successfully tested in the laboratory. The method has been designed such that errors in the experiment, and deviations of their actual optical properties from their theoretically assumed optical properties, become explicitly visible and can be interpreted as a measurement error.

The Chapter **Vector Radiative Transfer** describes how the former scalar radiative transfer model MOMO, which has a long tradition of successful applications at the Institute for Space Sciences at the *Freie Universität Berlin*, has been extended to a full vector model. It is now able to simulate the vector radiance field in a plane parallel system of a coupled atmosphere and ocean with a wind roughened interface. This allows to more accurately simulate the radiance field, since the simplifications of a scalar model can cause errors of the simulated radiance of a few percent. In addition, but not limited to, the vector components of the radiance can be used for the remote sensing of aerosols and hydrosols. The model is described, was extensively tested, and validated using several independent methods.

The validation of radiative transfer models is a key step in their development and implementation, and a new method for their validation was proposed. The method is based on the fact that it is much more difficult to implement a system that solves the radiative transfer equation, than to implement a system that verifies whether a given radiance field is in fact the solution of the radiative transfer equation for the system under consideration. Such a verification scheme for the simple case of Rayleigh scattering was implemented, its description published, and its implementation provided to the scientific community. Beyond that, a radiance data set with high spatial resolution, which was verified by the scheme, was made available and can now be used for the validation of radiative transfer models. The method can be extended to cases for which no validation data set is available, for example for the coupled atmosphere-ocean system or systems in which inelastic scattering cannot be neglected.

Described in the Chapter **Applications to Remote Sensing** are research results within the field of the remote sensing of aerosols and hydrosols, which were among other tools obtained by using the new vector MOMO model. In a first application, the influence of salinity and temperature of ocean water and the neglecting of polarization in radiative transfer simulations for the simulation of the radiance field at the upper boundary of the ocean and atmosphere was estimated. The obtained results are significant, because these effects are neglected in major ocean color remote sensing schemes. It was found that the upward directed radiance at the upper boundary of the ocean in the $412nm$ MERIS channel can change by up to 16%

[25] A highly condensed summary of Section 4.3 was submitted to the proceedings of the IRS 2012 Conference, for which a peer review process is applied.

when the salinity of the ocean changes by $25PSU$. Such a change in salinity is similar to the difference in salinity between ocean water and the northernmost parts of the Baltic Sea. The effect is strongest for clearest waters and decreases with increasing wavelength and chlorophyll concentration. A temperature change of $10°C$ can cause a radiance change of 2%, which has a strong spectral dependence. Neglecting polarization in the radiative transfer can cause errors of up to $\pm 8\%$, which depend strongly on viewing geometry. Taken together, the simulations have shown that for the simulation of case one waters, all three effects should be considered in order to minimize effects on ocean color remote sensing schemes.

Furthermore, the possibilities for the remote sensing of aerosol vertical distribution from spaceborne hyperspectral radiance measurements in oxygen absorption bands were discussed based on ESA's upcoming FLEX mission. A hypothetical instrument with much higher spectral resolution was additionally simulated and included into the discussion. The aerosol vertical profile was modeled as a sum of up to three logarithmic normal distribution functions. An analysis of measurements of the spaceborne LIDAR CALIOP has shown that on regional to global scales, the aerosol vertical distribution can be well approximated by using two modes. To estimate the expected retrieval error for the FLEX mission, synthetic simulations and inversions were used. It was found that a monomodal profile can be derived with an error of about 30% for the aerosol average height and width. The retrieval error highly depends on the spectral resolution of the instrument, its signal to noise ratio, the aerosol optical thickness, the reflectivity of the surface, and the number of to be inverted aerosol modes. The retrieval error for bimodal profiles is so high that standard cases can hardly be distinguished. If the inversion of a monomodal profile is used for a bimodal profile, the result is an intermediate value. This indicates that a monomodal approach could provide effective aerosol average heights and widths. Higher spectral resolution and a lower signal-to-noise ratio decrease the retrieval error. One advantage of the FLEX mission, if compared to the concepts of other upcoming missions, is its high spatial resolution, which can help to reduce additional errors and trends caused by surface inhomogeneities within a single measurement pixel.

Further described is how the techniques of the FLEX feasibility study are applied to measurements of the Fourier spectrometer TANSO-FTS, which is on board on the GOSAT satellite. Its measurements are characterized by a coarse spatial but very high spectral resolution in the oxygen A-band. A simple inversion scheme, based on a lookup table and the differential evolution technique, was implemented and applied to a data set of 104 measurements, and 80 of them could be reproduced with only minor residuals. Failed inversion attempts can be most likely explained by the influence of the measurement by clouds. The results provide a proof-of-concept for the developed techniques for the remote sensing of aerosol vertical distribution. Remaining systematic deviations of measurements and simulations are caused by the constant temperature profile used in the simulations, limits of the absorption model for molecular lines, and limitations of the HITRAN 2008 database. In particular affected are oxygen absorption lines, which are caused by line mixing and collision induced absorption. Also, the used Voigt line model caused a systematic overestimation of the absorption at the edge of the oxygen A-band. Despite the remaining deviations, the successful simulation of the measurements showed that the developed model is suitable for its application and gave promising results for the future remote sensing of the vertical aerosol distribution from spaceborne radiance measurements in oxygen absorption bands.

ZUSAMMENFASSUNG

Die vorliegende Arbeit beschäftigt sich mit einigen ausgewählten Aspekten, die für eine erfolgreiche Anwendung von Fernerkundungstechniken für Atmosphäre und Ozean wichtig sind. Die Unterkapitel der einzelnen Kapitel dieser Arbeit können unabhängig voneinander gelesen werden und wurden mit Ausnahme von Unterkapitel[26] 4.3 und 4.4 in Fachzeitschriften veröffentlicht, die ein *Peer Review* Verfahren anwenden. Die Unterkapitel wurden im Stil von Fachaufsätzen verfasst, so dass Lehrbuchwissen für das jeweilige Fachgebiet vorausgesetzt wird. Am Anfang eines jeden Kapitels wurde eine sehr kurze Einführung in das jeweilige Fachgebiet gegeben. In der folgenden Zusammenfassung werden kurz die wesentlichen Ergebnisse der einzelnen Arbeiten dargestellt.

Im Kapitel **Polarimetrie** werden Ergebnisse präsentiert, die den Aufbau von optimalen multispektralen Polarimetern, welche auf der Anwendung von Polarisationsfiltern und Wellenplatten bestehen, ermöglichen. Es wurde eine analytische Lösung für die optimale Positionierung von Polarisationsfiltern und Wellenplatten für ein Polarimeter mit vier Optiken gefunden und diskutiert. Darüber hinaus wurde ein nummerischer Minimierungsansatz angewendet, um eine optimale Polarimeterkonfiguration abzuleiten, die zusätzlich den Messfehler für die am häufigsten angenommenen Messungen minimiert. Ein zentrales optisches Element für die diskutierte Klasse von Polarimetern sind Wellenplatten, die im Wesentlichen als Konverter von linearer und zirkularer Polarisation fungieren. Ihre optischen Eigenschaften sind entscheidend für das Design eines Polarimeters sowie für die Ableitung des Polarisationszustandes aus den Messungen des Polarimeters. Es wurde eine robuste Methode für die Bestimmung der optischen Eigenschaften von Wellenplatten entwickelt, diskutiert und erfolgreich im Labor getestet. Die Methode wurde so konstruiert, dass Fehler im Experiment und Abweichungen der wirklichen optischen Eigenschaften von den theoretisch angenommenen optischen Eigenschaften explizit sichtbar werden und als Messfehler interpretiert werden können.

Im Kapitel **Vektor-Strahlungstransport** wurde beschrieben, wie das vormals skalare Strahlungstransportmodell MOMO, das seit langem erfolgreich am Institut für Weltraumwissenschaften der Freien Universität Berlin eingesetzt wird, zu einem vollen Vektormodell erweitert wurde. Es kann nun zur Simulation des vektoriellen Strahldichtefeldes für ein planparalleles System aus gekoppelter Atmosphäre und Ozean mit einer vom Wind aufgerauten Zwischenschicht benutzt werden. Dies ermöglicht bessere Simulationen des Strahldichtefeldes, da die Vereinfachungen eines skalaren Modells zu Abweichungen der Strahldichte in Bereiche von einigen Prozent führen können. Zudem können die Vektorkomponenten der Strahldichte unter anderem für die Fernerkundung von Aerosolen und Hydrosolen benutzt werden. Das Modell wurde beschrieben, umfangreich getestet und mit verschiedenen unabhängigen Methoden validiert.

Die Validierung von Strahlungstransportmodellen ist einer der wichtigsten Schritte in deren Entwicklung und Implementierung und in der vorliegenden Arbeit wurde eine neue Methode zur Validierung vorgeschlagen. Diese basiert auf der Tatsache, dass es weitaus schwieriger ist ein System zu implementieren, das die Strahlungstransportgleichung löst, als ein System zu implementieren, welches testet, ob ein gegebenes Strahldichtefeld die Lösung der Strahlungstransportgleichung für das betrachtete System ist. Ein solches Verifikationssystem für den einfachen Fall von Rayleigh-Streuung wurde implementiert, publiziert und der wissenschaftlichen Gemeinschaft zur Verfügung gestellt. Zusätzlich wurde ein räumlich hoch aufgelöster Strahldichtedatensatz zur Verfügung gestellt, der mit dem System verifiziert wurde und nun für die Validierung von Strahlungstransportmodellen eingesetzt werden kann. Die Methode kann ohne besondere Schwierigkeiten auf Fälle erweitert werden, für die noch kein Validierungsdatensatz zur Verfügung steht, so zum Beispiel für das gekoppelte Atmosphären-Ozean-System oder Systeme, in denen inelastische Streuung nicht vernachlässigt werden kann.

Im Kapitel **Anwendungen in der Fernerkundung** wurden Forschungsergebnisse aus dem Bereich der Fernerkundung von Aerosolen und Hydrosolen beschrieben, die unter anderem mit Hilfe des erweiterten MOMO Modells gewonnen wurden. In einer ersten Anwendung wurde

[26] Eine stark verkürzte Zusammenfassung von Unterkapitel 4.3 wurde als Beitrag zum Tagungsbericht der IRS 2012 Konferenz eingereicht, für den das *Peer Review* Verfahren angewendet wurde.

der Einfluss von Salzgehalt und Temperatur von Ozeanwasser sowie die Vernachlässigung von Polarisation in Strahlungstransportsimulationen auf Strahldichten am Oberrand von Ozean und Atmosphäre abgeschätzt. Die daraus gewonnenen Ergebnisse sind bedeutsam, da die untersuchten Einflüsse bisher in den wichtigsten Ozeanfarben-Fernerkundungssystemen vernachlässigt werden. Es zeigte sich, dass sich die Strahldichte am Ozeanoberrand im $412nm$ MERIS Kanal um bis zu 16% ändern kann, wenn sich der Salzgehalt des Ozeans um $25PSU$ ändert. Eine solche Änderung des Salzgehaltes entspricht in etwa dem Unterschied zwischen Ozeanwasser und den nördlichsten Gebieten der Ostsee. Der Effekt ist am stärksten für klares Wasser und wird kleiner mit ansteigender Wellenlänge und Chlorophyllkonzentration. Eine Temperaturänderung von $10°C$ kann für solche Gewässer zu einer Strahldichteänderung von 2% führen, welche eine starke spektrale Abhängigkeit aufweist. Wird Polarisation im Strahlungstransfer vernachlässigt, so kann dies zu Fehlern von bis zu $\pm 8\%$ führen, die stark von der Beobachtungsgeometrie abhängen. Zusammen genommen haben die Simulationen gezeigt, dass bei der Simulation von *Case One Waters* alle drei Effekte berücksichtigt werden sollten, um Effekte auf Ozeanfarben-Fernerkundungssysteme zu minimieren.

Des Weiteren wurden in der vorliegenden Arbeit die Möglichkeiten zur Fernerkundung der vertikalen Aerosolverteilung aus weltraumgestützten hyperspektralen Strahldichtemessungen in Sauerstoff Absorptionsbanden anhand der bevorstehenden ESA Mission FLEX diskutiert. Ebenfalls wurde ein hypothetisches Instrument mit deutlich höherer spektraler Auflösung simuliert und in die Diskussion mit einbezogen. Das vertikale Aerosolprofil wurde als Summe von bis zu drei logarithmischen Normalverteilungsfunktionen modelliert. Eine Analyse von Messungen des weltraumgestützten Lidars CALIOP hat gezeigt, dass auf regionalen wie globalen Skalen die Aerosolverteilung mit Hilfe von zwei Moden gut approximiert werden kann. Um den Ableitungsfehler für die FLEX-Mission abzuschätzen, wurden synthetische Simulationen und Invertierungen benutzt. Es zeigte sich, dass ein monomodales Profil mit einem Fehler von circa 30% für die mittlere Aerosolhöhe und -ausdehnung abgeleitet werden konnte. Der Ableitungsfehler ist stark von der spektralen Auflösung des Instrumentes, dessen Signal-Rausch-Verhältnisses, der Aerosol optischen Dicke, der Reflektivität des Erdbodens und der Anzahl der Aerosolmoden abhängig. Der Ableitungsfehler für bimodale Profile ist so hoch, dass Standardfälle kaum voneinander unterschieden werden können. Wird eine monomodale Inversion auf ein bimodales Profil angewendet, so ist das Ergebnis ein Zwischenwert. Das bedeutet, dass ein monomodaler Ansatz effektive Aerosolmittelwertshöhen und -breiten liefern könnte. Eine größere spektrale Auflösung und ein geringeres Signal-Rausch-Verhältnis verringern den Ableitungsfehler. Ein Vorteil des FLEX-Konzeptes im Vergleich zu Konzepten anderer bevorstehender Missionen ist dessen hohe räumlich Auflösung, die dazu beitragen kann, zusätzliche Ableitungsfehler und Tendenzen, die von Bodeninhomogenitäten innerhalb eines Messpixels verursacht werden, zu verkleinern.

Weiter wurde beschrieben, wie die Techniken aus der obig beschriebenen FLEX Machbarkeitsstudie auf Messungen des Fourier Spektrometers TANSO-FTS, welches sich an Bord des Satelliten GOSAT befindet, angewendet wurden. Dessen Messungen sind durch eine grobe räumliche, aber sehr hohe spektrale Auflösung in der Sauerstoff A-Bande charakterisiert. Ein einfaches auf einer Nachschlagetabelle und der *differential evolution* Technik basierendes Inversionssystem wurde implementiert und auf einen Datensatz von 104 Messungen angewendet. Davon konnten 80 mit nur geringen Fehlern reproduziert werden. Fehlgeschlagene Inversionen sind höchst wahrscheinlich durch die Beeinflussung der Messung durch Wolken zu erklären. Die Ergebnisse stellen einen Machbarkeitsbeweis für die entwickelten Konzepte zur Fernerkundung der vertikalen Aerosolverteilung dar. Systematische Abweichungen von Messungen und Simulationen können durch das konstante Temperaturprofil in den Simulationen, Limitierungen des Absorptionsmodell für molekulare Linien und Limitierungen der HITRAN 2008 Datenbank erklärt werden. Insbesondere betroffen sind Sauerstoff-Absorptionslinien, die durch *line mixing* und *collision induced absorption* verursacht werden. Zusätzlich zeigte sich, dass das benutzte Voigt Linien Modell eine systematische Überschätzung der Absorption am Rand der Sauerstoff A-Bande verursacht. Trotz der beschriebenen Abweichungen zeigt die erfolgreiche Simulation der Messungen, dass das entwickelte Vorwärtsmodell für die Anwendung geeignet ist. Insgesamt wurden vielversprechende Ergebnisse für die zukünftige Ableitung der vertikalen Aerosolverteilung aus Strahldichtemessungen in Sauerstoff-Absorptionsbanden erbracht.

BIBLIOGRAPHIE

[1] René Preusker and Thomas Ruhtz. Airborne Multi-Spectral Sunphoto- & Polarimeter (AMSSP). DFG - Proposal. 1, 2.2.5, 2.3.2

[2] André Hollstein, Thomas Ruhtz, Jürgen Fischer, and René Preusker. Optimization of system parameters for a complete multispectral polarimeter. *Applied Optics*, 48:4767–4773, 2009.

[3] André Hollstein and Thomas Ruhtz. Method for retrieving the polarization properties of a waveplate assembled in a multispectral, complete polarimeter. *Opt. Lett.*, 34(17):2599–2601, Sep 2009.

[4] André Hollstein. Entwicklung und Aufbau eines Flugzeug gestützten, multispektralen Polarimeters zur Fernerkundung der Atmosphäre. Master's thesis, Freie Universtät Berlin,Institute for Space Science, 12 2008. `http://userpage.fu-berlin.de/geoiss/ress/dipl/Diplom_Hollstein_Andre.pdf`. 1, 2.3.2

[5] André Hollstein and Jürgen Fischer. Radiative Transfer Solutions for Coupled Atmosphere Ocean Systems Using the Matrix Operator Technique. *Journal of Quantitative Spectroscopy and Radiative Transfer*, 113(7):536 – 548, 2012. 3.3.4, 3.3.4, 4.2.2, 4.2.3, 4.2.5, 4.2.5, 4.3.5

[6] André Hollstein. Verification of radiative transfer results by inserting them into the RTE: A demonstration for rayleigh scattering. *Journal of Quantitative Spectroscopy and Radiative Transfer*, 113(15):1970 – 1973, 2012.

[7] André Hollstein and Jürgen Fischer. Effects of salinity, temperature, and polarzation on top of atmosphere and water leaving radiances for case one waters. *Applied Optics*, 10 2012. doc. ID 169561, accepted 10/17/2012.

[8] André Hollstein and Jürgen Fischer. Salinity, temperature and polarization effects for simulated radiances in a case one waters atmosphere ocean system. IRS2012-9, 8 2012.

[9] André Hollstein and Jürgen Fischer. Possibilities for remote sensing of aerosol vertical structure using the O_2A band: A sensitivity study concerning polarization, spectral resolution, instrument level, and various scenes over land. IRS2012-65, 8 2012.

[10] André Hollstein and Florian Filipitsch. Possibilities for the retrieval of aerosol vertical profiles from space using hyper spectral radiance measurements in oxygen absorption bands. submitted to the Proceedings of IRS2012, 8 2012.

[11] Michael I. Mishchenko. Directional radiometry and radiative transfer: A new paradigm. *Journal of Quantitative Spectroscopy and Radiative Transfer*, In Press, Corrected Proof:–, 2011. 2, 1

[12] Michael I. Mishchenko. Poynting–stokes tensor and radiative transfer in discrete random media: the microphysical paradigm. *Opt. Express*, 18(19):19770–19791, Sep 2010. 2

[13] J. P. Woerdman A.Aiello. Linear Algebra for Mueller Calculus. *arXiv:math-ph/0412061v3*, 2006. 3, 2.2.2, 2.3.3, 3.2.3

[14] Gábor Horváth and Dezsö Varju. *Polarized Light in Animal Vision: Polarization Patterns in Nature*. Springer, 2003. 2.1

[15] S. N. Patek, W. L. Korff, and R. L. Caldwell. Biomechanics: Deadly strike mechanism of a mantis shrimp. *Nature*, 428(6985):819–820, 2004. `http://dx.doi.org/10.1038/428819a`. 2.1

[16] Sonja Kleinlogel and Andrew G. White. The secret world of shrimps: Polarisation vision at its best. *PLoS ONE*, 3(5):e2190, 05 2008. 2.1, 2.1.2

[17] Silke Baron. Closeup of a stomatopod crustacean (mantis shrimp) Odontodactylus scyllarus taken in the Andaman Sea off Thailand in February, 2008. Image from Wikimedia Commons under the Creative Commons Attribution 2.0 Generic licence. `http://en.wikipedia.org/wiki/File:OdontodactylusScyllarus.jpg`, 2008. 2.1.3

[18] Brian Cairns, editor. *The Need for Aerosol and Cloud Measurements from Space: Essential Contributions from a Rapid Reflight of the Aerosol Polarimetry Sensor*. NASA Goddard Institute for Space Studies, July 2011. 2.1

[19] B.N. Holben, T.F. Eck, I. Slutsker, D. Tanré, J.P. Buis, A. Setzer, E. Vermote, J.A. Reagan, Y.J. Kaufman, T. Nakajima, F. Lavenu, I. Jankowiak, and A. Smirnov. Aeronet a federated instrument network and data archive for aerosol characterization. *Remote Sensing of Environment*, 66(1):1 – 16, 1998. 2.1, 4.4.2

[20] Bréon et al. Cloud droplet effective radius from spaceborne polarization measurements. *Geophys. Res Letters*, 25:11, 1998. `http://smsc.cnes.fr/POLDER/lien7_pub.htm`. 2.1

[21] R. C. Jones. A new calculus for the treatment of optical systems V.A more general formulation, and description of another calculus. *J. Opt. Soc.*, 37, 1947. 2.2.2

[22] Leonard Mandel and Emil Wolf. *Optical Coherence and Quantum Optics*. Cambridge University Press, 1995. 2.2.2

[23] E.Wolf M. Born. *Principles of Optics*. Cambridge U. Press, 7th edition, 1999. 2.2.2, 2.3.3

[24] D. S. Sabatke, M. R. Descour, E. L. Dereniak, W. C. Sweatt, S. A. Kemme, and G. S. Phipps. Optimization of retardance for a complete Stokes polarimeter. *Optics Letters,*, 25(11):802–804, 2000. 2.2.2, 2.2.3, 2.2.3, 2.3.2

[25] Amrit Ambirajan and Jr. Dwight C. Look. Optimum angles for a polarimeter: part i. *Optical Engineering*, 34(6):1651–1655, 1995. 2.2.3, 2.2.3, 2.2.4, 2.3.2

[26] J. Scott Tyo. Design of Optimal Polarimeters: Maximization of Signal-to-Noise Ratio and Minimization of Systematic Error. *Applied Optics*, 41(4):619–630, February 2002. 2.2.3, 2.2.3, 2.2.5

[27] J. S. Tyo. Optimum linear combination strategy for an n-channel polarization-sensitive imaging or vision system. *J. Opt. Soc. Am. A*, 15(2):359–366, Feb 1998. 2.2.4

[28] Thomas Ruhtz. Development Guidelines URMS/AMSSP Version 1.01, 7. Januar 2008. Contact: thomas.ruhtz@fu-berlin.de; Freie Universität Berlin, Institute for Space Sciences. 2.2.5, 2.3.2

[29] Subrahmanyan Chandrasekhar. *Radiative transfer*. Courier Dover Publications, 1960. 1, 3.2.8, 4.2.3

[30] Clive D. Rodgers. *Inverse methods for athmospheric sounding*. World Scientific Publishing Co. Pte. Ltd., 2000. 2, 4.3.9

[31] K.L. Coulson, J.V. Dave, and Z. Sckera. *Tables related to radiation emerging from a planetary atmosphere with Rayleigh scattering*. University of California Press,Berkeley, 1960. 4, 3.2.7, 3.2.8, 3.3.2

[32] Vijay Natraj, King-Fai Li, and Yuk L. Yung. Rayleigh scattering in planetary atmospheres: Corrected tables through accurate computation of x and y functions. *The Astrophysical Journal*, 691(2):1909, 2009. 4, 3.2.7, 3.2.8, 3.2.7, 3.3.2, 3.3.4

[33] Alexander A. Kokhanovsky, Vladimir P. Budak, Celine Cornet, Minzheng Duan, Claudia Emde, Iosif L. Katsev, Dmitriy A. Klyukov, Sergey V. Korkin, L. C-Labonnote, Bernhard Mayer, Qilong Min, Teruyuki Nakajima, Yoshifumi Ota, Alexander S. Prikhach, Vladimir V. Rozanov, Tatsuya Yokota, and Eleonora P. Zege. Benchmark results in vector atmospheric radiative transfer. *Journal of Quantitative Spectroscopy and Radiative Transfer*, In Press, Corrected Proof:–, 2010. 4, 3.2.7, 3.2.9, 3.2.8, 3.3.2

[34] Bernhard Mayer and Claudia Emde. International working group on polarized radiative transfer (IPRT). `http://www.meteo.physik.uni-muenchen.de/~iprt/doku.php`. 4

[35] George W. Kattawar and Charles N. Adams. Stokes vector calculations of the submarine light field in an atmosphere-ocean with scattering according to a rayleigh phase matrix: Effect of interface refractive index on radiance and polarization. *Limnology and Oceanography*, 34(8):1453–1472, 1989. 3.2.2, 3.2.4, 3.2.17, 3.3.3, 4.2.3, 4.2.5

[36] Teruyuki Nakajima and Masayuki Tanaka. Effect of wind-generated waves on the transfer of solar radiation in the atmosphere-ocean system. *Journal of Quantitative Spectroscopy and Radiative Transfer*, 29(6):521 – 537, 1983. 3.2.2, 3.2.17, 4.2.3

[37] Tsutomu Takashima. Polarization effect on radiative transfer in planetary composite atmospheres with interacting interface. *Earth, Moon, and Planets*, 33:59–97, 1985. 3.2.2

[38] Malik Chami, Richard Santer, and Eric Dilligeard. Radiative transfer model for the computation of radiance and polarization in an ocean-atmosphere system: Polarization properties of suspended matter for remote sensing. *Appl. Opt.*, 40(15):2398–2416, May 2001. 3.2.2, 3.2.6, 3.2.17, 4.2.4, 4.2.4

[39] Frank Fell and Jürgen Fischer. Numerical simulation of the light field in the atmosphere-ocean system using the matrix-operator method. *Journal of Quantitative Spectroscopy and Radiative Transfer*, 69(3):351 – 388, 2001. 3.2.2, 3.2.4, 3.2.11, 4.2.2, 4.2.5, 4.3.5

[40] Jacek Chowdhary, Brian Cairns, and Larry D. Travis. Contribution of water-leaving radiances to multiangle, multispectral polarimetric observations over the open ocean: bio-optical model results for case 1 waters. *Appl. Opt.*,

45(22):5542–5567, Aug 2006. 3.2.2, 3.2.6, 3.2.11, 4.2.4, 4.2.4

[41] Xianqiang He, Yan Bai, Qiankun Zhu, and Fang Gong. A vector radiative transfer model of coupled ocean-atmosphere system using matrix-operator method for rough sea-surface. *Journal of Quantitative Spectroscopy and Radiative Transfer*, 111(10):1426 – 1448, 2010. 3.2.2

[42] Peng-Wang Zhai, Yongxiang Hu, Jacek Chowdhary, Charles R. Trepte, Patricia L. Lucker, and Damien B. Josset. A vector radiative transfer model for coupled atmosphere and ocean systems with a rough interface. *Journal of Quantitative Spectroscopy and Radiative Transfer*, 111(7-8):1025 – 1040, 2010. 3.2.2, 7, 3.2.14, 3.3.2, 4.2.5, 4.2.5

[43] Jürgen Fischer and Hartmut Grassl. Radiative transfer in an atmosphere-ocean system: an azimuthally dependent matrix-operator approach. *Appl. Opt.*, 23(7):1032–1039, Apr 1984. 3.2.2, 4.3.5

[44] Ralf Bennartz and Jürgen Fischer. A modified k-distribution approach applied to narrow band water vapour and oxygen absorption estimates in the near infrared. *Journal of Quantitative Spectroscopy and Radiative Transfer*, 66(6):539 – 553, 2000. 3.2.2, 4.2.5, 4.3.5, 4.4.5

[45] Thomas Heege and Jürgen Fischer. Mapping of water constituents in lake constance using multispectral airborne scanner data and a physically based processing scheme. *Canadian Journal of Remote Sensing*, 30(1):77–86, 2004. 3.2.2

[46] L. Guanter, L. Alonso, L. Gomez-Chova, M. Meroni, R. Preusker, J. Fischer, and J. Moreno. Developments for vegetation fluorescence retrieval from spaceborne high-resolution spectrometry in the O_2A and O_2B absorption bands. *Journal of Geophysical Research*, 115, 2010. 3.2.2

[47] Tinglu Zhang, Frank Fell, Zhi-Shen Liu, Rene Preusker, Jürgen Fischer, and Ming-Xia He. Evaluating the performance of artificial neural network techniques for pigment retrieval from ocean color in case i waters. *JOURNAL OF GEOPHYSICAL RESEARCH*, 108, 2003. 3.2.2, 4.2.4

[48] Rasmus Lindstrot, Rene Preusker, and Jürgen Fischer. The retrieval of land surface pressure from meris measurements in the oxygen a band. *Journal of Atmospheric and Oceanic Technology*, 26(7):1367–1377, 2009. 3.2.2

[49] J. Scott Tyo. Design of optimal polarimeters: Maximization of signal-to-noise ratio and minimization of systematic error. *Appl. Opt.*, 41(4):619–630, Feb 2002. 3.2.3

[50] S. Twomey, H. Jacobowitz, and H. B. Howell. Matrix methods for multiple-scattering problems. *Journal of Atmospheric Sciences*, 23:289–298, 1966. 3.2.4, 3.2.4

[51] I. P. Grant and G. E. Hunt. Discrete space theory of radiative transfer. i. fundamentals. *Proceedings of the Royal Society of London. Series A, Mathematical and Physical Sciences*, 313(1513):183–197, 1969. 3.2.4, 3.2.4

[52] I. P. Grant and G. E. Hunt. Solution of radiative transfer problems using the invariant s_n method. *Monthly Notices of the Royal Astronomical Society*, 141:27–41, 1968. 3.2.4

[53] Van de Hulst. A new look at multiple scattering. *NASA Institute for Space Studies*, 1965. 3.2.4

[54] I. P. Grant and G. E. Hunt. Discrete space theory of radiative transfer. ii. stability and non- negativity. *Proceedings of the Royal Society of London. Series A, Mathematical and Physical Sciences*, 313:199–216, 1969. 3.2.4

[55] Rüdiger Röttgers, Roland Doerfer, David McKee, and Wolfgang Schönfeld. Pure water spectral absorbtion, scattering, and real part of refractive index model. Algorithm Technical Basis Document, 2010. 3.2.5, 3.2.5, 3.2.5, 4.2.3, 4.2.3

[56] Xiaodong Zhang and Lianbo Hu. Estimating scattering of pure water from densityfluctuation of the refractive index. *Opt. Express*, 17(3):1671–1678, 2009. 3.2.5, 3.2.5, 4.2.3

[57] André Morel and Louis Prieur. Analysis of variations in ocean color. *Limnology and Oceanography*, 22(4):709–722, 1977. 3.2.5, 4.2.5

[58] Robin M. Pope and Edward S. Fry. Absorption spectrum (380–700 nm) of pure water. ii. integrating cavity measurements. *Appl. Opt.*, 36(33):8710–8723, 1997. 3.2.5, 5

[59] Z. Lu. *Optical absorbtion of pure water in the blue and ultraviolet.* PhD thesis, Texas A&M University, 2006. 3.2.5, 5

[60] L. Wang. *Measuring optical absorption coefficient of pure water in UV using the integrating cavity absorption meter,.* PhD thesis, Texan A&M University, 2008. 3.2.5, 5

[61] David J. Segelstein. *The complex refractive index of water*. PhD thesis, Department of Physics, University of Missouri Kansas City, 1981. 3.2.5, 5, 4.2.3

[62] David M. Wieliczka, Shengshan Weng, and Marvin R. Querry. Wedge shaped cell for highly absorbent liquids: infrared optical constants of water. *Appl. Opt.*, 28(9):1714–1719, 1989. 3.2.5, 5

[63] Jean-Joseph Max and Camille Chapados. Isotope effects in liquid water by infrared spectroscopy. iii. H_2O and D_2O spectra from 6000 to 0 cm^{-1}. *The Journal of Chemical Physics*, 131(18):184505, 2009. 3.2.5, 4.2.3, 5

[64] Rüdiger Röttgers. Technical note. unpublished data, 2010. 3.2.5, 5

[65] Annick Bricaud, Andre Morel, and Louis Prieur. Optical efficiency factors of some phytoplankters. *Limnology and Oceanography*, 28(5):pp. 816–832, 1983. 3.2.6, 4.2.4

[66] André Morel, David Antoine, and Bernard Gentili. Bidirectional reflectance of oceanic waters: Accounting for raman emission and varying particle scattering phase function. *Appl. Opt.*, 41(30):6289–6306, Oct 2002. 3.2.6, 4.2.4, 4.2.4

[67] André Morel and Annick Bricaud. Theoretical results concerning light absorption in a discrete medium, and application to specific absorption of phytoplankton. *Deep Sea Research Part A. Oceanographic Research Papers*, 28(11):1375 – 1393, 1981. 3.2.6, 4.2.4

[68] R. D. M. Garcia and C. E. Siewert. A generalized spherical harmonics solution for radiative transfer models that include polarization effects. *Journal of Quantitative Spectroscopy and Radiative Transfer*, 36(5):401 – 423, 1986. 3.2.7

[69] R. D. M. Garcia and C. E. Siewert. The fn method for radiative transfer models that include polarization effects. *Journal of Quantitative Spectroscopy and Radiative Transfer*, 41(2):117 – 145, 1989. 3.2.7

[70] K. F. Evans and G. L. Stephens. A new polarized atmospheric radiative transfer model. *Journal of Quantitative Spectroscopy and Radiative Transfer*, 46(5):413 – 423, 1991. 3.2.7, 3.3.2

[71] W.M.F. Wauben and J.W. Hovenier. Polarized radiation of an atmosphere containing randomly-oriented spheroids. *Journal of Quantitative Spectroscopy and Radiative Transfer*, 47(6):491 – 504, 1992. 3.2.7

[72] A. Rozanov, V. Rozanov, M. Buchwitz, A. Kokhanovsky, and J.P. Burrows. Sciatran 2.0 - a new radiative transfer model for geophysical applications in the 175-2400nm spectral region. *Advances in Space Research*, 36(5):1015 – 1019, 2005. 3.2.7

[73] Curtis D. Mobley, Bernard Gentili, Howard R. Gordon, Zhonghai Jin, George W. Kattawar, André Morel, Phillip Reinersman, Knut Stamnes, and Robert H. Stavn. Comparison of numerical models for computing underwater light fields. *Appl. Opt.*, 32(36):7484–7504, Dec 1993. 3.2.11, 3.3.2

[74] Jacek Chowdhary. *Multiple scattering of polarized light in atmosphere- ocean systems: Application to sensitivity analyses of aerosol polarimetry*. PhD thesis, COLUMBIA UNIVERSITY, 2000. 3.2.11

[75] J. I. Antonov, D. Seidov, T. P. Boyer, R. A. Locarnini, A. V. Mishonov, H. E. Garcia, O. K. Baranova, M. M. Zweng, and D. R. Johnson. *World Ocean Atlas 2009 - Volume 2: Salinity*. NOAA Atlas NESDIS 69, U.S. Government Printing Office, Washington, D.C., 2009. 3.2.15, 4.1, 4.1.3a, 4.2.2, 4.2.5

[76] M. Sancer. Shadow-corrected electromagnetic scattering from a randomly rough surface. *IEEE Transactions on Antennas and Propagation*, 17:577 – 585, 1969. 3.2.17, 4.2.3

[77] Charles Cox and Walter Munk. Measurement of the roughness of the sea surface from photographs of the sun's glitter. *J. Opt. Soc. Am.*, 44(11):838–850, 1954. 3.2.17

[78] Naoto Ebuchi and Shoichi Kizu. Probability distribution of surface wave slope derived using sun glitter images from geostationary meteorological satellite and surface vector winds from scatterometers. *Journal of Oceanography*, 58:477–486, 2002. 3.2.17

[79] S.A. Clough, M.W. Shephard, E.J. Mlawer, J.S. Delamere, M.J. Iacono, K. Cady-Pereira, S. Boukabara, and P.D. Brown. Atmospheric radiative transfer modeling: a summary of the aer codes. *Journal of Quantitative Spectroscopy and Radiative Transfer*, 91(2):233 – 244, 2005. 3.3.2

[80] Svetlana Y. Kotchenova, Eric F. Vermote, Raffaella Matarrese, and Jr. Frank J. Klemm. Validation of a vector version of the 6s radiative transfer code for atmospheric correction of satellite data. part i: Path radiance. *Appl. Opt.*, 45(26):6762–6774, Sep 2006. 3.3.2

[81] B. Mayer and A. Kylling. Technical note: The libradtran software package for radiative transfer calculations - description and examples of use. *Atmospheric Chemistry and Physics*, 5(7):1855–1877, 2005. 3.3.2

[82] W. A. Stein et al. *Sage Mathematics Software*. The Sage Development Team. `http://www.sagemath.org`. 3.3.2

[83] Inc. Wolfram Research. *Mathematica Edition: Version 8.0*. Wolfram Research, Inc., 2010. 3.3.2

[84] S. Rocks, P. Harrison, and D. Crump. *Proceedings of the Twelfth Annual UK Review Meeting on Outdoor and Indoor Air Pollution Research, 20-21 April 2009, Cranfield University*. Institute of Environment and Health, 2009. 4.1.1a

[85] NMFS/NOAA Dr. Yaqin "Judy" Li. fish1903, NOAA's fisheries collection. National Oceanic Atmospheric Administration (NOAA), source: `http://www.photolib.noaa.gov/htmls/fish1903.htm`. 4.1.1b

[86] M. Rast, J. L. Bezy, and S. Bruzzi. The ESA medium resolution imaging spectrometer MERIS a review of the instrument and its mission. *International Journal of Remote Sensing*, 20(9):1681–1702, 1999. 4.1, 4.2.2, 4.2.5

[87] Charles R. McClain. A decade of satellite ocean color observations. *Annual Review of Marine Science*, 1(1):19–42, 2009. 4.1, 4.2.2, 4.3.2

[88] D. Antoine, L. Bourg, C. Brockmann, R. Doerffer, J. Fischer, G. Moore, R. Santer, and F. Zagolski. *Reference Model for MERIS Level 2 Processing Third MERIS reprocessing: Ocean Branch*. ESA, ARGANS, ACRI, 2011. 4.1, 4.2.2

[89] L. Kendall, F. Carder, Chen Robert, Lee Zhongping, Steve K. Hawes, and Jennifer P. Cannizzaro. *MODIS Ocean Science Team Algorithm Theoretical Basis Document*. College of Marine Science University of South Florida, 2003. 4.1, 4

[90] R. A. Locarnini, A. V. Mishonov, J. I. Antonov, T. P. Boyer, H. E. Garcia, O. K. Baranova, M. M. Zweng, and D. R. Johnson, editors. *World Ocean Atlas 2009 Volume 1: Temperature*. NOAA Atlas NESDIS 68, U.S. Government Printing Office, Washington, D.C., U.S. Government Printing Office, Washington, D.C., 2010. 4.1.3b, 4.2.2, 4.2.5

[91] Susan Solomon, Dahe Qin, and Martin Manning, editors. *IPCC Fourth Assessment Report Working Group Report: "The Physical Science Basis"*. Intergovernmental Panel on Climate Change, 2007. `http://www.ipcc.ch/ipccreports/ar4-wg1.htm`. 4.1.4, 4.1.5

[92] James Haywood and Olivier Boucher. Estimates of the direct and indirect radiative forcing due to tropospheric aerosols: A review. *Rev. Geophys.*, 38(4):513–543, 2000. 4.1.5

[93] F. Janssen, C. Schrum, and J. O. Backhaus. A climatological data set of temperature and salinity for the baltic sea and the north sea. *Ocean Dynamics*, 51:5–245, 1999. 4.2.2

[94] R.W. Macdonald, F.A. McLaughlin, and E.C. Carmack. Fresh water and its sources during the sheba drift in the canada basin of the arctic ocean. *Deep Sea Research Part I: Oceanographic Research Papers*, 49(10):1769 – 1785, 2002. 4.2.2

[95] Miles G. McPhee, Timothy P. Stanton, James H. Morison, and Douglas G. Martinson. Freshening of the upper ocean in the arctic: Is perennial sea ice disappearing? *Geophys. Res. Lett.*, 25(10):1729–1732, 1998. 4.2.2, 4.2.5

[96] D.M.A. Schaap and G. Maudire. SeaDataNet - Pan-European infrastructure for marine and ocean data management: Unified access to distributed data sets. *Geophysical Research Abstracts*, 11, 2009. EGU 2009. 4.2.2

[97] SeaDataNet Regional Product Prototype. Diva 4d analysis of sali.19752005, salinity masked using relative error threshhold 0.3. http://gher-diva.phys.ulg.ac.be/web-vis/clim.html, last visited 11/2011. 4.2.2

[98] Dean Roemmich and John Gilson. The 2004 - 2008 mean and annual cycle of temperature, salinity, and steric height in the global ocean from the argo program. *Progress In Oceanography*, 82(2):81 – 100, 2009. 4.2.2

[99] Jean-Rene Donguy and Gary Meyers. Seasonal variations of sea-surface salinity and temperature in the tropical indian ocean. *Deep Sea Research Part I: Oceanographic Research Papers*, 43(2):117 – 138, 1996. 4.2.2

[100] U. Klein, B. Berruti, F. Borde, J. Frerick, J. Nieke, J. Stroede, and C. Mavrocordatos. Sentinel-3 payload overview. *Proc. SPIE 7474, 747405*, 2009. 4.2.2, 4.2.5, 4.3.9

[101] M. Smoluchowski. Molekular-kinetische theorie der opaleszenz von gasen im kritischen zustande, sowie einiger verwandter erscheinungen. *Annalen der Physik*, 330(2):205–226, 1908. 4.2.3

[102] A. Einstein. Theorie der Opaleszenz von homogenen Flüssigkeiten und Flüssigkeitsgemischen in der Nähe des kritischen Zustandes. *Annalen der Physik*, 14:368–391, 1910. 4.2.3

[103] James E. Hansen and Larry D. Travis. Light scattering in planetary atmospheres. *Space Science Reviews*, 16(4):527–610, 1974. 4.2.3

[104] Lord Rayleigh. On the scattering of light by a cloud of similar small particles of any shape and oriented at random. *Phil. Mag.*, 35:373, 1918. 4.2.3

[105] A. Morel. Optical properties of pure water and pure sea water. *Optical aspects of oceanography*, 1974. 4.2.3

[106] Stephen G. Warren. Optical constants of ice from the ultraviolet to the microwave. *Appl. Opt.*, 23(8):1206–1225, Apr 1984. 8

[107] Theodore J. Petzold. Volume scattering functions for selected ocean waters. *SCRIPPS INSTITUTION OF OCEANOGRAPHY LA JOLLA CA VISIBILITY LAB*, 1972. 4.2.4, 4.2.4

[108] Kenneth J. Voss and Edward S. Fry. Measurement of the mueller matrix for ocean water. *Appl. Opt.*, 23(23):4427–4439, Dec 1984. 4.2.4

[109] E. S. Fry and K. J. Voss. Measurement of the mueller matrix for phytoplankton. *Limnology and Oceanography*, 30(6):pp. 1322–1326, 1985. 4.2.4

[110] H. Volten, J. F. de Haan, J. W. Hovenier, R. Schreurs, W. Vassen, A. G. Dekker, H. J. Hoogenboom, F. Charlton, and R. Wouts. Laboratory measurements of angular distributions of light scattered by phytoplankton and silt. *Limnology and Oceanography*, 43(6):pp. 1180–1197, 1998. 4.2.4

[111] Ankur Gogoi, Alak K. Buragohain, Amarjyoti Choudhury, and Gazi A. Ahmed. Laboratory measurements of light scattering by tropical fresh water diatoms. *Journal of Quantitative Spectroscopy and Radiative Transfer*, 110(14-16):1566 – 1578, 2009. ¡ce:title¿XI Conference on Electromagnetic and Light Scattering by Non-Spherical Particles: 2008¡/ce:title¿. 4.2.4

[112] C. B. Markwardt. Non-linear Least Squares Fitting in IDL with MPFIT. *Astronomical Data Analysis Software and Systems XVIII*, Vol. 411:251–254, 2008. 10, 4.3.9

[113] R. A. McClatchey, R. W. Fenn, J. E. A. Selby, F. E. Volz, and J. S. Garing. *Optical Properties of the Atmosphere (Third Edition)*. AIR FORCE CAMBRIDGE RESEARCH LABS HANSCOM AFB MA, 1972. 4.2.5, 4.4.4

[114] L.S. Rothman, I.E. Gordon, A. Barbe, D.Chris Benner, P.F. Bernath, M. Birk, V. Boudon, L.R. Brown, A. Campargue, J.-P. Champion, K. Chance, L.H. Coudert, V. Dana, V.M. Devi, S. Fally, J.-M. Flaud, R.R. Gamache, A. Goldman, D. Jacquemart, I. Kleiner, N. Lacome, W.J. Lafferty, J.-Y. Mandin, S.T. Massie, S.N. Mikhailenko, C.E. Miller, N. Moazzen-Ahmadi, O.V. Naumenko, A.V. Nikitin, J. Orphal, V.I. Perevalov, A. Perrin, A. Predoi-Cross, C.P. Rinsland, M. Rotger, M. Simecková, M.A.H. Smith, K. Sung, S.A. Tashkun, J. Tennyson, R.A. Toth, A.C. Vandaele, and J. Vander Auwera. The hitran 2008 molecular spectroscopic database. *Journal of Quantitative Spectroscopy and Radiative Transfer*, 110(9-10):533 – 572, 2009. 4.2.5, 4.3.5

[115] George W. Kattawar, Gilbert N. Plass, and Stephen J. Hitzfelder. Multiple scattered radiation emerging from rayleigh and continental haze layers. 1: Radiance, polarization, and neutral points. *Appl. Opt.*, 15(3):632–647, Mar 1976. 4.2.5, 4.2.5

[116] Howard R. Gordon, James W. Brown, and Robert H. Evans. Exact rayleigh scattering calculations for use with the nimbus-7 coastal zone color scanner. *Appl. Opt.*, 27(5):862–871, Mar 1988. 4.2.5, 4.2.5

[117] George W. Kattawar and Charles N. Adams. Errors induced when polarization is neglected in radiance calculations for an atmosphere-ocean. *Proceedings of SPIE*, 1749, 1992. 4.2.5, 4.2.5

[118] Barry A. Bodhaine, Norman B. Wood, Ellsworth G. Dutton, and James R. Slusser. On rayleigh optical depth calculations. *Journal of Atmospheric and Oceanic Technology*, 16:1854–1861, 1999. 12

[119] Mian Chin, Ralph A. Kahn, and Stephen E. Schwartz, editors. *CCSP 2009: Atmospheric Aerosol Properties and Climate Impacts, A Report by the U.S. Climate Change Science Program and the Subcommittee on Global Change Research.* National Aeronautics and Space Administration, Washington, D.C., USA, 2009. 4.3.2

[120] U. Lohmann and J. Feichter. Global indirect aerosol effects: a review. *Atmospheric Chemistry and Physics*, 5(3):715–737, 2005. 4.3.2

[121] A.J. McMichael, D.H. Campbell-Lendrum, C.F. Corvalán, K.L. Ebi, A.K. Githeko, J.D. Scheraga, and A. Woodward, editors. *Climate change and human health*. WHO Library Cataloguing-in-Publication Data, 2003. 4.3.2

[122] Ulrich Pöschl. Atmospheric aerosols: Composition, transformation, climate and health effects. *Angewandte Chemie International Edition*, 44(46):7520–7540, 2005. 4.3.2

[123] A. L. Quijano, I. N. Sokolik, and O. B. Toon. Influence of the aerosol vertical distribution on the retrievals of aerosol optical depth from satellite radiance measurements. *Geophys. Res. Lett.*, 27(21):3457–3460, 2000. 4.3.2

[124] Lucile Duforêt, Robert Frouin, and Philippe Dubuisson. Importance and estimation of aerosol vertical structure in satellite ocean-color remote sensing. *Appl. Opt.*, 46:1107–1119, 2007. 4.3.2, 4.3.2

[125] J.-P. Muller, R. Preusker, J. Fischer, M. Zuhlke, C. Brockmann, and P. Regner. Albedomap: Meris land surface albedo retrieval using data fusion with modis brdf and its validation using contemporaneous eo and in situ data products. *Geoscience and Remote Sensing Symposium, 2007. IGARSS 2007. IEEE International*, pages 2404 – 2407, 2007. 4.3.2, 4.3.10, 4.3.13, 4.4.3, 4.4.5a

[126] A. Amodeo, G. Pappalardo, J. Bösenberg, A. Ansmann, A. Apituley, L. Alados-Arboledas, D. Balis, C. Böckmann, A. Chaikovsky, A. Comeron, V. Freudenthaler, O. Gustaffson, G. Hansen, V. Mitev, D. Nicolae, A. Papayannis, M.R. Perrone, A. Pietruczuk, M. Pujadas, J.P. Putaud, F. Ravetta, V. Rizi, V. Simeonov, N. Spinelli, D. Stoyanov, T. Trickl, and M. Wiegner. A european research infrastructure for the aesorol study on a continental scale: Earlinet-asos. *Proceedings of the SPIE 6367*, pages 6745–67450Y, 2007. 4.3.2, 4.4.6

[127] Paul Zieger, Thomas Ruhtz, Réne Preusker, and Jürgen Fischer. Dual-aureole and sun spectrometer system for airborne measurements of aerosol optical properties. *Applied Optics*, 46(35):8542–8552, 2007. 4.3.2

[128] J. M. Rosen, D. J. Hofmann, and Jean Laby. Stratospheric aerosol measurements ii: The worldwide distribution. *J. Atmos. Sci.*, 32(7):1457–1462, July 1975. 4.3.2

[129] David M. Winker, Mark A. Vaughan, Ali Omar, Yongxiang Hu, Kathleen A. Powell, Zhaoyan Liu, William H. Hunt, and Stuart A. Young. Overview of the calipso mission and caliop data processing algorithms. *J. Atmos. Oceanic Technol.*, 26(11):2310–2323, November 2009. 4.3.2, 4.3.5, 4.4.2, 4.4.6

[130] D. M. Winker, J. Pelon, J. A. Coakley, S. A. Ackerman, R. J. Charlson, P. R. Colarco, P. Flamant, Q. Fu, R. M. Hoff, C. Kittaka, T. L. Kubar, H. Le Treut, M. P. McCormick, G. Mégie, L. Poole, K. Powell, C. Trepte, M. A. Vaughan, and B. A. Wielicki. The calipso mission: A global 3d view of aerosols and clouds. *Bull. Amer. Meteor. Soc.*, 91(9):1211–1229, March 2010. 4.3.2

[131] Marco Gabella, Vlatcheslav Kisselev, and Giovanni Perona. Retrieval of aerosol profile variations from reflected radiation in the oxygen absorption a band. *Appl. Opt.*, 38(15):3190–3195, May 1999. 4.3.2

[132] KOPPERS G. A. A., JANSSON J., and MURTAGH D. P. Aerosol optical thickness retrieval from gome data in the oxygen a-band. *ERS symposium on space at the service of our environment No3, Florence , ITALIE (14/03/1997)*, 1997. 4.3.2

[133] Stefano Corradini and Marco Cervino. Aerosol extinction coefficient profile retrieval in the oxygen a-band considering multiple scattering atmosphere. test case: Sciamachy nadir simulated measurements. *Journal of Quantitative Spectroscopy and Radiative Transfer*, 97(3):354 – 380, 2006. 4.3.2

[134] Bruno Pelletier, Robert Frouin, and Philippe Dubuisson. Retrieval of the aerosol vertical distribution from atmospheric radiance. *Proc. SPIE 7150*, 71501R, 2008. 4.3.2

[135] S. Sanghavi, J. V. Martonchik, J. Landgraf, and U. Platt. Retrieval of aerosol optical depth and vertical distribution using O_2A- and B-band sciamachy observations over kanpur: a case study. *Atmospheric Measurement Techniques Discussions*, 4(6):6779–6809, 2011. 4.3.2

[136] C. Frankenberg, O. Hasekamp, C. O'Dell, S. Sanghavi, A. Butz, and J. Worden. Aerosol information content analysis of multi-angle high spectral resolution measurements and its benefit for high accuracy greenhouse gas retrievals. *Atmospheric Measurement Techniques Discussions*, 5(2):2857–2885, 2012. 4.3.2

[137] Andrew K. Heidinger and Graeme L. Stephens. Molecular line absorption in a scattering atmosphere. part ii: Application to remote sensing in the o2 a band. *J. Atmos. Sci.*, 57(10):1615–1634, May 2000. 4.3.2

[138] Philippe Dubuisson, Robert Frouin, David Dessailly, Lucile Duforêt, Jean-Francois Léon, Kenneth Voss, and David Antoine. Estimating the altitude of aerosol plumes over the ocean from reflectance ratio measurements in the o2 a-band. *Remote Sensing of Environment*, 113(9):1899 – 1911, 2009. 4.3.2

[139] L. G. Tilstra, I. Aben, and P. Stammes. Quality of the radiometric calibration of sciamachy v6.03. *SRON-EOS-RP-08-025*, March 11 2008. 4.3.2

[140] S. Slijkhuis and J. Frerick. Sciamachy polarisation sensitivity. *Looking Down to Earth in the New Millennium: Proceedings ERS/Envisat Symposium Gothenborg, Eur. Space Agency Spec. Publ., ESA-SP-461*, 2000. 4.3.2

[141] N. A. J. Schutgens and P. Stammes. A novel approach to the polarization correction of spaceborne spectrometers. *J. Geophys. Res.*, 108(D7):4229–, April 2003. 4.3.2

[142] Takashi Hamazaki, Yutaka Kaneko, Akihiko Kuze, and Kayoko Kondo. Fourier transform spectrometer for greenhouse gases observing satellite (gosat). *Proc. SPIE. Vol. SPIE*, 5659:73–80, 2005. 4.3.2

[143] T. Yokota, Y. Yoshida, N. Eguchi, Y. Ota, T. Tanaka, H. Watanabe, and S. Maksyutov. Global concentrations of CO_2 and CH_4 retrieved from GOSAT: First preliminary results. *SOLA*, 5:160–163, 2009. 4.3.2

[144] Robert Haring, Randy Pollock, Brian M. Sutin, and David Crisp. The orbiting carbon observatory instrument optical design. *Current Developments in Lens Design and Optical Engineering V*, 14. October 2004. 4.3.2

[145] David Crisp and Christyl Johnson. The orbiting carbon observatory mission. *Acta Astronautica*, 56:193–197, 2005. IAA International Symposium on Small Satellites for Earth Observation. 4.3.2

[146] J.-L. Bézy, P. Bensi, M. Berger, B.Carnicero, M. Davidson, M.Drinkwater, Y.Durand, F.Héliere, P.Ingmann, J. Langen, C.C. Lin, R. Meynart, H. Rebhan, P. Silvestrin, and A.Thompson. Esa future earth observation explorer missions. *Proc. of SPIE*, 7081:70810S, 2008. 4.3.2

[147] Y.J. Meijer, P. Ingmanna, A. Löscher, and the CarbonSat Mission Advisory Group Team. Carbonsat: Esa's earth explorer 8 candidate mission. *Geophysical Research Abstracts*, 14 EGU2012-2474-1, 2012. 4.3.2, 4.4.6

[148] P. Clissold, editor. *ESA SP-1313/4 Candidate Earth Explorer Core Missions - Reports for Assessment: FLEX - FLuorescence EXplorer*. ESA Communication Production Office, 2008. 4.3.2, 4.3.4

[149] Uwe Rascher, Beniamino Gioli, and Franco Miglietta. Flex - fluorescence explorer: A remote sensing approach to quantify spatio-temporal variations of photosynthetic efficiency from space. In John F. Allen, Elisabeth Gantt, John H. Golbeck, and Barry Osmond, editors, *Photosynthesis. Energy from the Sun*, pages 1388–1390. Springer Netherlands, 2008. 4.3.2, 4.3.4

[150] M.P. Stoll. The FLEX-fluorescence explorer mission project: motivations and present status of preparatory activities. *Geoscience and Remote Sensing Symposium, 2003. IGARSS '03. Proceedings. 2003 IEEE International*, 1:585 – 587, 2003. 4.3.2, 4.3.4, 4.4.6

[151] V. A. Velazco, M. Buchwitz, H. Bovensmann, M. Reuter, O. Schneising, J. Heymann, T. Krings, K. Gerilowski, and J. P. Burrows. Towards space based verification of CO_2 emissions from strong localized sources: fossil fuel power plant emissions as seen by a carbonsat constellation. *Atmospheric Measurement Techniques*, 4(12):2809–2822, 2011. 4.3.2

[152] P. Clissold, editor. *ESA SP-1313/4 Candidate Earth Explorer Core Missions - Reports for Assessment: FLEX - FLuorescence EXplorer*. ESA Communication Production Office, 2008. 4.3.2

[153] Stefan Kraft. FLORIS SNR estimation model. IPD-TN-ESA-261, 8. May 2012. 4.3.2, 4.3.4, 4.3.4, 4.3.8

[154] H. Bovensmann, M. Buchwitz, and J. P. Burrows. Carbon monitoring satellite (carbonsat) as an earth explorer opportunity mission mission overview. Version: 10 June 2010, June 2010. 4.3.2

[155] Jason O. Day, Christopher W. O'Dell, Randy Pollock, Carol J. Bruegge, David Rider, David Crisp, and Charles E. Miller. Preflight spectral calibration of the orbiting carbon observatory. *IEEE TRANSACTIONS ON GEOSCIENCE AND REMOTE SENSING*, 49:2793–2801, 2011. 4.3.2

[156] Akihiko Kuze, Hiroshi Suto, Masakatsu Nakajima, and Takashi Hamazaki. Thermal and near infrared sensor for carbon observation fourier-transform spectrometer on the greenhouse gases observing satellite for greenhouse gases monitoring. *Appl. Opt.*, 48(35):6716–6733, Dec 2009. 4.3.2

[157] T. Hamazaki, Y. Kaneko, and A. Kuze. Carbon dioxide monitoring from the gosat satellite. *Proceedings XXth ISPRS conference*, 2004. 4.3.2, 4.4.1b, 4.4.2, 4.4.3b

[158] Herbert J. Kramer. Observation of the earth and its environment: Survey of missions and sensors. `http://www.eoportal.org/directory/pres_MyriadeCNESMicrosatelliteProgram.html`. 4.3.3a

[159] L. Alonso, J. Verrelst, and J. Moreno. The determination of optimal spectral resolution (sr) and signal-to-noise ratio (snr) for floris. Technical Note, ESA FLUSS Project, 2012. 4.3.4

[160] Hess, M., P. Koepke, and I. Schult. Optical Properties of Aerosols and Clouds: The Software Package OPAC. *Bulletin of the American Meteorological Society*, 79:831 – 844, 1998. 4.3.5

[161] Oleg Dubovik, Brent Holben, Thomas F. Eck, Alexander Smirnov, Yoram J. Kaufman, Michael D. King, Didier Tanré, and Ilya Slutsker. Variability of absorption and optical properties of key aerosol types observed in worldwide locations. *J. Atmos. Sci.*, 59(3):590–608, February 2002. 4.3.5

[162] Lorraine A. Remer and Yoram J. Kaufman. Dynamic aerosol model: Urban/industrial aerosol. *J. Geophys. Res.*, 103(D12):13859–13871, 1998. 4.3.5

[163] W. J. Wiscombe. Improved mie scattering algorithms. *Applied Optics*, 19(9):1505–1509, 1980. 4.3.5

[164] Stéphane Jacquemoud, Wout Verhoef, Frédéric Baret, Cédric Bacour, Pablo J. Zarco-Tejada, Gregory P. Asner, Christophe Francois, and Susan L. Ustin. PROSPECT + SAIL models: A review of use for vegetation characterization. *Remote Sensing of Environment*, 113, Supplement 1(0):S56 – S66, 2009. ¡ce:title¿Imaging Spectroscopy Special Issue¡/ce:title¿. 4.3.10, 4.4.6

[165] R. Pedrós, Y. Goulas, S. Jacquemoud, J. Louis, and I. Moya. Fluormodleaf: A new leaf fluorescence emission model based on the prospect model. *Remote Sensing of Environment*, 114(1):155 – 167, 2010. 4.3.10, 4.4.6

[166] OpenMP Architecture Review Board. OpenMP application program interface version 3.0, May 2008. `http://openmp.org/wp/openmp-specifications/`. 4.3.5

[167] Aguirre Miguel, Berruti Bruno, Bezy Jean-Loup, Drinkwater Mark, Heliere Florence, Klein Ulf, Mavrocordatos Constantinos, Silvestrin Pierluigi, Greco Bruno, and Benveniste Jerome. Sentinel-3 - the ocean and medium-resolution land mission for gmes operational services. *ESA Bulletin (ISSN 0376-4265)*, 131:24 – 29, 2007. 4.3.9

[168] Peter North, Will Grey, Andreas Heckel, Jürgen Fischer, Rene Preusker, and Carsten Brockmann. Meris/aatsr synergy algorithms for cloud screening, aerosol retrieval, and atmospheric correction. Technical report, ESRIN Contract No. 21090/07/I-LG, 2009. 4.3.9

[169] Peter R. J. North. Estimation of aerosol opacity and land surface bidirectional reflectance from atsr-2 dual-angle imagery: Operational method and validation. *JOURNAL OF GEOPHYSICAL RESEARCH*, 107, 2002. 4.3.9

[170] William M. F. Greya, Peter R. J. North, Sietse O. Los, and Ross M. Mitchell. Aerosol optical depth and land surface reflectance from multiangle aatsr measurements: Global validation and intersensor comparisons. *IEEE TRANSACTIONS ON GEOSCIENCE AND REMOTE SENSING,*, 44(8), 2006. 4.3.9

[171] Peter R. J. North, Stephen A. Briggs, Stephen E. Plummer, and Jeffery J. Settle. Retrieval of land surface bidirectional reflectance and aerosol opacity from ATSR-2 multiangle imagery. *IEEE TRANSACTIONS ON GEOSCIENCE AND REMOTE SENSING*, 37(1), 1999. 4.3.9

[172] F. Molteni, R. Buizza, T. N. Palmer, and T. Petroliagis. The ECMWF ensemble prediction system: Methodology and validation. *Quarterly Journal of the Royal Meteorological Society*, 122(529):73–119, 1996. 4.3.9

[173] Tom G. Farr, Paul A. Rosen, Edward Caro, Robert Crippen, Riley Duren, Scott Hensley, Michael Kobrick, Mimi Paller, Ernesto Rodriguez, Ladislav Roth, David Seal, Scott Shaffer, Joanne Shimada, Jeffrey Umland, Marian Werner, Michael Oskin, Douglas Burbank, and Douglas Alsdorf. The shuttle radar topography mission. *Rev. Geophys.*, 45(2):RG2004–, May 2007. 4.3.9

[174] Rui M. Ponte and Joel Dorandeu. Uncertainties in ECMWF surface pressure fields over the ocean in relation to sea level analysis and modeling. *J. Atmos. Oceanic Technol.*, 20(2):301–307, February 2003. 4.3.9

[175] David A. Salstein, Rui M. Ponte, and Karen Cady-Pereira. Uncertainties in

atmospheric surface pressure fields from global analyses. *J. Geophys. Res.*, 113(D14):D14107, jul 2008. 4.3.9

[176] Kenneth Levenberg. A method for the solution of certain non-linear problems in least squares. *Quarterly of Applied Mathematics*, 2:164–168, 1944. 4.3.9

[177] E. F. Vermote, N. El Saleous, C. O. Justice, Y. J. Kaufman, J. L. Privette, L. Remer, J. C. Roger, and D. Tanre. Atmospheric correction of visible to middle-infrared EOS-MODIS data over land surfaces: Background, operational algorithm and validation. *J. Geophys. Res.*, 102(D14):17131–17141, 1997. 4.3.10

[178] Crystal B Schaaf, Feng Gao, Alan H Strahler, Wolfgang Lucht, Xiaowen Li, Trevor Tsang, Nicholas C Strugnell, Xiaoyang Zhang, Yufang Jin, Jan-Peter Muller, Philip Lewis, Michael Barnsley, Paul Hobson, Mathias Disney, Gareth Roberts, Michael Dunderdale, Christopher Doll, Robert P d'Entremont, Baoxin Hu, Shunlin Liang, Jeffrey L Privette, and David Roy. First operational BRDF, albedo nadir reflectance products from MODIS. *Remote Sensing of Environment*, 83(1-2):135–148, 2002. http://www.sciencedirect.com/science/article/pii/S0034425702000913. 4.3.10

[179] Japan Aerospace Exploration Agency (JAXA). Greenhouse Gases Observing Satellite "IBUKI" (GOSAT) "First Light" Acquired by Onboard Sensors. Press Release from February 9, 2009, http://www.jaxa.jp/press/2009/02/20090209_ibuki_e.html, last visited 09/2012. 4.4.2, 4.4.3a

[180] Japan Aerospace Exploration Agency, editor. *GOSAT/IBUKI Data User Handbook*. National Institute for Environmental Studies Ministry of the Environment, 2011. 4.4.2

[181] Robert L. Kurucz. New atlases for solar flux, irradiance, central intensity, and limb intensity. *Memorie della Società Astronomica Italiana Supplement*, 8:189, 2005. 4.4.3, 4.4.4, 4.4.4

[182] G. Kirchhoff. Über die Fraunhofer'schen linien. *Annalen der Physik*, 185(1):148–150, 1860. 4.4.3

[183] A. Jarvis, H.I. Reuter, A. Nelson, and E. Guevara. Hole-filled seamless srtm data v4. International Centre for Tropical Agriculture (CIAT), available from http://srtm.csi.cgiar.org., 2008. 4.4.3, 4.4.5b

[184] H.I. Reuter, A. Nelson, and A. Jarvis. An evaluation of void filling interpolation methods for srtm data. *International Journal of Geographic Information Science*, 21:9:983–1008, 2007. 4.4.3, 4.4.5b

[185] Rainer Storn and Kenneth Price. Differential evolution - a simple and efficient heuristic for global optimization over continuous spaces. *Journal of Global Optimization*, 11:341–359, 1997. 10.1023/A:1008202821328. 4.4.4

[186] Inc. Wolfram Research. Numerical nonlinear global optimization. http://reference.wolfram.com/mathematica/tutorial/ConstrainedOptimizationGlobalNumerical.html, last visited: 10/2012, 2012. 4.4.4

[187] John A. Nelder and R. Mead. A simplex method for function minimization. *Computer Journal*, 7:308–313, 1965. 4.4.4

[188] J. F. GRAINGER and J. RING. Anomalous fraunhofer line profiles. *Nature*, 193(4817):762–762, 1962. http://dx.doi.org/10.1038/193762a0. 4.4.5

[189] Christopher E. Sioris and Wayne F. J. Evans. Impact of rotational raman scattering in the O_2A band. *Geophys. Res. Lett.*, 27(24):4085–4088, 2000. 4.4.5

[190] H. Tran and J.-M. Hartmann. An improved O_2A band absorption model and its consequences for retrievals of photon paths and surface pressures. *J. Geophys. Res.*, 113:D18104, September 2008. 4.4.5, 4.4.9a

[191] R. Lindstrot and R. Preusker. On the efficient treatment of temperature profiles for the estimation of atmospheric transmittance under scattering conditions. *Atmospheric Measurement Techniques Discussions*, 5(3):4473–4494, 2012. 4.4.5, 4.4.9b

[192] Bjorn Stevens and Graham Feingold. Untangling aerosol effects on clouds and precipitation in a buffered system. *Nature*, 461(7264):607–613, 2009. 4.4.6

[193] Frank Raes. Entrainment of free tropospheric aerosols as a regulating mechanism for cloud condensation nuclei in the remote marine boundary layer. *J. Geophys. Res.*, 100(D2):2893–2903, 1995. 4.4.6

[194] Ralph R. Basilio, Thomas R. Livermore, Y. Janet Shen, and H. R. Pollock. The quest for an OCO (orbiting carbon observatory) re-flight. *Proc. SPIE 7827 Remote Sensing of Clouds and the Atmosphere XV*, pages 78270A–78270A–9, 2010. http://dx.doi.org/10.1117/12.867042. 4.4.6

DANKSAGUNG

Ich danke meinem Doktorvater Herrn Prof. Dr. Jürgen Fischer für die Möglichkeit am Institut für Weltraumwissenschaften der Freien Universität Berlin promovieren zu können und im Besonderen für die großen gestalterischen Freiräume, die er mir bei der Bearbeitung der behandelten wissenschaftlichen Fragestellungen eingeräumt hat, sowie Herrn Prof. Dr. Ralf Bennartz für die Übernahme des Zweitgutachtens. Ich bedanke mich bei allen Institutsangehörigen, die mir mit Rat und Tat sowie ungezählten Diskussionen und Gesprächen zur Seite gestanden haben. Besonders, und ohne Bedeutung der Reihenfolge, möchte ich mich bei Jonas von Bismarck, Rasmus Lindstrot, René Preusker, und Thomas Ruhtz bedanken. Auch gilt mein Dank allen Mitautoren der im Rahmen dieser Arbeit entstandenen Veröffentlichungen für die sehr gute und kollegiale Zusammenarbeit.

Ich versichere, dass ich diese Arbeit selbständig verfasst und keine anderen, als die angegebenen Quellen und Hilfsmittel benutzt habe. Diese Arbeit wurde in keinem früheren Promotionsverfahren eingereicht. Die Arbeit wurde ohne unzulässige Hilfe Dritter verfasst.

Ort, Datum

Unterschrift

Freie Universität  Berlin